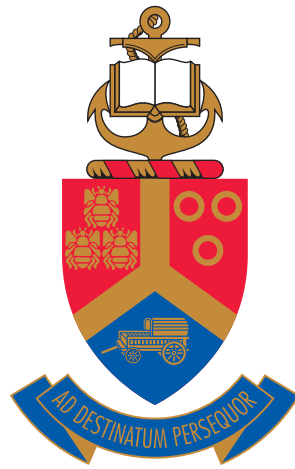


# Development and characterization of a tuneable AlGaIn-based solar-blind UV-sensitive Schottky photodiode



by

**Louwrens van Schalkwyk**

Submitted in partial fulfilment of the requirements for the degree

*Magister Scientiae*

in the Department of Physics

in the Faculty of Natural and Agricultural Sciences

University of Pretoria

Pretoria

September 2015

Supervisor: Prof. W.E. Meyer

Co-supervisor: Prof. F.D. Auret

## Declaration of originality

1. I, Louwrens van Schalkwyk, understand what plagiarism is and am aware of the University of Pretoria's policy in this regard.
2. I declare that this dissertation, which I hereby submit for the degree *Magister Scientiae* at the University of Pretoria, is my own original work and has not previously been submitted by me for a degree at this or any other tertiary institution. Where other people's work has been used (either from a printed source, Internet or any other source), this has been properly acknowledged and referenced in accordance with departmental requirements.
3. I have not used work previously produced by another student or any other person to hand in as my own.
4. I have not allowed, and will not allow, anyone to copy my work with the intention of passing it off as his or her own work.

Signature: .....

Louwrens van Schalkwyk

Student number: 0425 0540

Date: September 2015



Concern for man himself and his fate must always form the chief objective of all technological endeavors . . . in order that the creations of our minds shall be a blessing and not a curse to mankind. Never forget this in the midst of your diagrams and equations.

~ From an address entitled "Science and Happiness,"  
presented at the California Institute of Technology,  
Feb. 16, 1931. Quoted in the *New York Times*,  
Feb. 17 and 22, 1931. Einstein Archives 36-320



Moenie eers skryf en dan dink nie.  
Dink liever eers en skryf dan.  
Skryfwoorde is nie mondwoorde wat wegwaai nie.  
Of wat jy later kan oorstry nie.

~ C.J. Langenhoven



Your standard of excellence is what will separate you from others. The greatest enemy of excellence is compromise: whatever it takes to get by at the time. Consistency is the foundation for excellence. If you are consistent in the application of excellence in all things, then this will become instinctive. Creating a culture of excellence is a huge win for any leader. Since we have learned that culture is difficult to learn, then it must be a part of who we are at all times.

~ Dave Dungan



## Acknowledgements

---

I wish to extend my sincere gratitude to the following people and institutions for their contribution toward the completion of this research study and dissertation:

My supervisor Prof. W.E. Meyer, co-supervisor Prof. F.D. Auret and the rest of the staff in the Electronic Materials and Thin Film Research Group for their assistance, guidance and continuous support throughout.

Dr. S.M.M. Coelho for his assistance and guidance with the operating of the physical vapour deposition systems, along with proof reading this text.

Mr. P.J. Janse van Rensburg for the use of the electrical characterization NI LabVIEW routine (GUP) developed by him and his assistance during the programming of the spectral characterization NI LabVIEW routine.

Mr. H. de Meyer for his help with solving NI LabVIEW related programming challenges and moral support.

Mr. J. Wallis, Mr. R. Stolper, Mr. C. Coetzer and Mr. W. van der Westhuizen of the SST competence area of the CSIR MSM unit for their guidance and demonstrating the working solar-blind UV-sensitive electro-optic device.

The Heads of the Department of Physics, Prof. C.C. Theron, and his predecessor Prof. J.B. Malherbe, for approving this study and for part-time work in the department.

Our department secretary, Mrs. E.A. Meyburgh, for her administrative assistance, especially with the placing of orders.

The technical support staff and the staff from the other research groups for their willingness to assist.

My friends, Gideon Hanekom, Hein Meiring, Tienie Schoeman, Sampie Smit and Kobus van Wyk for their moral support and encouragement.

My parents Jasper & Hannelie, and my brother André for their faith in my abilities and support in completing this endeavour by giving me the environment and opportunity to do so.

## Financial support

---

This work is based upon research supported by the Technology Innovation Agency (TIA) and the National Research Foundation<sup>†</sup> (NRF).

<sup>†</sup> *Disclaimer:* Any opinion, findings and conclusions or recommendations expressed in this material are those of the author(s) and therefore the NRF does not accept any liability in regard thereto.

## Abstract

---

### Development and characterization of a tuneable AlGa<sub>N</sub>-based solar-blind UV-sensitive Schottky photodiode

by

**Louwrens van Schalkwyk**

Supervisor: Prof. W.E. Meyer  
Co-supervisor: Prof. F.D. Auret  
Degree: *Magister Scientiae*  
Keywords: aluminium gallium nitride, iridium(IV) oxide, optoelectronic, photodiode, Schottky, solar-blind, ultraviolet, UV-to-visible rejection ratio

Several applications require the detection of terrestrial UV-C signatures. Efficiency, compactness, environmentally friendly and cost-effective requirements for UV-C-detectors resulted in a research interest in wide-bandgap (WBG) semiconductor-based photovoltaic diodes with a 280 nm cut-off wavelength. Advances in producing group-III-nitride materials allowed the growth of high quality Al<sub>x</sub>Ga<sub>1-x</sub>N, a direct-WBG ternary semiconductor in which the Al mole fraction ( $x$ ) could be varied, allowing for a tuneable bandgap that made the semiconductor intrinsically 'blind' to longer wavelengths and responsive to selected wavelengths shorter than 360 nm.

This dissertation reports on the development and characterization of a tuneable AlGa<sub>N</sub>-based solar-blind UV-sensitive Schottky photodiode. A fabrication procedure was established using optimized metallization techniques derived from literature. This included metallization schemes, metal thicknesses and annealing methods for metallization of both the ohmic and Schottky contacts for a front-irradiated photodiode.

Characterization was done with a newly constructed optoelectronic characterization system. Electrical characterization was performed inside a light-tight shield.

ded enclosure and a software routine aided in applying current–voltage and capacitance–voltage measurements on a Schottky diode. Spectral characterization made use of either a UV source or a visible-to-near-infrared source that was coupled to a monochromator that allowed for wavelength selection. The monochromatic electromagnetic radiation was guided by an optical fibre from the monochromator into the enclosure where the photodiode was irradiated. An additional software routine was developed that allowed for the automation of the spectral characterization. The system was calibrated against standards traceable to the National Institute of Standards and Technology (NIST) by following the photodetector substitution method.

The study concluded with the manufacturing of an epoxy wire-bonded front-irradiated four-quadrant detector that was mounted on a commercial microchip carrier. Metal depositions were done through physical contact masks. The quadrants were surrounded with optimized layered ohmic contacts and a quadrant consisted of a thin-film iridium(IV) oxide ( $\text{IrO}_2$ ) as Schottky contact that is UV transmissive with a Au contact on top to which a wire was bonded.

Optoelectronic characterization verified that the four-quadrant detector was intrinsically solar-blind and showed good uniformity across the quadrants. Electrical parameters obtained included an average ideality factor of  $1.97 \pm 0.09$ , a Schottky barrier height of  $(1.22 \pm 0.08)$  eV, a reverse leakage current density of  $(2.1 \pm 3.3)$   $\text{nA} \cdot \text{cm}^{-2}$  and a series resistance of  $(120 \pm 30)$   $\Omega$ . Spectral parameters obtained included a  $(275 \pm 5)$  nm cut-off wavelength, an average current responsivity at 250 nm of  $(28 \pm 1.0)$   $\text{mA} \cdot \text{W}^{-1}$  with a quantum efficiency of  $(14 \pm 0.5)$  % and an UV-to-visible and near-infrared rejection ratio between  $10^3$  and  $10^5$  for 400 nm to 1100 nm wavelengths. These characteristics allowed for the detector to be used in demonstrating a working solar-blind UV-sensitive electro-optic device.

## Samevatting

---

### Ontwikkeling en karakterisering van 'n gedefinieerde AlGa<sub>N</sub>-gebaseerde sonblinde UV-sensitiewe Schottky-fotodiode

deur

**Lourens van Schalkwyk**

Studieleier: Prof. W.E. Meyer  
Medestudieleier: Prof. F.D. Auret  
Graad: *Magister Scientiae*  
Sleutelwoorde: aluminium gallium nitried, iridium(IV)-oksied, op-toëlektronies, fotodiode, Schottky, sonblind, ultraviolet, UV-tot-sigbare onderdrukkingsverhouding

Verskeie toepassings vereis die opsporing van aardse UV-C-seine. Doeltreffendheid, kompaktheid, omgewingsvriendelike en koste-effektiewe vereistes vir UV-C-detektors het aanleiding gegee tot 'n belangstelling in navorsing van wye-bandgaping (WBG) halfgeleiergebaseerde fotovoltaïese diodes met 'n 280 nm afsnygolflengte. Vooruitgang in die vervaardiging van groep-III-nitried materiale het gelei tot die groei van hoëgehalte Al<sub>x</sub>Ga<sub>1-x</sub>N, 'n direkte-WBG driedigige halfgeleier waarin die molbreuk Al (x) sodanig verander kon word, dat 'n gedefinieerde bandgaping die halfgeleier wesenlik 'blind' maak vir langer golflengtes en die golflengtesensitiwiteit tot bepaalde goflengtes korter as 360 nm beperk.

Hierdie verhandeling doen verslag rakende die ontwikkeling en karakterisering van 'n gedefinieerde AlGa<sub>N</sub>-gebaseerde sonblinde UV-sensitiewe Schottky-fotodiode. 'n Vervaardigingsprosedure is gevestig met behulp van geoptimaliseerde metalliseringstegnieke wat uit literatuur afgelei is. Dit het metallisering-skemas, metaaldiktes en uitgloeiingsmetodes vir die metallisering van beide die ohmiese en Schottky-kontakte vir 'n frontbestraalde fotodiode ingesluit.

Karakterisering is gedoen met 'n nuutgeboude optoëlektroniese karakterisering-

stelsel. Elektroniese karakterisering is binne 'n ligdigte afgeskermd hok uitgevoer, en 'n sagtewareroetine is vir die uitvoering van stroom- en kapasitan-siespanningsmetings op 'n Schottky-diode aangewend. Spektraalkarakterisering het gebruik gemaak van óf 'n UV-bron, óf 'n sigbare-tot-naby-infrarooi bron wat aan 'n monochromator gekoppel was om bepaalde golflengtes te selekteer. Die monochromatiese elektromagnetiese straling is deur 'n optiese vesel gelei vanaf die monochromator tot in die afgeskermd hok na binne waar die fotodiode be-straal is. 'n Bykomende sagtewareroetine is ontwikkel wat die outomatisering van die spektraalkarakteriseringstegnieke moontlik gemaak het. Verder is die stelsel deur die aanwending van die fotodetektor-vervangingsmetode teen standarde gekalibreer wat na die Nasionale Instituut vir Standarde en Tegnologie (NIST) spoorbaar is.

Die studie is afgehandel met die vervaardiging van 'n epoksie-draad-verbinde frontbestraalde vierkwadrant-detektor wat op 'n kommersiële mikroskyfiedraer gemonteer is. Metaalneerslag is deur middel van fisiese kontakmaskers bewerkstellig. Die kwadrante is met geoptimaliseerde ohmiese kontakte omring, en 'n kwadrant het bestaan uit 'n dun-lagie iridium(IV)-oksied ( $\text{IrO}_2$ ) as Schottky-kontak wat UV deurlatend is, en met 'n Au-kontak daarop waaraan 'n draad verbind kon word.

Optoëlektroniese karakterisering het bewys gelever dat die vierkwadrant-detektor wesenlik sonblind was, en die kwadrante het goeie eenvormigheid getoon. Die bepaalde elektiese parameters wat verkry is, was 'n gemiddelde idealiteitsfaktor van  $1.97 \pm 0.09$ , 'n Schottky walhoogte van  $(1.22 \pm 0.08)$  eV, 'n lekstroomdigtheid van  $(2.1 \pm 3.3)$   $\text{nA} \cdot \text{cm}^{-2}$  by 1 V truvoorspanning en 'n serieweerstand van  $(120 \pm 30)$   $\Omega$ . Die bepaalde spektraalparameters was 'n  $(275 \pm 5)$  nm afsnygolflengte, 'n gemiddelde stroom-responsievermoë by 250 nm van  $(28 \pm 1.0)$   $\text{mA} \cdot \text{W}^{-1}$  met 'n kwantumdoeltreffendheid van  $(14 \pm 0.5)$  %, en 'n



UV-tot-sigbare en naby-infrarooi onderdrukkingsvermoë van tussen  $10^3$  en  $10^5$  vir 400 nm tot 1100 nm golflengtes. Hierdie eienskappe het dit moontlik gemaak om die detektor in die demonstrasie van 'n werkende sonblinde UV-sensitiewe elektro-optiese toestel te gebruik.

# Contents

<b>List of figures</b>	<b>vi</b>
<b>List of tables</b>	<b>vii</b>
<b>1 Introduction</b>	<b>1</b>
1.1 Background . . . . .	1
1.2 Research problem . . . . .	3
1.2.1 Aims . . . . .	3
1.2.2 Objectives . . . . .	4
1.3 Layout of the dissertation . . . . .	5
<b>2 Electromagnetic radiation</b>	<b>8</b>
2.1 Nature of electromagnetic radiation . . . . .	8
2.2 Introductory radiometry . . . . .	10
2.2.1 The solid angle . . . . .	11
2.2.2 Radiometric terms . . . . .	15
2.2.3 Radiant energy interaction with media . . . . .	17
2.2.4 Geometrical invariance of radiance . . . . .	18
2.3 Sources of EMR . . . . .	20
2.3.1 The Sun . . . . .	21
2.3.2 Incandescent lamps . . . . .	23
2.3.3 Discharge lamps . . . . .	23
2.4 UV radiation . . . . .	23
2.4.1 Classification . . . . .	23
2.4.2 Applications . . . . .	25

2.4.3	Detection . . . . .	28
<b>3</b>	<b>Optoelectronics</b>	<b>33</b>
3.1	Solid-state physics . . . . .	34
3.1.1	Electron energy-band structures . . . . .	34
3.1.2	Semiconductor physics . . . . .	38
3.2	The AlGaIn semiconductor . . . . .	44
3.3	Schottky diodes . . . . .	46
3.3.1	The ideal Schottky diode . . . . .	46
3.3.2	Electrical characteristics . . . . .	59
3.4	Photovoltaic diodes . . . . .	69
3.4.1	Photocurrent generation . . . . .	69
3.4.2	Spectral characteristics . . . . .	72
<b>4</b>	<b>The optoelectronic characterization system</b>	<b>75</b>
4.1	Construction overview . . . . .	75
4.2	Calibration theory and method . . . . .	79
4.2.1	Radiometric calibration theory . . . . .	80
4.2.2	Photodetector substitution method . . . . .	82
4.3	Technical specifications . . . . .	83
4.3.1	flexOptometer system . . . . .	83
4.3.2	Electronic equipment . . . . .	84
4.3.3	Control and measurement . . . . .	86
4.3.4	Lamps . . . . .	86
4.3.5	Monochromator . . . . .	88
4.3.6	Optical fibre . . . . .	89
4.4	Properties of the optical fibre . . . . .	89
4.4.1	Numerical aperture . . . . .	90
4.4.2	Spot-size . . . . .	92
4.4.3	Spatial irradiation distribution . . . . .	93
4.5	Experimental set-up . . . . .	94
4.6	Calibration of lamps . . . . .	102

<b>5</b>	<b>Schottky photodiode fabrication</b>	<b>104</b>
5.1	Introduction . . . . .	104
5.2	Experimental . . . . .	105
5.2.1	The AlGaIn semiconductor wafer . . . . .	105
5.2.2	Preparation . . . . .	106
5.2.3	Contact deposition masks . . . . .	109
5.2.4	Ohmic contact fabrication . . . . .	109
5.2.5	Schottky contact fabrication . . . . .	111
5.2.6	Probe contact pad fabrication . . . . .	112
5.2.7	Radiation hardness . . . . .	115
5.2.8	Annealing of the Au probe contacts . . . . .	115
5.2.9	Optoelectronic characterization . . . . .	116
5.3	Results and discussion . . . . .	119
5.3.1	Electrical characterization . . . . .	119
5.3.2	Spectral characterization . . . . .	126
5.3.3	Overall analysis . . . . .	130
5.4	Conclusion . . . . .	135
5.5	Publication . . . . .	135
<b>6</b>	<b>The four-quadrant detector</b>	<b>139</b>
6.1	Introduction . . . . .	139
6.2	Experimental . . . . .	140
6.2.1	The AlGaIn semiconductor wafer . . . . .	140
6.2.2	Contact deposition masks . . . . .	141
6.2.3	Ohmic contact fabrication . . . . .	142
6.2.4	Schottky contact fabrication . . . . .	144
6.2.5	Probe contact pad fabrication . . . . .	144
6.2.6	Epoxy wire bonding . . . . .	145
6.2.7	Optoelectronic characterization . . . . .	146
6.3	Results and discussion . . . . .	149
6.3.1	Electrical Characterization . . . . .	149
6.3.2	Spectral Characterization . . . . .	154

6.4	Conclusion . . . . .	161
6.5	Publication . . . . .	163
<b>7</b>	<b>Conclusions</b>	<b>165</b>
7.1	General . . . . .	165
7.2	Further research . . . . .	166
<b>A</b>	<b>List of symbols</b>	<b>A–1</b>
<b>B</b>	<b>Physical constants</b>	<b>B–1</b>
<b>C</b>	<b>List of acronyms and chemical symbols</b>	<b>C–1</b>
<b>D</b>	<b>Contact mask drawings</b>	<b>D–1</b>
<b>E</b>	<b>Publications</b>	<b>E–1</b>
	Characterization of AlGaIn-based metal–semiconductor solar-blind UV photodiodes with IrO <sub>2</sub> Schottky contacts . . . . .	E–2
	Implementation of an AlGaIn-based solar-blind UV four-quadrant detector	E–7
	<b>References</b>	<b>R–1</b>
	<b>Index</b>	

# List of Figures

2.1	Illustrations of the geometric and the projected solid angles . . . . .	12
2.2	Illustrations of the radiometric terms . . . . .	16
2.3	The spectral solar irradiation of the Sun . . . . .	22
2.4	Illustrations of how UV-C-sensitive electro-optic systems function . . . . .	30
3.1	The possible electron energy-band structures in solids at 0 K . . . . .	35
3.2	Illustrations of direct- and indirect-bandgap semiconductors . . . . .	39
3.3	The AlGa <sub>N</sub> bandgap variation as a function of Al mole fraction . . . . .	45
3.4	The energy-level diagrams of a metal and an <i>n</i> -type semiconductor . . . . .	48
3.5	A detailed energy-level diagram of an ideal Schottky diode . . . . .	55
3.6	The equivalent circuit of a Schottky diode . . . . .	64
3.7	The theoretical <i>J–V</i> characteristics for an arbitrary Schottky diode . . . . .	64
3.8	The theoretical <i>C–V</i> characteristics for an arbitrary Schottky diode . . . . .	67
3.9	The energy-level diagrams of Schottky photodiodes . . . . .	70
4.1	An illustration of the optoelectronic characterization system set-up . . . . .	77
4.2	A photograph of the optoelectronic characterization system . . . . .	78
4.3	An illustration of a radiating source and an irradiated receiver . . . . .	80
4.4	The absolute spectral responsivity of the standard detector . . . . .	85
4.5	A screenshot of the spectral characterization LabVIEW routine . . . . .	87
4.6	An illustration of a step-index optical fibre . . . . .	91
4.7	The SID 90 mm from the optical fibre end at 555 nm . . . . .	96
4.8	The SID 90 mm from the optical fibre end at 675 nm . . . . .	97
4.9	The SID 9 mm from the optical fibre end at 555 nm and 675 nm . . . . .	99
4.10	The irradiance dependence on the axial displacement . . . . .	101

4.11	Typical spectral irradiances from the lamps after calibration . . . . .	103
5.1	Photograph of how samples were typically mounted onto a holder . . . . .	108
5.2	Photographs of the fabricated Schottky photodiodes on A1 . . . . .	113
5.3	Photographs of the fabricated Schottky photodiodes on A2 . . . . .	114
5.4	Photograph of A1 after being irradiated with He-ions . . . . .	125
5.5	The $I-V$ characteristics of a typical Schottky photodiode . . . . .	137
5.6	The spectral responsivities of a typical Schottky photodiode . . . . .	138
6.1	A schematic illustration of the four-quadrant detector . . . . .	142
6.2	Photograph of the first fabricated four-quadrant detector . . . . .	145
6.3	Photographs of the epoxy wire-bonded four-quadrant detector . . . . .	147
6.4	The $I-V$ characteristics of the first four-quadrant detector . . . . .	150
6.5	The $I-V$ characteristics of the second four-quadrant detector . . . . .	151
6.6	The spectral responsivities of the first four-quadrant detector . . . . .	157
6.7	The spectral responsivities of the second four-quadrant detector . . . . .	158
6.8	The UV-to-VIS/NIR rejection of the first four-quadrant detector . . . . .	159
6.9	The UV-to-VIS/NIR rejection of the second four-quadrant detector . . . . .	160
6.10	The UV-C-sensitive electro-optic demonstration device . . . . .	164
Appendix D	Layout of all the four-quadrant detector metal contact masks	D-2
Appendix D	The ohmic contact mask for the four-quadrant detector . . . . .	D-2
Appendix D	The Schottky contact mask for the four-quadrant detector . . . . .	D-3
Appendix D	The Au contact mask for the four-quadrant detector . . . . .	D-3

# List of Tables

2.1	The radiometric terms and their SI derived units . . . . .	17
2.2	Classification of the UVR spectrum . . . . .	25
4.1	The tolerance limits of the Si-based detector . . . . .	84
5.1	The 11OK1234-3 AlGa <sub>N</sub> -based wafer specifications . . . . .	105
5.2	The electrical parameters of the Schottky photodiodes on A1 . . . .	120
5.3	The electrical parameters of the Schottky photodiodes on A2 . . . .	121
5.4	The spectral parameters of the Schottky photodiodes on A1 . . . .	127
5.5	The spectral parameters of the Schottky photodiodes on A2 . . . .	128
5.6	The three Schottky photodiodes with similar electrical trends . . . .	133
5.7	The three Schottky photodiodes with similar spectral trends . . . .	134
5.8	The average electrical parameters of the Schottky photodiodes . . .	137
5.9	The average spectral parameters of the Schottky photodiodes . . . .	138
6.1	The 7LS3825-2 AlGa <sub>N</sub> -based wafer specifications . . . . .	141
6.2	The electrical parameters of the first four-quadrant detector . . . .	150
6.3	The electrical parameters of the second four-quadrant detector . . .	151
6.4	The spectral parameters of the first four-quadrant detector . . . . .	157
6.5	The spectral parameters of the second four-quadrant detector . . . .	158



# Chapter 1

## Introduction

### 1.1 Background

Research and development of electro-optic systems sensitive to specific electromagnetic radiation (EMR) spectra are a high priority. These systems are used to observe and characterize objects that radiate at specific wavelengths, may it be in the infrared (IR, 760 nm to 1.00 mm), visible (VIS, 380 nm to 760 nm) or ultraviolet (UV, 10.0 nm to 400 nm) regions [ISO, 2007:9]. Electro-optic systems use a variety of sensors that normally consist of photomultiplier tubes (PMTs) and Si-based photodetectors [Muñoz, 2007:2859].

Electro-optic systems have been well researched and developed for use in both the IR and VIS spectral regions. UV radiation (UVR) research only began in the latter half of the 19th century. Great interest in the development of electro-optic systems for studying objects radiating in the UV region was stimulated after World War II, because of their military, industrial and scientific applications [Goldberg, 1999:R41–R42; Monroy *et al.*, 2003:R34; Razeghi and Rogalski, 1996:7434].

Although the Sun radiates over the entire UVR spectrum, the Earth's atmosphere absorbs strongly in specific regions of the UVR spectrum. Specifically, wavelengths between 200 nm and 350 nm are mainly absorbed by molecular

oxygen and stratospheric ozone [Andrews, 2010:73–74; Goldberg, 1999:R41; Haigh, 2007:27–29; Razeghi and Rogalski, 1996:7434]. Solar-blind UV-sensitive detectors are photodetectors sensitive only to wavelengths in the UV-C region (200 nm to 280 nm). These photodetectors can therefore only respond to terrestrial sources radiating in the UV-C region [van Schalkwyk *et al.*, 2012:1529].

The broad wavelength response of PMTs and Si-based photodetectors have the disadvantage that electro-optic systems based on these technologies require additional filters to obtain wavelength selectivity [Muñoz, 2007:2860; Razeghi and Rogalski, 1996:7457]. These filters do not only lower efficiency, but also reduce the signal-to-noise ratio, which requires additional electronics to correct [Muñoz, 2007:2860]. Where high photosensitivity is required, PMTs are needed, which require high-voltage power supplies and result in expensive bulky systems [Muñoz, 2007:2860]. Furthermore, for military, industrial and scientific applications, UV-sensitive systems and their components need to be robust, efficient, withstand UVR and have good signal-to-noise ratios. They are also required to be compact, environmentally friendly and cost effective.

Advances in material growth techniques and processing of group-III-nitrides resulted in a unique direct wide-bandgap (WBG) semiconductor system [Razeghi and McClintock, 2009:3067; Razeghi, 2011:263]. The  $\text{Al}_x\text{N}$ ,  $\text{Ga}_{(1-x-y)}\text{N}$ , and  $\text{In}_y\text{N}$  semiconductors offer a direct WBG that is tuneable over a broad spectral range by varying the Al (x) and In (y) mole fractions, in the alloy composition [Muñoz, 2007:2860]. This tuneability allows the manufacture of photodetectors that do not respond to certain (longer) wavelengths, making them intrinsically ‘blind’ to specific wavelengths. Moreover, this may eliminate the need for expensive filters in systems. Indium nitride (InN) has its absorption edge in the IR region at about 1.8  $\mu\text{m}$  (bandgap of 0.7 eV), gallium nitride (GaN) at 360 nm (3.44 eV) and aluminium nitride (AlN) at 200 nm (6.2 eV) [Muñoz, 2007:2860].

Group-III-nitride optoelectronic devices promise to be more reliable, have higher efficiencies, are environmentally friendly and robust and furthermore, being compact, will diversify their application [Razeghi, 2011:263]. The ternary aluminium gallium nitride (AlGa<sub>N</sub>) semiconductor has proven to be an excellent photonic material for use as a tuneable solar-blind UV-sensitive material in sensors [Razeghi, 2011:264].

## **1.2 Research problem**

International interest in the research and development of intrinsically solar-blind UV-sensitive sensors motivated this research study. The purpose of the study was to realize an optimized tuneable front-irradiated AlGa<sub>N</sub>-based solar-blind UV-sensitive Schottky photodiode. Also, as fundamental optical-to-electrical transducers, their feasibility for implementation in future UV-sensitive electro-optic systems are discussed in this dissertation.

### **1.2.1 Aims**

The first aim of the study was to establish a fabrication procedure for Schottky photodiodes on AlGa<sub>N</sub> semiconductors. The second, was to develop an optimized four-quadrant detector to complete a joint initiative with the Sensor Science & Technology (SST) competence area of the Council for Scientific and Industrial Research (CSIR) Materials Science and Manufacturing (MSM) unit. They aimed to integrate the four-quadrant detector in a housing with electronics and UV optics and demonstrate a working solar-blind UV-sensitive electro-optic device.

## 1.2.2 Objectives

The first objective was to construct an optoelectronic characterization system for electrical and spectral characterization of the UV-sensitive photodiodes. A system for electrical characterization was already well established for current–voltage ( $I$ – $V$ ) and capacitance–voltage ( $C$ – $V$ ) measurements in a light-tight shielded enclosure that minimized electromagnetic interference (EMI) from external noise sources. The optoelectronic characterization system was envisaged to be developed by adding radiating sources, together with a monochromator for wavelength selection and filters, onto the existing system.

The second objective was to calibrate the optoelectronic characterization system against standards traceable to the National Institute of Standards and Technology (NIST). This could be done using the photodetector substitution method that required the use of a standard detector with an absolute responsivity calibration. In addition, a computer program was written to automate the spectral characterization part of the optoelectronic characterization system. This routine aided in recording, incorporating and saving the standard detector calibration data together with the measured spectral irradiation data of the photodiode.

The third objective was to establish a fabrication procedure for tuneable front-irradiated AlGaIn-based solar-blind UV-sensitive Schottky photodiodes. Front-irradiated photodiodes required the use of materials with high optical transmittance in the UV region as Schottky contacts. Kim *et al.* [2002] showed the effective use of iridium(IV) oxide ( $\text{IrO}_2$ ) as a Schottky barrier material for GaIn metal–semiconductor–metal UV-sensitive photodetectors. Therefore, a fabrication procedure was investigated by using metallization techniques found in literature and investigating the effects of each fabrication step on the optoelectronic characteristics.

The final objective was to realize an optimized metallization technique for the ohmic and Schottky contacts to fabricate a four-quadrant detector once a tuneable front-irradiated **AlGaIn**-based solar-blind **UV**-sensitive Schottky photodiode has been developed and characterized. The feasibility for the implementation of the four-quadrant detector in future **UV**-sensitive electro-optic systems could then be considered.

### **1.3 Layout of the dissertation**

Chapter 1 provides some background on electro-optic systems and their shortcomings as solar-blind **UV**-sensitive devices. There is also a brief look at how group-III-nitrides can potentially address some of the shortcomings.

Chapter 2 focusses on **EMR** and introduces some fundamental concepts in radiometry that are relevant in this study to familiarise the reader with the terminology and notation. This is needed to further understand the methodology behind the spectral characterization technique discussed later in Chapter 3 and the calibration theory and method of the optoelectronic characterization system in Chapter 4. Furthermore, sources of **EMR** are discussed and the solar irradiance spectrum presented to help position the solar-blind **UV** region. The chapter also looks at the detail around **UVR** classification, important applications, some detection methods and how **WBG** semiconductors can be advantageous for solar-blind **UV**-sensitive devices.

Chapter 3 considers the physics of **AlGaIn**-based Schottky photodiodes. First, the three typical categories of solids with respect to their electron energy-band structures are discussed and a fourth category, being **WBG** semiconductors, is introduced. Then, the differences between direct and indirect bandgap semiconductors are discussed together with the band-to-band optical transitions that are

possible within them. With that in mind, the idea and benefits of a tuneable **AlGaIn** semiconductor that is intrinsically solar-blind is briefly looked at. Because Schottky photodiodes are of interest, the Schottky diode and its electrical characterization is discussed. Lastly, the photocurrent generation processes and the spectral characterization of a Schottky photodiode are covered.

In Chapter 4 the construction, calibration and technical details of the optoelectronic characterization system are discussed. The system was calibrated by following the photodetector substitution method and the theory behind the calibration is derived from a radiometric foundation. The system was used to optoelectronically characterise Schottky photodiodes and is unique in that it uses an optical fibre to irradiate the photodiodes. Therefore, the chapter also looks at the properties of a step-index optical fibre and its experimental set-up. The spot-size and spatial irradiation distribution (**SID**) are experimentally measured and compared to that expected theoretically. Finally, typical calibrated spectral irradiances of the deuterium and tungsten-halogen lamps are considered.

The initial development and characterization of a tuneable **AlGaIn**-based solar-blind **UV**-sensitive Schottky photodiode is covered in Chapter 5. Here, the technical details of the sourced **AlGaIn** semiconductor wafer on which the Schottky photodiodes were to be fabricated, are presented. Then, the fabrication procedure and the optoelectronic characterization together with the results are discussed that led to a publication which has been included in Appendix E.

Once the Schottky photodiode fabrication procedure was established, Chapter 6 describes the continuation of the work toward the development and characterization of two **UV**-sensitive four-quadrant detectors. Moreover, through additional literature the metallization techniques for the fabrication of optimized ohmic contacts and **UV** transmissive Schottky contacts are discussed. The technical details of the two sourced **AlGaIn** semiconductor wafers on which the four-quadrant

detectors were to be fabricated are presented and the deposition techniques explained to obtain the envisioned layout of the detectors. The second four-quadrant detector was mounted onto a commercial microchip carrier, epoxy wire-bonded and then optoelectronically characterized. The results obtained for the second four-quadrant detector that led to another publication, which has been included in Appendix E, is covered. In addition, how the second four-quadrant detector was used to demonstrate a working solar-blind UV-sensitive electro-optic device is also discussed.

Finally, Chapter 7 concludes the study in terms of the objectives and aims set out in the previous section 1.2 and considers some further research.

## Chapter 2

# Electromagnetic radiation

### 2.1 Nature of electromagnetic radiation

The form of electromagnetic radiation (EMR) to which the human eye is sensitive and on which our visual awareness of the universe and its contents relies, is known as (visible) *light* [Isaacs, 2003:264–265]. Sir Isaac Newton was the first to regard rays of light as very small particles travelling in straight lines, emitted in streams from a light source and became the most famous advocate of the particle (corpuscular) theory of light during the seventeenth century [Pedrotti and Pedrotti, 1993:2]. Later, Christiaan Huygens' wave theory of light allowed him to derive the laws of reflection and refraction, championing Newton's corpuscular theory [Pedrotti and Pedrotti, 1993:2]. Huygens described the propagation of the light wave with the concept of a wave front, defined as "the locus of all adjacent points at which the phase of vibration of a physical quantity associated with the wave is the same" [Young and Freedman, 2004:1249]. Furthermore, a vector can be constructed such that it is perpendicular to the wave front, hence representing an optical ray which is "an imaginary line along the direction of travel of the wave" [Young and Freedman, 2004:1249]. James Clerk Maxwell predicted the electromagnetic wave (EMW) nature of light and calculated its speed of propaga-



tion in 1873 [Young and Freedman, 2004:1248]. Heinrich Hertz started in 1887 with experimental work that confirmed that light is EMWs [Young and Freedman, 2004:1248]. By the nineteenth century, EMR has been shown to be either considered as particles moving, or as waves with electric and magnetic components propagating through a medium.

In 1900, Max Planck was able to mathematically derive the correct blackbody radiation spectrum by making the assumption that atoms radiate energy in discrete bundles called *quanta* or *photons* [Pedrotti and Pedrotti, 1993:3; Young and Freedman, 2004:1248]. In modelling EMR as photons, Planck showed that a photon has discrete energy  $E$  that is proportional to the frequency of the radiation  $\nu$  or inversely proportional to the wavelength of that radiation  $\lambda$ ,

$$E = h\nu = \frac{hc}{\lambda}, \quad (2.1)$$

where  $h$  is Planck's constant and  $c$  the speed of the EMWs in the medium [Pedrotti and Pedrotti, 1993:3]. In 1905, Albert Einstein showed that the photoelectric effect<sup>1</sup> could only be explained by considering EMR as a stream of photons whose energy is related to frequency as by Planck's equation [Isaacs, 2003:360; Pedrotti and Pedrotti, 1993:3]. The photon model is best used for understanding radiant energy interaction with media and therefore used in radiometry where the photon flux of an optical field is considered [Young and Freedman, 2004:1248]. In modelling EMR as a wave propagating through a medium, the concepts of wavelength and frequency are considered. In the planning of an optical system the wave front and ray models are mostly used in aberration calculations.

---

<sup>1</sup>"The liberation of electrons from a substance exposed to EMR." [Isaacs, 2003:359]

## 2.2 Introductory radiometry

*Radiometry* is the science of the measurement of EMR [Pedrotti and Pedrotti, 1993:10]. The Optical Technology Division of the NIST have published the *Self-Study Manual on Optical Radiation Measurements* that describes the fundamentals of radiometry [Nicodemus *et al.*, 1976]. The units and nomenclature that are used depend on the experiment performed, as explained by Nicodemus *et al.* [1976:7],

A mechanical engineer, concerned with dissipating frictional heat, wants to know how much energy flows away from an exposed hot surface as optical (heat) radiation. He is concerned with the rate of energy flow – the power – in the radiation beam, usually expressed in watts. An atomic physicist, studying the light emitted by individual particle interactions, wants to know the number of photons flowing in a beam, the number of quanta per second. An illumination engineer, trying to provide adequate lighting on a desk for comfortable and efficient reading and writing, measures light in terms of its effect upon the average human eye, using lumens<sup>2</sup> for units. Thus, there are different ways of stating the amount of optical radiation determined by a measurement; we can use different units of flux, the general term for the quantity of radiation per unit time flowing in a beam.

One of the most difficult physical quantities to measure accurately is EMR, because of the varying parameters of direction, polarization, position, time and wavelength. Furthermore, the responsivity of most radiometers may not only vary because of the same latter parameters, but also environmental and instrumental parameters. Therefore, it is common to have a disagreement of between 10 % and 50 % in measurements obtained by different instruments or techniques [Nicodemus *et al.*, 1976:iii].

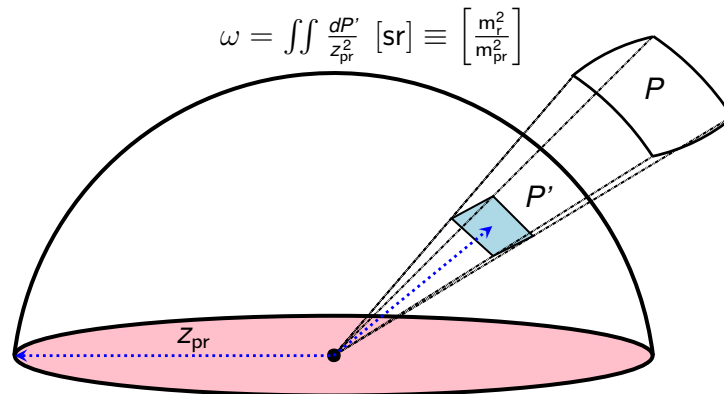
<sup>2</sup>Photometry use lumen and is the measurement of optical radiation with detectors having a specified spectral responsivity related to that of the human eye [Nicodemus *et al.*, 1976:7–8].

Radiometric terms can be defined in radiant (watt), photon (quanta per second) or photometric (lumen) quantities [Nicodemus *et al.*, 1976:7; Pedrotti and Pedrotti, 1993:10]. Therefore, subscripts *e* (*radiant*), *p* (*photon*) and *v* (*photometric*) are denoted to distinguish between the nature of the quantities [Nicodemus *et al.*, 1976:7; Pedrotti and Pedrotti, 1993:10,15]. It should be noted that the underlying concepts are the same, irrespective of the nature of the quantities [Nicodemus *et al.*, 1976:7]. This study mainly considers radiant quantities and in some instances may utilise photon quantities where interactions between radiation and matter is considered.

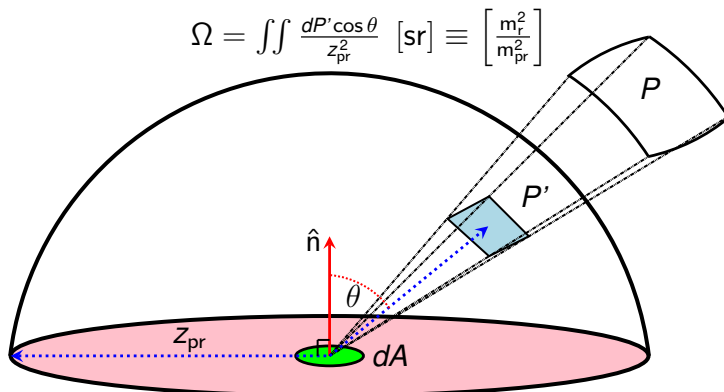
The following subsections first look at the concept of a solid angle, which is important to understand before any radiometry can be performed. Secondly, a number of radiometric terms are defined to better understand the differences between them. Thirdly, the interaction of EMR with media is discussed briefly. Finally, a mathematical equation that is similar to the measurement equation is derived to address radiometric problems in this research study.

### **2.2.1 The solid angle**

The solid angle is a two-dimensional extension on the concept of the plane angle and is expressed as the ratio of an area and the square of a length with unit  $\text{m}^2/\text{m}^2 = 1$ , called a steradian [sr] [Thompson and Taylor, 2008:77]. Palmer and Grant [2009:15] defines one steradian as “the solid angle that, having its vertex in the center of a sphere, cuts off an area on the surface of the sphere equal to that of the square with sides of length equal to the radius of the sphere.” Solid angles are fundamental in describing how sources radiate and how receivers at a distance observe the radiation. The two types of solid angles that are used in solving radiometric problems are illustrated in Figure 2.1.



(a) The geometric solid angle is the ratio of a surface area  $P'$  of the projection of an arbitrary surface  $P$  onto the surface of the hemisphere of radius  $z_{pr}$  as seen from a point at the center of the hemisphere.



(b) The projected solid angle is the geometric solid angle weighted with a factor  $\cos \theta$ , because of the dependence of the projected area with respect to the surface area at the center of the hemisphere.

Figure 2.1: Illustrations of the geometric and the projected solid angles used in solving radiometric problems.

The *geometric solid angle* ( $\omega$ ), illustrated in Figure 2.1(a), is the ratio of the surface area  $P'$  in  $[\text{m}_p^2]$  of the projection of an arbitrary surface  $P$  onto the surface of a hemisphere of radius  $z_{pr}$   $[\text{m}_{pr}]$  (along the optical axis) as seen from a point at the center of the hemisphere. An infinitesimal portion of the projected area  $P'$  can be described in spherical coordinates, such that

$$\begin{aligned} dP' &= z_{pr} d\theta \times z_{pr} \sin \theta d\phi \\ &= z_{pr}^2 \sin \theta d\theta d\phi. \end{aligned}$$

Therefore, the geometric solid angle subtended at the center of the hemisphere (origin) by the infinitesimal portion of the projected area  $P'$  is given by

$$\omega = \iint \frac{dP'}{z_{pr}^2} = \iint \sin \theta d\theta d\phi. \quad (2.2)$$

The geometric solid angle can be calculated by integrating over  $0 \leq \theta \leq \Theta$  and  $0 \leq \phi \leq 2\pi$  in Eq. 2.2, such that

$$\omega = 4\pi \sin^2 \left( \frac{\Theta}{2} \right). \quad (2.3)$$

Here,  $\Theta$  is the half apex angle of a cone with its apex at the center of the hemisphere. If  $\Theta = \pi/2$  sr the cone covers the whole hemisphere and  $\omega = 2\pi$  sr. When  $\Theta = 2\pi$  sr, the cone covers a whole sphere and  $\omega = 4\pi$  sr [Nicodemus *et al.*, 1976:62–70; Pedrotti and Pedrotti, 1993:11].

The *projected solid angle* ( $\Omega$ ), illustrated in Figure 2.1(b), is the ratio of the surface area  $P'$  in  $[\text{m}_p^2]$  of the projection of an arbitrary surface  $P$  onto the surface of a hemisphere of radius  $z_{pr}$   $[\text{m}_{sr}]$ , as seen from the surface  $dA$  at the center of the hemisphere, multiplied by a weighting factor  $\cos \theta$ , where  $\theta$  is the angle between

the normal vector  $\hat{n}$  of  $dA$  and the line from the center of the hemisphere to where the projected area  $P'$  is located on the hemisphere. The weighting factor of  $\cos \theta$  is required, because the contribution of the projected area  $P'$  to the solid angle  $\Omega$  depends on where  $P'$  is located on the hemisphere, relative to the normal vector  $\hat{n}$  of the area  $dA$ . An infinitesimal portion of the area  $P'$  can be described in spherical coordinates as

$$dP' = z_{pr}^2 \sin \theta d\theta d\phi.$$

Therefore, the projected solid angle subtended at the surface  $dA$  by the infinitesimal portion of the projected area  $P'$  is given by

$$\Omega = \iint \frac{dP' \cos \theta}{z_{pr}^2} = \iint \sin \theta \cos \theta d\theta d\phi. \quad (2.4)$$

The projected solid angle can now be calculated by evaluating the integral for  $0 \leq \theta \leq \Theta$ ,  $0 \leq \phi \leq 2\pi$  and weighting  $dP'$  with a factor  $\cos \theta$  in Eq. 2.4, such that

$$\Omega = \pi \sin^2 \Theta. \quad (2.5)$$

Here,  $\Theta$  is still the half apex angle of a cone. If  $\Theta = \pi/2$  sr, the cone covers the whole hemisphere, but with  $\Omega = \pi$  sr. Hence, the projected solid angle in this case is only half that of the geometric solid angle, because of the weighting factor  $\cos \theta$ . The projected solid angle is particularly used when the radiance from the source is independent of direction, that is a Lambertian source [Palmer and Grant, 2009:32,58]. The geometric solid angle can be used when the range between the source and receiver are large enough, such that the half apex angle is very small and  $\cos \theta \approx 1$  [Nicodemus *et al.*, 1976:70–77].

## 2.2.2 Radiometric terms

This section covers the main radiometric terms, that include the radiant flux, radiance, radiant intensity, radiant exitance and irradiance as well as a summary of their International System of Units (SI) in Table 2.1 and illustrations in Figure 2.2.

*Radiant flux* is the rate at which energy of EMR (radiant energy) flows from a source to a receiver. As illustrated in Figure 2.2(a), consider an infinitesimal portion of the (directed) surface area  $dA_s$  of a source and similarly that of a receiver  $dA_r$ , a distance  $z_{sr}$ , apart in an optical system. The radiant flux ( $\Phi_e$ ) is the amount of radiant energy ( $Q_e$ ) [J] flowing over time ( $t$ ) [s] from the source to the receiver and is therefore measured in watt [W] [Nicodemus *et al.*, 1976:23–25].

*Radiance* is the radiant flux per unit surface area (radiant-flux density) of the source and projected solid angle. In Figure 2.2(b), a radiating source is considered that is either self emitting, reflecting or both. The radiance is therefore, the radiant flux  $d^2\Phi_e$  per unit surface area  $dA_s$  of the source and projected solid angle  $d\Omega_a$  of that source. The projected solid angle is subtended at  $dA_s$  by the cross-sectional area  $da$  of a spherical element at a distance  $z_{sa}$  from the source. The symbol used for radiance is  $L_e$  in  $[W \cdot m^{-2} \cdot sr^{-1}]$  [Nicodemus *et al.*, 1976:19–23].

*Radiant intensity* is the radiant flux per geometric solid angle. Figure 2.2(c) illustrates a point source where the radiant flux flows outward from the point source per unit of geometric solid angle  $d\omega_a$  subtended at the source origin by the cross-sectional area  $da$  of a spherical element at a distance  $z_{sa}$  from the source. The radiant intensity symbol is  $I_e$  in  $[W \cdot sr^{-1}]$  [Nicodemus and Kostkowski, 1978:9].

*Radiant exitance* is defined as the radiant-flux density flowing outward from the surface area of a source, as in Figure 2.2(d). The symbol  $M_e$  is used for radiant exitance in  $[W \cdot m^{-2}]$  [Nicodemus and Kostkowski, 1978:9–14].

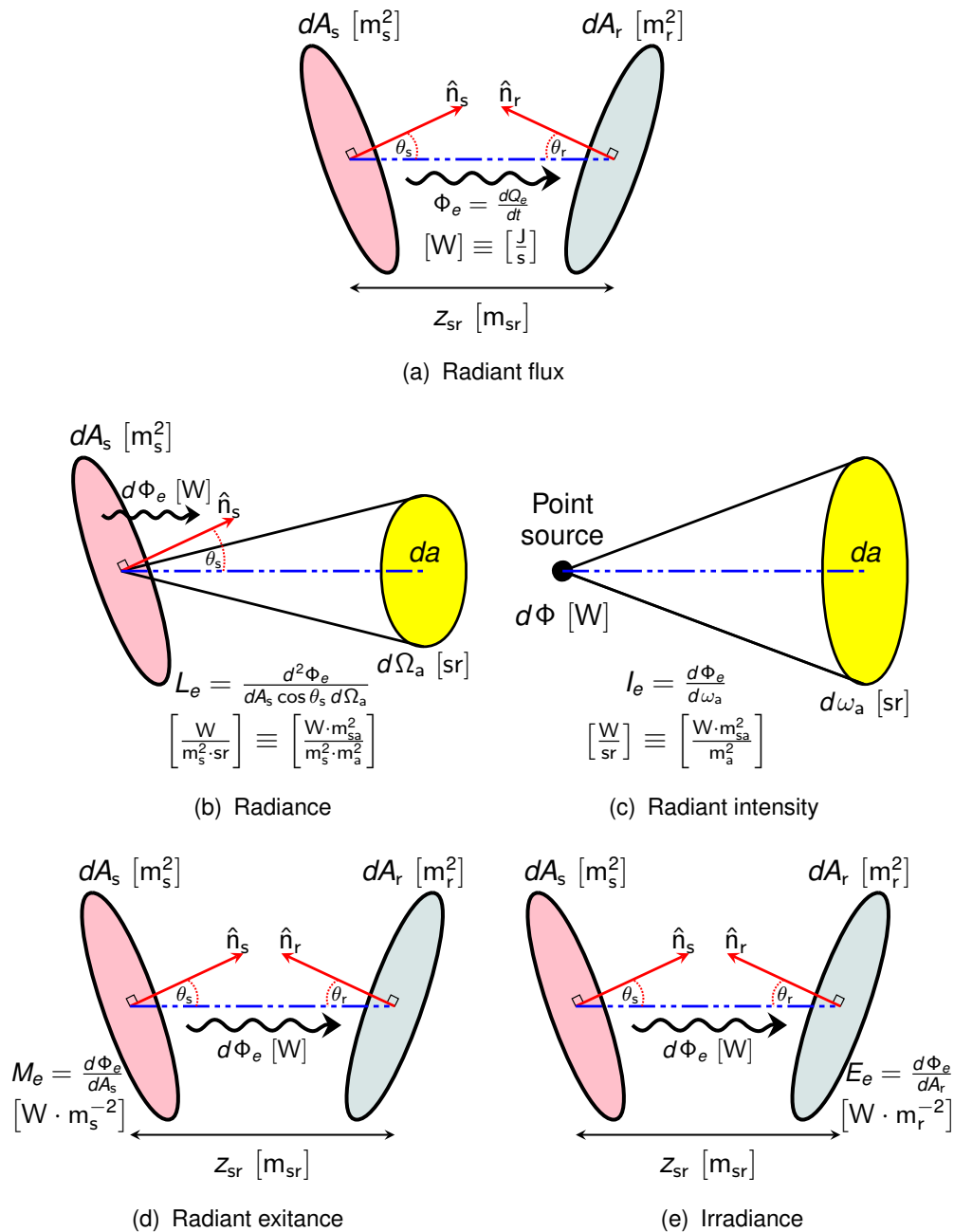


Figure 2.2: Illustrations of the radiometric terms. (a) illustrates the rate at which radiant energy flows from a source to a receiver, (b) the radiant flux per unit surface area and projected solid angle, (c) the radiant flux per geometric solid angle flowing outward from a point source, (d) the radiant-flux density flowing outward from the surface of a source and (e) the radiant-flux density incident on the surface of a receiver from a distant source.



Table 2.1: The radiometric terms and their SI derived units.

Term	Symbol	Defining equation	SI units
Radiant energy	$Q_e$		[J]
Radiant flux	$\Phi_e$	$\frac{dQ_e}{dt}$	[W]
Radiance	$L_e$	$\frac{d^2\Phi_e}{dA_s \cos \theta_s d\Omega_a}$	[W · m <sup>-2</sup> · sr <sup>-1</sup> ]
Radiant intensity	$I_e$	$\frac{d\Phi_e}{d\omega_a}$	[W · sr <sup>-1</sup> ]
Radiant exitance	$M_e$	$\frac{d\Phi_e}{dA_s}$	[W · m <sup>-2</sup> ]
Irradiance	$E_e$	$\frac{d\Phi_e}{dA_r}$	[W · m <sup>-2</sup> ]

*Irradiance* is the radiant-flux density incident on the area of a receiver from a source at a distance, as in Figure 2.2(e). Here  $E_e$  is used for irradiance, also in [W · m<sup>-2</sup>] [Nicodemus and Kostkowski, 1978:9–14].

### 2.2.3 Radiant energy interaction with media

A medium can reflect, absorb and transmit radiant energy incident on it. The incident radiant energy  $Q_i$  can therefore be related as follows

$$Q_i = Q_r + Q_a + Q_t. \quad (2.6)$$

Furthermore, by dividing Eq. 2.6 by the incident radiant energy value, one has that

$$\begin{aligned} \frac{Q_i}{Q_i} &= \frac{Q_r}{Q_i} + \frac{Q_a}{Q_i} + \frac{Q_t}{Q_i} \\ 1 &= \rho + \alpha + \tau, \end{aligned} \quad (2.7)$$

where  $\rho$  is the fraction of incident radiant energy being reflected (radiant or spec-

tral reflectance),  $\alpha$  is the absorbed fraction (absorptivity or attenuation coefficient of the medium) and  $\tau$  the transmitted fraction (transmission coefficient) [Isaacs, 2003:2,414,507].

## 2.2.4 Geometrical invariance of radiance

Radiant flux transfer between two arbitrary objects can be derived, starting with a graphical illustration as presented in Figure 2.2(a). Consider an infinitesimal portion of the source area  $dA_s$  and receiver area  $dA_r$  separated by a distance  $z_{sr}$ . The angles  $\theta_s$  and  $\theta_r$  are the angles between the line-of-sight and the normal unit vectors  $\hat{n}_s$  and  $\hat{n}_r$  to the two infinitesimal areas. Radiant energy flows from the source to the receiver through a lossless optical medium. The source and receiver radiance is given by

$$L_s = \frac{d^2\Phi_e}{dA_s \cos \theta_s d\Omega_r} \quad (2.8)$$

and

$$L_r = \frac{d^2\Phi_e}{dA_r \cos \theta_r d\Omega_s}. \quad (2.9)$$

Here, the projected solid angle  $d\Omega_r$  subtended at  $dA_s$  by  $dA_r$  is defined as

$$d\Omega_r = \frac{dA_r \cos \theta_r}{z_{sr}^2}, \quad (2.10)$$

and the projected solid angle  $d\Omega_s$  subtended at  $dA_r$  by  $dA_s$  as

$$d\Omega_s = \frac{dA_s \cos \theta_s}{z_{sr}^2}. \quad (2.11)$$

Substituting Eq. 2.10 into Eq. 2.8, and Eq. 2.11 into Eq. 2.9, shows that  $L_s = L_r$ ,

hence, proving that radiance is conserved. Now

$$L_e = \frac{d^2\Phi_e z_{sr}^2}{dA_s \cos \theta_s dA_r \cos \theta_r} \quad (2.12)$$

and solving for  $d^2\Phi_e$ , gives

$$d^2\Phi_e = \frac{L_e dA_s \cos \theta_s dA_r \cos \theta_r}{z_{sr}^2}. \quad (2.13)$$

Equation 2.13 is used to calculate the monochromatic radiant flux transferred between two arbitrary objects in a lossless medium [Nicodemus *et al.*, 1976:23–44; Pedrotti and Pedrotti, 1993:11–13].

In a more general format, Eq. 2.13 can be multiplied with the transmittance coefficient for a lossy medium  $\tau$  between the two objects for a small spectral bandwidth  $d\lambda$ , such that

$$d^3\Phi_e = \frac{L_e dA_s \cos \theta_s dA_r \cos \theta_r \tau d\lambda}{z_{sr}^2}. \quad (2.14)$$

Equation 2.14 provides the total radiant flux in a beam of small spectral bandwidth at its intersection with a reference surface, after passing through a lossy medium [Nicodemus and Kostkowski, 1978:65]. Figure 2.2(a) together with Eq. 2.14 is fundamental in solving radiometric problems and deriving all radiometric terms.

“The *measurement equation* is the mathematical expression that quantitatively relates the output of a measuring instrument to the radiometric quantity that is being measured taking into account all of the pertinent factors contributing to the measurement result” [Nicodemus *et al.*, 1976:4]. The measurement equation is similar to Eq. 2.14, but is different in that each radiant flux element is ‘weighted’ by a corresponding responsivity value [Nicodemus and Kostkowski, 1978:65–67].

## 2.3 Sources of EMR

Charged particles in accelerated motion are the fundamental sources of all EMR. Any object at a non-zero temperature radiates EMR, which is called *thermal radiation* and is a mixture of various wavelengths. Thermal radiation is EMR emitted by an object, because of the accelerated motion of charged particles under thermal agitation. The level of accelerated motion of charged particles depends on their thermal energy [Young and Freedman, 2004:1248].

The thermal radiation spectrum is mathematically described by Planck's radiation law for a *blackbody*, which is an ideal surface that radiates (and absorbs) all wavelengths of EMR [Pedrotti and Pedrotti, 1993:15; Young and Freedman, 2004:1248]. The spectral radiant exitance for a thermal radiator at temperature  $T$  [K] as a function of wavelength ( $\lambda$ ) is given by Planck's blackbody radiation law as

$$M_e(\lambda, T) = 2\pi hc^2 / \left[ \lambda^5 \left( e^{\frac{hc}{\lambda kT}} - 1 \right) \right],$$

where  $c$  and  $k$  represents the speed of EMWs and the Boltzmann constant, respectively [Pedrotti and Pedrotti, 1993:15]. When using the known values of these constants and  $\lambda$  in [nm], the radiant exitance result is

$$M_e(\lambda, T) = 3.742 \times 10^{22} / \left[ \lambda^5 \left( e^{\frac{1.439 \times 10^7}{\lambda T}} - 1 \right) \right] \quad [\text{W} \cdot \text{m}^{-2} \cdot \text{nm}^{-1}]. \quad (2.15)$$

Sources of EMR may be natural thermal radiators, such as solar radiation from the Sun, or artificial, as with incandescent or discharge lamps. Furthermore, radiating sources may be classified as continuous, spectral line or monochromatic [Pedrotti and Pedrotti, 1993:17].

### 2.3.1 The Sun

Solar radiation from the Sun can be classified basically as extraterrestrial and terrestrial solar irradiance. Terrestrial solar irradiance is commonly referred to as daylight and experienced as a combination of sunlight and skylight. Skylight has a predominantly blue hue, where direct sunlight has a distinctly different spectral distribution that is modified by absorption in the atmosphere of the earth. Extraterrestrial solar irradiance is the solar irradiance experienced above the Earth's atmosphere [Pedrotti and Pedrotti, 1993:18].

The reference spectral solar irradiance generated by the [Simple Model of the Atmospheric Radiative Transfer of Sunshine \(SMARTS\)](#) version 2.9.2 for extraterrestrial (E490-00) and direct normal terrestrial irradiance (G173-03) are presented in the top graph of Figure 2.3 for wavelengths ranging from 100 nm to 2000 nm. The [National Renewable Energy Laboratory \(NREL\)](#) uses SMARTS to predict clear-sky spectral solar irradiance, as developed by Dr. C. Gueymard [NREL, 2010]. The model is implemented to generate the extraterrestrial and the terrestrial reference [solar spectra](#) at sea-level for the American Society for Testing and Materials (ASTM) [NREL, 2010]. The ASTM developed the standard extraterrestrial spectrum reference E-490-00 in 2000 for use by the aerospace community and the reference was reapproved in 2006 [ASTM Standard E490-00a, 2006]. They also developed the standard terrestrial spectrum reference G173-03 for use by the photovoltaic industry in 2003 that was reapproved in 2012 [ASTM Standard G173-03, 2012].

The extraterrestrial spectral solar irradiance indicates that the behaviour of the Sun is approximately that of a 5770 K blackbody [Pedrotti and Pedrotti, 1993:18; Woan, 2000:176]. For comparison, the ideal terrestrial spectral solar irradiance of the Sun modelled as a 5770 K blackbody is also plotted in Figure 2.3.

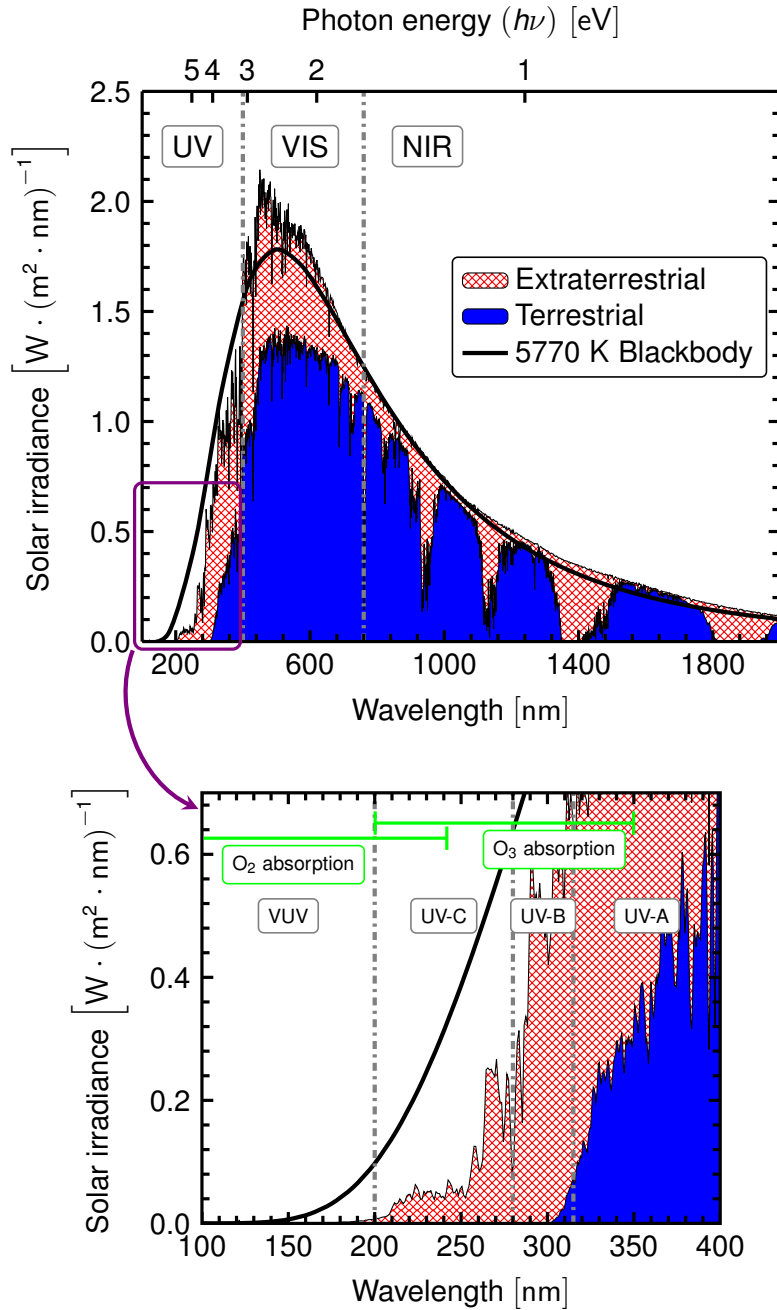


Figure 2.3: *Top Graph:* The ASTM E490-00 extraterrestrial, ASTM G173-03 (direct normal) terrestrial and ideal 5770 K blackbody terrestrial spectral solar irradiance of the Sun [NREL, 2010]. *Bottom Graph:* Magnified UV region of spectral solar irradiance from the Sun. VUV is absorbed by O<sub>2</sub>. The Sun does radiate deleterious UV-C, but UV-C is absorbed by O<sub>2</sub> and stratospheric ozone. UVR reaching the Earth's surface consists of 10 % carcinogenic UV-B, partially absorbed by stratospheric ozone, and 90 % UV-A that stimulates photosynthesis and pigmentation.

### **2.3.2 Incandescent lamps**

Incandescent lamps produce **EMR** by heating a material to incandescence using an electric current. The de-excitation of the atoms or molecules of the material after they have been thermally excited results in radiation over a broad continuum of wavelengths. The most popular source for continuous radiation in the **VIS** and into the **IR** region is the tungsten-halogen lamp [Pedrotti and Pedrotti, 1993:18–19].

### **2.3.3 Discharge lamps**

Discharge lamps produce **EMR** dependent on the gas, ionized by accelerated electrons in the electric field between two electrodes through which a current is passed. Radiant energy is released by the de-excitation of the excited vapour atoms. Deuterium arc lamps are, for instance, ideal for **UV** spectroscopy because they produce a continuous background in the **UV** region with high radiant energy [Pedrotti and Pedrotti, 1993:20–22].

## **2.4 UV radiation**

### **2.4.1 Classification**

The **UV** radiation (**UVR**) spectrum is commonly defined as **EMR** with wavelengths ranging from 10 nm (long X-rays) to 400 nm (violet light) and is a highly ionising radiation, activating many chemical processes [Goldberg, 1999:R41; Isaacs, 2003:516; Monroy *et al.*, 2003:R33; Razeghi and Rogalski, 1996:7434]. The **UVR** spectrum can be subdivided in a number of ways according to definition and border wavelengths between the regions [Envall *et al.*, 2006:063110-1]. In this dissertation, the **UVR** is classified into four subdivided spectral ranges presented

in the lower graph of Figure 2.3 and summarized in Table 2.2, together with the main absorber. The ranges were chosen in conjunction with the International Organization for Standardization (ISO)'s 21348:2007(E) standard on determining solar irradiances, which classifies UVR wavelength ranges [ISO, 2007:9]. The first three ranges are classified according to their main biological action or effect on human skin, and the last according to the required experimental environment for its useful detection in the laboratory.

*UV-A* (315 nm to 400 nm) stimulates photosynthesis, and is involved in the synthesis of basic biochemical compounds and some vitamins, such as vitamin D [Isaacs, 2003:516; Monroy *et al.*, 2003:R34]. UV-A is also pigmentational radiation, i.e. causing skin tanning [Goldberg, 1999:R41].

*UV-B* (280 nm to 315 nm) is mainly carcinogenic radiation and excessive exposure is dangerous to human beings, causing skin cancer, cataracts, burns etc. [Goldberg, 1999:R41; Isaacs, 2003:516; Monroy *et al.*, 2003:R34]. UV-B is partially absorbed by the stratospheric ozone (O<sub>3</sub>) layer and contributes to 10 % of the total UVR reaching the surface of the Earth [Monroy *et al.*, 2003:R34].

*UV-C* (200 nm to 280 nm) is mainly used for its bactericidal properties in water, air and food as a disinfectant [Goldberg, 1999:R41]. Although the Sun radiates in the more deleterious UV-C region, this EMR is also almost completely absorbed by atmospheric molecular oxygen (O<sub>2</sub>) and the stratospheric O<sub>3</sub> layer [Andrews, 2010:73–74; Haigh, 2007:27–29; Monroy *et al.*, 2003:R34; Razeghi and Rogalski, 1996:7434].

Vacuum UV (VUV) ranges from 10 nm to 200 nm and is called VUV because, due to absorption by air, detecting this EMR requires the use of a vacuum chamber [Isaacs, 2003:516; Monroy *et al.*, 2003:R34; Razeghi and Rogalski, 1996:7434]. Wavelengths shorter than 100 nm are absorbed by atomic oxy-



Table 2.2: Classification of the UVR spectrum, subdivided into four ranges according to their main biological effect on the human skin or required experimental environment for its useful detection. The ISO 21348:2007(E) standard on determining solar irradiances describes the wavelength ranges [ISO, 2007:9].

Classification	Wavelength range [nm]	Photon energy range [eV]	Absorber
Ultraviolet–A (UV-A) (pigmentational radiation)	315 to 400	3.94 to 3.10	
Ultraviolet–B (UV-B) (carcinogenic radiation)	280 to 315	4.43 to 3.94	O <sub>2</sub>
Ultraviolet–C (UV-C) (bactericidal radiation)	200 to 280	6.20 to 4.43	O <sub>2</sub> & O <sub>3</sub>
Vacuum UV (VUV)	10 to 200	124 to 6.20	O, O <sub>2</sub> & N <sub>2</sub>

gen (O), O<sub>2</sub> and molecular nitrogen (N<sub>2</sub>) [Andrews, 2010:73–74; Haigh, 2007:27–29]. Also, wavelengths between 100 nm and 200 nm are predominately absorbed by O<sub>2</sub>, hence requiring experimentation in vacuum [Andrews, 2010:73–74; Haigh, 2007:27–29; Monroy *et al.*, 2003:R34; Razeghi and Rogalski, 1996:7434].

## 2.4.2 Applications

UVR was discovered by W. Ritter and W.H. Wollaston in 1801, and during the last two centuries numerous applications and measuring instruments have been found in civil, industrial, military, medical and scientific fields [Goldberg, 1999:R41; Monroy *et al.*, 2003:R34]. UV-sensitive sensor applications can be summarized as biological, chemical and combustion sensors, optical communications and UV-emitter calibration [Monroy *et al.*, 2001:537].

## Biological

In biological applications, UV sensors can be in the form of personal solar UV-B exposure dosimeters, monitors of UV-B and C exposure in food, air disinfection processes for long term storage solutions and in personal water purification systems [Goldberg, 1999:R41; Muñoz, 2007:2859; Razeghi and Rogalski, 1996:7453]. Agricultural industries may want to monitor UV-A and B exposure in hotbed and hothouse agrotechnics [Goldberg, 1999:R41]. Biological agents (such as anthrax and the plague) and organic compounds can be detected through UV luminescence (after UV irradiation) and analysed by studying UV absorption lines [Monroy *et al.*, 2001:537; Monroy *et al.*, 2003:R34; Muñoz, 2007:2859; Razeghi, 2011:263–264]. In the medical and scientific fields, biological sensors can monitor UV-B and C disinfection methods of blood intended for transfusion, or UV-B usage in physiotherapeutics by dermatologists in the treatment of certain diseases [Envall *et al.*, 2006:063110-1; Goldberg, 1999:R41; Muñoz, 2007:2859]. UV-B is used for vitamin-synthesis (such as D<sub>2</sub> and D<sub>3</sub>) as part of biotechnology and in photobiology, to study the photobiological effects of the human skin, both areas in need of UV-sensitive sensors [Envall *et al.*, 2006:063110-1; Goldberg, 1999:R41].

## Chemical

Chemical application for UV sensors are to detect and analyze chemical agents by studying UV absorption lines [Monroy *et al.*, 2001:537; Monroy *et al.*, 2003:R34]. Photochemistry research requires chemical sensors to monitor both UVR and chemical changes and can so be used in, for example, industrial resin curing of polymeric materials [Envall *et al.*, 2006:063110-1; Muñoz, 2007:2859].

## **Combustion**

UV combustion sensors aim to detect specific UV signatures in combustion processes, where UVR is a natural by-product in hostile high temperature environments, such as in the aerospace, automotive and petroleum industries [Razeghi and Rogalski, 1996:7453,7471]. Interior and outdoor fire alarms can use these sensors in conjunction with IR fire sensors as flame safeguard systems [Monroy *et al.*, 2000:2081; Monroy *et al.*, 2001:537; Monroy *et al.*, 2003:R34; Muñoz, 2007:2859; Razeghi and Rogalski, 1996:7435]. For fire control purposes, gas supply to large high temperature furnace and boiler systems can be controlled with combustion sensors monitoring UV signatures in the presence of hot backgrounds and help advance combustion engineering [Monroy *et al.*, 2001:537; Monroy *et al.*, 2003:R34; Muñoz, 2007:2859; Razeghi and Rogalski, 1996:7435]. In the military field, key UV signatures can aid in missile plume detection and UV location (in addition to IR location) of objects [Goldberg, 1999:R41; Monroy *et al.*, 2000:2081; Monroy *et al.*, 2001:537; Monroy *et al.*, 2003:R34; Muñoz, 2007:2859; Razeghi and Rogalski, 1996:7453].

## **Optical communication**

In optical communication applications, secure short range non-line-of-sight ground-based optical space communication technologies are made possible because of the fact that below the atmosphere any UV source with  $\lambda < 280$  nm has to have a human origin [Muñoz, 2007:2859; Razeghi, 2011:264]. Furthermore, UV-sensitive sensor applications for secure space-to-space (or free space) transmission (particularly inter-satellite communication) and astronavigation can also become possible [Goldberg, 1999:R41; Monroy *et al.*, 2000:2081; Monroy *et al.*, 2001:537; Monroy *et al.*, 2003:R34; Muñoz, 2007:2859; Razeghi and Rogalski,

1996:7471; Razeghi, 2011:264].

### **Applications for UV-emitter calibration**

UV-emitter calibration applications have to do with measurement comparisons. Industries can apply UV-emitter calibration techniques as a means to study art, detect faults, non-destructive testing and investigation of materials, detect and monitor pollution, UV lithography and large area sterilization using, for instance, UV luminescences or absorption line analyses [Envall *et al.*, 2006:063110-1; Goldberg, 1999:R41-R42; Monroy *et al.*, 2003:R34; Muñoz, 2007:2859]. Scientific space and astronomical research studies use the UV emission ability of objects to study solar and stellar spectra in an effort to monitor solar UV and thus calibrate sources [Envall *et al.*, 2006:063110-1; Goldberg, 1999:R41; Monroy *et al.*, 2000:2081; Monroy *et al.*, 2001:537; Monroy *et al.*, 2003:R34; Muñoz, 2007:2859; Razeghi, 2011:264]. Other scientific fields can use UV-emitter calibration in scintillator registration of nuclear particles, investigating the electron structure of matter, ozone layer and plasma research [Envall *et al.*, 2006:063110-1; Goldberg, 1999:R41; Monroy *et al.*, 2001:537; Monroy *et al.*, 2003:R34; Muñoz, 2007:2859].

### **2.4.3 Detection**

#### **Photomultiplier tubes and Si-based electro-optic systems**

UVR can be selectively detected with UV-sensitive electro-optic systems that fall into two classes, namely ‘visible-blind’ and ‘solar-blind’ systems. *Visible-blind* systems are defined as systems operating on UV-sensitive sensors with a *cut-off wavelength*<sup>3</sup> shorter than 400 nm [Schühle and Hochedez, 2013:467]. I.e.

---

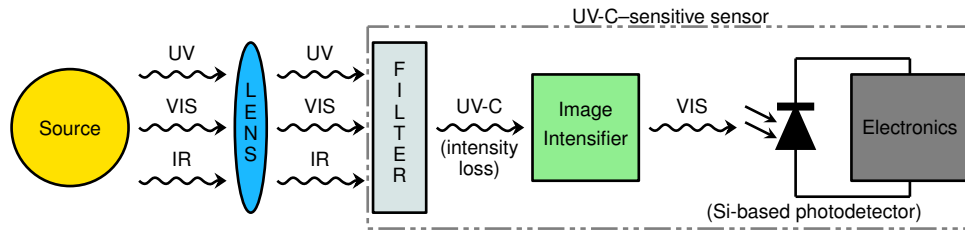
<sup>3</sup>The cut-off wavelength is defined as the wavelength at which photosensitivity is less than half that of the maximum photosensitivity.

referring back to Figure 2.3, visible-blind systems only respond to wavelengths shorter than 400 nm and are ‘blind’ to the longer wavelengths in the ‘visible’ region of the terrestrial solar irradiance spectrum.

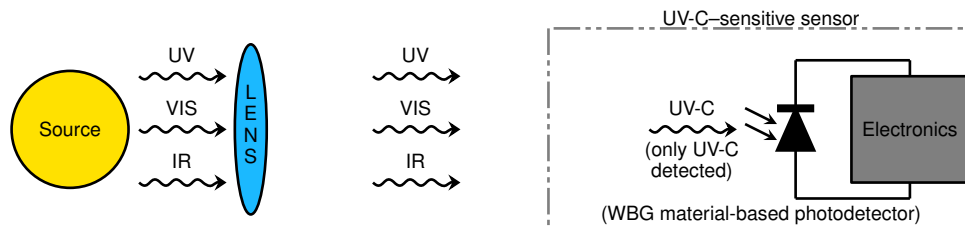
*Solar-blind* systems are defined as systems operating on UV-sensitive sensors with a cut-off wavelength shorter than 280 nm [Schühle and Hochedez, 2013:468]. I.e. referring back to Figure 2.3 again, solar-blind systems only respond to wavelengths shorter than 280 nm and are ‘blind’ to the longer wavelengths of ‘solar’ radiation that can penetrate the atmosphere of the Earth.

Because of the strong absorption of UV-C by the Earth’s stratospheric ozone layer, a solar-blind system on the surface of the Earth is effectively ‘blind’ to solar UV-C, unless it originates from a terrestrial source. This opens the door to a number of terrestrial applications, whereby sources radiating in the UV-C region can be observed with minimum background interference originating from terrestrial solar irradiation. Therefore, international interest grew in the research and development of solar-blind UV-sensitive electro-optic systems, however, as explained by Muñoz [2007:2859–2860], the solar-blind UV-sensitive electro-optic systems based on photomultiplier tube (PMT) and Si-based photodetector technology end-up being expensive and bulky, particularly due to the high-voltage power supplies needed for the PMTs. UV-sensitive systems consisting of PMTs and Si-based photodetectors require additional filters to allow for the transmission of specific UV wavelength ranges to these photodetectors because of their broad wavelength response [Muñoz, 2007:2860; Rzeghi and Rogalski, 1996:7457].

Consider an electro-optic system aimed at observing the UV-C signature of a source radiating over a broad spectral range (UV, VIS and IR). This is a typical example of a solar-blind UV-sensitive electro-optic system. Figure 2.4 illustrates how two types of solar-blind UV-sensitive electro-optic systems can function and what they require to detect UV-C radiation.



(a) A typical UV-C-sensitive electro-optic system observing a source radiating over a broad spectral range. The sensor is based on **PMT** and **Si-based photodetector** technologies, therefore it requires the use of a UV lens, an UV-C filter, an image intensifier and additional electronics to improve signal-to-noise ratios.



(b) The future UV-C-sensitive electro-optic system with a sensor based on **WBG** material technology only requires the use of a UV lens and less additional electronics to improve signal-to-noise ratios.

Figure 2.4: Illustrations of how UV-C-sensitive electro-optic systems with (a) **PMT** & **Si-based** and (b) **WBG** material-based sensors can function and what they require to be solar-blind.

The system illustrated in Figure 2.4(a) requires a quartz lens for focusing since glass strongly absorbs UV wavelengths shorter than 300 nm. A filter is then needed to filter UV-C from the broad range of wavelengths that passed through from the lens. The filtering process results in an intensity loss of UV-C radiation. An image intensifier using, for instance, a **PMT** can amplify the UV-C signal and in the process of doing so, transform the signal to a **VIS** wavelength range. These wavelengths are then detectable by readily available Si-based photodetectors. To complete the sensor, additional electronics may aid in improving signal-to-noise ratios. In the end, the UV-C-sensitive sensor consists of a UV-C filter, an image intensifier, a Si-based photodetector and additional electronics.

### **WBG-based photodetector electro-optic systems**

The drive to develop more compact and cost effective solar-blind UV-sensitive electro-optic systems inspired renewed research efforts on the photodetector component of the sensor. The photodetector is constructed from arrays of optical-to-electrical transducers (such as microchannel array plates, charge coupled devices or photodiodes) that absorb incident photons that interact with electrons and this interaction is observed as an electrical signal. Photodetectors have a selective wavelength of maximum spectral sensitivity per unit incident radiant flux and measure the arrival rate of quanta [Razeghi and Rogalski, 1996:7435].

*Photoelectric* and thermal detectors are two classes of photodetectors. Photoelectric detectors have greater response stability, are more sensitive and provide better linearity. Photoelectric detectors can be subdivided according to their electric signal generation process. These include external photoemissive, internal photoemissive, photovoltaic and photoconductive detectors [Razeghi and Rogalski, 1996:7435].

*External photoemissive detectors* generate an electric signal through the *external photoelectric effect*, i.e. electrons are excited with energies higher than the vacuum energy-level and the wavelength range of sensitivity is related to the work function of the surface thin-film material [Razeghi and Rogalski, 1996:7436].

*Internal photoemissive detectors* generate an electric signal through the *internal photoelectric effect*. I.e. incident photons with radiant energy greater than the bandgap energy of the semiconductor are absorbed in the bulk of the semiconductor. Electrons can then be raised to the conduction band producing electron-hole pairs that are separated by an applied electrical field. The wavelength range of sensitivity is related to the bandgap energy of the semiconductor [Razeghi and Rogalski, 1996:7436].

The *photovoltaic detector* generates an electrical signal similar to that of the internal photoelectric effect. The difference is that the electron-hole pairs are separated by the built-in electric field of the *p-n* junction, Schottky barrier, or metal–insulator–semiconductor photocapacitor [Razeghi and Rogalski, 1996:7436].

Lastly, a *photoconductive detector* is essentially a radiation-sensitive resistor. In this case, an incident photon with energy greater than the bandgap energy of a semiconductor is absorbed to produce an electron-hole pair and the electrical conductivity of the semiconductor changes [Razeghi and Rogalski, 1996:7439].

The last decade has seen a number of studies in UV-sensitive photodetectors based on wide-bandgap (WBG) materials [Muñoz, 2007:2860]. If photodetectors are based on WBG materials, the photodetector can then selectively respond to incident photons with radiant energy greater than the WBG energy, or shorter UV wavelengths. This may result in improved cost and size of future solar-blind UV-sensitive electro-optic systems.

Consider the UV-C–sensitive system illustrated in Figure 2.4(b). The system still requires a quartz lens for focusing. But, the need for a filter and image intensifier can be eliminated, because of the WBG material-based photodetector. With increased efficiency less additional electronics are required to improve signal-to-noise ratios. In this case, the UV-C–sensitive sensor consists only of a WBG-based photodetector and some additional electronics.

The advances in growth techniques and processing of, especially, group-III-nitrides launched the material from being promising to a unique realized WBG semiconductor system [Muñoz, 2007:2860; Razeghi and Rogalski, 1996:7453–7454, 7462–7471; Razeghi and McClintock, 2009:3067; Razeghi, 2011:263]. As a fundamental optical-to-electrical transducer in sensors, the fabrication of Schottky photodiodes on one of these WBG materials will be investigated.



## Chapter 3

# Optoelectronics

Several fields of science and technology have identified numerous studies and applications that require the detection and observation of UV-C signatures. These signatures usually originate from terrestrial sources radiating [EMR](#) over a broad spectral range. The detection of wavelengths in only the UV-C region (200 nm to 280 nm) demands the development of solar-blind UV-sensitive electro-optic systems, with sensors that have a cut-off wavelength of shorter than 280 nm. Furthermore, these systems and their components need to withstand [UVR](#), be robust, efficient, compact, environmentally friendly, cost-effective and have good signal-to-noise ratios.

The sensor in an electro-optic system may use a particular class of photodetector, depending on the application. The fundamental elements of a photoelectric class detector are optoelectronic devices. Optoelectronics is a field of study concerned with the ability of electronic devices, especially solid-state devices, to generate, transmit, modulate and detect [EMR](#) [[Isaacs, 2003:338](#)]. Optoelectronic devices are either optical-to-electrical or electrical-to-optical transducers, that are fabricated in various forms and produce signals through a number of different processes.

Fundamentally, optoelectronics requires an understanding of solid-state physics. One form of an optical-to-electrical transducer is the semiconductor-based photovoltaic diode, or just photodiode. Photodiodes produce an electrical signal through either the internal photoemissive or photovoltaic processes, whereby incident photons interact with the semiconductor to generate a photocurrent.

To understand the interaction processes of EMR with photodiodes, the physical differences between the types of solid-state materials are discussed by considering their electron energy-band structures. Then, it is determined what a semiconductor is and, moreover, where WBG semiconductors fit in, followed by a summary of the relevant semiconductor physics. Thereafter, the AlGaIn semiconductor is briefly looked at.

## **3.1 Solid-state physics**

### **3.1.1 Electron energy-band structures**

The magnitude of the electrical conductivity of a solid-state material depends on the number of electrons that are 'free' to participate in the conduction process. In single isolated atoms, electrons are configured in discrete energy levels. Electrons occupy or fill energy states, starting with the levels having the lowest energies, in accordance with the Pauli exclusion principle. With the forming of solids, the atoms are brought closer together and electrons are acted upon, or perturbed, by the electrons and nuclei of adjacent atoms. Discrete energy levels start to overlap and a series of closely spaced discrete energy levels develop. This forms what is termed an electron energy-band. Furthermore, between adjacent energy-bands there can exist forbidden energy-bands that are not available for electrons to fill, referred to as bandgaps. The electron energy-band structure of a solid-state material accounts for its electrical properties [Callister, 2003:614–

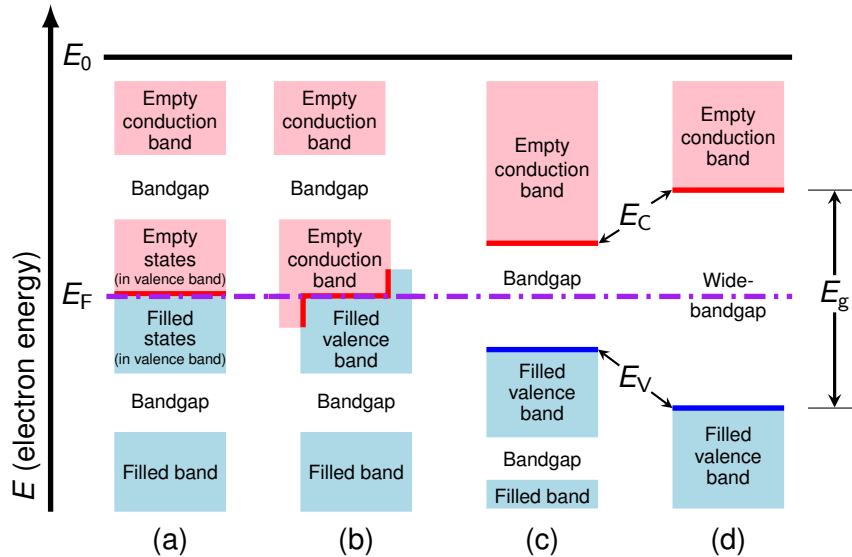


Figure 3.1: The four possible electron band structures in solids at 0 K. (a) The electron band structure for metals, where in the same band available electron states are above and adjacent to filled states (e.g. Au). (b) The electron band structure for metals, wherein the filled and empty outer bands overlap (e.g. Ir). (c) The electron band structure found in semiconductors, where the filled valence band is separated from the empty conduction band by a relatively narrow bandgap ( $E_g < 3$  eV, e.g. Si). Here, electrons can be thermally excited from the highest possible valence band energy-level  $E_V$  to the lowest possible conduction band energy-level  $E_C$ . (d) The electron band structure in WBG semiconductors and insulators are similar to semiconductors, but the filled valence band is separated from the empty conduction band by a relatively wide bandgap. The bandgap energy for WBG semiconductors can be  $3 \text{ eV} < E_g < 8 \text{ eV}$  (e.g. GaN) and is  $E_g > 8 \text{ eV}$  for insulators (e.g. SiO<sub>2</sub>). Adapted from Callister [2003:616].

616].

At zero Kelvin, four different types of electron energy-band structures are possible, as illustrated in Figure 3.1. An important energy-level is present in each of these structures, known as the *Fermi level* ( $E_F$ ) and is defined to be the highest energy-level at which the occupation probability of a quantum state by an electron (fermion) is 0.5 at 0 K. When the Fermi level is such that an electron can change form one quantum state to another empty quantum state of the same energy, then electrons can move freely through a solid. That is, conduction can only occur when a valence energy-band is partially filled or an empty conduction energy-

band is available to be filled. Electrons cannot change quantum states in the same filled valence energy-band, because there are no empty quantum states of the same energy available. The relative positioning of the Fermi level in the two outermost energy-bands divides solids into four categories, namely metals, semiconductors, WBG semiconductors and insulators [Callister, 2003:616; Isaacs, 2003:155–156,169].

### Metals

*Metals* can have two electron energy-band structures. Figure 3.1(a) illustrates the first structure that is typical for metals that have a single *s*-subshell valence electron, such as *Au*. Individual *Au* atoms have one 6*s* valence electron, but in the solid state the *Au* metal is comprised of *N* atoms. The 6*s* valence energy-band can therefore accommodate  $2N$  electrons, hence, only filling half of the available electron energy states in the valence energy-band. The second structure is illustrated in Figure 3.1(b). Here there is an overlap of a filled valence energy-band and an empty conduction energy-band. This occurs in metals where two valence electrons are found in the *s*-subshell, as in *Ir*. An individual *Ir* atom has two 6*s* valence electrons, but in the solid state the 6*s* and 6*p* energy-bands overlap. The Fermi level in metals lies either within the partially filled valence band or it lies within the overlapping region of the valence and conduction bands. This allows electrons to move around freely within and between these energy-bands, giving metals their high electrical conductivity properties (up to the order of  $10^7 \text{ S} \cdot \text{m}^{-1}$ ) [Callister, 2003:614,616].

### Semiconductors, WBG semiconductors and insulators

The last two energy-band structures, (c) and (d) in Figure 3.1, are similar in that at 0 K the completely filled valence band is separated by a bandgap from the empty

conduction band. The difference between the two energy-band structures is the magnitude of the bandgap [Callister, 2003:616-617]. This magnitude or *bandgap energy*  $E_g$  is the minimum energy required to excite an electron from the highest possible valence band energy-level  $E_V$  to the lowest possible conduction band energy-level  $E_C$  [Sze and Ng, 2007:13]. Thus, the bandgap energy is given by

$$E_g = E_C - E_V. \quad (3.1)$$

*Semiconductors* have a narrow bandgap between the valence and conduction band, as illustrated in Figure 3.1(c). The bandgap energy is usually defined to be  $0 \text{ eV} < E_g < 3 \text{ eV}$ . The valence band is completely filled with electrons and there are no free electrons in the conduction band. However, electrons can be excited from  $E_V$  to  $E_C$  because the bandgap energies for semiconductors are usually less than 3 eV, such as for Si with a bandgap energy of 1.12 eV at 300 K. Therefore, semiconductors are said to have intermediate electrical conductivities (between the orders of  $10^{-6} \text{ S} \cdot \text{m}^{-1}$  and  $10^4 \text{ S} \cdot \text{m}^{-1}$ ) [Callister, 2003:614,616].

In 1973, Strehlow and Cook published a compilation of energy bandgaps in elemental and binary compound semiconductors and insulators. By their definition, if  $0 \text{ eV} < E_g < 3 \text{ eV}$  the material is considered to be a semiconductor and if  $3 \text{ eV} < E_g < 12 \text{ eV}$  it is considered to be an insulator. During the 1990's and into the 21st century, advances in the growth of WBG semiconductors made fabrication of various solid-state devices possible. Therefore, the WBG semiconductors as a category of solid-state materials is introduced in this dissertation.

*WBG semiconductors* differ from standard semiconductors by the fact that their bandgaps are much wider, usually  $3 \text{ eV} < E_g < 8 \text{ eV}$ , as comparatively illustrated in Figure 3.1(d). Some materials, such as GaN and AlN, would earlier have been classified as insulators, but have found their way into a number of

optoelectronic applications as WBG semiconductors.

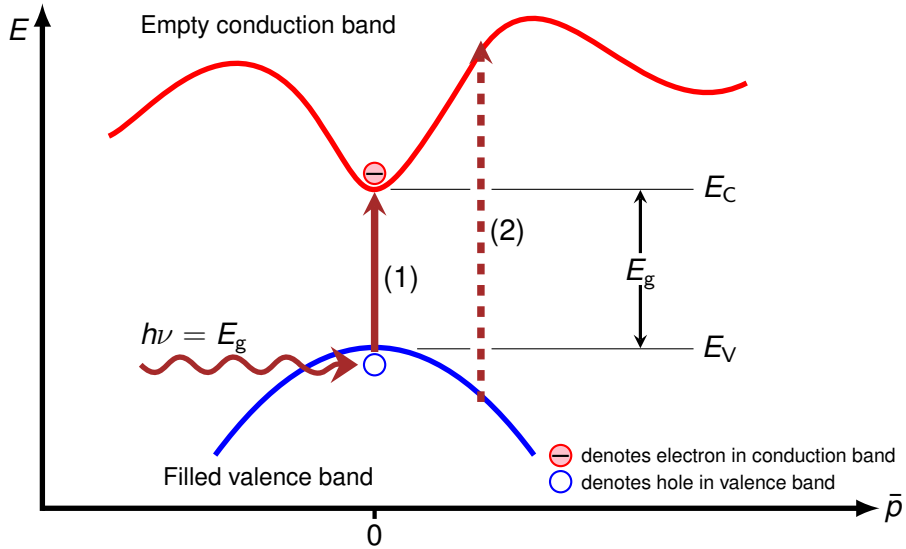
*Insulators* have an even wider bandgap between the valence and conduction bands, compared to WBG semiconductors, but the electron energy-band structure will be similar to that illustrated in Figure 3.1(d). Electrons in an insulator will require excitation energies of between 8 eV and 12 eV to move from the valence band to the conduction band. Therefore, the electrical conductivity of insulators is lower than  $10^{-15} \text{ S} \cdot \text{m}^{-1}$  [Callister, 2003:614,616].

### 3.1.2 Semiconductor physics

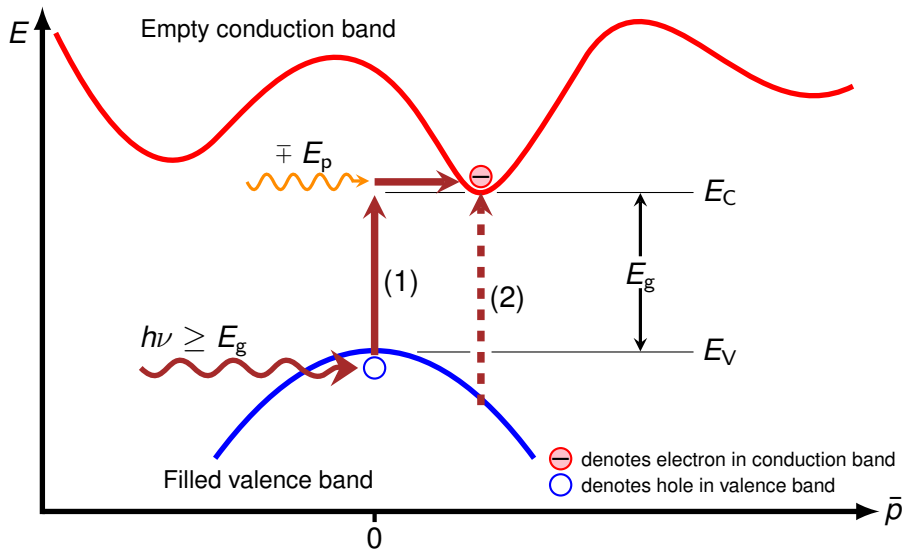
In very pure (intrinsic) semiconductors the Fermi level lies close to the middle of the bandgap (forbidden energy-band) at 0 K. Because of this Fermi level positioning there are fewer free carriers and these solid-state materials can only conduct electrically under specific conditions. Electrons can only move into the empty conduction band, if they are excited from the filled valence band by some minimum amount of energy to overcome the bandgap energy. This property opened the door to various applications, whereby electron excitations can be triggered by various sources in a number of ways, including thermal excitation, by exposure to high energy particles (electrons, protons, alpha particles, etc.) or by incident photons with energies greater than or equal to the bandgap energy. The process involving photons forms part of what is referred to as optical transitions within semiconductors.

#### Direct and indirect bandgaps

Semiconductors can either have direct or indirect bandgaps, depending on their energy-band structure in energy–momentum ( $E-\bar{p}$ ) space. Simplified energy-level diagrams are drawn in Figure 3.2 to illustrate the difference between most



(a) The threshold (1) and an arbitrary (2) direct-transition in a direct-bandgap semiconductor.



(b) The threshold indirect (1) and a direct transition (2) in an indirect-bandgap semiconductor.

Figure 3.2: Energy–momentum ( $E$ – $\bar{p}$ ) space diagrams of (a) direct- and (b) indirect-bandgap semiconductors together with illustrated band-to-band optical transitions.

direct- and indirect-bandgap semiconductors and the way in which optical transitions can occur. The  $E-\bar{p}$  relationship for the band edges near the maximum in the valence band and minimum in the conduction band, can be approximated by a quadratic equation

$$E = \frac{\bar{p}^2}{2m^*}, \quad (3.2)$$

where  $m^*$  is the relevant *effective mass*<sup>1</sup> and  $\bar{p}$  the crystal momentum [Sze, 1985:13–14; Sze and Ng, 2007:12–13].

A *direct-bandgap* semiconductor has both the maximum in the valence band and minimum in the conduction band at the same  $\bar{p}$  value, and for most it is at  $\bar{p} = 0$ , as illustrated in Figure 3.2(a). Therefore, when an electron makes an energy transition from the valence band maximum to conduction band minimum, there is no significant change in crystal momentum required. An *indirect-bandgap* semiconductor, however, has its maximum in the valence band and minimum in the conduction band at different  $\bar{p}$  values. For most indirect-bandgap semiconductors, the maximum in the valence band is still at  $\bar{p} = 0$ , but the minimum in the conduction band is at some different  $\bar{p} \neq 0$  value, as drawn in Figure 3.2(b). Here an electron requires a change in crystal momentum for a threshold transition to occur [Streetman and Banerjee, 2006:69–70; Sze and Ng, 2007:14–15].

### Band-to-band optical transitions

There essentially exist two types of band-to-band optical transitions, that is, a direct and an indirect transition. The *direct transition* is an (almost) vertical transition between the valence and conduction bands at the same  $\bar{p}$  value. Therefore, when an electron makes a direct transition from the valence band to conduction band, there is no change needed in crystal momentum and this only involves

<sup>1</sup>The concept of effective-mass allows for the treating of holes and electrons essentially as classical charged particles [Sze, 1985:13].



a photon. The threshold direct transition, which requires the least energy, occurs between the maximum in the valence band and minimum in the conduction band for a direct-bandgap semiconductor. Figure 3.2(a) illustrates two different direct transitions in a typical direct-bandgap semiconductor. The threshold direct transition, labelled (1), occurs for an incident photon of  $h\nu = E_g$  and is used in determining the bandgap energy experimentally. The other possible direct transitions require incident photons of higher energies ( $h\nu > E_g$ ), as illustrated by (2) in Figure 3.2(a). [Grundmann, 2010:272–274; Kittel, 2005:188–190; Sze and Ng, 2007:52].

The *indirect transition* between the valence and conduction bands is a transition from one  $\bar{p}$  value to a different  $\bar{p}$  value. Therefore, when an electron makes an indirect transition from the valence band to the conduction band, a change in crystal momentum is needed and, apart from a photon, a second particle is required to provide the missing difference to conserve momentum. The involvement of a *phonon*<sup>2</sup> can provide the momentum and also some amount of energy  $E_p$ . In indirect-bandgap semiconductors, the threshold transition is indirect and the transition energy is equal or greater than the true bandgap energy. Figure 3.2(b) illustrates the threshold indirect and a direct transition in a typical indirect-bandgap semiconductor, labelled (1) and (2) respectively. The threshold indirect transition starts with an electron being excited from the maximum in the valence band by an incident photon of some energy  $h\nu$ . Depending on the energy transferred to the electron and the crystal temperature, the transition to the minimum in the conduction band can be completed by either the emission or absorption of a phonon. The resulting total transition energy is then  $h\nu \mp E_p$ . The other direct transitions that are possible in an indirect-bandgap semiconductor

<sup>2</sup>Thermal energy in the crystal lattice give rise to quanta of lattice vibrations called phonons [Sze and Ng, 2007:50].

require, once again, incident photons of higher energies [Grundmann, 2010:272–274; Kittel, 2005:188–190; Sze and Ng, 2007:52].

### **Intrinsic and extrinsic semiconductors**

The *intrinsic* semiconductor is undoped and has equal concentrations of electrons and holes equal to the intrinsic carrier concentration per unit volume in [ $\text{cm}^{-3}$ ] ( $n_i$ ) and is determined by the density of states and the bandgap of the material, and the temperature. *Extrinsic* semiconductors, on the other hand, are semiconductors in which the type of *free carrier concentration*  $N_d$  was manipulated by the addition of controlled amounts of specific impurity atoms through a process called doping. Doping can either increase the free hole concentration  $p$  to form what is called a *p*-type semiconductor, or increase the free electron concentration  $n$  to form what is called an *n*-type semiconductor. Since an *n*-type semiconductor was used in this study, the focus is on this type [Isaacs, 2003:444; Pierret, 1989:30–36].

### ***n*-type semiconductor**

An *n*-type semiconductor has excess electrons in the conduction band, contributed by donor impurities, making conduction possible by majority negative ( $n$ ) carriers (electrons). Moreover, impurities are ionized, because their electrons are donated to the conduction band, resulting in ionized donor sites just below the lowest possible conduction band energy-level. Therefore, impurity energy-levels are introduced that lie within the bandgap. For an extrinsic semiconductor, the free carrier concentration is the difference between the donor impurity concentration  $N_D$  and the acceptor impurity concentration  $N_A$  [Taylor *et al.*, 2004:458–460].

### Intrinsic direct-WBG semiconductors

Morkoç *et al.* [1994] discusses how research in each of the intrinsic direct-WBG semiconductors, SiC, GaN and ZnSe, has led to major advances for realizing device applications. The need for optoelectronic devices that are active in the blue and UV wavelength ranges is one of a number of reasons for the interest in these types of semiconductors, especially the (Al,Ga,In)N semiconductors.

The group-III-nitrides have always had the potential of promising compact optoelectronic devices that are more reliable, have higher efficiencies, are environmentally friendly and robust thus diversifying their application due to their fundamental physical and electronic properties. However, development of group-III-nitride-based materials was mainly held back by the lack of an ideal substrate material and growth infrastructure, compared to SiC and ZnSe. This changed with the development of the Aixtron 200-4/HT metal-organic chemical vapour deposition (MOCVD) system during 1994 through a collaboration between Prof. M. Razeghi and Aixtron, as a World first in commercial reactors designed for the growth of GaN [Morkoç *et al.*, 1994:1379; Razeghi, 2011:263; Razeghi and Rogalski, 1996:7462].

Normally, GaN crystallizes in the wurtzite (hexagonal) crystal structure, but has also been known to have a zinc-blende (cubic) polytype [Razeghi and Rogalski, 1996:7463]. The small lattice mismatch between GaN and AlN permits flexibility in heterostructure design over a great range. Moreover, as a property of the wurtzite nitride polytypes, a continuous ternary alloy system can be formed so that the direct-WBG ranges from 6.20 eV in AlN to 3.44 eV in GaN [Morkoç *et al.*, 1994:1379].

The direct-WBG of the AlGaIn semiconductor can therefore in principle be engineered to any value between 6.20 eV and 3.44 eV, by varying the Al and Ga mole

fractions in the alloy composition. Moreover, this material is then also sensitive to **EMR** ranging from 200 nm to 360 nm and takes advantage of the direct-transition process, making it suitable for optoelectronic devices that are active in the **UV** region.

### 3.2 The AlGa<sub>x</sub>N semiconductor

A *tuneable* semiconductor is simply a material in which the bandgap can be engineered by varying the mole fractions of the constituents and, in doing so, changing the bandgap and making the material sensitive (responsive) to specific wavelengths. Furthermore, if the semiconductor does not respond to certain (longer) wavelengths, then the material is referred to as being *intrinsically* 'blind' to specific wavelengths.

The direct-bandgap of the ternary **AlGa<sub>x</sub>N** semiconductor alloy material can be varied by changing the **Al** mole fraction ( $x$ ) in the  $\text{Al}_x\text{Ga}_{1-x}\text{N}$  compound. **Om-  
nés et al. [1999:5287–5288]** related the variation of the bandgap at 300 K as a function of the **Al** mole fraction in the solid phase to

$$E_g(\text{Al}_x\text{Ga}_{1-x}\text{N}) = 3.42(1 - x) + 6.2x - bx(1 - x). \quad (3.3)$$

Here,  $b$  is the bowing parameter with a determined value of  $(0.8 \pm 0.1)$  eV and is plotted in Figure 3.3, showing the relationship to the wavelengths as well. The relation was determined from samples grown in **AlN** nucleation on *c*-orientated sapphire ( $\text{Al}_2\text{O}_3$ ). The bandgap was measured by photothermal deflection spectroscopy (**PDS**) as a function of the **Al** fraction, which was measured by a calibrated energy-dispersion spectroscopy (**EDS**) system.

This study investigates tuneable **AlGa<sub>x</sub>N**-based solar-blind **UV**-sensitive Schottky

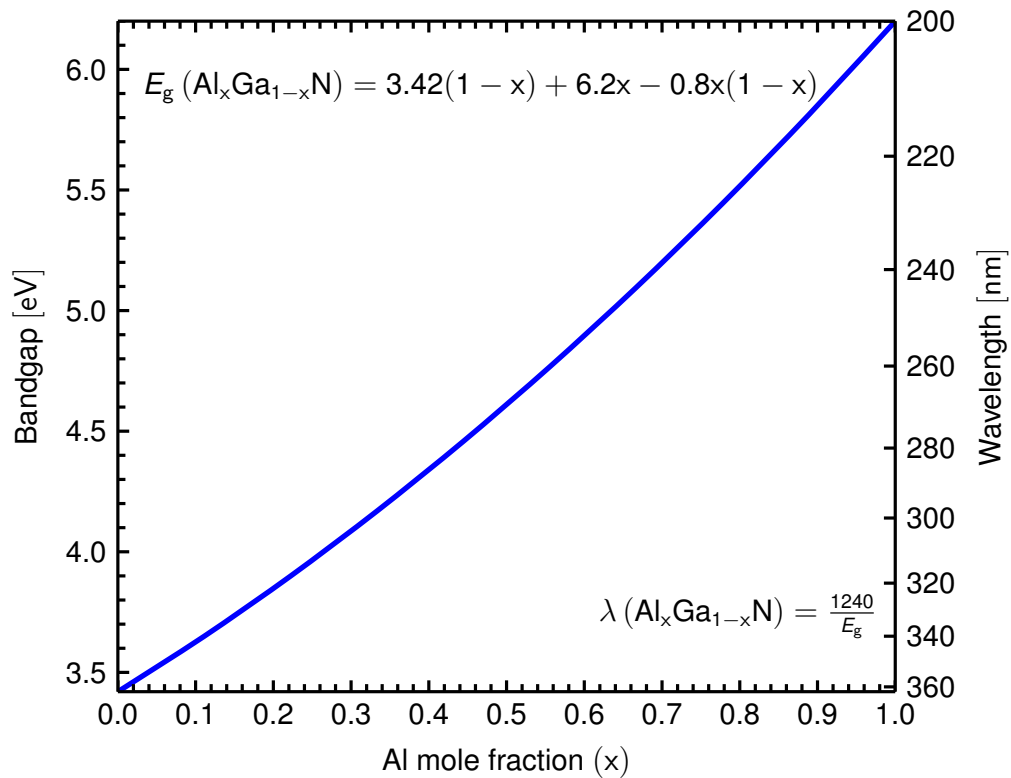


Figure 3.3: Variation of the bandgap at 300 K for the Al<sub>x</sub>Ga<sub>1-x</sub>N semiconductor. The relation was determined from samples grown in AlN nucleation (measured by PDS) as a function of the Al fraction in the solid phase (measured by calibrated EDS). Adapted from [Omnés et al. \[1999:5288\]](#).

photodiodes. Therefore, the next section looks at the physics of the Schottky diode and its electrical characterization. Thereafter, the photocurrent generation processes and the spectral characterization thereof are explained.

### 3.3 Schottky diodes

Metal–semiconductor rectifiers are the oldest solid-state devices used in electronics and were first investigated by Braun who published his observations in 1874 [Rhoderick, 1970:1153; Sze and Ng, 2007:134]. The theory that modelled the suggested potential barrier for the ideal metal–semiconductor diode was described by Schottky during the 1930s [Schroder, 2006:127; Sze and Ng, 2007:134]. To honour Schottky’s contribution, Schottky barrier diodes or just Schottky diodes refer to metal–semiconductor diodes and the metal that forms the potential barrier, a Schottky contact. Schottky contacts display distinctly non-linear  $I$ – $V$  characteristics. For electronic measurements, a second metal contact is fabricated which displays linear or quasi-linear  $I$ – $V$  characteristics, called an ohmic contact [Schroder, 2006:127].

The purpose of this section is to discuss the physics around Schottky diodes based on an  $n$ -type semiconductor. Subsection 3.3.1 describes the potential barrier formation in a Schottky diode and 3.3.2 the electrical characterization thereof. Section 3.4 considers the photovoltaic diode and explains two photocurrent generation processes and the spectral characterization of the Schottky photodiode.

#### 3.3.1 The ideal Schottky diode

Historically, the rectifying properties of a Schottky barrier became clear with the evaporation of metal films onto single-crystal semiconductor surfaces under very clean conditions. Because these metal– $n$ -type semiconductor contacts displayed near ideal rectification characteristics, the physics of Schottky barriers can be explained by considering the ideal metal– $n$ -type semiconductor contact without surface states or other anomalies [Rhoderick, 1970:1153–1154; Sze and Ng, 2007:135–139].

### Metal and $n$ -type semiconductor as separate systems

Consider the energy-level diagrams in Figure 3.4(a) for a metal and an  $n$ -type semiconductor, both electrically neutral and in separate isolated systems. The metal has a high *work function*<sup>3</sup> denoted by  $q\phi_m$ . The work function is the energy difference between the vacuum energy-level ( $E_0$ ) and the Fermi level. The Fermi levels of the metal and semiconductor are indicated with  $E_{Fm}$  and  $E_{Fs}$ , respectively. As in Sze and Ng [2007], the value of  $\phi_m$  is in units of volt [V]. By multiplying  $\phi_m$  by the unit electronic elementary charge ( $q$ ), the value of  $q\phi_m$  is in units of *electron-volt*<sup>4</sup> [eV]. Also, the values of the energy-levels are in units of eV and therefore

$$q\phi_m = E_0 - E_{Fm} \quad [\text{eV}]. \quad (3.4)$$

The donor energy-level, the energy of the donor levels below the conduction band edge, is indicated by  $E_D$  in Figure 3.4(a). The  $n$ -type semiconductor is electrically neutral, since for every positive donor ion a free electron resides in the conduction band. For an  $n$ -type semiconductor  $N_D \gg N_A$  and therefore  $N_d \approx N_D$  [Sze and Ng, 2007:21–27].

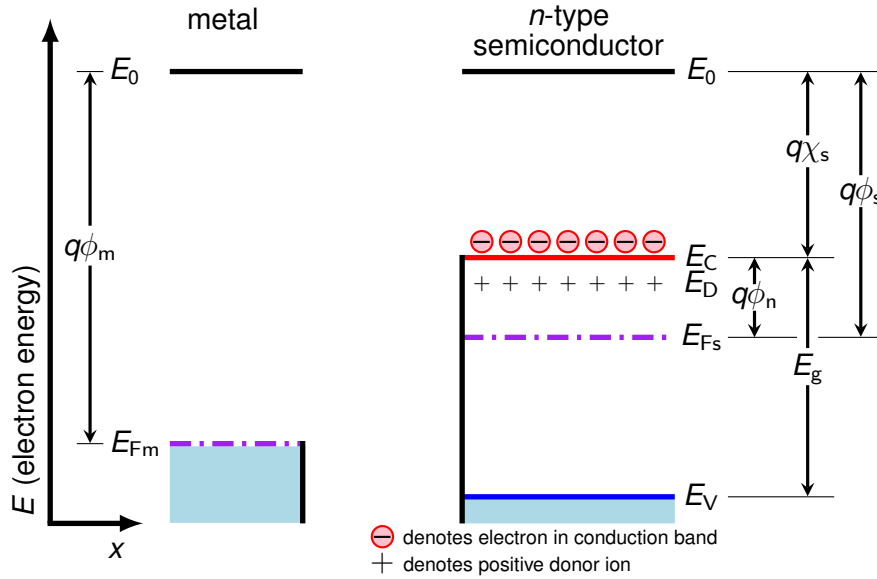
The bandgap energy for a semiconductor is given by Eq. 3.1 and in Figure 3.4(a) the highest possible valence band energy-level is again denoted by  $E_V$  and  $E_C$  denotes the lowest possible conduction band energy-level.

The intrinsic Fermi level of an intrinsic semiconductor lies close to the middle of the bandgap and is given by

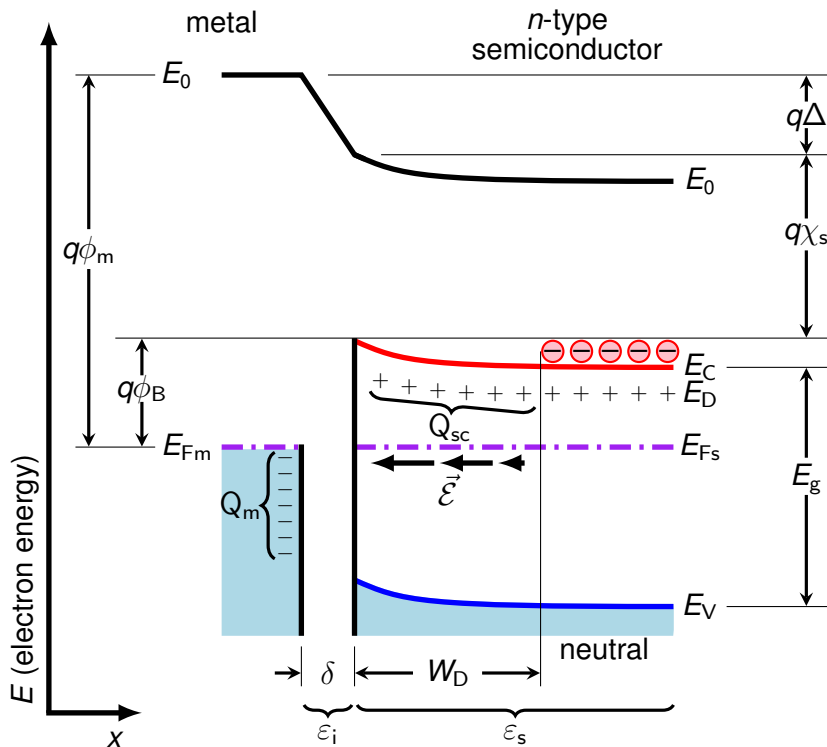
$$E_i = \frac{E_C + E_V}{2} + \frac{kT}{2} \ln \left( \frac{N_V}{N_C} \right). \quad (3.5)$$

<sup>3</sup>Energy required to liberate electrons from a material to the vacuum energy-level.

<sup>4</sup>Energy equal to the work done on an electron in moving it through a potential difference of 1 V [Isaacs, 2003:146].



(a) Electrically neutral metal and *n*-type semiconductor in separate isolated systems.



(b) Metal–*n*-semiconductor contact with an interfacial layer of atomic dimensions.

Figure 3.4: The energy-level diagrams of a metal and an *n*-type semiconductor with  $q\phi_m > q\phi_s$ .



Here  $N_V$  is the effective density of states in the valence band, given by

$$N_V = 2 \left( \frac{2\pi m_{dh} kT}{h^2} \right)^{\frac{3}{2}}, \quad (3.6)$$

with  $m_{dh}$  the density-of-state effective mass for holes in the valence band,

$$m_{dh} = \left[ (m_{lh}^*)^{\frac{3}{2}} + (m_{hh}^*)^{\frac{3}{2}} \right]^{\frac{2}{3}}, \quad (3.7)$$

where the subscripts refer to 'light' and 'heavy' hole masses.  $N_C$  is the effective density of states in the conduction band given by

$$N_C = 2 \left( \frac{2\pi m_{de} kT}{h^2} \right)^{\frac{3}{2}} M_C, \quad (3.8)$$

with  $M_C$  the number of equivalent minima in the conduction band and  $m_{de}$  the density-of-state effective mass for electrons in the conduction band, where

$$m_{de} = (m_1^* m_2^* m_3^*)^{\frac{1}{3}}. \quad (3.9)$$

Here,  $m_1^*$ ,  $m_2^*$  and  $m_3^*$  are the effective masses along the principle axes of the ellipsoidal energy surface.

The Fermi level for extrinsic semiconductors depends on the doping type and the donor or acceptor impurity concentration. For a nondegenerate  $n$ -type semiconductor with the dopants totally ionized, the Fermi level as a function of free electron concentration is given by

$$E_{Fs} = E_i + kT \ln \left( \frac{n}{n_i} \right), \quad (3.10)$$

where  $n$  is the free electron concentration,

$$n = N_C \exp\left(\frac{E_i - E_C}{kT}\right), \quad (3.11)$$

and  $n_i$  is the intrinsic carrier concentration obtained from

$$n_i = \sqrt{N_C N_V} \exp\left(-\frac{E_g}{2kT}\right). \quad (3.12)$$

Therefore, since  $N_D \gg N_A$  and  $n \approx N_D$ ,

$$E_{F_s} = E_i + kT \ln\left(\frac{N_D}{n_i}\right). \quad (3.13)$$

Equations 3.5 and 3.13 show that the Fermi level is dependent on the temperature, and at  $T = 0$  K it lies in the middle of the bandgap. For  $n$ -type semiconductors, Eq. 3.13 shows that as the donor impurity concentration  $N_D$  increases, the Fermi level  $E_{F_s}$  moves systematically upward in energy from the intrinsic Fermi level  $E_i$  and hence the reason for drawing  $E_{F_s}$  closer to  $E_C$  in Figure 3.4(a) [Pierret, 1989:42–54; Sze and Ng, 2007:17–19].

The energy difference between  $E_0$  and  $E_{F_s}$  of the  $n$ -type semiconductor in Figure 3.4(a), is its work function denoted by  $q\phi_s$ , but depends on  $N_D$ , since the position of  $E_{F_s}$  depends on  $N_D$ . The energy difference between  $E_0$  and  $E_C$ , however, is independent of  $N_D$ . Therefore, a fundamental property of a semiconductor is its *electron affinity*<sup>5</sup> indicated by  $q\chi_s$  and the work function of the semiconductor

<sup>5</sup>Energy released for the electron-attachment reaction, when an atom or molecule gains an electron to form a negative ion [Isaacs, 2003:141].

is given by

$$\begin{aligned}
 q\phi_s &= q\chi_s + (E_C - E_{F_s}) \\
 &= q(\chi_s + \phi_n) \quad [\text{eV}],
 \end{aligned}
 \tag{3.14}$$

where  $q\phi_n$  is the energy difference between  $E_C$  and  $E_{F_s}$ .

For the formation of a Schottky barrier, the work function of the metal must be greater than that of the  $n$ -type semiconductor. The difference between the work functions,  $\phi_m - (\chi_s + \phi_n)$ , is referred to as the contact potential. Therefore, if the materials are separated and there is no electric field between the materials with  $q\phi_m > q\phi_s$ , then the Fermi level of the  $n$ -type semiconductor  $E_{F_s}$  is greater in energy than the Fermi level of the metal  $E_{F_m}$ , as shown in Figure 3.4(a). As a result, the average energy of electrons in the  $n$ -type semiconductor is greater than the average energy of the electrons in the metal. Hence, it is expected that when the two materials are connected electrically, there is a transfer of electrons from the  $n$ -type semiconductor to the metal. The electron transfer continues until the average electron energies are equal and the system has returned to thermal equilibrium [Neudeck, 1989:127–128].

### **Metal and $n$ -type semiconductor brought into contact**

When a metal and a semiconductor are brought into contact, an electrostatic barrier is created, which gives the Schottky diode its rectifying properties [Rohderick, 1970:1153]. To understand how this arises, imagine that the metal and  $n$ -type semiconductor illustrated in Figure 3.4(a) are brought closer together and connected electrically, as in Figure 3.4(b). The gap between the metal and  $n$ -type semiconductor represents an interfacial layer of atomic dimensions and has thickness  $\delta$  with permittivity  $\epsilon_i$ .

In this approach to the ideal Schottky diode, the region within the gap is considered to be a perfect vacuum and has permittivity equal to one. Furthermore, the gap is considered very small compared to the inter-atomic distances, so that it is transparent to electrons (connected electrically) and can still have a potential difference across the gap [Sze and Ng, 2007:139–140].

As the two materials are brought closer, negative charge is built up at the metal surface as electrons (with greater energy) flow from the semiconductor to the metal, due to the difference in Fermi levels. At the same time, a built-in electric field  $\vec{\mathcal{E}}$  develops between the metal and  $n$ -type semiconductor. The electron transfer continues until the Fermi levels on both sides line up (the average electron energies are equal) and the system has returned to thermal equilibrium. The total negative surface-charge density on the metal  $Q_m$  is in equilibrium with the same amount of positive space-charge density in the semiconductor  $Q_{sc}$ . The positive space-charge density in the  $n$ -type semiconductor results from the ionized donor atoms. The alignment process of the Fermi levels causes an upward bending of the conduction and valence energy bands, because the balancing positive donor ions occupy a layer of substantial thickness. This is due to the donor impurity concentration being many orders of magnitude less than the electron concentration in the metal. The energy bands become constant deeper into the neutral bulk region of the semiconductor, where for every positive donor ion a free electron resides in the conduction band. The metal work function and electron affinity of the semiconductor do not change as the metal and semiconductor are brought into contact [Neudeck, 1989:128–129; Rhoderick, 1970:1153–1154; Sze and Ng, 2007:135].

The built-in electric field is directed from the bulk of the semiconductor to the metal surface, i.e. from right to left as indicated in Figure 3.4(b), increasing in strength toward the interface and opposing the flow of electrons. The electric field

within the vacuum gap is constant. The electrostatic potential  $\Delta$  across the gap is obtained by applying Gauss' law to the surface-charge density on the metal, yielding

$$\Delta = -\frac{\delta Q_m}{\epsilon_i}, \quad (3.15)$$

and therefore the magnitude of the electric field within the gap is given by

$$|\vec{\mathcal{E}}|_\delta = \frac{d\Delta}{d\delta} = -\frac{Q_m}{\epsilon_i}. \quad (3.16)$$

The built-in electric field causes the formation of a region next to the interface within the semiconductor that is depleted of electrons (and holes). This region is called the depletion region with depletion width  $W_D$ .

In Figure 3.4(b) the Schottky barrier is indicated by  $q\phi_B$  and the Schottky barrier height (SBH) is measured in units of eV. This particular illustration is similar to those in which unavoidable interface layers and interface states are taken into account when describing the SBH. Therefore, also considering Bardeen's theory, which shows that the SBH for an  $n$ -type semiconductor can be approximately expressed in the form

$$\phi_B = \gamma(\phi_m - \chi_s) + (1 - \gamma) \left( \frac{E_g}{q} - \phi_0 \right), \quad (3.17)$$

where

$$\gamma = \frac{\epsilon_i}{\epsilon_i + q^2 \delta D_{it}}.$$

Here  $\phi_0$  is the so-called neutral level<sup>6</sup> and  $D_{it}$  is the interface-trap density per eV per unit area in the bandgap of the semiconductor surface [Rhoderick, 1970:1154–1155; Sze and Ng, 2007:142].

<sup>6</sup>The neutral level,  $\phi_0$  is the level at which the surface states are occupied up to  $\phi_0$  and empty above  $\phi_0$ , the surface is electrically neutral [Rhoderick, 1970:1154].

### The ideal Schottky barrier diode electrostatics

The ideal metal– $n$ -type semiconductor contact is formed when the gap between the two materials becomes truly zero ( $\delta = 0$  m) and the electrostatic potential across the gap becomes zero as well ( $\Delta = 0$  V). Hence, there is no interface layer and no interface (surface) states.

Figure 3.5 illustrates the ideal intimate contact made between a metal and an  $n$ -type semiconductor at thermal equilibrium. First and foremost, if there is no interface layer and interface states, then  $\gamma = 1$  in Eq. 3.17 and the SBH is described by the relationship

$$q\phi_B = q(\phi_m - \chi_s), \quad (3.18)$$

as derived by Schottky [Rhoderick, 1970:1154–1155].

The one-dimensional Poisson equation relates the charge to the electric field and is one of the most important electrostatic equations. The electrostatic equations are one of the three groups of basic equations that describe the static and dynamic behaviour of carriers in semiconductors under external influences. These external influences can be applied fields or optical excitations that cause deviations from thermal-equilibrium conditions. The one-dimensional Poisson equation is given in a more useful form as

$$\frac{d^2\psi_i}{dx^2} = -\frac{d|\vec{\mathcal{E}}|}{dx} = -\frac{\rho}{\epsilon_s} = \frac{q(n - p + N_A - N_D)}{\epsilon_s}, \quad (3.19)$$

where  $\psi_i (\equiv -E_i/q)$  is the semiconductor potential,  $\epsilon_s$  the permittivity of the semiconductor and  $p$  the free hole concentration. The distance from the contact point into the bulk of the semiconductor is denoted by  $x$ . Poisson's equation is solved to determine the built-in electric field  $|\vec{\mathcal{E}}|$  and semiconductor potential  $\psi_i$

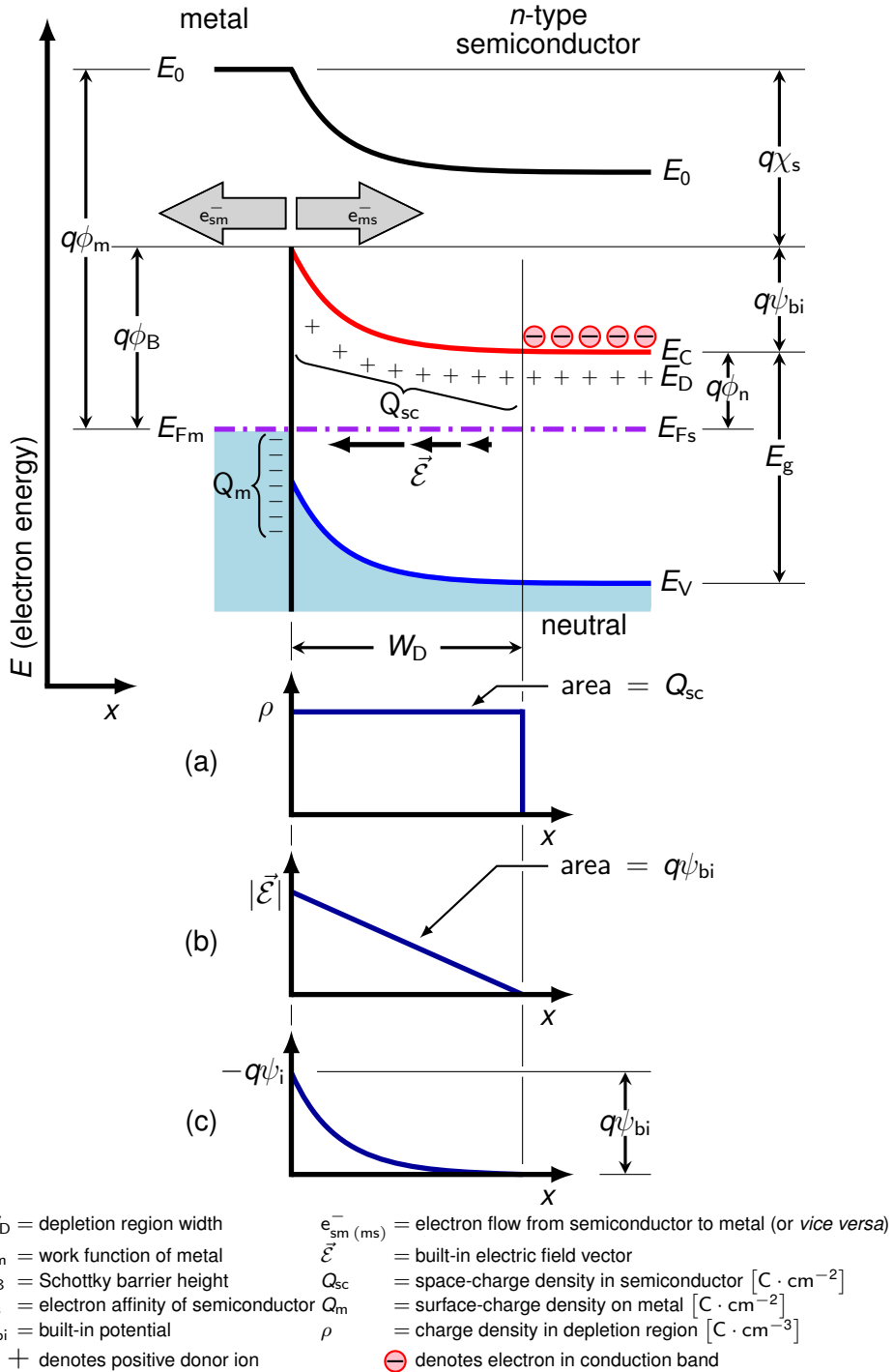


Figure 3.5: Detailed energy-level diagram of an ideal metal–*n*-semiconductor contact at thermal equilibrium (without an interfacial layer and interface states). Also illustrated are the depletion approximation (a) charge density, (b) built-in electric field and (c) potential.

caused by a charge density  $\rho$  within the depletion region [Sze and Ng, 2007:62].

The depletion region of the ideal metal– $n$ -type semiconductor contact can be considered as an one-sided abrupt junction. Because, within the depletion region, the ionized donor impurity concentration  $N_D^+$  is many orders greater than the electron concentration  $n_n$  in an  $n$ -type semiconductor. Therefore, the *depletion approximation* is used for obtaining an explicit solution of Poisson's equation [Neudeck, 1989:28–29; Sze and Ng, 2007:80,136].

Under the depletion approximation, the following results are obtained within the depletion region of an  $n$ -type semiconductor. Because, in the depletion region  $N_D^+ \gg n_n$  and  $N_D \approx N_D^+$ , the charge density is obtained as

$$\rho(x) \approx \begin{cases} qN_D & \text{if } 0 \leq x \leq W_D \\ 0 & \text{if } x > W_D \end{cases} . \quad (3.20)$$

Applying Eq. 3.20, implies that the charge density drops abruptly at the depletion edge, as illustrated in Figure 3.5(a). Integrating equation 3.20 over  $0 \leq x \leq W_D$ , the space-charge density in the semiconductor is obtained,

$$Q_{sc} = \int_0^{W_D} \rho(x) dx = qN_D W_D. \quad (3.21)$$

The space-charge density in the semiconductor  $Q_{sc}$  is positive (we are using a negative test charge in this derivation). The negative surface-charge density on the metal  $Q_m$  is equal to  $Q_{sc}$ . Furthermore, from Eq. 3.20 it follows that Eq. 3.19 simplifies to

$$\frac{d^2\psi_i}{dx^2} = -\frac{d|\vec{\mathcal{E}}|}{dx} = -\frac{qN_D}{\epsilon_s}. \quad (3.22)$$



The built-in electric field is obtained by integrating Eq. 3.22 as follows,

$$\begin{aligned}
 |\vec{\mathcal{E}}|(x) &= - \int_{W_D}^x \frac{qN_D}{\epsilon_s} dx \\
 &= - \frac{qN_D (x - W_D)}{\epsilon_s} = \frac{qN_D (W_D - x)}{\epsilon_s}.
 \end{aligned} \tag{3.23}$$

Figure 3.5(b) illustrates Eq. 3.23, from which is seen that the built-in electric field has a maximum strength at the interface ( $x = 0$  cm) and decreases linearly to zero for  $x \geq W_D$ . By integrating Eq. 3.23 a second time, the semiconductor potential is obtained as

$$\begin{aligned}
 \psi_i(x) &= - \int_{W_D}^x |\vec{\mathcal{E}}|(x) dx \\
 &= - \frac{qN_D (W_D - x)^2}{2\epsilon_s}.
 \end{aligned} \tag{3.24}$$

Equation 3.24 demonstrates that the semiconductor potential is a parabolic function and is illustrated in Figure 3.5(c). Therefore, the bending of the conduction and valence bands is parabolic in shape within the depletion region. However, deep into the neutral bulk region of the semiconductor the energy bands become constant again. Moreover, an electron will experience a maximum electric potential of  $\psi_{bi}$  relative to the conduction band edge in the bulk of the semiconductor when placed at the interface. This maximum electric potential, called the built-in potential, is the amount by which the Fermi level of the semiconductor was shifted at the interface to reach equilibrium. This is simply the ideal contact potential

and is also equal to the area under the built-in electric field, that yields

$$\psi_{\text{bi}} = \phi_{\text{m}} - (\chi_{\text{s}} + \phi_{\text{n}}) \quad (3.25)$$

$$= \phi_{\text{B}} + \phi_{\text{n}} \quad (3.26)$$

$$= \phi_{\text{B}} + kT \ln \left( \frac{N_{\text{C}}}{N_{\text{D}}} \right). \quad (3.27)$$

The depletion width is obtained by solving for  $W_{\text{D}}$  in Eq. 3.24 at  $x = 0$  cm, yielding

$$W_{\text{D}} = \sqrt{\frac{2\varepsilon_{\text{s}}\psi_{\text{bi}}}{qN_{\text{D}}}}. \quad (3.28)$$

The preceding discussion made use of the depletion approximation. If the contributions from majority carriers in addition to the impurity concentration are considered in the Poisson equation, then the properties obtained in the depletion region are more accurate, i.e. in the  $n$ -type semiconductor  $\rho(x) \approx q[N_{\text{D}} - n(x)]$  and a correction factor  $kT/q$  is introduced in Eq. 3.28, because of the majority carrier distribution tail near the edge of the depletion region,

$$W_{\text{D}} = \sqrt{\frac{2\varepsilon_{\text{s}}}{qN_{\text{D}}} \left( \psi_{\text{bi}} - \frac{kT}{q} \right)}. \quad (3.29)$$

Furthermore, the depletion width as a function of the applied voltage  $V$  is given by

$$W_{\text{D}} = \sqrt{\frac{2\varepsilon_{\text{s}}}{qN_{\text{D}}} \left( \psi_{\text{bi}} - V - \frac{kT}{q} \right)}, \quad (3.30)$$

because the total electrostatic potential change across the junction is given by  $(\psi_{\text{bi}} - V)$ , where the applied voltage is positive for forward biasing and negative for reverse biasing [Sze and Ng, 2007:83].

### 3.3.2 Electrical characteristics

Electrical characterization allows for the understanding of the current transport processes and quantifying of the quality of the rectifying properties of a Schottky diode. The current transport processes and the associated theory are reviewed in an article by Rhoderick [1982] and covered in detail by Sze and Ng [2007:153–170]. The  $I$ – $V$  and  $C$ – $V$  measurements are important electrical characterization techniques. Parameters, such as the ideality factor ( $\eta$ ), SBH ( $q\phi_B$ ), reverse leakage current density ( $J_R$ ) at 1 V reverse biasing and series resistance ( $R_S$ ) are obtained from the  $I$ – $V$  relationship. From the  $C$ – $V$  relationship the donor impurity concentration and, also, the SBH can be obtained.

#### The thermionic-emission $J$ – $V$ relationship with series resistance

Consider the ideal Schottky diode on an  $n$ -type semiconductor at thermal equilibrium, as illustrated in Figure 3.5. The current transport process in this ideal case is the emission of electrons from the semiconductor over the top of the barrier into the metal, called the thermionic-emission current [Rhoderick, 1982:4]. The thermionic-emission theory assumes that (1) the SBH is much greater than  $kT$ , (2) the Fermi level is horizontal throughout the depletion region, because the current is limited to the emission process and (3) the electron flow from the semiconductor to the metal ( $e_{sm}^-$ ) would be equal to that flowing from the metal to the semiconductor ( $e_{ms}^-$ ), i.e. the net current is in equilibrium so that the two currents can be superimposed. Therefore, under these assumptions the current only depends on the SBH [Rhoderick, 1982:4; Sze and Ng, 2007:154–155].

When forward biasing the Schottky diode, only electrons with energy greater than the SBH contribute to the forward current and the free electron concentration is

then given by

$$n = N_C \exp\left(-\frac{q(\phi_B - V_d)}{kT}\right). \quad (3.31)$$

Here,  $V_d$  is the diode voltage across the depletion region exclusively and does not include any voltage drops across the metal– $n$ -type semiconductor quasi-neutral regions [Schroder, 2006:186]. Furthermore, the average thermal velocity for randomly moving carriers across a plane (semiconductor to metal) follows a Maxwellian velocity distribution, therefore

$$v_{\text{avg}} = \sqrt{\frac{8kT}{\pi m^*}}, \quad (3.32)$$

and the current density (current per unit Schottky contact area  $A_c$  in  $\text{cm}^2$ ) from the random motion of carriers across a plane is

$$J_{\text{sm}} = nq \frac{v_{\text{avg}}}{4}. \quad (3.33)$$

Assuming that  $M_C = 1$  and  $m_{\text{de}} = m^*$  for the ideal Schottky diode, Eqs. 3.8, 3.31 and 3.32 can be substituted into Eq. 3.33. The thermionic-emission current density is then given by

$$J_{\text{sm}}(V_d) = A^* T^2 \exp\left(-\frac{q\phi_B}{kT}\right) \left[ \exp\left(\frac{qV_d}{kT}\right) \right], \quad (3.34)$$

where  $A^*$  is known as the effective Richardson constant, which can be theoretically calculated from

$$A^* = \frac{4\pi q m^* k^2}{h^3} = 120 \left(\frac{m^*}{m_0}\right) [\text{A} \cdot \text{cm}^{-2} \cdot \text{K}^{-2}], \quad (3.35)$$

where  $(m^*/m_0)$  is the effective electron mass. The effective Richardson con-

stant for thermionic emission neglects the effects of optical-phonon scattering and quantum mechanical reflection [Sze and Ng, 2007:156–158].

The SBH  $\phi_B$  depends on the biasing for several reasons. One significant factor, particularly for highly doped semiconductors, is the image force experienced by electrons close to the metal contact. Sze and Ng [2007:146–150] discusses image-force lowering that causes the SBH to be reduced by

$$\Delta\phi = \sqrt{\frac{q|\vec{\mathcal{E}}|}{4\pi\epsilon_s}}. \quad (3.36)$$

Another such reduction can be due to the presence of interfacial layers between the metal and the semiconductor that results in a voltage drop across the interfacial layers [Schroder, 2006:231].

However, when supposing that the ideal SBH depends linearly on the biasing, which is true for small potential differences, then the SBH is given by

$$\phi_B = \phi_{B0} + \beta V_d, \quad (3.37)$$

where the  $\beta$  coefficient is positive, because  $\phi_B$  always increases with increased forward bias and  $\phi_{B0}$  is the SBH without image-force lowering [Rhoderick, 1982:5; Schroder, 2006:231].

Since the SBH remains the same for electrons moving from the metal to the semiconductor under reverse bias, the applied voltage does not affect the current into the semiconductor. Therefore, when a Schottky diode is zero-biased, the current density  $J_{ms}$  is obtained from Eq. 3.34 by setting  $V_d = 0$  V, so that

$$J_{ms} = -J_{ms}(0) = -A^* T^2 \exp\left(-\frac{q\phi_B}{kT}\right). \quad (3.38)$$

The total thermionic-emission current density is the sum of Eqs. 3.34 and 3.38. The current density–voltage ( $J$ – $V$ ) relationship for the ideal Schottky diode is therefore expressed as

$$J = A^* T^2 \exp\left(-\frac{q\phi_B}{kT}\right) \left[ \exp\left(\frac{qV_d}{kT}\right) - 1 \right]. \quad (3.39)$$

Substituting Eq. 3.37 into Eq. 3.39 yields

$$J = J_0 \left[ \exp\left(\frac{qV_d(1-\beta)}{kT}\right) \right] \left[ 1 - \exp\left(-\frac{qV_d}{kT}\right) \right], \quad (3.40)$$

where

$$J_0 = A^* T^2 \exp\left(-\frac{q\phi_{B0}}{kT}\right), \quad (3.41)$$

referred to as the saturation current density [Schroder, 2006:157–158; Sze and Ng, 2007:157].

A real Schottky contact is rarely uniform over its entire area. This can lead to other current transport processes, such as thermionic-field emission. In addition, there can be interface damage and interface layers [Schroder, 2006:158, 232]. Therefore, the ideality factor  $\eta$  is introduced to account for these and other (unknown) effects that occur in real Schottky diodes and is defined as

$$\frac{1}{\eta} = 1 - \beta = 1 - \frac{\partial\phi_B}{\partial V_d}, \quad (3.42)$$

allowing Eq. 3.40 to be written as

$$J = J_0 \left[ \exp\left(\frac{qV_d}{\eta kT}\right) \right] \left[ 1 - \exp\left(-\frac{qV_d}{kT}\right) \right]. \quad (3.43)$$

The ideality factor is constant, when  $\partial\phi_B/\partial V_d$  is constant [Rhoderick, 1982:5].

Also, Eq. 3.43 not only considers deviations from the ideal case when forward biased, but also when it is reverse biased. This is important because image-force lowering affects the electron flow from the semiconductor to the metal and *vice versa* [Rhoderick, 1982:5; Schroder, 2006:231].

The performance of a Schottky diode is generally degraded by a very large series resistance. The series resistance depends on the contact resistance, semiconductor resistivity and on geometric factors. For a reverse-biased photodiode with a photocurrent in the nA range, the series resistance is of minor concern, however, the aim is to have the series resistance as low as possible [Schroder, 2006:183].

Figure 3.6 is the equivalent circuit of a Schottky diode. The circuit consists of an ideal diode with a voltage drop  $V_d$  across it, a capacitor  $C_D$  that models the depletion-region capacitance and a resistor  $R_P$ , all in parallel. These three components are connected in series with a resistor  $R_S$ . For a (forward) current  $I$  through the circuit, the applied voltage  $V$  across the whole circuit is given by

$$V = V_d + IR_S. \quad (3.44)$$

The thermionic-emission  $J$ - $V$  relationship for a Schottky diode with series resistance then becomes

$$J = J_0 \left[ \exp \left( \frac{q(V - IR_S)}{\eta kT} \right) \right] \left[ 1 - \exp \left( -\frac{q(V - IR_S)}{kT} \right) \right]. \quad (3.45)$$

Theoretical plots of two  $J$ - $V$  characteristics are presented in Figure 3.7 for an arbitrary Schottky diode. The Schottky diode is forward and reverse biased up to 1 V at 300 K, with  $A_c = 1 \text{ cm}^2$ ,  $A^* = 120 \text{ A} \cdot \text{cm}^{-2} \cdot \text{K}^{-2}$  and  $\phi_{B0} = 1.2 \text{ eV}$ . The solid (gray) line shows the thermionic-emission current for the ideal case

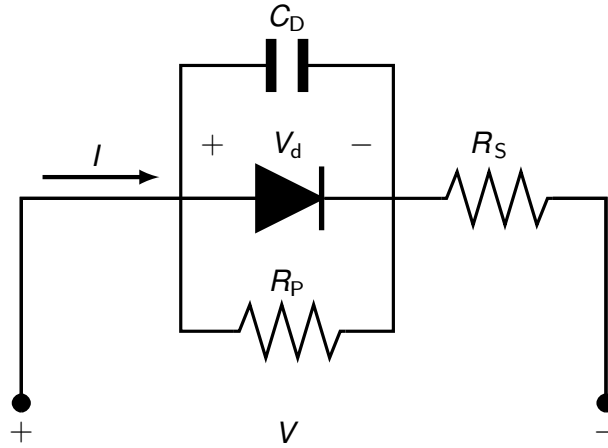


Figure 3.6: The equivalent circuit of a Schottky diode, consisting of an ideal diode with a voltage drop  $V_d$  across it, together with a capacitor  $C_D$  that models the depletion-region capacitance and a resistor  $R_P$ , all in parallel. The three components are connected in series with resistor  $R_S$ . Applying a voltage  $V$  across the whole circuit results in a current  $I$  through the circuit.

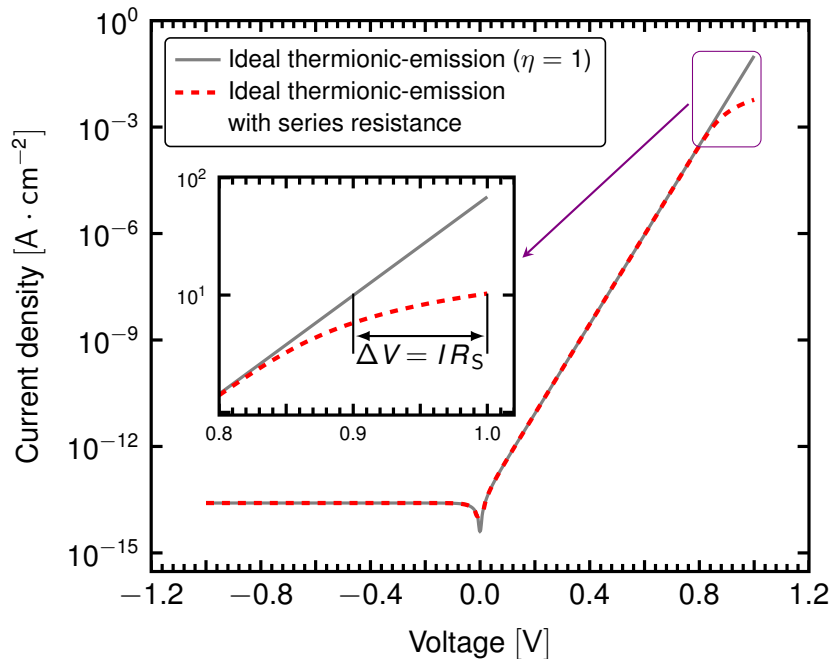


Figure 3.7: Two theoretical  $J$ - $V$  characteristics for an arbitrary Schottky diode when forward and reverse biased up to 1 V at 300 K, with  $A_c = 1 \text{ cm}^2$ ,  $A^* = 120 \text{ A} \cdot \text{cm}^{-2} \cdot \text{K}^{-2}$  and  $\phi_{B0} = 1.2 \text{ eV}$ . The solid (gray) line shows the thermionic-emission current for the ideal case. The dashed (red) line shows the current characteristic for a series resistance of  $1 \text{ m}\Omega$ . Inset: The deviation from linearity at high current is clearly seen for forward biasing from (0.8 to 1.0) V.



(Eq. 3.43). The dashed (red) line shows the  $J$ – $V$  curve for a series resistance of  $1 \text{ m}\Omega$  (Eq. 3.45) and as a result, the curve deviates from linearity at high current.

### Parameters extracted from the $J$ – $V$ relationship

The ideality factor and SBH are determined from the  $I$ – $V$  measurements where the logarithm of the current depends linearly on the forward-bias voltage. This linear region is typically found where  $3kT/q < V \ll IR_S$ , such that Eq. 3.45 becomes

$$J = J_0 \exp\left(\frac{qV}{\eta kT}\right). \quad (3.46)$$

Equation 3.46 can be transformed to a straight-line equation by taking the logarithm<sup>7</sup>, resulting in

$$\log J = \log J_0 + \frac{q}{\eta kT \ln 10} V. \quad (3.47)$$

The ideality factor is determined from the slope of  $\log J$  versus  $V$  and is inversely proportional to it, that is

$$\eta = \frac{q}{kT \ln 10} \left[ \frac{d(\log J)}{dV} \right]^{-1}. \quad (3.48)$$

The  $\log J_0$  is the intercept value on the  $\log J$ -axis at zero biasing and used to determine the saturation current density,  $J_0$ . Using the determined saturation current density together with the (known) effective Richardson constant obtained through Eq. 3.35, the SBH without image-force lowering is calculated from

$$\phi_{B0} = \frac{kT}{q} \log\left(\frac{A^* T^2}{J_0}\right). \quad (3.49)$$

<sup>7</sup>The logarithm to base 10 ( $\log$ ) is used instead of the natural logarithm ( $\ln$ ), because usually experimental data is plotted on a logarithmic scale of base 10 [Schroder, 2006:186].

The series resistance can be determined from the deviation in linearity of the  $\log J-V$  curve at high forward bias currents, as shown by the the inset in Figure 3.7. A number of methods can be used to determine the series resistance and more detail can be found in Schroder [2006:187–188,190–192] and Sze and Ng [2007:181–187]. One typical method is to obtain the difference between the measured voltage drop and the expected voltage across the ideal diode ( $\Delta V = V - V_d$ ) at each current density  $J$ , followed by plotting  $\Delta V$  versus  $I$  on a linear scale. The series resistance  $R_S$  is then obtained from the slope [Neudeck, 1989:86–87].

### The C–V relationship

The metal to the depletion region to the bulk semiconductor form a parallel plate like capacitor with the depletion region acting as the insulator [Neudeck, 1989:140]. Moreover, the depletion width is voltage dependent and broadens with an increase in reverse biasing, as described by Eq. 3.30. By superimposing a small-voltage sinusoidal AC signal upon a DC bias, incremental charges are induced on the metal surface of one sign and, thus, the surface-charge density on the metal changes by  $dQ_m$ . Simultaneously, charges of opposite sign are induced in the semiconductor, changing the space-charge density in the semiconductor by  $dQ_{sc}$ . Therefore, the small-signal (differential) depletion-region capacitance over a Schottky contact area  $A_c$  can be defined as

$$C_D = -A_c \frac{dQ_m}{dV} = A_c \frac{dQ_{sc}}{dV}. \quad (3.50)$$

The amplitude of the small-voltage sinusoidal AC signal can vary between (10 and 20) mV for frequencies ranging from 10 kHz to 1 MHz. However, other small-voltage amplitudes and frequencies can also be considered [Schroder, 2006:62]

Differentiating Eq. 3.21 and substituting Eq. 3.30, the  $C$ - $V$  relationship is obtained as

$$C_D = \sqrt{\frac{q \varepsilon_s N_D A_c^2}{2 \left( \psi_{bi} - V - \frac{kT}{q} \right)}}. \quad (3.51)$$

Equation 3.51 is plotted by the solid (black) line for an arbitrary Schottky diode in Figure 3.8. The Schottky diode is biased from  $(-1$  to  $0)$  V at 300 K, with  $K_s = 10$ ,  $N_D = 10^{15} \text{ cm}^{-3}$ ,  $A_c = 1 \text{ cm}^2$ ,  $N_C = 10^{18} \text{ cm}^{-3}$  and  $\phi_{B0} = 1.2 \text{ eV}$ .

In some instances, the capacitance is measured for a forward bias. These measurements can deviate from linearity, because of the existence of a diffusion capacitance in addition to the depletion-region capacitance [Sze and Ng, 2007:85].

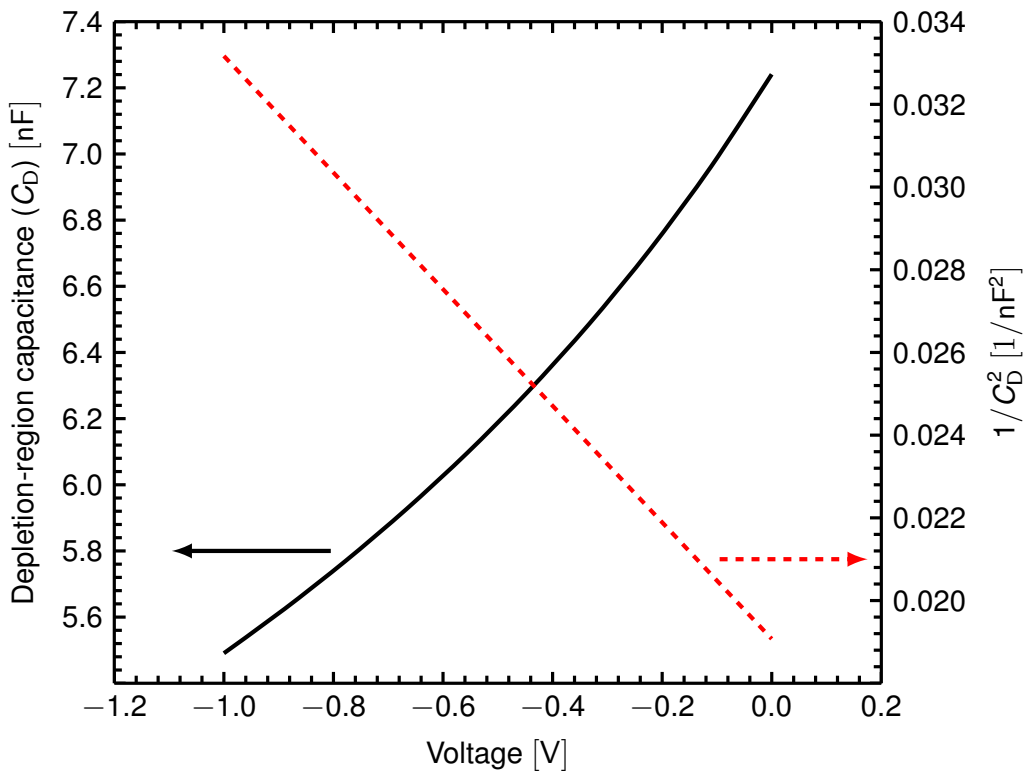


Figure 3.8: The theoretical  $C$ - $V$  characteristics for an arbitrary Schottky diode when biased from  $(-1$  to  $0)$  V at 300 K, with  $K_s = 10$ ,  $N_D = 10^{15} \text{ cm}^{-3}$ ,  $A_c = 1 \text{ cm}^2$ ,  $N_C = 10^{18} \text{ cm}^{-3}$  and  $\phi_{B0} = 1.2 \text{ eV}$ .

### Parameters extracted from the $C-V$ relationship

To determine the donor impurity concentration and SBH from  $C-V$  measurements, Eq. 3.51 can be inverted to obtain a straight-line equation, that is,

$$\begin{aligned} \frac{1}{C_D^2} &= \frac{2}{q\epsilon_s N_D A_c^2} \left( \psi_{bi} - V - \frac{kT}{q} \right) \\ &= - \left( \frac{2}{q\epsilon_s N_D A_c^2} \right) V + \frac{2}{q\epsilon_s N_D A_c^2} \left( \psi_{bi} - \frac{kT}{q} \right), \end{aligned} \quad (3.52)$$

which is also plotted in Figure 3.8, as the dashed (red) line.

The slope of  $1/C_D^2$  versus  $V$  is negative, because an  $n$ -type semiconductor is being considered and its majority carriers are electrons. The donor impurity concentration is inversely proportional to the slope, such that

$$N_D = \frac{2}{q\epsilon_s A_c^2} \left[ \frac{d(1/C_D^2)}{dV} \right]^{-1}. \quad (3.53)$$

The projection to where  $1/C_D^2 = 0$  yields an intercept on the  $V$ -axis, such that

$$V_i = \psi_{bi} - \frac{kT}{q}. \quad (3.54)$$

Substituting Eq. 3.54 into Eq. 3.27, yields

$$\phi_{B0} = V_i + \frac{kT}{q} + kT \ln \left( \frac{N_C}{N_D} \right), \quad (3.55)$$

from which the SBH is determined (without image-force lowering) [Neudeck, 1989:141; Schroder, 2006:63,161; Sze and Ng, 2007:85,175].

## 3.4 Photovoltaic diodes

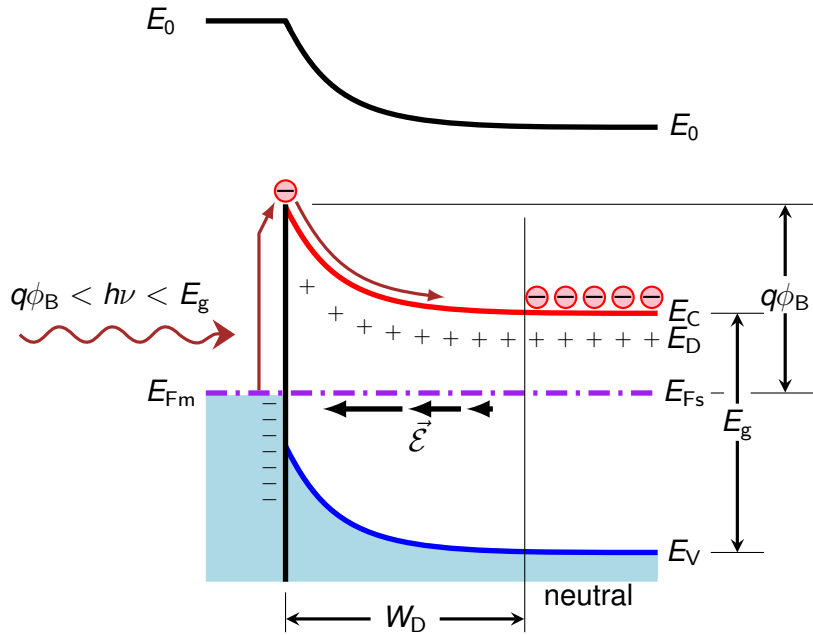
Schottky photodiodes are of particular interest, because of their advantages over  $p$ - $n$  junction photodiodes. Such as, simpler fabrication techniques, the absence of high-temperature diffusion processes, higher short-wavelength sensitivity (electron-hole pair generation occurs in the depletion region, separated by a built-in electric field) and faster response (transport of majority charge carriers generates the photocurrent and not through a recombination-generation process). However, some disadvantages are lower breakdown voltages and large reverse leakage currents [Goldberg, 1999:R51; Razeghi and Rogalski, 1996:7450].

The Schottky photodiode is part of a family of photovoltaic diodes, which include  $p$ - $i$ - $n$ ,  $p$ - $n$ , and heterojunction photodiodes [Sze and Ng, 2007:671]. The photodiode falls under the photoelectric class of detectors and generates an electrical signal through either the internal photoemissive process or the photovoltaic process. The photocurrent generation in Schottky photodiodes depends on the energy of the incident photons that can either interact with the metal contact or the direct-bandgap  $n$ -type semiconductor [Razeghi and Rogalski, 1996:7435–7436,7442].

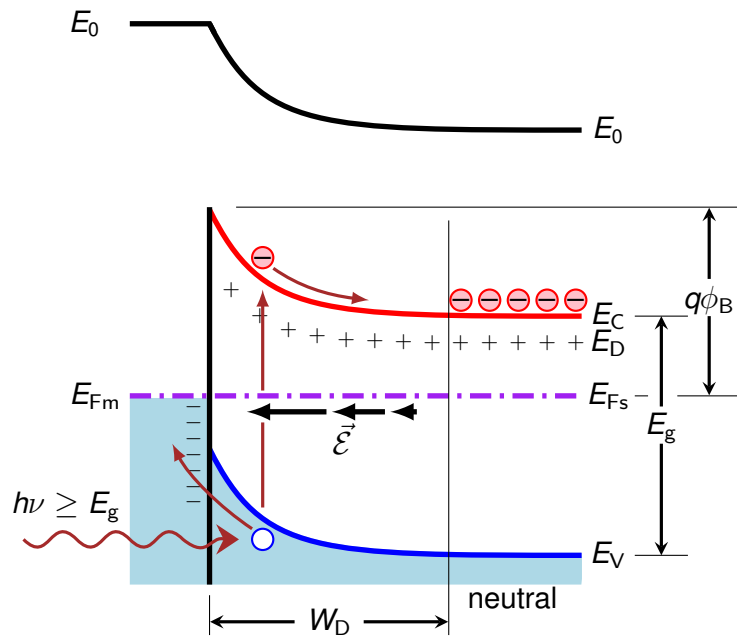
### 3.4.1 Photocurrent generation

#### Internal photoemissive process

If an incident photon has an energy greater than the SBH, but less than the bandgap energy of the semiconductor ( $q\phi_B < h\nu < E_g$ ), then an electron can be excited from the metal. This photoexcited electron can overcome the barrier and be collected by the semiconductor, generating a photocurrent through the internal photoelectric effect [Goldberg, 1999:R51–R52; Sze and Ng, 2007:681].



(a) Internal photoemissive process, whereby a photon is absorbed in the metal, exciting an electron with energy greater than the SBH (internal photoelectric effect).



(b) Photovoltaic process, whereby a direct band-to-band photoexcited electron-hole pair in the depletion region is separated by the built-in electric field.

Figure 3.9: The energy-level diagrams illustrating photocurrent generation in Schottky photodiodes.

Figure 3.9(a) is an energy-level diagram that illustrates the internal photoemissive process, whereby the internal photoelectric effect generates the photocurrent. This process has been used as an accurate and direct method of determining the SBH in photoelectric measurements. It was also used to study hot-electron transport processes in metal films. These photoexcited electrons, however, have momentum in random directions. Hence, only electrons with excess energy greater than the SBH and momentum toward the semiconductor contribute to the photocurrent. This is therefore a very inefficient process with quantum efficiencies that are typically lower than 1 % [Goldberg, 1999:R51–R52; Sze and Ng, 2007:176–178,681–682].

### Photovoltaic process

If an incident photon has an energy greater or equal to the bandgap energy of a direct-bandgap  $n$ -type semiconductor ( $h\nu \geq E_g$ ), then an electron can undergo a direct band-to-band transition. This results in an electron-hole pair within the depletion region that is then separated by the built-in electric field and, thus, generating a photocurrent [Goldberg, 1999:R51–R52; Sze and Ng, 2007:680–681].

Figure 3.9(b) is an energy-level diagram that illustrates the photovoltaic process, whereby a photoexcited electron-hole pair results after a direct band-to-band transition in the depletion region and is then separated by the built-in electric field. The electron moves to the bulk of the semiconductor and the hole is absorbed by the Schottky barrier material. The generated photocurrent is in the reverse current direction and can, therefore, be operated as an avalanche photodiode at high reverse-bias voltages. Moreover, because the photocurrent is in the reverse current direction, small dark (when zero biased) and reverse leakage currents would be advantageous for sensitive photodiodes. Furthermore, for

front-irradiation, the metal has to be very thin ( $< 10$  nm) and the Schottky barrier material should have a high work function for minimum absorption. Lastly, the photovoltaic process is usually more efficient than the internal photoemissive process [Goldberg, 1999:R51–R52; Sze and Ng, 2007:682].

### 3.4.2 Spectral characteristics

Through spectral characterization, the quality of the electrical signal generated by the interaction of photons with a photodiode can be quantified. The three main quantifying parameters considered include the spectral responsivity, quantum efficiency and the UV-to-VIS and NIR (UV-to-VIS/NIR) rejection ratios with respect to a desired wavelength.

#### Current responsivity

The *spectral responsivity* is the ratio of the electrical signal from a photodiode to the spectral radiant flux incident on the photodiode [Larason and Houston, 2008:1]. The electrical signal can either be a generated photocurrent in the photodiode, or a potential difference across the photodiode.

The spectral characteristics of a photodiode can be investigated at zero bias, operating it in the photovoltaic mode and, hence, the current responsivity is considered. The *current responsivity* is the ratio between the short-circuit photocurrent density (PCD)  $J_p$  in  $[A \cdot cm^{-2}]$  and the irradiance ( $E_e$ ) in  $[W \cdot cm^{-2}]$  from a monochromatic EMR source [Goldberg, 1999:R44]. The current responsivity at a specific wavelength can be calculated from

$$\mathcal{R}_\lambda = \frac{J_p}{E_e(\lambda)} \quad [A \cdot W^{-1}]. \quad (3.56)$$

The *cut-off wavelength* ( $\lambda_{\text{cut-off}}$ ) was defined as the wavelength at which the cur-



rent responsivity ( $\mathcal{R}$ ) dropped to less than 50 % of its maximum value.

### Quantum efficiency

The *quantum efficiency* is the ratio between the number of electron-hole pairs generated and the number of incident photons [Goldberg, 1999:R44]. The PCD is a direct measure of the number of electron-hole pairs generated per unit time per photosensitive area. Irradiance is proportional to the number of incident photons per unit time per photosensitive area (photon-flux density).

The number of photons ( $Q_p$ ) is in unit of quantum [q] and is the quotient between the radiant energy ( $Q_e$ ) of the EMR and the discrete energy ( $E$ , Eq. 2.1 in Chapter 2) of a single photon that is proportional to the wavelength at which that photon is travelling, so that

$$Q_p(\lambda) = \frac{Q_e}{E} = (hc)^{-1} \cdot \lambda \cdot Q_e \quad [\text{q}] \quad (3.57)$$

$$= (5.034 \times 10^{15} [\text{q} \cdot \text{J}^{-1} \cdot \text{nm}^{-1}]) \cdot \lambda [\text{nm}] \cdot Q_e [\text{J}]. \quad (3.58)$$

The number of photons in a ray of radiation is frequently regarded as a pure (dimensionless) number. However, this number is in fact a measure of the ‘amount of radiation’ in a ray. Accordingly, the useful quantity of quanta per second [ $\text{q} \cdot \text{s}^{-1}$ ] is assigned as the unit of photon flux ( $\Phi_p$ ) [Nicodemus *et al.*, 1976:61].

It follows from Eq. 3.57 that the incident photon-flux density ( $E_p$ ) in [ $\text{q} \cdot \text{s}^{-1} \cdot \text{cm}^{-2}$ ] can be related to the irradiance by

$$E_p(\lambda) = (hc)^{-1} \cdot \lambda \cdot E_e(\lambda). \quad (3.59)$$

The quantum efficiency for a specific wavelength can then be derived as follows:

$$\begin{aligned}\eta_{\lambda} &= \frac{J_p}{E_p(\lambda)} \\ &= \frac{J_p}{(hc)^{-1} \cdot \lambda \cdot E_e(\lambda)},\end{aligned}\quad (3.60)$$

substituting for  $J_p$  from Eq. 3.56 shows that the quantum efficiency is associated with the current responsivity by

$$\eta_{\lambda} = \frac{hc}{\lambda} \mathcal{R}_{\lambda}.\quad (3.61)$$

Furthermore, it can be shown that

$$\frac{hc}{\lambda} = \frac{1240}{\lambda [\text{nm}]},$$

and, hence, that the quantum efficiency for a specific wavelength in [nm] is determined from

$$\eta_{\lambda} = \frac{1240}{\lambda [\text{nm}]} \mathcal{R}_{\lambda}.\quad (3.62)$$

### UV-to-VIS/NIR rejection ratio

The UV-to-VIS/NIR rejection ratio is defined by

$$J_p(\lambda_s) / J_p(\lambda \geq \lambda_s) = \frac{J_p(\lambda_s)}{|J_p(\lambda_i) - J_d|},\quad (3.63)$$

where  $J_d$  is the dark current density (or noise).  $J_p(\lambda_i)$  is the measured PCD while being irradiated by an unwanted wavelength  $\lambda_i$  for which the rejection needs to be determined. The rejection ratio is determined with respect to the PCD  $J_p(\lambda_s)$  that was measured at a desired specified wavelength  $\lambda_s$ .

## Chapter 4

# The optoelectronic characterization system

### 4.1 Construction overview

An optoelectronic characterization system was constructed with the purpose to characterize optoelectronic devices. In particular, the system had to electrically and spectrally characterize UV-sensitive photodiodes. A system for the electrical characterization of Schottky diodes was already established. Electrical characterization was being performed inside a light-tight shielded enclosure to minimize EMI from external noise sources. A desktop computer running a National Instruments (NI) LabVIEW routine controlled a programmable pA meter/DC voltage source and a low frequency (LF) impedance analyzer for the application of  $I-V$  and  $C-V$  techniques, respectively on Schottky diodes.

Spectral characterization, however, requires the ability to select wavelengths of EMR to which the photosensitive area of the Schottky diode was exposed to, while measuring the photocurrent generated at each selected wavelength. The programmable pA meter/DC voltage source could be used to measure photocurrents, with or without biasing the photodiode. Only a radiating source was still

needed that could irradiate the photodiode.

The addition of radiating sources and a Czerny-Turner type monochromator outside of the already established electrical characterization system, allowed for different wavelength selection. An optical fibre was chosen for use in leading the selected wavelength of EMR, or just monochromatic EMR, from the monochromator to the photodiode inside the enclosure. This only required the making of a small (approx. 10 mm-diameter) hole through which the fibre could pass into the enclosure, without compromising the ability to shield EMI. Inside the enclosure the fibre was positioned perpendicular to the photodiode and fixed at a distance, such that the diameter of the irradiated area was large enough to ensure coverage of the whole photosensitive area of the photodiode.

Dark and irradiated electrical characterization is possible. Spectral characterization is done by measuring photocurrents generated in a photodiode, while it is irradiated with photons of specific energy that corresponds to the selected wavelength of EMR.

Figure 4.1 is a schematic illustration of the constructed optoelectronic characterization system and Figure 4.2 is a photograph of the system that was set-up in the laboratory of the Electronic Materials and Thin Film Research Group. From the schematic illustration it is seen that the EMR source radiates over a range of wavelengths producing a total radiant flux  $\Phi_e$  that enters the monochromator. An NI LabVIEW routine was used to control the monochromator and allow a selected wavelength  $\lambda$  to exit. The monochromatic EMR exits with a corresponding radiant flux  $\Phi_\lambda$ . Hereafter, the monochromatic EMR can pass through filters (as required), optics and the fibre, that leads to the inside of the shielded enclosure. The fibre irradiates the photodiode with monochromatic EMR for a total irradiance  $E_\lambda$  at the specific wavelength. The NI LabVIEW routine also controlled the programmable pA meter/DC voltage source to measure and record the gener-

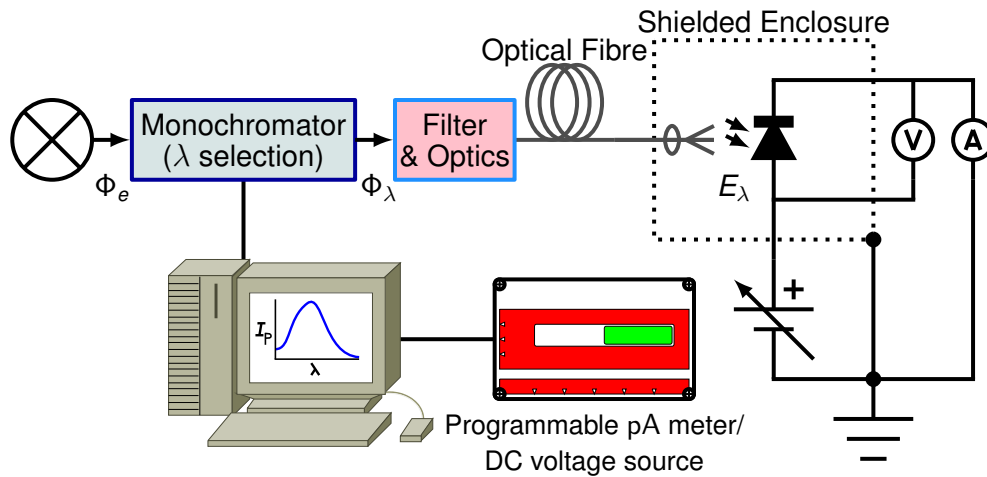


Figure 4.1: Schematic illustration of optoelectronic characterization system used for the electrical and spectral characterization of UV-sensitive photodiodes. The lamp radiates over a range of wavelengths producing a total radiant flux  $\Phi_e$  that enters the monochromator. A desktop computer running an NI LabVIEW routine controls the monochromator and allows for a selected wavelength  $\lambda$  to exit. The monochromatic EMR exits with a corresponding radiant flux  $\Phi_\lambda$ . Hereafter, the monochromatic EMR can pass through filters (as required), optics and the fibre, that leads to the inside of the shielded enclosure. The fibre irradiates the photodiode with monochromatic EMR for a total irradiance  $E_\lambda$  at the specific wavelength. The NI LabVIEW routine also controls the programmable pA meter/DC voltage source to measure and record the generated photocurrents ( $I_p$ ), with or without biasing the photodiode, at each of the selected wavelengths.

ated photocurrents ( $I_p$ ), with or without biasing the photodiode, at each of the selected wavelengths.

The PCD is the fundamental measurement in spectral characterization. The rest of the parameters are calculated from the measured PCD. The PCD  $J_p$  in  $[A \cdot cm^{-2}]$  is obtained by dividing the photocurrent by the known photosensitive area  $A_p$  of the photodiode. The first parameter is the current responsivity, that helps us quantify the quality of a photodiode. The current responsivity can, however, only be determined if the irradiance at the specific wavelength is also known and hence requires calibration of the radiating source.

This study considered a calibrated radiating source that was calibrated by following the photodetector substitution method. This method requires the use of

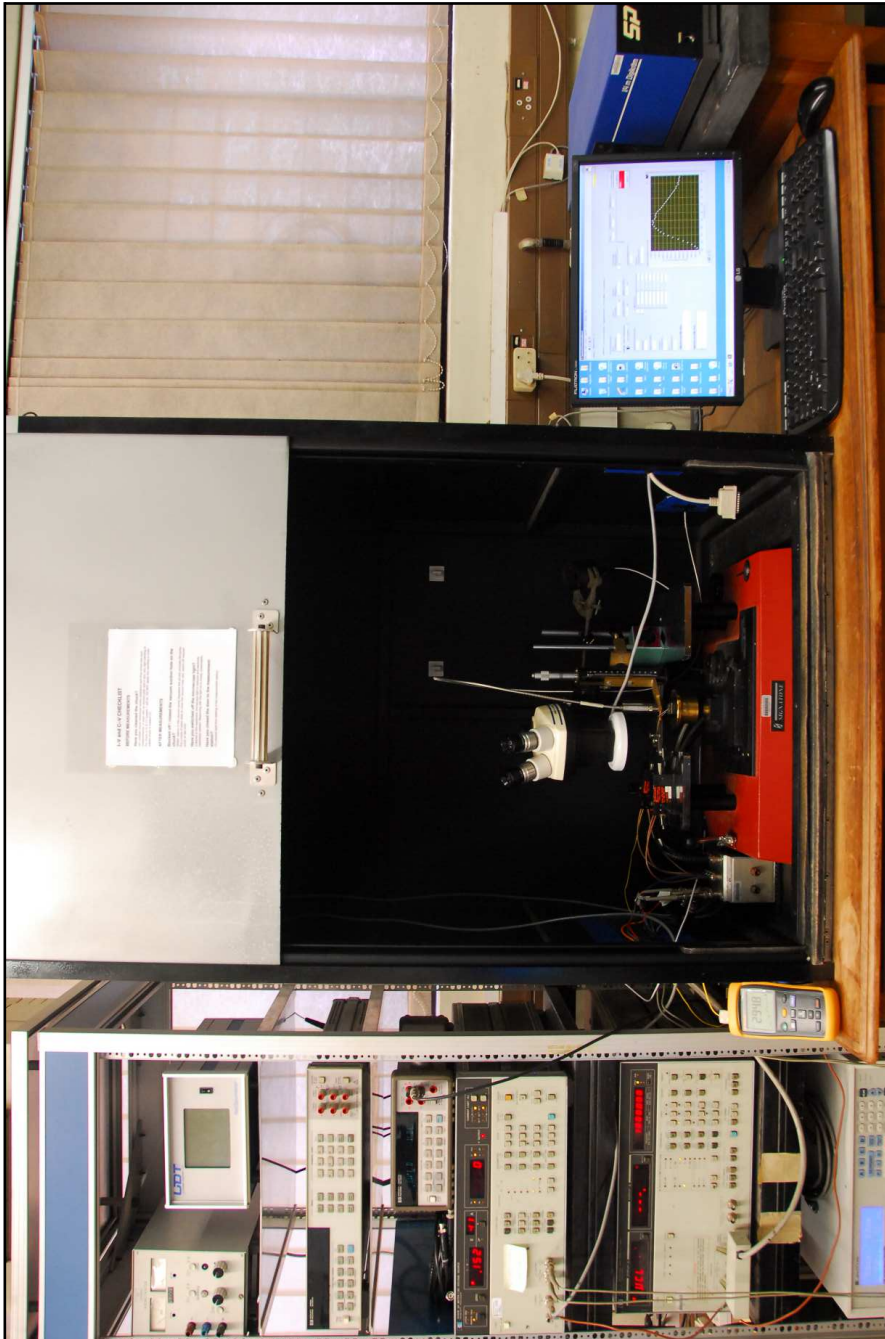


Figure 4.2: A photograph of the optoelectronic characterization system. The instrument rack is on the left-hand side of the open light-tight shielded enclosure. Inside the enclosure is a stereo microscope and to the right of it is the optical fibre positioned above a sample that is to be irradiated with the measurement probes in contact with the ohmic and Schottky contacts of the sample. The screen of the desktop computer running a NI LabVIEW routine, as well as the monochromator is seen on the right-hand side of the enclosure.

a *standard detector* with an absolute responsivity calibration and allows for the calibration of the optoelectronic characterization system against standards traceable to the [NIST](#). The following sections discuss the calibration theory, calibration method and the technical specifications of the equipment used in the construction of the optoelectronic characterization system. Lastly, because a step-index multi-mode optical fibre was used to irradiate the photodiodes, its relevant properties and experimental set-up are discussed.

## **4.2 Calibration theory and method**

The optoelectronic characterization system radiates monochromatic [EMR](#) from the optical fibre end. This [EMR](#) originates from a lamp and passes through the monochromator with its mirrors and grating, then a fibre adapter and the fibre itself. Each of these optical elements have their own wavelength dependent attenuation curves. Hence, the calculation of the final radiant exitance at the fibre end is a difficult task. Moreover, to determine the spectral current responsivity of a photodiode requires the radiometric calibration of the irradiance, which is the radiant-flux density incident on the photosensitive area of a photodiode from a monochromatic radiating source. One solution is to use a radiometric measurement tool that measures the irradiance with a detector calibrated beforehand. Here, standard [EMR](#) sources would have been used to determine the absolute spectral responsivity of a detector with a known photosensitive area. This detector is then used as a reference standard on other systems that require calibration.

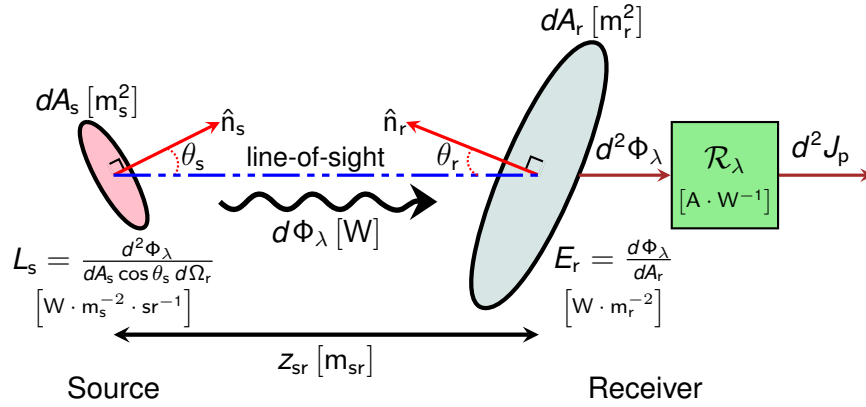


Figure 4.3: Schematic illustration of a radiating source and an irradiated receiver. The radiating source has an infinitesimal surface area  $dA_s$  and irradiates an infinitesimal surface area  $dA_r$  of a receiver. The line-of-sight distance from the source to the receiver is  $z_{sr}$ . The two angles  $\theta_s$  and  $\theta_r$  are between the line-of-sight and the normal unit vectors  $\hat{n}_s$  and  $\hat{n}_r$  to the source and receiver surfaces, respectively.

### 4.2.1 Radiometric calibration theory

The theory of the radiometric approach behind the calibration method is explained with the help of the schematic illustration in Figure 4.3. The illustration shows an infinitesimal surface area  $dA_s$  of a radiating source, irradiating an infinitesimal surface area  $dA_r$  of a receiver. The line-of-sight distance from the source to the receiver is indicated by  $z_{sr}$ . The two angles  $\theta_s$  and  $\theta_r$  are between the line-of-sight and the normal unit vectors  $\hat{n}_s$  and  $\hat{n}_r$  to the source and receiver surfaces, respectively.

Let the source radiate monochromatic EMR. The infinitesimal portion of monochromatic radiant flux  $d\Phi_\lambda$  flows from  $dA_s$  to  $dA_r$ . The monochromatic source radiance as seen from the receiver at a distance  $z_{sr}$  is given by

$$L_s = \frac{d^2\Phi_\lambda}{dA_s \cos\theta_s d\Omega_r}, \tag{4.1}$$



*The optoelectronic characterization system*      *Calibration theory and method*

---

where  $d\Omega_r$  is the projected solid angle subtended at  $dA_s$  by  $dA_r$ , such that

$$d\Omega_r = \frac{dA_r \cos \theta_r}{z_{sr}^2}. \quad (4.2)$$

Also, from Chapter 2 it follows that radiance is geometrically invariant and  $L_s = L_e$  (see 2.2.4 Geometrical invariance of radiance). Therefore, by substituting Eq. 4.2 into Eq. 4.1 and considering monochromatic radiant flux transfer between the source and receiver in a lossless medium, the monochromatic radiant flux transfer is given as

$$d^2\Phi_\lambda = \frac{L_e dA_s \cos \theta_s dA_r \cos \theta_r}{z_{sr}^2}. \quad (4.3)$$

Since, the receiver irradiance is defined by

$$E_r = \frac{d\Phi_\lambda}{dA_r}, \quad (4.4)$$

it is noted that by substituting Eq. 4.4 into Eq. 4.3, the radiance becomes

$$L_e = \frac{E_r z_{sr}^2}{dA_s \cos \theta_s \cos \theta_r}. \quad (4.5)$$

The source radiance can be calibrated by measuring the irradiance  $E_{SD}$  using a standard detector placed at a distance  $z_{SD}$ . Furthermore, by keeping the source and standard detector (receiver) parallel with one another, such that  $\theta_s = \theta_r = 0$  and, hence,  $\cos \theta_s = \cos \theta_r = 1$ , so that the calibrated radiance is given by

$$L_e^{\text{cali}} = \frac{E_{SD} z_{SD}^2}{dA_s}. \quad (4.6)$$

If the standard detector was to be substituted by another detector placed at a different distance  $z_{PD}$  and irradiated by the same source, it then follows from Eq. 4.6 that the irradiance of this other detector can be determined by evaluating

$$E_{PD} = \frac{L_e^{\text{cali}} dA_s}{z_{PD}^2}, \quad (4.7)$$

or after substituting Eq. 4.6 into Eq. 4.7, yields

$$E_{PD} = E_{SD} \left( \frac{z_{SD}}{z_{PD}} \right)^2. \quad (4.8)$$

### 4.2.2 Photodetector substitution method

It was shown that by measuring the irradiance with a standard detector that the irradiance of any other detector (photodiode) can be calculated using Eq. 4.8. Also, the irradiance is related by the ratio of the respective distances squared. This enables us to radiometrically calibrate the irradiance used to determine the current responsivity of a photodiode (Eq. 3.56 in Chapter 3).

The photodetector substitution method was used to calibrate the optoelectronic characterization system. The method can be done in two ways. The one is to exchange the standard and the photodiode under investigation at each wavelength, measuring and calculating the corresponding irradiances, photocurrents and responsivities. The main advantage to executing the method in this way, is that measurements are not affected by possible drift of the lamps between wavelength scans, but has the disadvantage of being slow [Larason and Houston, 2008:15–16].

The other way is to measure the irradiance with the standard over a whole wavelength range and, thus, doing a spectral irradiance calibration. Thereafter, photocurrent measurements are done over the same wavelength range for the photodiode and the corresponding spectral responsivity is determined. Drift of the source is possible during this latter way of performing the measurements, but the measurement is faster. Furthermore, the NIST Spectral Comparator Fa-

cilities (SCF) performs the photodetector substitution method in a similar way as part of their measurement services [Larason and Houston, 2008:15–16].

The drift of the sources used for this study during the duration of the measurements was not significant. This was concluded after comparing the spectral irradiance calibration before a set of photocurrent measurements to that measured afterwards. Thus, the latter photodetector substitution method was also followed in this study.

## 4.3 Technical specifications

### 4.3.1 flexOptometer system

The high-performance flexOptometer radiometer, manufactured and calibrated by Gamma Scientific, was used as the radiometric measurement tool. A UV/VIS/NIR (200 nm to 1100 nm) Si-based detector (model 24600) with a square 1 cm<sup>2</sup> photosensitive area and rear-mounted BNC connector was coupled to the flexOptometer model 51691/51640.

The Si-based detector and flexOptometer was calibrated using traceable standards, calibrated by the NIST for use at Gamma Scientific. Gamma Scientific certified that the instrument was calibrated on 2010-12-09 using standards traceable to NIST in accordance with ANSI/NCSL Z540-1-1994. The flexOptometer system can measure irradiances ranging from 1 pW · cm<sup>-2</sup> to 1 W · cm<sup>-2</sup>.

The absolute responsivity values are in  $\left[ \text{A} \cdot (\text{W} \cdot \text{cm}^{-2})^{-1} \right]$  for the standard detector with their corresponding wavelengths in [nm] and were pre-programmed into the flexOptometer. The flexOptometer measures the photocurrent in [A] that is generated in the standard detector while being irradiated by a specific wavelength of EMR. The measured photocurrent is then divided by the absolute

Table 4.1: The tolerance limits at various wavelength ranges of the Si-based standard detector.

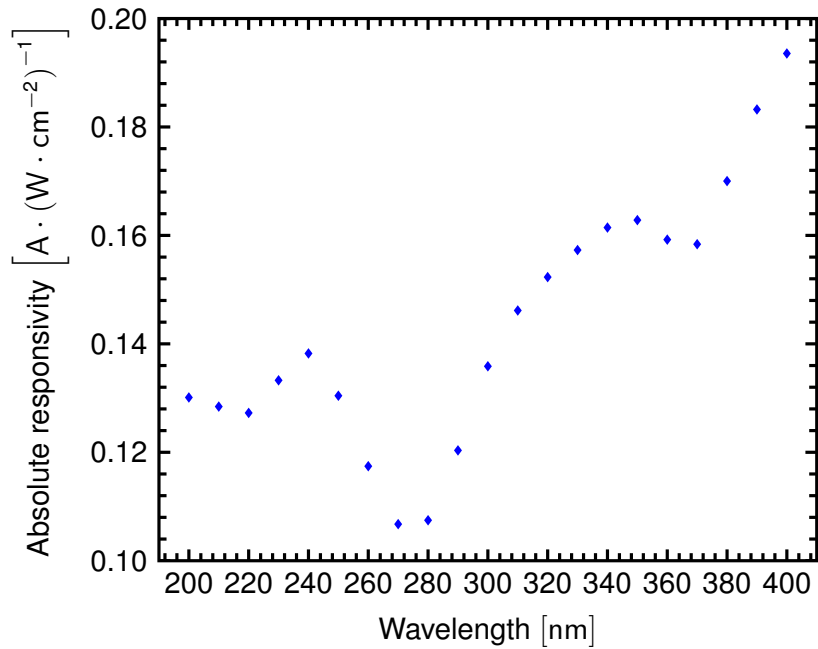
<b>Wavelength range</b>	<b>Tolerance</b>	<b>Wavelength range</b>	<b>Tolerance</b>
(200 to 250) nm	± 6.0 %	(900 to 1000) nm	± 1.5 %
(250 to 440) nm	± 2.0 %	(1000 to 1100) nm	± 2.0 %
(440 to 900) nm	± 1.1 %		

responsivity value that corresponds to the specific wavelength and the irradiance value is given in  $[W \cdot cm^{-2}]$ .

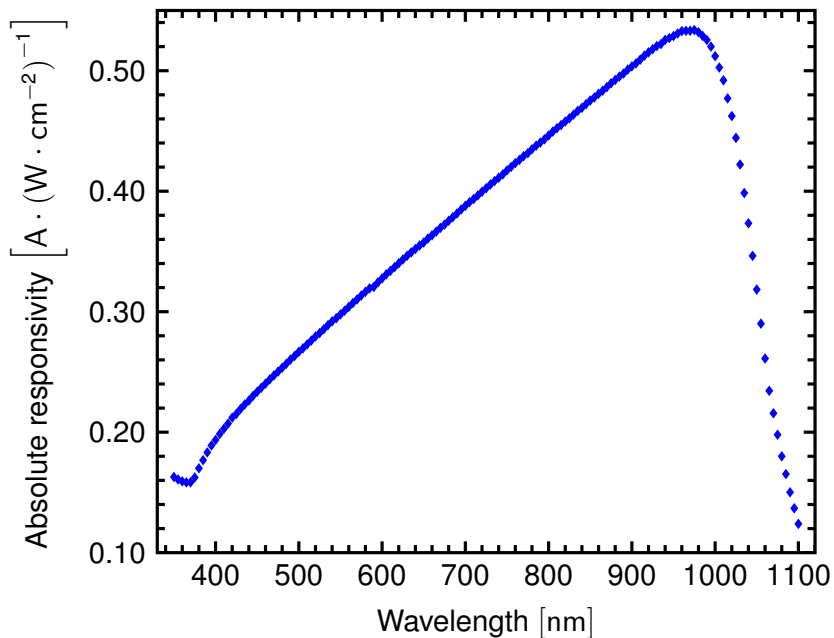
The flexOptometer system is calibrated for two wavelength ranges. The one ranged from 200 nm to 400 nm in 10 nm increments and the other from 350 nm to 1100 nm in 5 nm increments. Figure 4.4(a) presents the absolute spectral responsivity values for the wavelengths ranging from 200 nm to 400 nm and Figure 4.4(b) for the wavelengths ranging from 350 nm to 1100 nm. The calibration uncertainty is wavelength dependent, therefore, Table 4.1 was included in the calibration report from Gamma Scientific to show the tolerance limits at the various wavelength ranges (limits incorporated NIST and Gamma Scientific transfer uncertainties with the coverage factor  $k = 2$ ).

### 4.3.2 Electronic equipment

The optoelectronic characterization system was equipped with a programmable Hewlett-Packard (HP) model 4140B pA meter/DC voltage source for  $I-V$  measurements and a HP model 4192A LF impedance analyzer for  $C-V$  measurements. The pA meter/DC voltage source has a current measurement range of 1 fA to 20 mA and two separate voltage sources ranging from 10 mV to 1 V. The electronic equipment was placed outside of the light-tight shielded enclosure.



(a) Absolute spectral responsivity values for wavelengths ranging from 200 nm to 400 nm in 10 nm increments for the Si-based standard detector.



(b) Absolute spectral responsivity values for wavelengths ranging from 350 nm to 1100 nm in 5 nm increments for the Si-based standard detector.

Figure 4.4: Calibrated absolute spectral responsivity values of the flexOptometer system.

### **4.3.3 Control and measurement**

The present author developed the NI LabVIEW routine that controlled the monochromator which enabled the automation of the PCD versus wavelength measurements. A screenshot of the Front Panel of the spectral characterization routine is shown in Figure 4.5. This routine was used in conjunction with an existing routine that controlled the pA meter/DC voltage source and the LF impedance analyzer to record the  $I-V$ ,  $C-V$  and PCD versus wavelength measurements. The data from the  $I-V$  and  $C-V$  measurements could immediately be analyzed with the NI LabVIEW routine, yielding parameters such as the ideality factor, SBH, reverse leakage current density at 1 V reverse bias, series resistance and the free carrier concentration of the photodiodes.

### **4.3.4 Lamps**

The one lamp chosen for use as a UVR source was the 30 W Spectral Products (SP) model ASB-D-030 deuterium lamp. This lamp has a specified continuous output spectrum ranging from 180 nm to 400 nm and an average life of 1000 hours. The other lamp was the high stability 30 W SP model ASB-W-030 tungsten-halogen lamp with a specified continuous output spectrum ranging from 300 nm to 2600 nm.

The tungsten-halogen lamp is a near blackbody source of EMR with a fused silica envelope around the lamp filament. The transmission of the fused silica limits the longer wavelengths radiated from the lamp to 2600 nm. In addition, the lamp uses an adjustable constant current power supply. The current of the power supply can be continuously varied from 2.0 A to 3.5 A on a scale with 0.25 A divisions. The lamp has a nominal colour temperature of 3100 K when the power supply is set to 2.75 A, and an average life of 400 hours at this temperature.

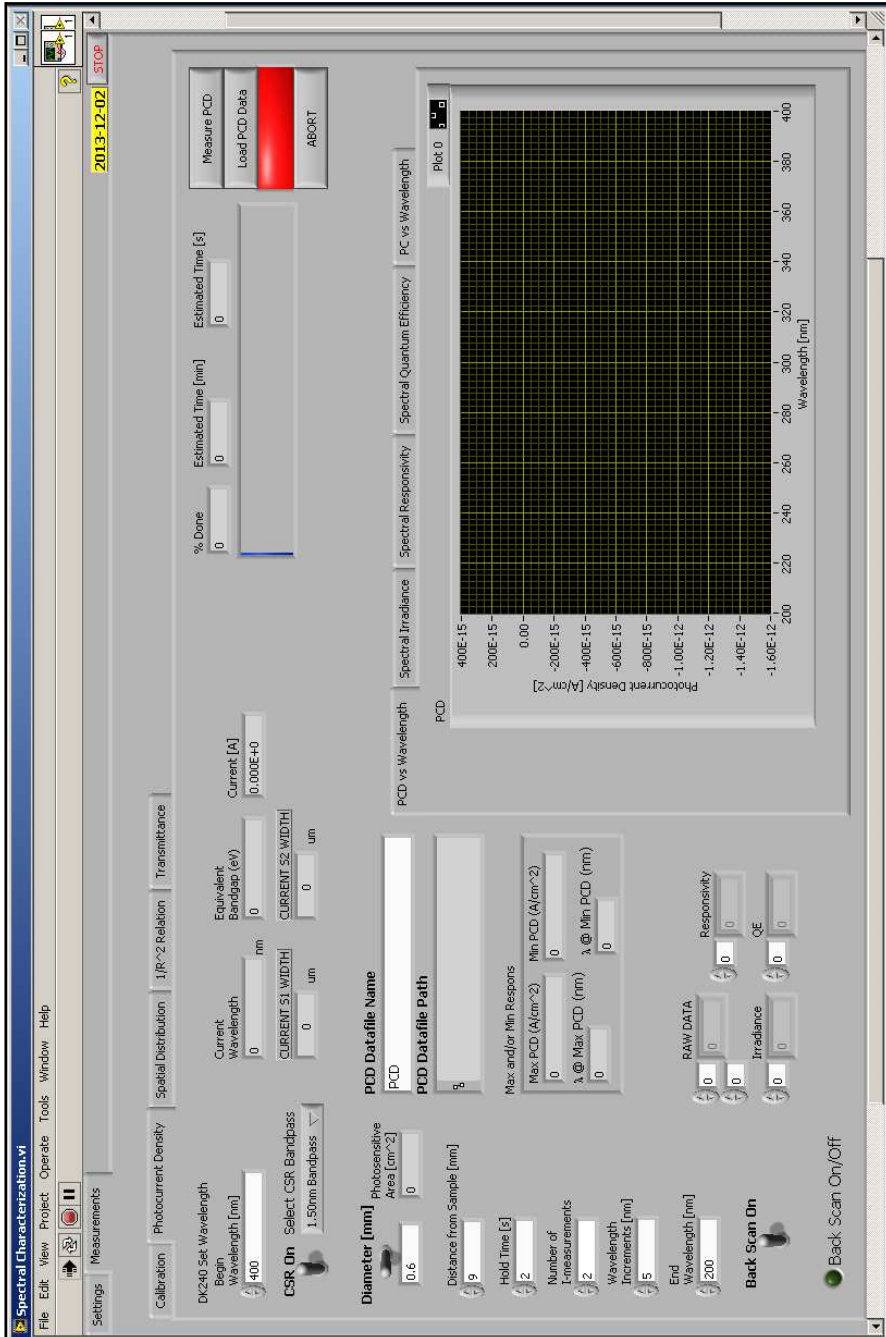


Figure 4.5: A screenshot of the Front Panel of the spectral characterization NI LabVIEW routine. The selected 'Photocurrent Density' tab allows the user to set the appropriate measurement setting on the left-hand side of the Front Panel. A measurement is started by pressing the 'Measure PCD' button (top right) and a real-time plot of the measurements are presented in the 'PCD vs Wavelength' graph window.

### 4.3.5 Monochromator

The Czerny-Turner type Digikröm DK240 ¼-meter monochromator from SP was used for the selection of different wavelengths while either one of the lamps were mounted directly on the monochromator. The monochromator has a 1200 lines/mm grating blazed for 300 nm with a wavelength accuracy of  $\pm 0.3$  nm. The grating is restricted to angles between  $0^\circ$  and  $70^\circ$  and, therefore, there is an upper wavelength selection limit of 1500 nm. The mirrors inside the monochromator are UV-enhanced protected aluminium mirrors that have more than 85 % average reflection from 200 nm to 1000 nm.

The entrance and exit slit widths are electronically controlled. The width of both slits can be varied from 10  $\mu\text{m}$  to 3000  $\mu\text{m}$  in 1  $\mu\text{m}$  increments and have fixed heights of approx. 10 mm. A constant spectral resolution (CSR) mode is available for maintaining a fixed spectral resolution across all wavelengths. The allowed bandpass (resolution) values for the 1200 lines/mm grating is 0.37 nm, 0.75 nm, 1.50 nm or 3.00 nm.

On the exit side of the monochromator, an  $f/\#$  matching SP model AFDK240-L-SM optical fibre adapter with an SMA 905 end plate was used to couple an optical fibre. The adapter comes standard with UV lenses, providing more than 90 % transmittance from 200 nm to 1900 nm. A SP model AB202 filter holder was also installed between the adapter and monochromator. This allowed for the option of inserting an order sorting filter, such as the 2.1 mm-thick and 25.4 mm-diameter long-pass SP model AB3040 filter with a 400 nm cut-on wavelength.



### 4.3.6 Optical fibre

An extreme solarization<sup>1</sup>-resistant optical fibre, manufactured by Ocean Optics (Custom-Patch ZFQ-7776, ZQP1000-2-SR; 0), was chosen for the most efficient transmittance in the wavelength range between 180 nm and 900 nm. The fibre has a  $(1000 \pm 20)$   $\mu\text{m}$ -diameter core, numerical aperture (NA) of  $0.22 \pm 0.02$  (approx.  $12.7^\circ$  half-acceptance angle) and is 2 m in length with a step-index multi-mode profile. The modal properties are important, when using optical fibres for their telecommunication applications. The fibre was, however, used to lead the EMR to the inside of the shielded enclosure and only act as a monochromatic EMR source that irradiates the photodiode and, hence, the modal properties was not of concern. The use of a fibre allowed for simple alignment of the fibre end at a fixed distance, measured using a calliper with a  $(0.05 \pm 0.025)$  mm-Vernier scale.

## 4.4 Properties of the optical fibre

A step-index fibre was used to irradiate the photodiodes. Therefore, the following subsections discuss the numerical aperture (NA), the properties of the fibre with regards to how the spot-size depends on the axial distance, as measured from the fibre end. Then, how the spot-size depends on the angle at which the EMR enters the fibre and it is shown that the spatial irradiation distribution (SID) has a Gaussian distribution. Finally, the experimental set-up is discussed together with experimental verification of the spot-size, SID and that the irradiance is related by the ratio of the respective distances squared (Eq. 4.8 derived in subsection 4.2.1).

---

<sup>1</sup>Solarization is the degradation in transmission in standard silica fibres, when working with UVR below 300 nm (an increase in absorption).

#### 4.4.1 Numerical aperture

The *core* and *cladding* are the two key elements of an optical fibre. The core is the inner part of a fibre that guides **EMR** and is completely surrounded by the cladding [Hecht, 2006:26]. A step-index fibre simply consists of two layers of material for the core and the cladding with different refractive indexes. If a cross-section of the fibre is drawn together with a plot of the refractive index, then a step at the core–cladding boundary would be seen, where the index changes abruptly [Hecht, 2006:69]. The refractive index  $n_0$  of the core is greater than that of the cladding  $n_1$ . When **EMR** enters the fibre and strikes the core–cladding boundary at any angle less or equal to the so-called confinement angle, the **EMR** is guided by total internal reflection through the fibre [Hecht, 2006:26].

The other preferred way to look at the guiding of **EMR** in a fibre is to consider the half-acceptance angle. The half-acceptance angle of a fibre is the maximum angle  $\theta_{NA}$  for which entering **EMR** is still guided by total internal reflection. Figure 4.6 is a schematic illustration of a step-index fibre and some of its properties. Here, only **EMR** falling in at an angle less or equal to the half-acceptance angle is guided along the fibre core with refractive index  $n_0$ . The core is completely surrounded by the cladding with refractive index  $n_1 < n_0$ . The half-acceptance angle is usually given in terms of the **NA**, such that

$$NA = \sqrt{n_0^2 - n_1^2} = \sin \theta_{NA}. \quad (4.9)$$

The **NA** is a standard measure of the half-acceptance angle and, therefore, an important characterizing parameter, since it directly relates to the **EMR**-gathering capacity of a fibre [Hecht, 2006:27,100–101; Khare, 2004:137].

The fibre properties can be calculated using the simple optical ray model, provided that the core diameter is many times larger than the wavelength it carries.

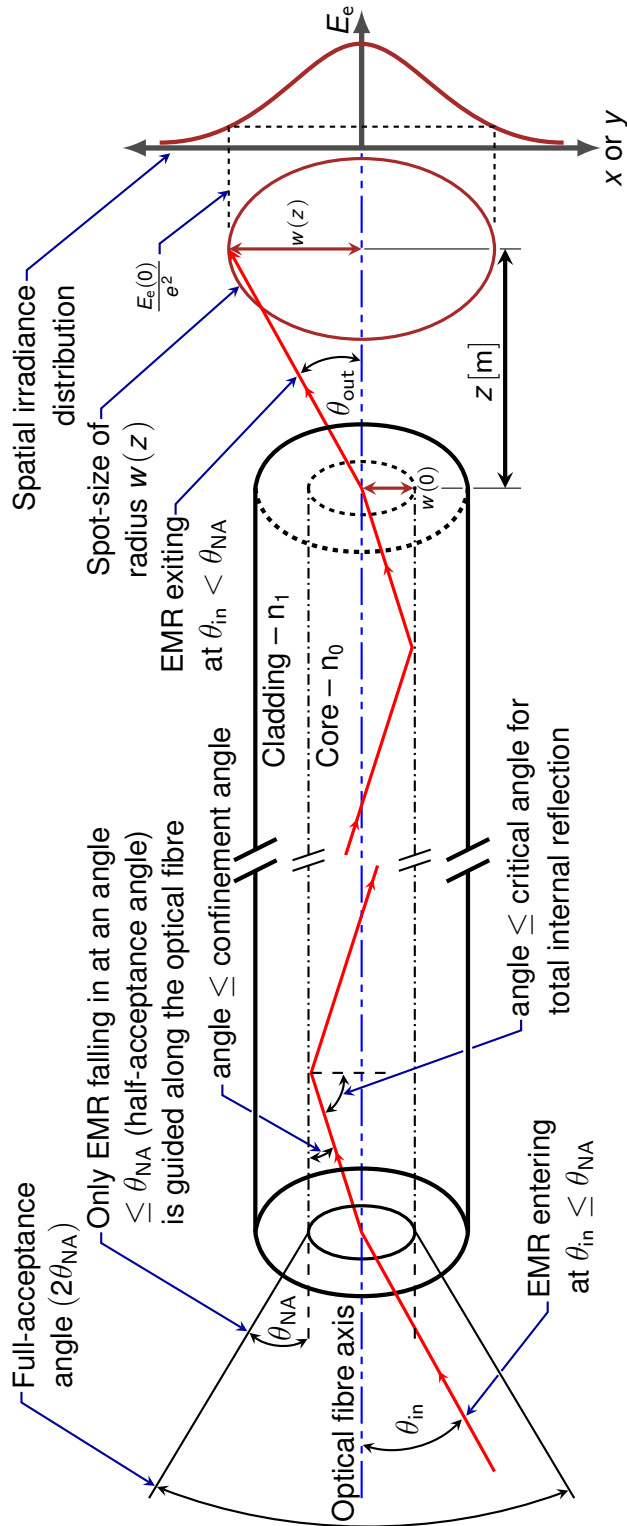


Figure 4.6: Schematic illustration of a step-index optical fibre and some of its properties. Only EMR falling in at an angle less or equal to the half-acceptance angle is guided along the fibre core with refractive index  $n_0$ . The core is completely surrounded by the cladding with refractive index  $n_1 < n_0$ . The optical ray model is used to illustrate a single ray of EMR entering the fibre at some angle  $\theta_{in} < \theta_{NA}$  and guided along the fibre core. Any EMR entering the fibre, striking the core-cladding boundary at an angle less or equal to the confinement angle, is guided by total internal reflection through the fibre. This ray later emerges at (roughly) the same angle  $\theta_{out}$  to the fibre axis, but may not emerge in the same direction. In fact, this single ray forms a ring at the original angle to the fibre axis, because of imperfections and other factors. At a distance  $z$  from the fibre end along the optical axis, the spot-size radius for a Gaussian distributed irradiance ( $E_e$ ) is defined to where the irradiance drops to  $1/e^2$  of its maximum.

ers. As in this case, the fibre that had a 1000  $\mu\text{m}$ -diameter core, which is many times larger than the 200 nm to 1100 nm wavelengths that it would carry. If the half-acceptance angle is doubled, the full-acceptance angle is obtained. The step-index (multi-mode) fibres were the first type of fibres developed and used for imaging applications and, hence, a good choice for its application in this study [Hecht, 2006:68–69].

#### 4.4.2 Spot-size

The optical ray model is used to illustrate a single ray of EMR entering the fibre at some angle  $\theta_{\text{in}} < \theta_{\text{NA}}$  and guided along the fibre core in Figure 4.6. Now, this ray later emerges at (roughly) the same angle  $\theta_{\text{out}}$  to the fibre axis, but may not emerge in the same direction. In fact, this single ray forms a ring at the original angle to the fibre axis. Fibre imperfections and other factors cause the EMR to emerge as a ring [Hecht, 2006:734–735].

If the exiting EMR has Gaussian characteristics, then there exists a half-angle of divergence  $\theta$  that is roughly equal to the half-angle at which the EMR entered the fibre. The spot-size radius for a Gaussian distributed irradiance ( $E_e$ ) is defined as the radius of the circle where the irradiance drops to  $1/e^2$  of its maximum by

$$w(z) = w(0) \left[ 1 + \left( \frac{z}{w(0)\theta} \right)^2 \right]^{\frac{1}{2}}, \quad (4.10)$$

where  $w(0)$  is the core radius and  $z$  the distance from the fibre end along the optical axis, as illustrated in Figure 4.6 [Pedrotti and Pedrotti, 1993:464–465].

For example, the standard detector was placed 90 mm from the fibre end to calibrate the irradiance thereof. Thus, the maximum expected spot-size radius is

$$w(90) = 0.5 \sqrt{1 + \left( \frac{90}{0.5} \sin^{-1} 0.22 \right)^2} \approx 20 \text{ mm.} \quad (4.11)$$

### 4.4.3 Spatial irradiation distribution

The mathematical representation for the electric field of an electromagnetic wave is given by

$$\Psi_e(x, y, z, t) = \Psi_e(0) e^{\frac{jk_e(x^2+y^2)}{2r(z)}} e^{j[k_e z + p(z) - \omega_e t]} e^{-\frac{(x^2+y^2)}{w(z)^2}}. \quad (4.12)$$

The first exponential term in Eq. 4.12 indicates that the wave-front geometry is a spherical surface with radius of curvature  $r(z)$ . The phase dependence on  $z$  is contained in the second exponential term. The last exponential term shows that there is a symmetric Gaussian function decrease in the electric field in the transverse plane around the peak value on the optical axis for any fixed  $z$  [Pedrotti and Pedrotti, 1993:463].

The irradiance is proportional to the square of the electric field amplitude [Pedrotti and Pedrotti, 1993:473]. Therefore, the SID along the  $x$ -axis is defined by

$$E_e(x) = |\Psi_e|^2 = E_e(0) \exp \left[ \frac{-2x^2}{w(z)^2} \right], \quad (4.13)$$

and the Gaussian representation of the normalized SID as

$$\tilde{E}_e(x) = \frac{E_e(x)}{E_e(0)} = \exp \left[ \frac{-2x^2}{w(z)^2} \right]. \quad (4.14)$$

Finally, after substituting Eq. 4.10 into Eq. 4.14, the normalized SID along the

x-axis for an irradiating fibre is given as

$$\tilde{E}_e(x) = \exp \left[ \frac{-2x^2}{w(0)^2 + (z\theta)^2} \right]. \quad (4.15)$$

## 4.5 Experimental set-up

The *f/#* matching adapter had to be fine tuned to ensure that the monochromatic *EMR* entering the fibre, enters optimally from the exit slit of the monochromator. This was done with the tungsten-halogen lamp coupled to the monochromator with both slits set to widths of 3 mm. The monochromator was then set to allow green light with a wavelength of 555 nm to pass through. The 400 nm order sorting filter was also installed to suppress higher order diffraction effects. At the fibre end, a green spot was illuminated on a flat piece of white paper, easily seen with the naked eye. The adapter was then fine tuned until a uniformly distributed green spot was seen on the paper.

The *SID* was studied by recording the irradiance through a 1.5 mm-diameter aperture for various horizontal displacements of the fibre end with respect to the aperture. The aperture was placed in front of the standard detector of the flexOptometer system. Then, the fibre end was aligned 90 mm from the aperture using a calliper. Thereafter, the fibre end was horizontally displaced with respect to the aperture from –30 mm to 30 mm in 1.5 mm increments. The 0 mm mark closely corresponded with the direct alignment of the fibre end to the aperture.

The solid (blue) dots in Figure 4.7(a) indicates the measured normalized irradiation for fixed 3 mm-wide slits on the monochromator. The horizontal  $\pm 0.75$  mm (blue) error bars serve to show the region that corresponds with the 1.5 mm-diameter aperture. A non-linear curve fit was performed on the measured *SID* by

applying Eq. 4.15, transformed to

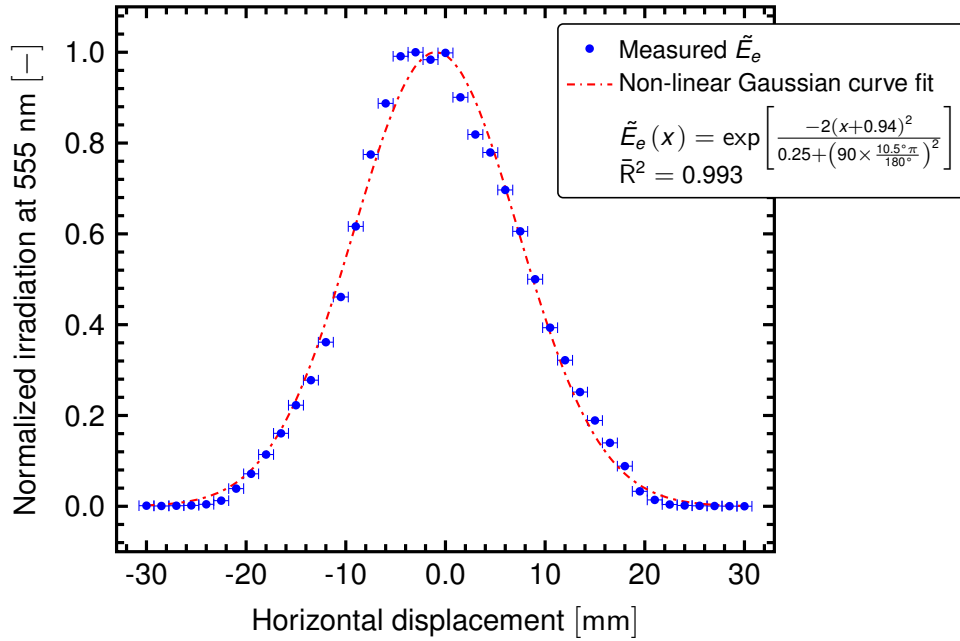
$$\tilde{E}_e(x) = \exp \left[ \frac{-2(x - x_c)^2}{0.25 + \left(z \times \frac{\theta_{\text{out}} \pi}{180^\circ}\right)^2} \right], \quad (4.16)$$

where  $x_c$  is the offset from the peak at 0 mm and  $\theta_{\text{out}}$  the half-angle at which the green light exits the fibre end in units of degree. In addition,  $\theta_{\text{out}}$  should almost be equal to the angle at which the green light would have entered the fibre.

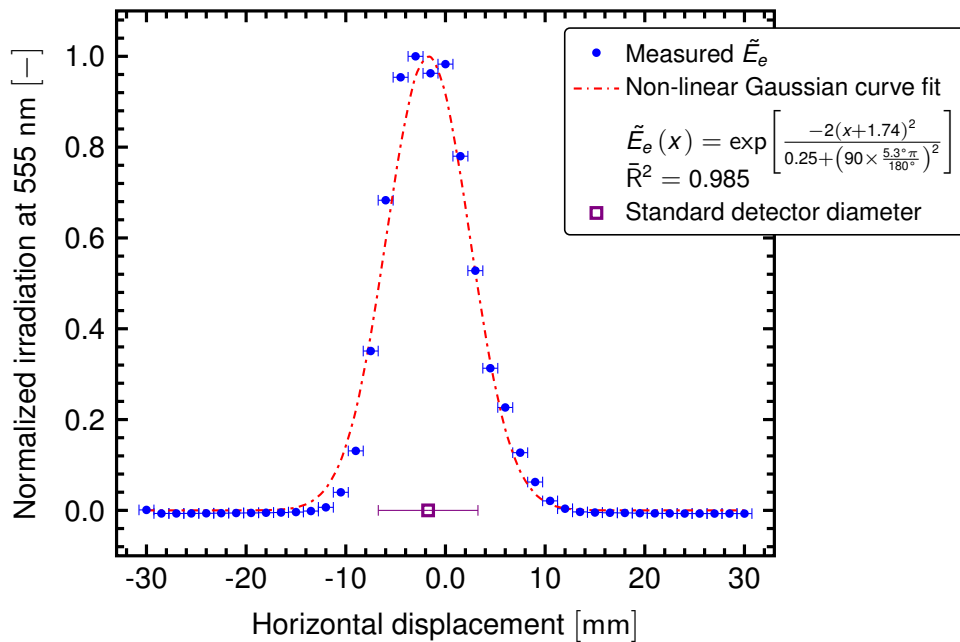
The (red) dash-dotted line in Figure 4.7(a) indicates the non-linear Gaussian curve that was fitted to the measured SID. The fitted Gaussian curve, as defined by Eq. 4.16, had a 0.993 adjusted coefficient of determination ( $\bar{R}^2$ ). It was determined that the peak had an offset of  $-0.94$  mm and that the EMR exited at an angle of  $10.5^\circ$ . Moreover, using Eq. 4.10 the spot-size diameter was calculated to be approx. 32.8 mm.

The proper evaluation of the photodiodes require the enabling of the CSR mode on the monochromator. The slit widths, however, changes for each selected wavelength. The 1.50 nm-bandpass CSR mode was used and both slit widths were set 439  $\mu\text{m}$ -wide for the 555 nm wavelength. Figure 4.7(b) shows the resulting measured SID with the solid (blue) dots indicating the measured normalized irradiances at each horizontal displacement. After performing a non-linear Gaussian curve fit, a 0.985 adjusted coefficient of determination was obtained, the peak had an offset of  $-1.74$  mm and the EMR exited at an angle of  $5.3^\circ$ , which is close to half the previous angle of  $10.5^\circ$ . Moreover, using Eq. 4.10, the spot-size diameter also almost halved to what was calculated to be approx. 16.7 mm.

The experimental investigation of the SID was also studied at 675 nm. This was done to confirm the measured findings and ensure repeatability, especially at a wavelength barely visible to the naked eye. In both Figures 4.8(a) and 4.8(b) the non-linear Gaussian curve fits, again, showed high adjusted coefficients of



(a) Measured SID for fixed 3 mm-wide slits.



(b) Measured SID for fixed 439 μm-wide slits.

Figure 4.7: SIDs at 555 nm of the optical fibre placed 90 mm from a 1.5 mm-diameter aperture in front of the standard detector, for two different fixed slit widths on the monochromator.



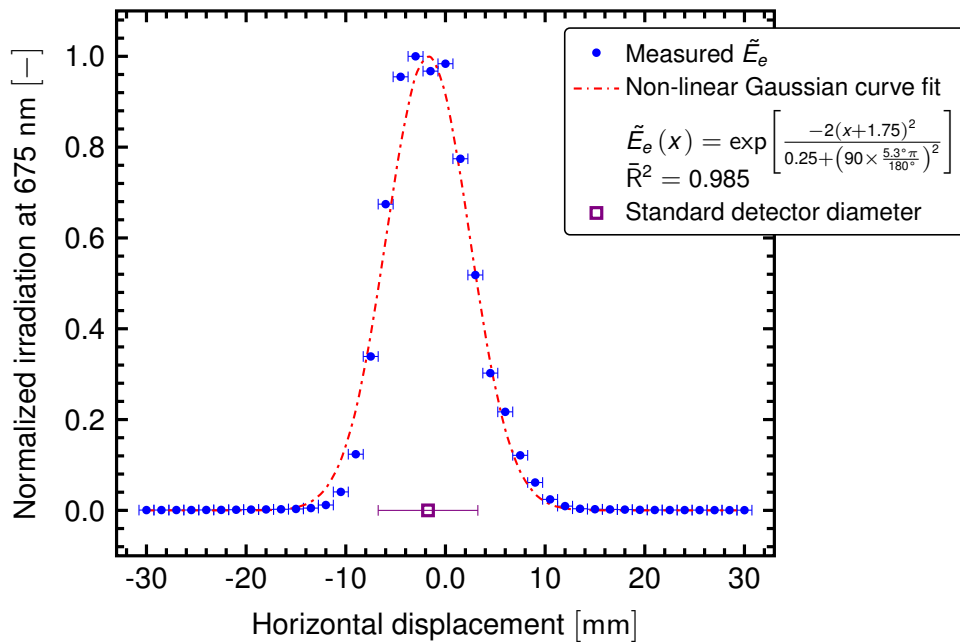
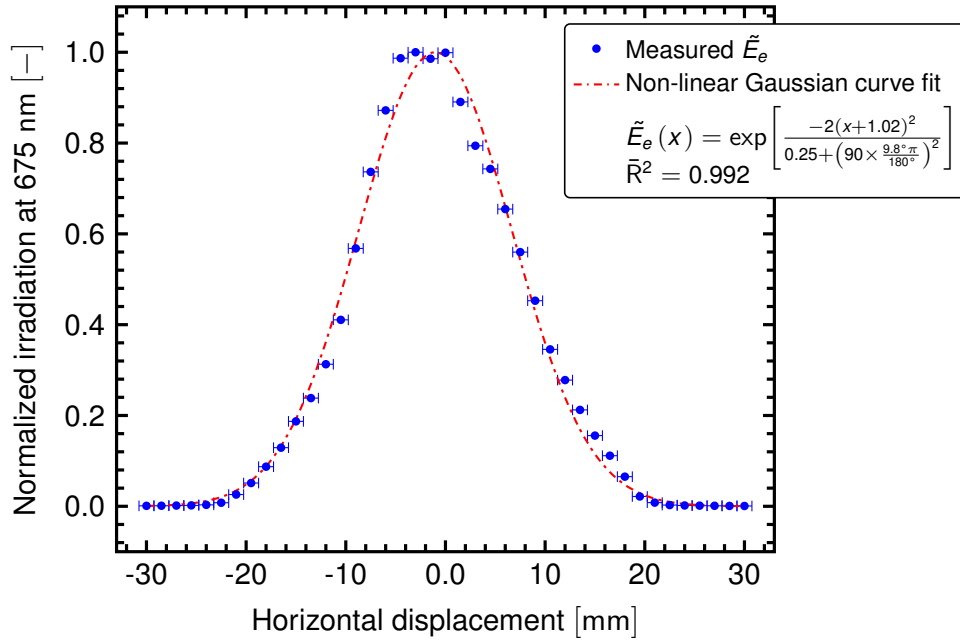


Figure 4.8: SIDs at 675 nm of the optical fibre placed 90 mm from a 1.5 mm-diameter aperture in front of the standard detector, for two different fixed slit widths on the monochromator.

determination. Also, the same exit angles of  $10.5^\circ$  and  $5.3^\circ$  were obtained for the fixed 3 mm-wide and  $439 \mu\text{m}$ -wide<sup>2</sup> slits, respectively. Thus, the approximate halving of the exit (and entrance) angles and resulting corresponding spot-sizes were again observed.

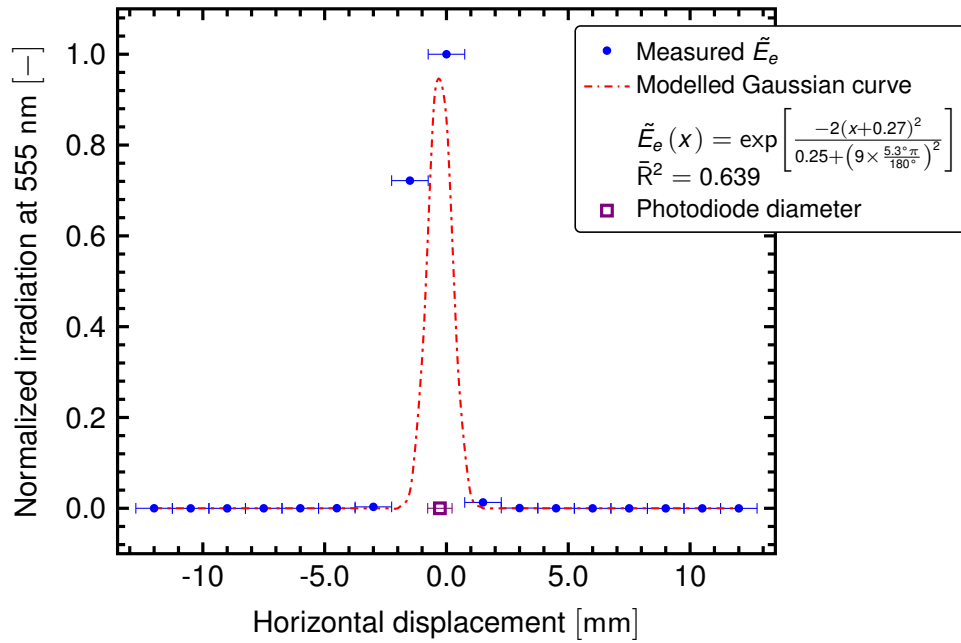
The exit slit width changed from 3 mm to  $439 \mu\text{m}$  (just under 0.5 mm-wide) and the slits had a fixed height of approx. 10 mm on the monochromator. Therefore, a  $439 \mu\text{m} \times 10 \text{ mm}$  projected line of monochromatic EMR exits the monochromator through the  $f/\#$  matching adaptor and irradiates approximately only half of the 1 mm-diameter fibre, compared to a  $3 \text{ mm} \times 10 \text{ mm}$  projected line. Thus, the 'halving' effect was observed.

For calibration purposes, though, the fibre end should be centrally aligned 90 mm from the square 10 mm-diameter standard detector. The detector would then be (uniformly) overfilled for calibration, as indicated by the empty (violet) square with horizontal  $\pm 5.0 \text{ mm}$  (violet) error bars in Figures 4.7(b) and 4.8(b).

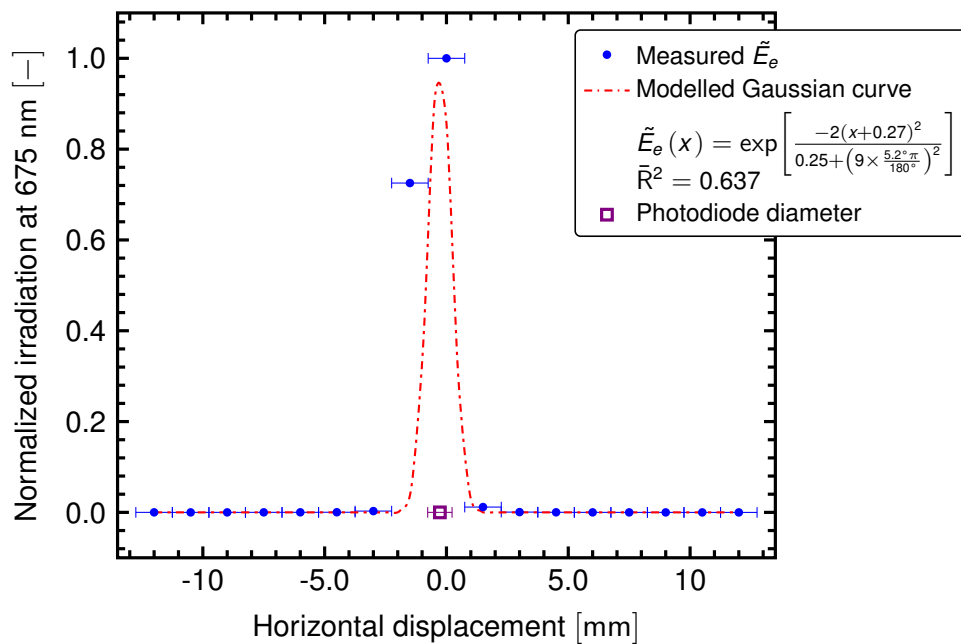
Lastly, the fibre end was positioned 9 mm from the aperture and the SID measured. This was done at both 555 nm and 675 nm with the 1.50 nm-bandpass CSR mode enabled on the monochromator. Figures 4.9(a) and 4.9(b) contain the measured normalized irradiation, indicated by the solid (blue) dots with horizontal  $\pm 0.75 \text{ mm}$  (blue) error bars that correspond to the 1.5 mm-diameter aperture region. Using the determined  $5.3^\circ$  exit angle for the  $439 \mu\text{m}$ -wide slits, a Gaussian curve with coefficients of determination of approx. 0.64 was fitted for variable  $x_c$ , as indicated by the (red) dash-dotted lines. The spot-size diameter was calculated to be approx. 1.94 mm from Eq. 4.10 and is expected to overfill 1 mm-diameter photosensitive areas or less of a photodiode, as indicated by the empty (violet) square with horizontal  $\pm 5.0 \text{ mm}$  (violet) error bars.

---

<sup>2</sup>Slit widths are set by the 1.50 nm-bandpass CSR mode and was the same as for 555 nm.



(a) Measured SID for fixed 439  $\mu\text{m}$ -wide slits.



(b) Measured SID for fixed 439  $\mu\text{m}$ -wide slits.

Figure 4.9: SIDs at (555 and 675) nm of the optical fibre placed 9 mm from a 1.5 mm-diameter aperture in front of the standard detector, for 439  $\mu\text{m}$ -wide fixed slit widths on the monochromator.

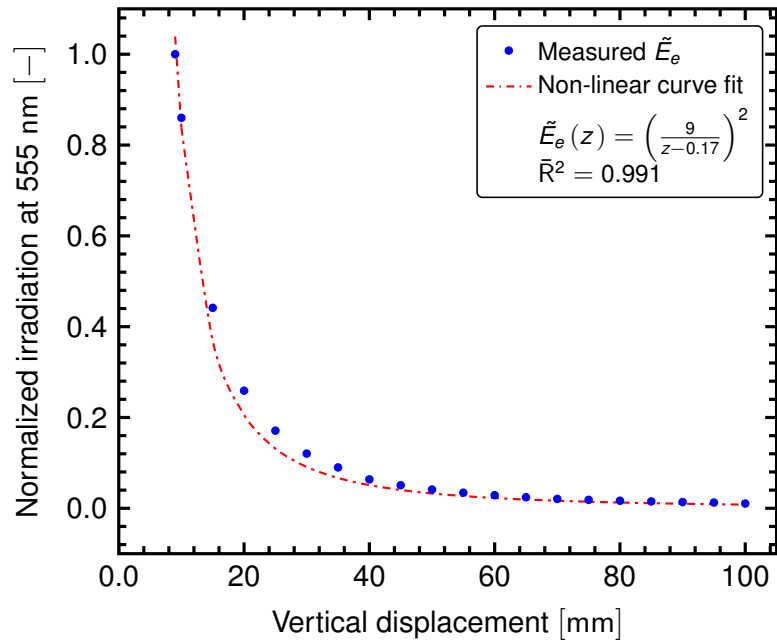
The irradiance dependence on the axial displacement was also verified, after studying the *SID* and having the *f/#* matching adapter optimally fine tuned. This was done by recording the irradiance through the same 1.5 mm-diameter aperture for various vertical displacements (along the optical *z*-axis) of the fibre end with respect to the aperture. The slits widths were set 3 mm-wide on the monochromator for these measurements. The fibre end was aligned 9 mm from the aperture using a calliper and vertically displaced with respect to the aperture. First to 10 mm, then from 10 mm to 100 mm in 5 mm increments.

The solid (blue) dots in Figures 4.10(a) and 4.10(b) indicate the measured normalized irradiation for the various axial displacements. By letting the irradiance measured by the standard detector at 9 mm be the calibrated value, the accuracy of the other measured irradiances which correspond to that predicted by Eq. 4.8 can be evaluated. This is done by performing a non-linear curve fit of the transformed Eq. 4.8, such that

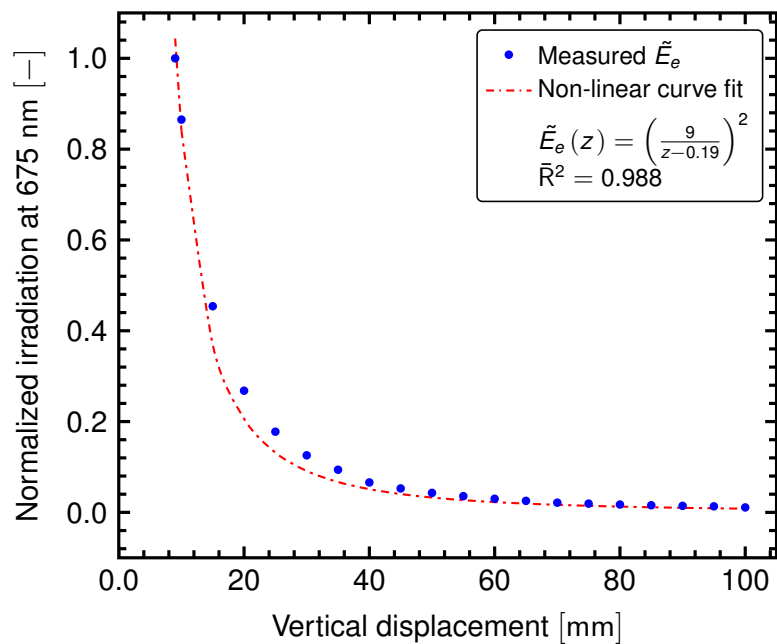
$$\tilde{E}_e(x) = \left( \frac{9}{z + z_0} \right)^2, \quad (4.17)$$

where  $z_0$  is the vertical offset of the fit.

The (red) dash-dotted lines in Figures 4.10(a) and 4.10(b) indicate the non-linear curve that was fitted to the measurements. The fitted curve, as defined by Eq. 4.17, had a 0.991 and 0.988 adjusted coefficient of determination with vertical offsets of  $-0.17$  mm and  $-0.19$  mm for the 555 nm and 675 nm measurements, respectively. Thus, the irradiation is related by the ratio of the respective distances squared.



(a) Measured irradiance at 555 nm for the axial displacements.



(b) Measured irradiance at 675 nm for the axial displacements.

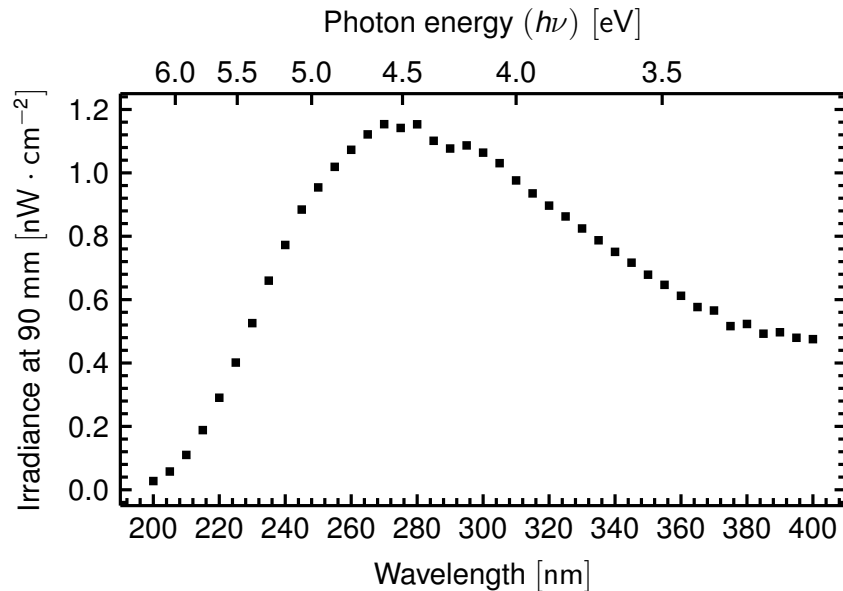
Figure 4.10: The irradiance dependence on the axial (vertical) displacement from 9 to 10 and then from (10 to 100) mm in 5 mm increments with respect to the 1.5 mm-diameter aperture.

## 4.6 Calibration of lamps

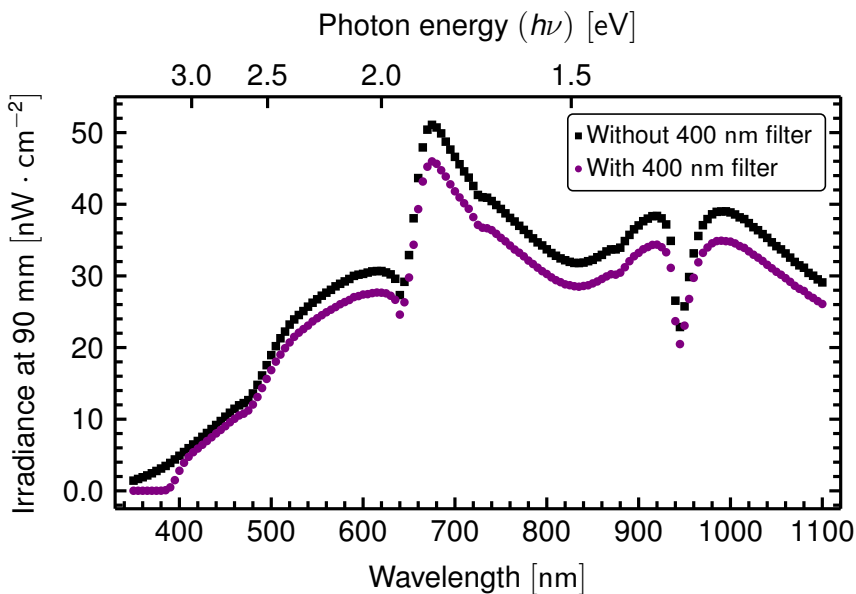
The spectral irradiance of the deuterium and tungsten-halogen lamps were calibrated against standards traceable to the [NIST](#) after the experimental set-up of the optoelectronic characterization system, using the flexOptometer system with the [Si](#)-based detector positioned at the fibre end. The fibre end was centrally aligned 90 mm from the standard detector, such that the 1 cm<sup>2</sup> photosensitive area was overfilled. The 1.50 nm-bandpass [CSR](#) mode was enabled on the monochromator, allowing the slit widths to be automatically set to the appropriate width for the corresponding selected wavelength.

A typical calibrated spectral irradiance of the deuterium lamp is plotted in [Figure 4.11\(a\)](#). This spectral irradiance was measured after the [EMR](#) has passed through each of the optical elements for wavelengths ranging from 200 nm to 400 nm in 5 nm increments.

The tungsten-halogen lamp would be used to investigate the [UV-to-VIS/NIR](#) rejection ratios of the photodiodes. Therefore, the use of the 400 nm order sorting filter is required, because the UV-C-sensitive photodiodes would also respond to wavelengths resulting from higher order diffraction effects in the 400 nm to 1100 nm wavelength range. The one calibrated spectral irradiance was obtained without the use of the 400 nm order sorting filter and the other with it, while the power supply set to 3.50 A for wavelengths ranging from 350 nm to 1100 nm in 5 nm increments, as seen in [Figure 4.11\(b\)](#). Looking at the two spectral irradiances, the suppression of [EMR](#) in the 350 nm to 400 nm range by the 400 nm order sorting filter is also clearly seen in [Figure 4.11\(b\)](#).



(a) Calibrated UV spectral irradiance of the 30 W deuterium lamp for wavelengths ranging from 200 nm to 400 nm in 5 nm increments.



(b) Calibrated VIS-to-NIR spectral irradiance of the 30 W tungsten-halogen lamp set to 3.50 A for wavelengths ranging from 350 nm to 1100 nm in 5 nm increments, with and without the 400 nm order sorting filter.

Figure 4.11: Typical spectral irradiances after calibrating the monochromatic EMR that exits the fibre end. Measurements were taken by the flexOptometer system with the Si-based detector placed 90 mm from the optical fibre end, such that the 1 cm<sup>2</sup> photosensitive area was overfilled.

## Chapter 5

# Schottky photodiode fabrication

### 5.1 Introduction

This part of the study aimed at establishing a fabrication procedure to develop and characterize tuneable front-irradiated **AlGaIn**-based solar-blind **UV**-sensitive Schottky photodiodes. Apart from the cleaning procedure, the metallization techniques found in literature for Schottky photodiodes were considered. The metallization techniques included metallization schemes, metal thicknesses and annealing methods for metallization. Two ( $3 \times 5$ ) mm<sup>2</sup> samples were taken from a single **AlGaIn** semiconductor wafer. The major fabrication steps, in sequence, were the as-deposited **Ir** Schottky contacts, followed by the annealing of **Ir** to form **IrO<sub>2</sub>**, then the deposition of the **Au** probe contact pads on top of the **IrO<sub>2</sub>** contacts and the annealing of the **Au** probe contact pads. The radiation hardness was investigated by irradiating one of the samples with 5.4 MeV **He**-ions from an <sup>241</sup>Am source. The effects on the optoelectronic characteristics of the two samples were investigated for each of the steps in the fabrication procedure and that of **He**-ion irradiation.



## 5.2 Experimental

### 5.2.1 The AlGaIn semiconductor wafer

The AlGaIn semiconductor wafer was custom grown by Technologies and Devices International, Inc. (TDI), using the hybrid vapour phase epitaxy (HVPE) growth method. The 11OK1234-3 wafer consisted of a four layer epitaxial structure. The epitaxial structure was grown on a 25.4 mm-diameter single side polished C-plane Al<sub>2</sub>O<sub>3</sub> substrate and was mechanically diced into smaller (3 × 5) mm<sup>2</sup> sample sizes. Two samples, referred to as A1 and A2, were taken from the wafer for the fabrication of the Schottky photodiodes.

The first layer of the wafer was undoped GaN with a thickness of (0.6 to 1.0) μm, followed by a (1.0 to 1.5) μm-thick layer of Si-doped GaN (GaIn:Si) with a free carrier concentration of (1.0 to 3.0) × 10<sup>18</sup> cm<sup>-3</sup>. The third layer was Si-doped AlGaIn (AlGaIn:Si) with an Al mole fraction varying from (36 to 40) % and a thickness of (0.15 to 0.25) μm. The fourth top layer was undoped AlGaIn with a thickness of (0.7 to 0.9) μm, also with an Al mole fraction varying from (36 to 40) %. Table 5.1 provides the specifications of the 11OK1234-3 wafer.

Table 5.1: The four layer epitaxial structure specifications of the 11OK1234-3 AlGaIn semiconductor wafer.

Layer	Material	Thickness [μm]	Al [%]
1	GaN	0.80 ± 0.20	0
2	GaN:Si	1.25 ± 0.25	0
3	AlGaIn:Si	0.20 ± 0.05	38.0 ± 2.0
4 (top)	AlGaIn	0.80 ± 0.10	38.0 ± 2.0

## 5.2.2 Preparation

### Glassware cleaning

The cleaning procedure started with the selection of appropriate glassware in which solutions for chemical degreasing and etching were to be prepared. The 100 ml Schott Duran crystallizing dishes with a spout (product-code 2131138) were selected. These specific crystallizing dishes have a 70 mm-diameter open-end and is 40 mm in height, suitable for inserting and removing samples during the cleaning process. The glassware was cleaned to remove any previous residues and chemicals that could have been left behind because of earlier use.

The glassware was placed inside a container that had a cleaning solution of  $\text{NH}_3$  (25 %) and  $\text{H}_2\text{O}_2$  (30 %) mixed in a 1:1 ratio and the glassware was left for two days in the cleaning solution. This was followed by rinsing the glassware five times in de-ionised (DI) water ( $R > 18 \text{ M}\Omega \cdot \text{cm}$ ) to ensure proper removal of the cleaning solution. To avoid cross-contamination during sample preparation, each element of glassware was designated to a single purpose and re-used for that particular purpose only.

### Sample surface cleaning

The surfaces of the  $\text{AlGaIn}$  semiconductor samples were prepared before the deposition of any of the metal contacts on it. These samples were prepared in the same manner as  $\text{GaIn}$  semiconductor samples and consisted of a chemical decreasing phase, followed by a wet chemical etching phase and finally a drying phase [Diale *et al.*, 2005:281; Janse van Rensburg *et al.*, 2009:4412; Liu and Lau, 1998:677–680].

Chemical degreasing removes possible loose dust and in particular organic substances. The organic substances can originate from glue of the tape that was

used on the wafer for the dicing process or oil from the human skin that may have contaminated the surface during handling.

The chemical degreasing phase comprised of boiling the samples in trichloroethylene (TCE) for three minutes. This was followed by rinsing them in boiling isopropanol for three minutes and thereafter rinsing in three batches of DI water. This first phase of cleaning required the use of at least four 100 ml crystallizing dishes; one for TCE, one for isopropanol and two for the DI water.

Chemical etching removes surface contaminants, carbon as well as oxides in the form of gallium(III) oxide ( $\text{Ga}_2\text{O}_3$ ) from the surfaces of the samples. In addition, the surface morphology of the samples was improved to enhanced the contact between the AlGaIn surface and the metal thin-films used in fabricating the metal contacts.

The wet chemical etching phase comprised of boiling the samples in a dilute aqua regia solution for ten minutes. The etching solution used was of HCl (32 %),  $\text{HNO}_3$  (70 %) and DI water in a 3:1:5 ratio. The samples were then rinsed in three batches of DI water and thereafter held for 60 s in a second acid solution of HCl:H<sub>2</sub>O (1:1) to remove oxides from the surface. Lastly, the samples were rinsed in two batches of DI water, blow-dried using  $\text{N}_2$  and placed in a wafer handling container. The samples were kept in a desiccator during overnight storage. In this second phase of cleaning, the use of at least two more 100 ml crystallizing dishes were required for the etching and oxide removal solutions. The two 100 ml crystallizing dishes used for the DI water during the first phase of cleaning, was used here again for the same purpose.

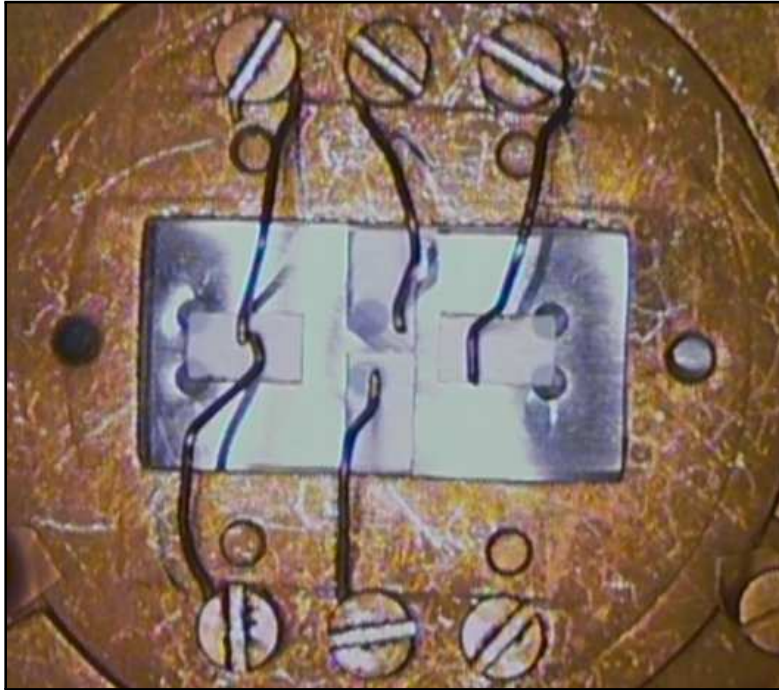


Figure 5.1: Photograph showing how samples were typically mounted onto a holder. Samples were held in place by wires pressing them down onto the metal mask and deposition was then done from the opposite side.

### **Deposition holder and masks**

Samples were mounted onto a holder and fixed in a vacuum system for physical vapour deposition (PVD). The PVD was done through a stainless steel contact mask that forms part of this holder. Figure 5.1 is a photograph taken to show how samples were typically mounted onto a holder. Samples were held in place by wires pressing them down onto the mask and deposition was then done through the open sections of the mask from the opposite side.

The holder and masks were also cleaned to avoid possible contamination to the already cleaned samples and to help keep conditions in the vacuum systems clean. The holder and masks were cleaned similarly to the chemical degreasing process used for the samples. Here, the holder and masks were boiled in TCE

for one minute and then rinsed in boiling isopropanol for one minute. Thereafter, they were rinsed in three batches of DI water, blow-dried using N<sub>2</sub> and placed in a storage container.

### **5.2.3 Contact deposition masks**

The ohmic contacts were deposited without the use of a particular mask. The samples were covered with a thin piece of glass such that less than 2 mm on one of the sides were exposed and the ohmic contacts were then deposited. The mask used for Schottky contact deposition had both 0.65 mm- and 1.0 mm-diameter holes. This particular mask was selected because of the uncertainty in the generation of measurable photocurrents over the smaller photosensitive areas during UV irradiation. The final probe contact pads were deposited on samples using a mask that had several 0.30 mm-diameter holes.

### **5.2.4 Ohmic contact fabrication**

Layered metal thin-film structures of ohmic contacts were fabricated in an electron-beam PVD (EBPVD) system under a pressure of less than 10<sup>-5</sup> mbar. The ohmic contacts were then annealed by following a two-step annealing procedure. In most cases, ohmic contacts form with the deposition of any metal with a work function equal or lower than that of the *n*-type AlGa<sub>0.3</sub>N semiconductor. The work function for an AlGa<sub>0.3</sub>N semiconductor should approximately be the same as that of GaN semiconductors and was taken to be 4.10 eV. The work function of Al is 4.08 eV and puts it in the ohmic category. It was also shown that Ti falls in the ohmic category, although it has a work function of 4.33 eV. Ti interacts with GaN in the AlGa<sub>0.3</sub>N semiconductor, forming a thin TiN layer on the surface, especially as N diffuses outward during annealing procedures. The majority of N vacancies

results in the surface GaN becoming highly *n*-type and the effective tunnelling of electrons through the surface layer is possible. Therefore, the formation of the TiN layer plays an important role in achieving low contact resistivity [Razeghi and Rogalski, 1996:7466; Ruvimov *et al.*, 1996:1556–1557].

Other research studies found that a bilayer contact metallization scheme consisting of Ti/Al exhibited near linear *I–V* characteristics prior to annealing. Different annealing procedures were followed to improve the contact characteristics. The bilayer contact was annealed first at 500 °C under N<sub>2</sub> ambient, then using a rapid thermal annealing (RTA) method at 700 °C for 20 s. After annealing the bilayer at 900 °C for 30 s, the specific contact resistivity lowered to 8.0 μΩ · cm<sup>2</sup> [Razeghi and Rogalski, 1996:7466].

Ruvimov *et al.* [1996:1558] experimented further with a four layer metal contact, also annealing it at 900 °C for 30 s using a RTA method. They found that the TiN layer at the interface was twice as thick, as that formed with the bilayer contact. Hayes *et al.* [2003:422] used this same four layer metal composite ohmic structure of Ti/Al/Ni/Au (150/2200/400/500 Å) and annealed the contact at only 500 °C for five minutes under Ar ambient.

The ohmic contacts fabricated on A1 and A2 were similar to those used in the study done by Hayes *et al.* [2003]. The metallization scheme was a layered structure of Ti/Al/Ni/Au (150/2000/450/500 Å) and was then two-step annealed under Ar ambient. The temperature was increased to 500 °C and annealed for five minutes, followed by annealing at 700 °C for five minutes as well [van Schalkwyk *et al.*, 2012:1529–1530].

### 5.2.5 Schottky contact fabrication

After the fabrication of the ohmic contacts, the Schottky contacts were deposited with the same EBPVD system under a pressure of less than  $10^{-5}$  mbar. Schottky contacts should form with the deposition of any metal with a work function greater than that of the *n*-type AlGaIn semiconductor. This study required the fabrication of front-irradiated photodiodes, that is, the photodiodes would be irradiated with UVR on the same side as where the Schottky contacts were deposited. This added to the challenge of finding a Schottky barrier material with a high optical transmittance in the UV region.

Based on the study done by Kim *et al.* [2002], it was decided to experiment with IrO<sub>2</sub> as the Schottky barrier material. They showed that 100 Å-thick IrO<sub>2</sub> Schottky contacts can effectively be used for GaN metal–semiconductor–metal UV-sensitive photodetectors. IrO<sub>2</sub> is one of the conducting metal oxides with the advantage of having a high work function (greater than 5 eV) and a low resistivity (approx.  $50 \mu\Omega \cdot \text{cm}$ ). Their 100 Å-thick Ir Schottky contacts were annealed at 500 °C under O<sub>2</sub> ambient for one minute to form IrO<sub>2</sub>. The IrO<sub>2</sub> had a high optical transmittance (greater than 60 %) in the UV region ranging from 300 nm to 400 nm.

Two circular 0.65 mm-diameter and four 1.0 mm-diameter, 50 Å-thick Ir contacts were deposited at a rate of  $0.2 \text{ \AA} \cdot \text{s}^{-1}$  on each of the two samples. Figures 5.2(a) and 5.3(a) are photographs taken of A1 and A2 with the as-deposited Ir contacts. The two-step annealed ohmic contact is seen on the left-side of each sample. Afterwards, the Ir Schottky contacts were annealed at 700 °C under O<sub>2</sub> ambient flowing at a rate of  $1 \text{ L} \cdot \text{min}^{-1}$  for 20 minutes. This allowed for the formation of the more UV transmissive IrO<sub>2</sub> Schottky contacts that were barely visible as observed in Figures 5.2(b) and 5.3(b) [van Schalkwyk *et al.*, 2012:1530].

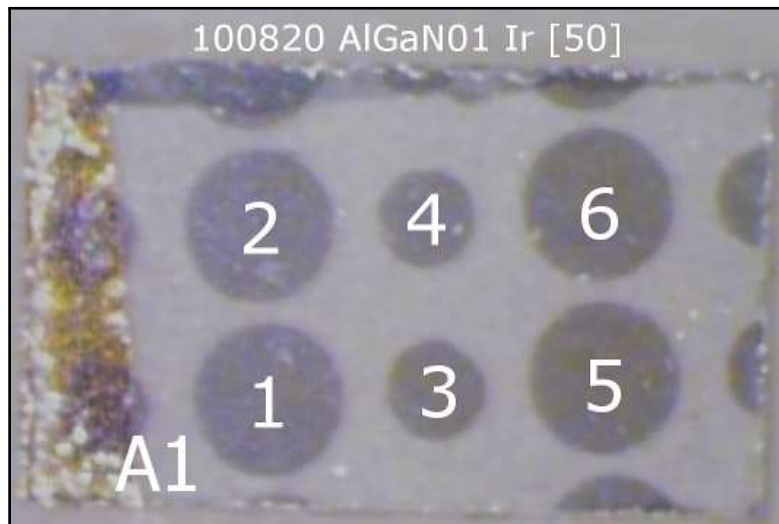
The 700 °C annealing temperature followed from studying the research done by Chalamala *et al.* [2000]. They annealed Ir thin films at 600 °C, 700 °C, 800 °C and 900 °C for 1 hour in a furnace that had a continuous flow of O<sub>2</sub> at 10 Torr (~ 13 mbar). Using x-ray diffraction (XRD) crystallography and x-ray photoelectron spectroscopy (XPS) depth profile measurements, the chemical composition of the thin films were investigated. They found no evidence of bulk oxidation at 600 °C. Only at 700 °C and 800 °C did oxygen start diffusing into the bulk of the film. The films annealed at 900 °C lost most of the deposited Ir, because of the sublimation of IrO<sub>2</sub>.

### 5.2.6 Probe contact pad fabrication

The 50 Å-thick IrO<sub>2</sub> Schottky contacts required probe contact pads for four reasons. The first was to prevent the measurement probe from possibly piercing through the thin Schottky contact and partly making contact with the surface of the semiconductor itself. Secondly, the deposition of an opaque material with a known surface area makes the calculation of the photosensitive area more precise, compared to determining an area shadowed by the measurement probe during irradiation. The third is that conductivity can improve because of a decrease in contact resistance. Lastly, the feasibility of wire bonding on the Schottky contacts needed to be investigated and, therefore, thicker contact pads were required to which wires can bond.

A resistive evaporation system was used for the deposition of the probe contact pads under a pressure of approximately 10<sup>-5</sup> mbar. Six circular 0.30 mm-diameter, 1000 Å-thick Au probe contact pads were deposited at 1.0 Å·s<sup>-1</sup>, on top of the annealed Ir Schottky contacts of A1 and A2. The Au probe contact pads were not annealed on A1, but were on A2. Figure 5.2(b) and 5.3(b) are photographs taken of A1 with the as-deposited Au probe contact pads, and A2 with



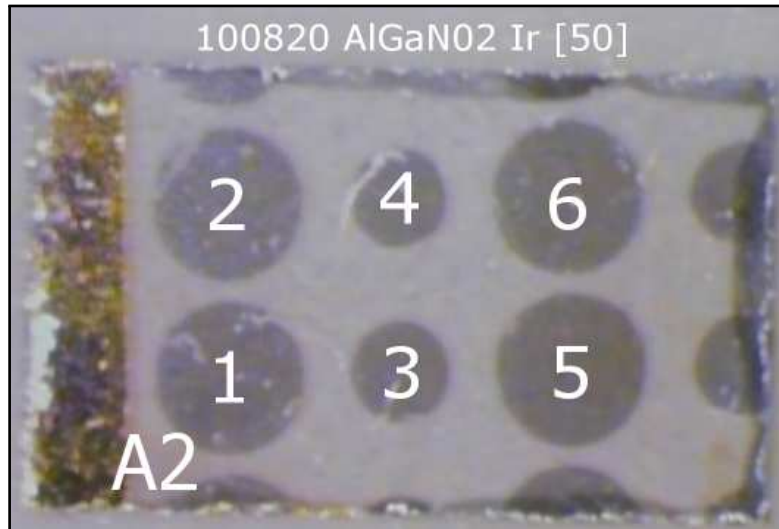


(a) The layered ohmic structure of  $\text{Ti}/\text{Al}/\text{Ni}/\text{Au}$  (150/2000/450/500 Å) was fabricated on the left-side of the sample. The ohmic contact was two-step annealed under  $\text{Ar}$  ambient for five minutes at both 500°C and 700°C. Afterwards, two circular 0.65 mm-diameter and four 1.0 mm-diameter, 50 Å-thick  $\text{Ir}$  Schottky contacts were deposited.

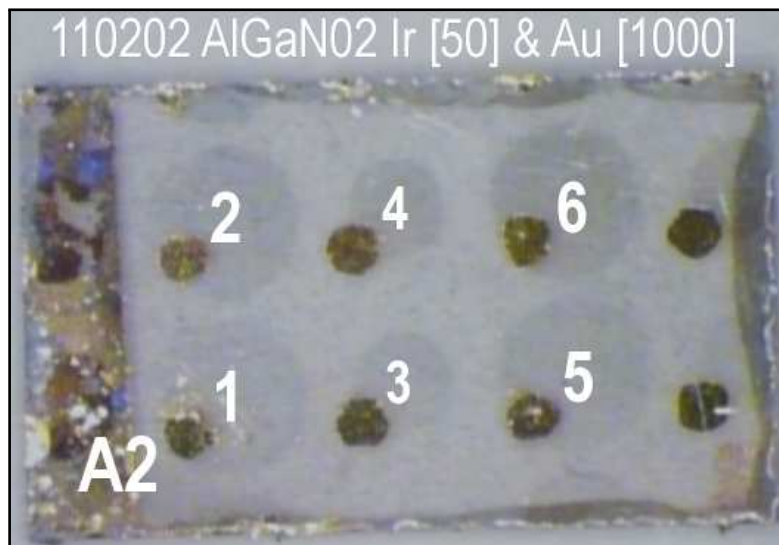


(b) The barely visible  $\text{IrO}_2$  Schottky contacts were formed after annealing the  $\text{Ir}$  Schottky contacts at 700°C under  $\text{O}_2$  ambient for 20 minutes. Thereafter, six circular 0.30 mm-diameter, 1000 Å-thick  $\text{Au}$  probe contact pads were deposited.

Figure 5.2: Photographs of the fabricated Schottky photodiodes on A1 taken from wafer 11OK1234-3. The photodiodes were optoelectronically characterized for each of the three fabrication steps and after being irradiated with 5.4 MeV  $\text{He}$ -ions from an  $^{241}\text{Am}$  source.



(a) The layered ohmic structure of  $\text{Ti}/\text{Al}/\text{Ni}/\text{Au}$  ( $150/2000/450/500 \text{ \AA}$ ) was fabricated on the left-side of the sample. The ohmic contact was two-step annealed under  $\text{Ar}$  ambient for five minutes at both  $500^\circ\text{C}$  and  $700^\circ\text{C}$ . Afterwards, two circular  $0.65 \text{ mm}$ -diameter and four  $1.0 \text{ mm}$ -diameter,  $50 \text{ \AA}$ -thick  $\text{Ir}$  Schottky contacts were deposited.



(b) The barely visible  $\text{IrO}_2$  Schottky contacts were formed after annealing the  $\text{Ir}$  Schottky contacts at  $700^\circ\text{C}$  under  $\text{O}_2$  ambient for 20 minutes. Thereafter, six circular  $0.30 \text{ mm}$ -diameter,  $1000 \text{ \AA}$ -thick  $\text{Au}$  probe contact pads were deposited and annealed at  $350^\circ\text{C}$  under  $\text{O}_2$  ambient for 10 minutes.

Figure 5.3: Photographs of the fabricated Schottky photodiodes on A2 taken from wafer 110K1234-3. The photodiodes were optoelectronically characterized for each of the four fabrication steps.

the annealed Au probe contact pads on top of the lower-left-side of the optically transparent 50 Å-thick IrO<sub>2</sub> Schottky contacts.

### 5.2.7 Radiation hardness

Group-III-nitride-based materials exhibit superior radiation hardness characteristics compared to Si-based materials, because of their WBG and chemical bond strength [Monroy *et al.*, 2003:R35–R36; Razeghi and Rogalski, 1996:7462]. The radiation hardness was investigated by irradiating A1 over a 1040 hour period with 5.4 MeV He-ions from an <sup>241</sup>Am source at  $7.1 \times 10^6 \text{ cm}^{-2} \cdot \text{s}^{-1}$  for a total fluence of  $3 \times 10^{13} \text{ cm}^{-2}$ . The reverse leakage current density and capacitance at 1 V reverse bias of the six photodiodes were measured after 1 hour, 3 hours, 10 hours, 20 hours, 30 hours, 40 hours, 104 hours, 167 hours, 251 hours, 335 hours and 1040 hours to look for any significant changes in their values. Only after 1040 hours were some changes observed and the sample was optoelectronically characterized to study the effects on the electrical and spectral parameters.

### 5.2.8 Annealing of the Au probe contacts

By annealing the deposited Au probe contact pads the adhesion between Au and the IrO<sub>2</sub> Schottky contacts can be improved. Moreover, annealing can also further improve conductivity by decreasing the contact resistance. Therefore, the Au probe contact pads on A2 were annealed at 350°C under O<sub>2</sub> ambient for approx. 10 minutes and subsequently characterized.

## 5.2.9 Optoelectronic characterization

Optoelectronic characterization was performed by the optoelectronic characterization system (described in Chapter 4). The characterization consisted of (dark) electrical, followed by spectral characterization. Measurements were conducted at an average room temperature of 298 K. The 300 K material constants used for the AlGa<sub>N</sub> semiconductors were an electron effective mass of  $0.18m_0$  [Elhamri *et al.*, 1998:1374], a dielectric constant ( $K_s$ ) of 8.9 [Monroy *et al.*, 2003:R36] and the number of equivalent minima in the conduction band of 4, both of the latter constants the same as for wurtzite Ga<sub>N</sub> semiconductors.

### Electrical characterization

Electrical characterization comprised of dark  $I-V$  and  $C-V$  measurements. The measurements were performed with the use of an already developed NI LabVIEW routine that controlled the HP 4140B pA meter/DC voltage source and HP 4192A LF impedance analyzer. The pA meter/DC voltage source used the single staircase wave mode for forward and reverse biasing, while a 3 s hold and a 7 s step delay time was typically selected. Forward and reverse biasing ranged from 0 V to 2 V and  $-2$  V to 0 V, respectively, in 100 mV increments for  $I-V$  measurements. For  $C-V$  measurements, a 100 mV sinusoidal AC signal of 1 MHz was superimposed upon a reverse (DC) biasing. The biasing ranged from  $-1.2$  V to 0 V in 50 mV increments with a 1.5 s hold time before each capacitance measurement. A desktop computer with an NI LabVIEW routine determined and presented the electrical parameters, using the methods described in subsection 3.3.2 of Chapter 3. The parameters of interest included the ideality factor, SBH, reverse leakage current density at 1 V reverse bias and series resistance obtained from the  $I-V$  characteristics. The free carrier concentration was

obtained from the  $C-V$  characteristics.

The measurements were performed on each of the six Schottky photodiodes on A1 and A2. The circular 0.65 mm-diameter and 1.0 mm-diameter Schottky contacts had contact areas of  $3.3 \times 10^{-3} \text{ cm}^2$  and  $7.9 \times 10^{-3} \text{ cm}^2$ , respectively. The characterization of A1 was done for the three fabrication steps that the Schottky contacts had undergone. These three steps were the as-deposited Ir (As-dep.), being annealed to form  $\text{IrO}_2$  (Annealed) and after the deposition of Au probe contact pads ( $\text{IrO}_2/\text{Au}$ ). Lastly, the effect of He-ion irradiation was investigated with A1 ( $\text{He}^+$ ). The characterization of A2 was done for the four fabrication steps, that included the as-deposited, being annealed, the deposition of Au probe contact pads and after the annealing of the Au probe contact pads ( $\text{IrO}_2/\text{Au}$  Annealed).

### **Spectral characterization**

Spectral characterization was performed after calibrating the monochromatic UVR that exits the fibre end when using the deuterium lamp. The lamp was switched on at least 30 minutes prior to a characterization procedure, allowing the lamp to warm-up and stabilize. Calibration was done with the flexOptometer system by following the photodetector substitution method as explained in section 4.6 of Chapter 4. An additional spectral characterization NI LabVIEW routine was developed that controlled the monochromator, flexOptometer system, HP 4140B pA meter/DC voltage source and recorded the measurements.

The NI LabVIEW routine recorded the calibrated UV spectral irradiance for the 200 nm to 350 nm range in 5 nm increments. A hold time of 5 s was used before an irradiance measurement was recorded at a specific wavelength. The expected spectral irradiance of a photodiode at 9 mm from the fibre end was then calculated by the NI LabVIEW routine using Eq. 4.8.

The NI LabVIEW routine recorded the generated photocurrent while the photodiode was being irradiated at a specific wavelength with the fibre end positioned 9 mm from the photodiode. A hold time of 2 s was used before the photocurrent was measured by the HP 4140B pA meter. The NI LabVIEW routine divided the photocurrents measured over the same wavelength range and increments by the photosensitive area of the photodiode to obtain the PCD at each wavelength.

The spectral characterization NI LabVIEW routine kept a record of the fibre end distance from the standard detector ( $z_{SD}$ ), the fibre end distance from the photodiode ( $z_{PD}$ ), the wavelengths, the standard detector irradiances ( $E_{SD}$ ), the calculated photodiode irradiances ( $E_{PD}$ ), the photocurrents ( $I_p$ ) and the PCDs  $J_p$ . The photodiode irradiances and PCDs were used to calculate and record the current responsivities ( $\mathcal{R}_\lambda$ ) together with the quantum efficiencies ( $\eta_\lambda$ ) using Eqs. 3.56 and 3.62, respectively. The recorded measurements were saved in a comma delimited data file.

The spectral characterizations of the Schottky photodiodes fabricated on A1 and A2 were done with the UVR source. The measurements were performed on each of the six photodiodes. The characterization of A1 was done for its three fabrication steps, together with investigating the effect of He-ion irradiation. The characterization of A2 was done for its four fabrication steps.

The photosensitive areas for the as-deposited Ir and annealed IrO<sub>2</sub> Schottky contacts were taken to be that of the contact itself. However, after the deposition of the circular 0.30 mm-diameter Au probe contact pads the photosensitive areas changed to  $2.6 \times 10^{-3} \text{ cm}^2$  and  $7.2 \times 10^{-3} \text{ cm}^2$  for the circular 0.65 mm-diameter and 1.0 mm-diameter Schottky contacts, respectively.

## 5.3 Results and discussion

This section covers the results obtained through the optoelectronic characterization process of A1 and A2 by measuring all 12 of the Schottky photodiodes. Thereafter, it is concluded which of the photodiodes were considered and reported on in the first publication.

### 5.3.1 Electrical characterization

The electrical parameters obtained from the electrical characterization of A1 for its fabrication steps and after He-ion irradiation are summarized in Tabel 5.2. The parameters obtained for A2 for its fabrication steps are summarized in Tabel 5.3. The photodiodes that displayed proper rectifying  $I-V$  characteristics are marked with an asterisk (\*). The photodiodes that were viewed as failures would either have had an ideality factor greater than 2 or a reverse leakage current density at 1 V reverse bias greater than  $200 \text{ nA} \cdot \text{cm}^{-2}$ .

Using the electrical parameters of the photodiodes marked with an asterisk (\*), the average value (Avg.\*) of each parameter was calculated together with its standard deviation (Std. dev.\*). The average values of the parameters were considered to identify trends in the fabrication procedure while the standard deviations were an indication of how strongly the parameters varied between the photodiodes after a fabrication step.

#### The ideality factor

Table 5.2 shows that the average ideality factor ( $\eta$ ) for the as-deposited fabrication step improved from 1.81 to 1.41 after being annealed and the standard deviations were less than 8.0 %, indicating that the ideality factors were very consisted between the five selected photodiodes. However, after the deposition



Table 5.2: The electrical parameters of the Schottky photodiodes on A1 for their three fabrication steps and after He-ion irradiation. The parameters included the ideality factor ( $\eta$ ), SBH ( $\phi_{B0}$ ), reverse leakage current density ( $J_R$ ) at 1 V reverse bias, series resistance ( $R_S$ ) and the free carrier concentration ( $N_d$ ).

Fabrication step	Photo-diode	$A_c$ [mm <sup>2</sup> ]	$\eta$	$\phi_{B0}$ [eV]	$J_R$ at $-1$ V [nA · cm <sup>-2</sup> ]	$R_S$ [ $\Omega$ ]	$N_d$ [10 <sup>18</sup> cm <sup>-3</sup> ]
As-dep.	A1-1*	0.79	1.88	1.43	0.038	1000	1.0
	A1-2*	0.79	1.64	1.53	11	1000	1.0
	A1-3*	0.33	1.93	1.40	0.44	1000	1.2
	A1-4*	0.33	1.72	1.48	0.040	1100	1.1
	A1-5	0.79	2.34	1.13	91	1400	1.2
	A1-6*	0.79	1.87	1.45	0.050	1400	1.0
	Avg.*:		1.81	1.46	2.3	1100	1.1
Std. dev.*:		0.12	0.05	4.9	140	0.10	
Annealed	A1-1*	0.79	1.30	1.68	0.0079	230	0.31
	A1-2	0.79	2.10	1.20	2.0	230	1.3
	A1-3*	0.33	1.35	1.62	15	310	1.4
	A1-4*	0.33	1.41	1.56	0.0048	230	0.18
	A1-5*	0.79	1.58	1.47	0.26	670	0.0038
	A1-6*	0.79	1.39	1.58	7.9	300	1.2
	Avg.*:		1.41	1.58	4.6	350	0.62
Std. dev.*:		0.11	0.08	6.6	180	0.64	
IrO <sub>2</sub> /Au	A1-1	0.79	2.75	0.74	1000	45	0.28
	A1-2*	0.79	1.31	1.05	0.59	77	1.2
	A1-3*	0.33	1.40	1.05	0.054	100	1.5
	A1-4*	0.33	1.70	1.15	150	110	1.3
	A1-5*	0.79	1.31	1.16	0.28	150	1.5
	A1-6*	0.79	1.85	0.82	170	130	0.71
	Avg.*:		1.51	1.05	63	110	1.2
Std. dev.*:		0.25	0.14	86	29	0.31	
He <sup>+</sup>	A1-1	0.79	—	—	—	—	—
	A1-2	0.79	—	—	—	—	—
	A1-3*	0.33	2.21	1.05	0.055	290	1.1
	A1-4*	0.33	1.51	1.29	0.11	330	0.82
	A1-5	0.79	—	—	—	—	—
	A1-6	0.79	—	—	—	—	—
	Avg.*:		1.86	1.17	0.080	310	0.94
Std. dev.*:		0.49	0.17	0.036	32	0.17	



Table 5.3: The electrical parameters of the Schottky photodiodes on A2 for their four fabrication steps. The parameters included the ideality factor ( $\eta$ ), SBH ( $\phi_{B0}$ ), reverse leakage current density ( $J_R$ ) at 1 V reverse bias, series resistance ( $R_S$ ) and the free carrier concentration ( $N_d$ ).

Fabrication step	Photo-diode	$A_c$ [mm <sup>2</sup> ]	$\eta$	$\phi_{B0}$ [eV]	$J_R$ at $-1$ V [nA · cm <sup>-2</sup> ]	$R_S$ [ $\Omega$ ]	$N_d$ [10 <sup>18</sup> cm <sup>-3</sup> ]
As-dep.	A2-1*	0.79	1.22	0.89	49	1100	0.077
	A2-2	0.79	2.06	1.30	0.22	470	0.96
	A2-3	0.33	—	—	—	—	—
	A2-4*	0.33	1.23	1.14	0.064	1600	0.94
	A2-5	0.79	2.11	1.34	2.8	500	0.63
	A2-6*	0.79	1.68	1.31	0.63	540	0.99
		Avg.*:	1.38	1.11	17	1100	0.67
	Std. dev.*:	0.26	0.21	28	520	0.51	
Annealed	A2-1*	0.79	1.75	1.18	2.0	270	0.062
	A2-2*	0.79	1.54	1.45	6.0	200	0.010
	A2-3	0.33	—	—	—	—	—
	A2-4*	0.33	1.38	1.37	0.68	200	1.0
	A2-5*	0.79	1.40	1.57	0.032	340	0.058
	A2-6*	0.79	1.82	1.32	29	250	0.78
		Avg.*:	1.58	1.38	7.5	250	0.39
	Std. dev.*:	0.20	0.15	12	57	0.48	
IrO <sub>2</sub> /Au	A2-1	0.79	—	—	—	—	—
	A2-2*	0.79	1.62	1.38	5.4	37	5.8
	A2-3	0.33	—	—	—	—	—
	A2-4*	0.33	1.62	1.36	0.62	92	4.2
	A2-5	0.79	1.92	0.74	$17 \times 10^3$	210	5.4
	A2-6	0.79	2.26	0.69	$1.3 \times 10^6$	190	2.8
		Avg.*:	1.62	1.37	3.0	65	5.0
	Std. dev.*:	0.00	0.01	3.4	40	1.1	
IrO <sub>2</sub> /Au Annealed	A2-1	0.79	—	—	—	—	—
	A2-2*	0.79	1.37	1.40	5.7	46	5.6
	A2-3	0.33	—	—	—	—	—
	A2-4*	0.33	1.47	1.25	0.85	86	3.9
	A2-5	0.79	1.52	0.86	340	140	5.5
	A2-6	0.79	3.48	0.66	$340 \times 10^3$	130	2.5
		Avg.*:	1.42	1.33	3.3	66	4.8
	Std. dev.*:	0.07	0.11	3.4	28	1.3	

of the Au probe contact pads the average ideality factor degraded slightly from 1.41 to 1.51, although this was still better than that of the as-deposited fabrication step, the standard deviation was approx. 17 % and indicated less consistency between the five selected photodiodes.

Only photodiodes A2-2 and A2-4 were characterized for the majority of the fabrication steps in Table 5.3. A small glassine bag was used for storing A2 and because of the weak adhesion between the as-deposited Ir contacts and the AlGaIn surface, the rest of the photodiodes were severely scratched and damaged during handling. The trends here with respect to the ideality factors were not the same as that of A1. Here the average ideality factor for the as-deposited step degraded from of 1.38 to 1.58 when the Ir contacts were annealed and degraded further to 1.62 with the deposition of the Au probe contact pads. However, it was noted in Figure 5.3(b) for the Schottky photodiode A2-4 that the Au probe contact pad was deposited only partly on top of the IrO<sub>2</sub> contact and mostly made direct contact with the AlGaIn surface. Although this happened the ideality factors were still in the same range of values compared to that of A1 in Table 5.2 and, in addition, the annealing of the Au probe contact pads as a fourth fabrication step did improve the average ideality factor to 1.42.

### **The Schottky barrier height**

The average SBH ( $\phi_{B0}$ ) of the photodiodes on A1 for the as-deposited Ir increased from 1.46 eV to 1.58 eV for the IrO<sub>2</sub> with standard deviations less than 5.5 %. Once the Au probe contact pads were deposited, an average SBH of 1.05 eV with a standard deviation of less than 14 % was obtained, as seen in Table 5.2.

For A2, the average SBH of the as-deposited Ir increased from 1.11 eV to 1.38 eV for the IrO<sub>2</sub> and stayed roughly the same at 1.37 eV for the deposited Au probe

contact pads. After annealing the Au probe contact pads, the average SBH slightly decreased to 1.33 eV, as seen in Table 5.3.

### **The reverse leakage current density at 1 V reverse bias**

The average reverse leakage current densities ( $J_R$ ) measured at 1 V reverse bias for A1 increased for each of the three fabrication steps to  $63 \text{ nA} \cdot \text{cm}^{-2}$  in Table 5.2. This can be attributed to the improved conductivity between the Schottky contact and the AlGaIn surface when the Ir was annealed to form IrO<sub>2</sub>, and even more so with the addition of the Au probe contact pads on top of the IrO<sub>2</sub>.

On the other hand, the average reverse leakage current densities for A2 decreased for the first three fabrication steps to  $3.0 \text{ nA} \cdot \text{cm}^{-2}$  and increased slightly to  $3.3 \text{ nA} \cdot \text{cm}^{-2}$  when the Au probe contact pads were annealed, as seen in Table 5.3.

Although the HP 4140B pA meter can detect currents as low as 1 fA, there were significant fluctuations when measuring reverse leakage currents of less than 1 nA. Therefore, the reverse leakage current densities also varied significantly and resulted in relative standard deviations ranging from 40 % to 220 %.

### **The series resistance**

The average series resistance ( $R_S$ ) of the photodiodes on both samples for the as-deposited Ir decreased from  $1100 \Omega$  to less than  $110 \Omega$  after the addition of the Au probe contact pads on top of the IrO<sub>2</sub> as well as annealing the Au probe contact pads on A2.

### **The free carrier concentration**

The second layer of the 11OK1234-3 wafer was a (1.0 to 1.5)  $\mu\text{m}$ -thick GaN:Si layer with a specified free carrier concentration of  $(1.0 \text{ to } 3.0) \times 10^{18} \text{ cm}^{-3}$ . The free carrier concentration ( $N_d$ ) was determined from the  $C-V$  characterization of the samples, which is not expected to change significantly because of the fabrication procedure. Therefore, the average free carrier concentration was determined from the  $C-V$  measurements done during the fabrication steps to be  $(2.0 \pm 0.63) \times 10^{18} \text{ cm}^{-3}$  and was within the range of that specified for the wafer.

### **Radiation hardness**

After irradiating A1 with the 5.4 MeV He-ions over a 1040 hour period, it was noticed that the as-deposited Au probe contact pads severely flaked off, as seen in Figure 5.4. This was progressively caused during the eleven times that the measurement probe of the optoelectronic characterization system were positioned on the IrO<sub>2</sub>/Au contacts and the weak adhesion between the as-deposited Au and annealed IrO<sub>2</sub> contacts was visible.

As seen in Table 5.2, only photodiodes A1-3 and A1-4 were characterized after the 1040 hour period. The ideality factor of A1-3 degraded from 1.40 to 2.21, its reverse leakage current density measured at 1 V reverse bias did not change significantly and the series resistance increased from 100  $\Omega$  to 290  $\Omega$  due to the reduced conductivity caused by the loss in the Au contact area.

The ideality factor of A1-4, however, improved from 1.70 to 1.51, its reverse leakage current density measured at 1 V reverse bias decreased from 150  $\text{nA} \cdot \text{cm}^{-2}$  to 0.11  $\text{nA} \cdot \text{cm}^{-2}$  and can possibly be due the positioning of the measurement probe on a 'good' spot on what was left of the Au probe contact pad. The series resistance also increased from 110  $\Omega$  to 330  $\Omega$  and can again be attributed to

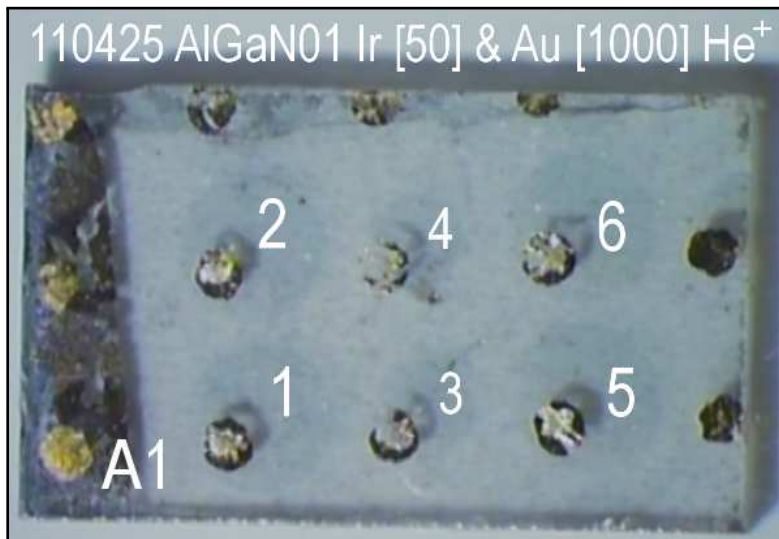


Figure 5.4: Photograph of the Schottky photodiodes on A1 after being irradiated over a 1040 hour period with 5.4 MeV He-ions from an  $^{241}\text{Am}$  source for a total fluence of  $3 \times 10^{13} \text{ cm}^{-2}$ . The as-deposited Au probe contact pads severely flaked off. This was progressively caused during the eleven times that the measurement probe of the optoelectronic characterization system were positioned on the  $\text{IrO}_2/\text{Au}$  contacts and the weak adhesion between the as-deposited Au and annealed  $\text{IrO}_2$  contacts were visible.

the reduced conductivity caused by the loss in the Au contact area.

The free carrier concentration did decrease on average from the  $C-V$  measurements done on both A1-3 and A1-4. For A1-3 the average free carrier concentration (calculated from the three fabrication steps) decrease by approx. 21 % from  $(1.4 \text{ to } 1.1) \times 10^{18} \text{ cm}^{-3}$  and for A1-4 by approx. 4.7 % from  $(0.86 \text{ to } 0.82) \times 10^{18} \text{ cm}^{-3}$ .

### 5.3.2 Spectral characterization

The spectral parameters obtained with the spectral characterization of A1 for its fabrication steps and after He-ion irradiation are summarized in Tabel 5.4. The parameters obtained for A2 for its fabrication steps are summarized in Tabel 5.5. Although all the photodiodes were spectrally characterized, the average value (Avg.\*) of each spectral parameter was calculated together with its standard deviation (Std. dev.\*) for the same photodiodes that displayed proper rectifying  $I-V$  characteristics that were marked with an asterisk (\*) in Tables 5.2 and 5.3.

#### The cut-off wavelength

The cut-off wavelength was found to be at approx. 295 nm and corresponded with 4.20 eV by Eq. 2.1 for all the photodiodes on A1 and A2. The cut-off wavelength ( $\lambda_{\text{cut-off}}$ ) was chosen where the current responsivity dropped to less than 50 % the (maximum) current responsivity at a specific wavelength ( $\mathcal{R}_\lambda$ ) which was selected to be at 275 nm.

Furthermore, it was determined that the cut-off wavelength corresponded to the absorption edge of a  $\text{Al}_{0.35}\text{Ga}_{0.65}\text{N}$  semiconductor, using Eq. 3.3 and solving for the Al mole fraction. When calculated from Eq. 3.3, the Al mole fraction of 35 % differed by less than 4 % from the lowest value of 36 % that was specified by TDI for the 11OK1234-3 wafer (Table 5.1).

#### The current responsivity and quantum efficiency

An average current responsivity at 275 nm ( $\mathcal{R}_{275}$ ) of  $(52 \pm 17) \text{ mA} \cdot \text{W}^{-1}$  was obtained for the as-deposited Ir on A1 with an average quantum efficiency ( $\eta_{275}$ ) of  $(23 \pm 7.8) \%$ , as seen in Table 5.4. After annealing the Ir to form the more UV transmissive  $\text{IrO}_2$ , the average current responsivity increased, as expected,

Table 5.4: The spectral parameters of the Schottky photodiodes on A1 for their three fabrication steps and after He-ion irradiation. The parameters included the cut-off wavelength ( $\lambda_{\text{cut-off}}$ ), current responsivity ( $\mathcal{R}_{275}$ ) and quantum efficiency ( $\eta_{275}$ ) at 275 nm.

Fabrication step	Photo-diode	$A_p$ [mm <sup>2</sup> ]	$\lambda_{\text{cut-off}}$ [nm]	$\mathcal{R}_{275}$ [mA · W <sup>-1</sup> ]	$\eta_{275}$ [%]
As-dep.	A1-1*	0.79	295	27	12
	A1-2*	0.79	295	71	32
	A1-3*	0.33	295	65	29
	A1-4*	0.33	295	46	21
	A1-5	0.79	295	54	24
	A1-6*	0.79	295	48	22
	Avg.*: Std. dev.*:			17	52 7.8
Annealed	A1-1*	0.79	295	39	17
	A1-2	0.79	295	86	39
	A1-3*	0.33	295	70	32
	A1-4*	0.33	295	21	9.6
	A1-5*	0.79	295	89	40
	A1-6*	0.79	295	91	41
	Avg.*: Std. dev.*:				62 31
IrO <sub>2</sub> /Au	A1-1	0.72	—	—	—
	A1-2*	0.72	295	33	15
	A1-3*	0.26	295	58	26
	A1-4*	0.26	295	65	29
	A1-5*	0.72	295	59	27
	A1-6*	0.72	295	38	17
	Avg.*: Std. dev.*:				51 14
He <sup>+</sup>	A1-1	0.72	—	—	—
	A1-2	0.72	—	—	—
	A1-3*	0.26	295	70	31
	A1-4*	0.26	295	59	27
	A1-5	0.72	—	—	—
	A1-6	0.72	—	—	—
	Avg.*: Std. dev.*:				64 7.6

Table 5.5: Spectral parameters of the Schottky photodiodes on A2 for their four fabrication steps. The parameters included the cut-off wavelength ( $\lambda_{\text{cut-off}}$ ), current responsivity ( $\mathcal{R}_{275}$ ) and quantum efficiency ( $\eta_{275}$ ) at 275 nm.

Fabrication step	Photo-diode	$A_p$ [mm <sup>2</sup> ]	$\lambda_{\text{cut-off}}$ [nm]	$\mathcal{R}_{275}$ [mA · W <sup>-1</sup> ]	$\eta_{275}$ [%]
As-dep.	A2-1*	0.79	295	19	8.8
	A2-2	0.79	295	42	19
	A2-3	0.33	—	—	—
	A2-4*	0.33	295	34	18
	A2-5	0.79	295	28	13
	A2-6*	0.79	295	37	17
	Avg.*: Std. dev.*:			30 9	15 5.0
Annealed	A2-1*	0.79	295	20	9.1
	A2-2*	0.79	295	14	6.3
	A2-3	0.33	—	—	—
	A2-4*	0.33	295	29	13
	A2-5*	0.79	295	11	5.0
	A2-6*	0.79	295	51	23
	Avg.*: Std. dev.*:			25 16	11 7.2
IrO <sub>2</sub> /Au	A2-1	0.72	—	—	—
	A2-2*	0.72	295	26	12
	A2-3	0.26	—	—	—
	A2-4*	0.26	295	32	15
	A2-5	0.72	—	—	—
	A2-6	0.72	—	—	—
	Avg.*: Std. dev.*:			29 4.5	13 2.1
IrO <sub>2</sub> /Au Annealed	A2-1	0.72	—	—	—
	A2-2*	0.72	295	37	17
	A2-3	0.26	—	—	—
	A2-4*	0.26	295	80	36
	A2-5	0.72	—	—	—
	A2-6	0.72	—	—	—
	Avg.*: Std. dev.*:			58 30	26 14



to  $(62 \pm 31) \text{ mA} \cdot \text{W}^{-1}$  with an average quantum efficiency of  $(28 \pm 14) \%$ . The photosensitive areas ( $A_p$ ) were taken to be that of the contact areas ( $A_c$ ) for the spectral characterization of these first two fabrication steps. However, the measurement probe of the optoelectronic characterization system that was positioned on the Schottky contacts would have caused some of the photosensitive area to be shadowed when being irradiated with monochromatic UVR. The actual shadowed area is hard to determine and the large standard deviation (greater than 30 %) in both  $\mathcal{R}_{275}$  and  $\eta_{275}$  are an indication of how the actual irradiated photosensitive area changed.

Once the Au probe contact pads were deposited on A1, the average current responsivity at 275 nm decreased to  $(51 \pm 14) \text{ mA} \cdot \text{W}^{-1}$  with an average quantum efficiency of  $(23 \pm 6.4) \%$  and were similar to that obtained for the as-deposited Ir in Table 5.4. Although this may seem like a step backwards in the fabrication procedure at first, the  $\mathcal{R}_{275}$  and  $\eta_{275}$  values have actually improved. This is because the photosensitive area has also decreased significantly more than what would have been shadowed by the measurement probe during the characterization of the first two fabrication steps, moreover, the standard deviation is smaller as well (less than 30 %).

The average current responsivity at 275 nm of the photodiodes on A2 for the as-deposited Ir was  $(30 \pm 9) \text{ mA} \cdot \text{W}^{-1}$  with an average quantum efficiency of  $(15 \pm 5.0) \%$  (Table 5.5), which was notably less than the values obtained for A1. Furthermore, after annealing the Ir to form IrO<sub>2</sub>, the average current responsivity decreased to  $(25 \pm 16) \text{ mA} \cdot \text{W}^{-1}$  with an average quantum efficiency of  $(11 \pm 7.2) \%$ . The decrease was also evident when considering only A2-2 and A2-4 that were characterized for the majority of the fabrication steps. These results can again be attributed to the inaccurate photosensitive areas, not only caused by the shadowing of the measurement probe, but also by possible

scratches due to the use of the glassine bag.

After the Au probe contact pads were deposited on A2, the average current responsivity at 275 nm increased to  $(29 \pm 4.5) \text{ mA} \cdot \text{W}^{-1}$  with an average quantum efficiency of  $(13 \pm 2.1) \%$  and were again similar to that obtained for the as-deposited Ir in Table 5.5. Once the Au probe contact pads were annealed, the average current responsivity at 275 nm improved further to  $(58 \pm 30) \text{ mA} \cdot \text{W}^{-1}$  with an average quantum efficiency of  $(26 \pm 14) \%$ . However, by considering the Au probe contact pad again that was deposited only partly on top of the IrO<sub>2</sub> contact of A2-4 in Figure 5.3(b), would mean that the actual photosensitive area was larger than what the current responsivity of  $80 \text{ mA} \cdot \text{W}^{-1}$  with quantum efficiency of 36 % were calculated on and is actually expected to be lower. Be that as it may, the trend does hold for A2-2 with a current responsivity of  $37 \text{ mA} \cdot \text{W}^{-1}$  and quantum efficiency of 17 %.

### **Radiation hardness**

Although unexpected improvements in the average current responsivity and quantum efficiency at 275 nm of the He-ion irradiated photodiodes on A1 were observed, these 'improvements' were again attributed to a loss in the as-deposited Au probe contact pads that severely flake off, as was seen in Figure 5.4, causing the irradiated photosensitive areas to be greater than that used in calculating the current responsivity and quantum efficiency.

### **5.3.3 Overall analysis**

The three (smaller) circular 0.65 mm-diameter photodiodes (A1-3, A1-4 and A2-4) displayed similar trends and, therefore, only their electrical and spectral parameters are considered in Tables 5.6 and 5.7, respectively.

In studying the electrical parameters in Table 5.6, it follows that on average the ideality factor improved after annealing the as-deposited Ir from 1.63 to 1.38 for the IrO<sub>2</sub>. With the deposition of the Au probe contact pads on top of the IrO<sub>2</sub> contacts, the ideality factor degraded to 1.57, but was still better than for the as-deposited Ir, provided that the Au did not make direct contact with the AlGaIn surface as with A2-4. The ideality factor was further improved to 1.47 after annealing the Au probe contact pad on A2-4.

The overall SBH increased from 1.34 eV for the as-deposited Ir to 1.52 eV for the IrO<sub>2</sub> and this increase in SBH was also observed by Jeon and Lee [2004:700]. The deposition of the Au probe contact pads on top of the IrO<sub>2</sub> contacts caused the SBH to decrease to 1.19 eV and after being annealed on A2-4 the SBH increased slightly to 1.25 eV.

The average series resistance decreased significantly during the first three fabrications steps. It started off from 1200 Ω for the as-deposited Ir, then decreased to 250 Ω for the IrO<sub>2</sub> and finally the series resistance decreased to 100 Ω after the deposition of the Au probe contact pads. The corresponding standard deviations in the series resistance were at first approx. 25 % for the as-deposited Ir and IrO<sub>2</sub> fabrication steps and finally stabilized to a standard deviation of less than 10 % for the Au probe contact pads. Once the Au probe contact pad was annealed on A2-4, the series resistance decreased to below 90 Ω.

The average reverse leakage current densities measured at 1 V reverse bias increased as the corresponding series resistance decreased during the first three fabrication steps. Even the reverse leakage current density of A2-2 after annealing the Au probe contact pad increased in correspondence with the decrease in series resistance. There were, however, large relative standard deviations because of the significant fluctuations when measuring reverse leakage currents of less than 1 nA.

The fabrication procedure cannot cause a significant change in the free carrier concentration and, hence, the averages obtained for each of the first three fabrication steps were used to calculate an average free carrier concentration of  $(1.4 \pm 0.8) \times 10^{18} \text{ cm}^{-3}$ . Also, by including the free carrier concentration obtained after the fourth fabrication step of A2-4 in Table 5.6, the average free carrier concentration becomes  $(2.0 \pm 0.8) \times 10^{18} \text{ cm}^{-3}$  and, moreover, both of these free carrier concentrations are within the range of that specified for the wafer.

It was observed from the spectral parameters in Table 5.7 that the cut-off wavelength was at approx. 295 nm (4.20 eV), corresponding to the absorption edge of a  $\text{Al}_{0.35}\text{Ga}_{0.65}\text{N}$  semiconductor and, hence, a property of the material and independent of the fabrication procedure. On the other hand, the average current responsivity at 275 nm for the as-deposited Ir decreased from  $(48 \pm 16) \text{ mA} \cdot \text{W}^{-1}$  to  $(40 \pm 27) \text{ mA} \cdot \text{W}^{-1}$  after being annealed to form the more UV transmissive  $\text{IrO}_2$ . With the addition of the Au probe contact pads, the current responsivity improved to  $(52 \pm 17) \text{ mA} \cdot \text{W}^{-1}$ . Although, the Au probe contact pad was deposited only partly on top of the  $\text{IrO}_2$  contact of A2-4 in Figure 5.3(b), a further improvement of the current responsivity was expected after annealing the Au probe contact pad. The corresponding average quantum efficiencies followed the trends of the average current responsivities.

Apart from the free carrier concentration, the effects of the He-ion irradiation on the rest of the electrical and spectral parameters were inconclusive, because of the loss in the as-deposited Au probe contact pads. The free carrier concentration did, however, seem to have decreased by at least 30 % to approx.  $1.0 \times 10^{18} \text{ cm}^{-3}$ .

Table 5.6: The electrical parameters of the three circular 0.65 mm-diameter Schottky photodiodes A1-3, A1-4 and A2-4 that displayed similar electrical trends.

Fabrication step	Photo-diode	$A_c$ [mm <sup>2</sup> ]	$\eta$	$\phi_{B0}$ [eV]	$J_R$ at $-1$ V [nA · cm <sup>-2</sup> ]	$R_S$ [ $\Omega$ ]	$N_d$ [10 <sup>18</sup> cm <sup>-3</sup> ]
As-dep.	A1-3	0.33	1.93	1.40	0.440	1000	1.2
	A1-4	0.33	1.72	1.48	0.040	1100	1.1
	A2-4	0.33	1.23	1.14	0.064	1600	0.94
	Avg.:		1.63	1.34	0.18	1200	1.1
	Std. dev.:		0.36	0.18	0.23	310	0.14
Annealed	A1-3	0.33	1.35	1.62	15	310	1.4
	A1-4	0.33	1.41	1.56	0.0048	230	0.18
	A2-4	0.33	1.38	1.37	0.68	200	1.0
	Avg.:		1.38	1.52	5.2	250	0.87
	Std. dev.:		0.03	0.13	8.4	58	0.62
IrO <sub>2</sub> /Au	A1-3	0.33	1.40	1.05	0.054	100	1.5
	A1-4	0.33	1.70	1.15	150	110	1.3
	A2-4	0.33	1.62	1.36	0.62	92	4.2
	Avg.:		1.57	1.19	49	100	2.3
	Std. dev.:		0.16	0.16	84	7.3	1.6
He <sup>+</sup>	A1-3	0.33	2.21	1.05	0.055	290	1.1
	A1-4	0.33	1.51	1.29	0.11	330	0.82
	Avg.:		1.86	1.17	0.080	310	0.94
	Std. dev.:		0.50	0.17	0.036	32	0.17
IrO <sub>2</sub> /Au Annealed	A2-4	0.33	1.47	1.25	0.85	86	3.9

Table 5.7: The spectral parameters of the three circular 0.65 mm-diameter Schottky photodiodes A1-3, A1-4 and A2-4 that displayed similar spectral trends.

Fabrication step	Photo-diode	$A_p$ [mm <sup>2</sup> ]	$\lambda_{\text{cut-off}}$ [nm]	$\mathcal{R}_{275}$ [mA · W <sup>-1</sup> ]	$\eta_{275}$ [%]
As-dep.	A1-3	0.33	295	65	29
	A1-4	0.33	295	46	21
	A2-4	0.33	295	34	18
	Avg.:			48	23
	Std. dev.:			16	5.7
Annealed	A1-3	0.33	295	70	32
	A1-4	0.33	295	21	9.6
	A2-4	0.33	295	29	13
	Avg.:			40	18
	Std. dev.:			27	12
IrO <sub>2</sub> /Au	A1-3	0.26	295	58	26
	A1-4	0.26	295	65	29
	A2-4	0.26	295	32	15
	Avg.:			52	23
	Std. dev.:			17	7.7
He <sup>+</sup>	A1-3	0.26	295	70	31
	A1-4	0.26	295	59	27
	Avg.:			64	29
	Std. dev.:			7.6	3.4
IrO <sub>2</sub> /Au Annealed	A2-4	0.26	295	80	36

## 5.4 Conclusion

A tuneable front-irradiated **AlGaN**-based solar-blind **UV**-sensitive Schottky photodiode was developed with the deposition of a layered ohmic contact structure on a **AlGaN** semiconductor, followed by a two-step annealing method. Thereafter, a circular **Ir** Schottky contact was deposited and annealed under **O<sub>2</sub>** ambient for a more **UV** transmissive **IrO<sub>2</sub>** Schottky contact. The extracted electrical parameters for the Schottky photodiode included an average ideality factor of  $1.38 \pm 0.03$ , **SBH** of  $1.52 (1 \pm 15 \%)$  eV, reverse leakage current density at 1 V reverse bias of  $(5.2 \pm 8.4) \text{ nA} \cdot \text{cm}^{-2}$  and an average series resistance of  $250 (1 \pm 25 \%) \Omega$ . Spectral parameters included a cut-off wavelength at 295 nm (4.20 eV) that corresponded to the absorption edge of a **Al<sub>0.35</sub>Ga<sub>0.65</sub>N** semiconductor, an average current responsivity at 275 nm of  $(40 \pm 27) \text{ mA} \cdot \text{W}^{-1}$  and a corresponding quantum efficiency of  $(18 \pm 12) \%$ .

The deposition and annealing of a smaller circular **Au** contact on top of the **IrO<sub>2</sub>** contact reduced the contact resistance, provided that the **Au** did not make direct contact with the **AlGaN** surface. Electrical parameters included an average ideality factor of  $1.42 \pm 0.07$ , **SBH** of  $1.33 (1 \pm 10 \%)$  eV, reverse leakage current density at 1 V reverse bias of  $(3.3 \pm 3.4) \text{ nA} \cdot \text{cm}^{-2}$  and an average series resistance of  $66 (1 \pm 45 \%) \Omega$ . The spectral parameters included an average current responsivity at 275 nm of  $(58 \pm 30) \text{ mA} \cdot \text{W}^{-1}$  and a corresponding quantum efficiency of  $(26 \pm 14) \%$ .

## 5.5 Publication

The results obtained from the optoelectronic characterization of each of the first three fabrication steps are covered in the publication which has been included in

Appendix E. These fabrication steps included the as-deposited Ir Schottky contacts, followed by the annealing of Ir to form IrO<sub>2</sub> and then the deposition of the Au probe contact pads on top of the IrO<sub>2</sub> contacts. Only the optoelectronic characterization after the fourth fabrication step, being the annealing of the Au probe contact pad on the IrO<sub>2</sub> contact, was excluded from the publication because of limited space. The publication did, however, also include the results of the investigation into the radiation hardness.

The  $I-V$  and spectral characteristics of the fabricated Schottky photodiode A1-4 in Figure 5.2 was selected as a typical example to show the trends observed graphically in Figures 5.5 and 5.6. In Figure 5.5, the circled data points were negative current readings obtained during forward bias measurements that were made positive by the NI LabVIEW routine in order to perform logarithmic calculations. Tables 5.8 and 5.9 were constructed from the relevant average values of the electrical and spectral parameters in Tables 5.6 and 5.7, respectively. Figures 5.5 and 5.6 together with Table 5.8 were presented and discussed in the publication in Appendix E.



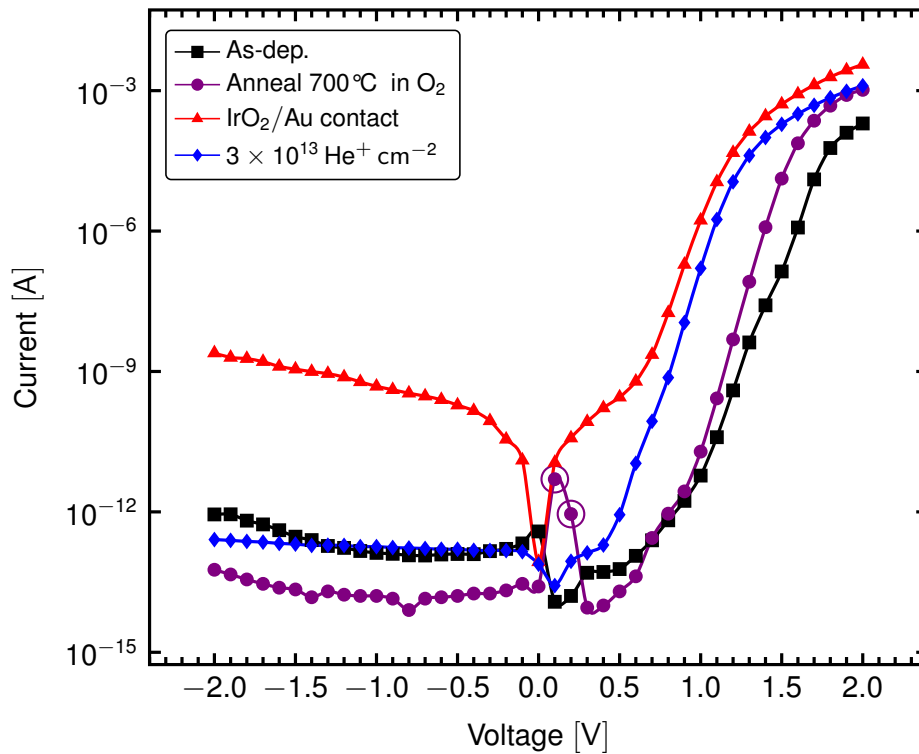


Figure 5.5:  $I$ - $V$  characteristics of the Ir Schottky photodiode for each of the fabrication steps and after 5.4 MeV He-ion irradiation. Circled data points were negative current readings obtained during forward bias measurements. Reprinted from van Schalkwyk *et al.* [2012:1530], Copyright (2011), with permission from Elsevier.

Table 5.8: Average ideality factor, SBH, reverse leakage current density and series resistance of the Ir Schottky photodiodes for each of the fabrication steps and after He-ion irradiation. Adapted from van Schalkwyk *et al.* [2012:1530], Copyright (2011), with permission from Elsevier.

Fabrication step	$\eta$	$\phi_{B0} \pm 15\%$ [eV]	$J_R$ at $-1$ V [nA · cm <sup>-2</sup> ]	$R_S \pm 25\%$ [ $\Omega$ ]	$N_d$ [10 <sup>18</sup> cm <sup>-3</sup> ]
As-dep.	1.63	1.34	0.18 ± 0.23	1200	1.1
Annealed	1.38	1.52	5.2 ± 8.4	250	0.87
IrO <sub>2</sub> /Au	1.57	1.19	49 ± 84	100	2.3
He <sup>+</sup>	1.86	1.17	0.080 ± 0.036	310	0.94

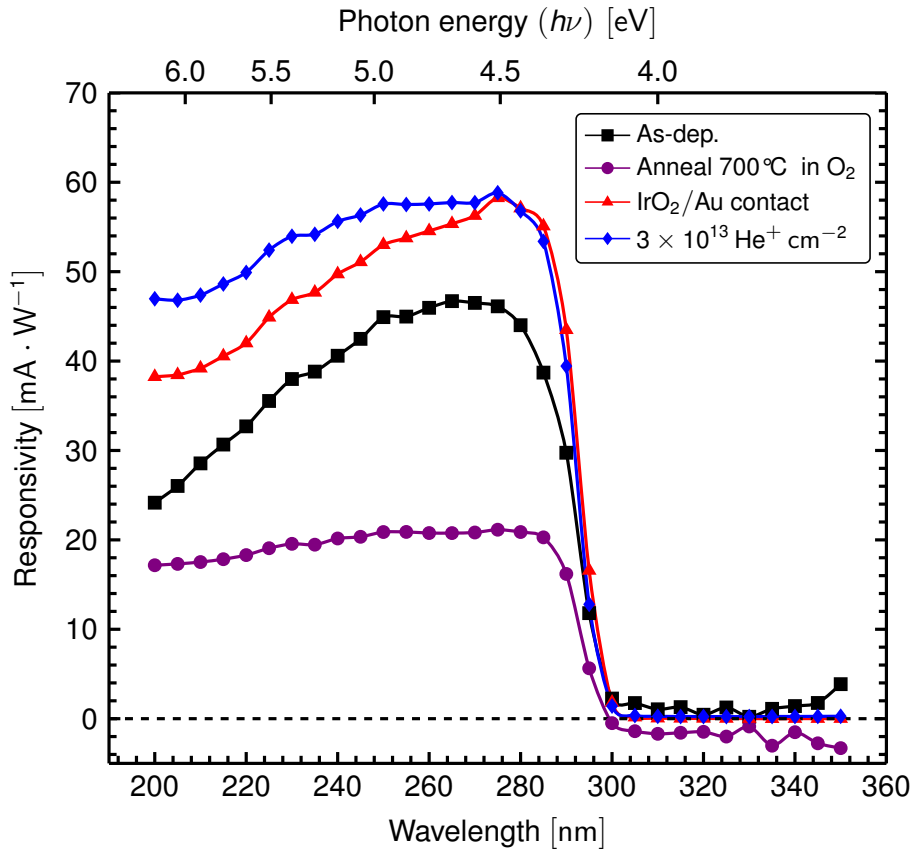


Figure 5.6: Spectral responsivities of the Ir Schottky photodiode for each of the fabrication steps and after 5.4 MeV He-ion irradiation at zero biasing. Adapted from van Schalkwyk *et al.* [2012:1531], Copyright (2011), with permission from Elsevier.

Table 5.9: The average spectral parameters that included the cut-off wavelength ( $\lambda_{\text{cut-off}}$ ), current responsivity ( $\mathcal{R}_{275}$ ) and quantum efficiency ( $\eta_{275}$ ) at 275 nm.

Fabrication step	$\lambda_{\text{cut-off}}$ [nm]	$\mathcal{R}_{275}$ [mA · W <sup>-1</sup> ]	$\eta_{275}$ [%]
As-dep.	295	48	23
Annealed	295	40	18
IrO <sub>2</sub> /Au	295	52	23
He <sup>+</sup>	295	64	29

## Chapter 6

# The four-quadrant detector

### 6.1 Introduction

This part of the study aimed at developing and characterizing two tuneable front-irradiated AlGaIn-based UV-sensitive *four-quadrant* detectors. Moreover, through additional literature the metallization techniques for the fabrication of optimized ohmic contacts and UV transmissive Schottky contacts were realized. The four-quadrant detectors were fabricated with the use of three different stainless steel masks that defined the ohmic contacts, Schottky contacts and probe contact pads, respectively, on  $(3 \times 5)$  mm<sup>2</sup> samples taken from the AlGaIn semiconductor wafers. Using stainless steel masks allowed for the demonstration of a four-quadrant detector without the need for photomasks, however, photolithography techniques would be needed for commercial production. The previous chapter established that the Schottky photodiode fabrication procedure comprised of at least six steps, (1) the deposition of a layered ohmic contact structure, (2) the annealing of the ohmic contact, (3) the deposition of the Ir Schottky contact, (4) the annealing of the Ir to form the more UV transmissive IrO<sub>2</sub> Schottky contact, (5) the deposition of the Au probe contact pad and (6) the annealing thereof.

The first four-quadrant detector was optoelectronically characterized only after the fabrication procedure was completed and the electrical and spectral parameters were then investigated and compared to that found in the previous chapter. The first four-quadrant detector was, however, an intrinsically visible-blind UV-sensitive detector that displayed proper characteristics. Therefore, a second four-quadrant detector was fabricated on an AlGa<sub>N</sub> semiconductor with a high Al mole fraction specification and mounted onto a commercial microchip carrier, wire bonded and optoelectronically characterized. The second four-quadrant detector was an intrinsically solar-blind UV-sensitive detector and, therefore, used to demonstrate a solar-blind UV-sensitive electro-optic device.

## 6.2 Experimental

### 6.2.1 The AlGa<sub>N</sub> semiconductor wafer

The research study was conducted on samples taken from two different wafers that were also custom grown by TDI, using the HVPE growth method. The 7LS3205-3 wafer consisted of a single epitaxial layer, while the 7LS3825-2 wafer consisted of a four layer epitaxial structure. Each of them were grown on a 25.4 mm-diameter single side polished C-plane Al<sub>2</sub>O<sub>3</sub> substrate and were mechanically diced into smaller (3.0 × 5.0) mm<sup>2</sup> sample sizes. Two samples, referred to as B1 and B2, were taken from wafers 7LS3205-3 and 7LS3825-2, respectively, for the fabrication of a four-quadrant detector on each of them.

The top layer of the 7LS3205-3 wafer was AlGa<sub>N</sub>:Si with a free carrier concentration of less than  $1.0 \times 10^{18} \text{ cm}^{-3}$ . The Al mole fraction varied from (11 to 40) % and the layer thickness was approx. 1.0 μm.

The first layer of the 7LS3825-2 wafer was undoped Ga<sub>N</sub> with a thickness of (0.6 to 1.0) μm, followed by a (1.0 to 1.5) μm-thick layer of Ga<sub>N</sub>:Si with a free

Table 6.1: The four layer epitaxial structure specifications of the 7LS3825-2 AlGa<sub>N</sub> semiconductor wafer.

Layer	Material	Thickness [ $\mu\text{m}$ ]	Al [%]
1	GaN	$0.80 \pm 0.20$	0
2	GaN:Si	$1.25 \pm 0.25$	0
3	AlGa <sub>N</sub> :Si	$0.20 \pm 0.05$	$38.0 \pm 2.0$
4 (top)	AlGa <sub>N</sub>	$0.95 \pm 0.05$	$42.5 \pm 2.5$

carrier concentration of  $(1.0 \text{ to } 3.0) \times 10^{18} \text{ cm}^{-3}$ . The third layer was AlGa<sub>N</sub>:Si with an Al mole fraction varying from (36 to 40) % and a thickness of (0.15 to 0.25)  $\mu\text{m}$ . The fourth top layer was undoped AlGa<sub>N</sub> with a thickness of (0.9 to 1.0)  $\mu\text{m}$  and an Al mole fraction varying from (40 to 45) %. Table 6.1 provides the specifications of the 7LS3825-2 wafer.

## 6.2.2 Contact deposition masks

The envisioned layout of the four-quadrant detector is schematically illustrated in Figure 6.1. Fabrication of a four-quadrant detector required performing depositions through three different masks. One defining the ohmic contacts, one the Schottky contacts and one the probe contact pads. The present author designed three such masks and their drawings are in Appendix D on a scale of 100:1. The final layout of the metal contacts forming the four-quadrant detector are on the top of page D-2 in Appendix D. These masks were laser-cut from a 0.13 mm-thick stainless steel plate by Micro Etch CC in Johannesburg.

Two large 0.80 mm-diameter holes were made on either side of each of the three masks forming the four-quadrant detector. Deposition through them allowed for the alignment of the following mask under a stereo microscope for the deposition of the next set of contacts. The first contacts, being the ohmic contacts, were

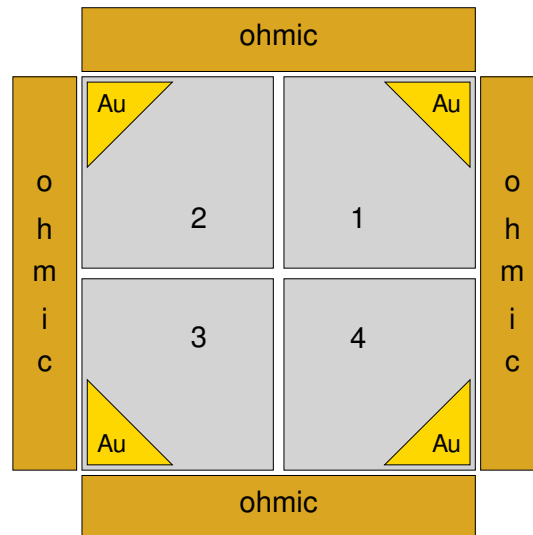


Figure 6.1: Schematic illustration of the deposited metal contacts forming the envisioned layout for the front-irradiated four-quadrant detector. Adapted from [van Schalkwyk \*et al.\* \[2014:94\]](#), Copyright (2013), with permission from Elsevier.

deposited using the mask design on the bottom of page D–2 in Appendix D. The Schottky contacts and probe contact pads were done using the layouts on the top and bottom of page D–3 in Appendix D, respectively.

### 6.2.3 Ohmic contact fabrication

The structure and multi-step annealing process used for the fabrication of the ohmic contacts were developed after studying the research done by [Jacobs \*et al.\* \[2002\]](#) and [Feng \*et al.\* \[2009\]](#). An optimization study of the Ti/Al/Ni/Au ohmic contact metallization scheme was done by [Jacobs \*et al.\* \[2002\]](#). They used the circular transfer length method (CTLM) to determine the contact and specific contact resistances. They found that the Ti/Al thickness ratio should be 1:6 with Ti having an optimized thickness of 300 Å. To prevent the oxidation of the Ti and Al, Au was considered as a capping layer, however, Au and Al form highly resistive alloys at temperatures above 250 °C, such as the compound AuAl<sub>2</sub> referred to as the

'purple plague' [Jacobs *et al.*, 2002:17; Philofsky, 1970:1398]. Therefore, Ni was used to form a diffusion barrier to prevent the formation of these highly resistive Au-Al-alloys [Jacobs *et al.*, 2002:17]. Jacobs *et al.* [2002:18] concluded that the lowest contact ( $1.3 \Omega \cdot \text{mm}$ ) and specific contact ( $27 \mu\Omega \cdot \text{cm}^2$ ) resistances were obtained for an ohmic contact consisting of a Ti/Al (300/1800 Å) bilayer with a 400 Å-thick Ni diffusion barrier layer between it and a 1500 Å-thick Au capping layer, which then undergone a one-step RTA process at 900°C for 30 s under N<sub>2</sub>. Feng *et al.* [2009] found that, a Ti/Al/Ni/Au (200/900/550/450 Å) ohmic contact improved by applying a multi-step annealing method under N<sub>2</sub> ambient. They increased the temperature to 400°C and annealed for three minutes, then to 700°C for 20 s and finally to 830°C for 30 s. It was suggested that, annealing at 400°C for such a long time allows the substrate to uniformly reach 400°C and also eliminates contamination and oxide layer effects. Annealing at 700°C promotes the diffusion of Al to the AlGa<sub>0.5</sub>N film, where Ti, Al and AlGa<sub>0.5</sub>N/GaN can preliminarily react. The last high temperature annealing at 830°C reduced the specific contact resistance to between (3.0 and 4.0)  $\mu\Omega \cdot \text{cm}^2$ , without degrading the contact morphology.

The optimized metallization scheme proposed by Jacobs *et al.* [2002] was used and layered ohmic structures of Ti/Al/Ni/Au (300/1800/400/1500 Å) were deposited through the first contact mask in an EBPVD system under a pressure of less than  $10^{-5}$  mbar. Thereafter, the ohmic contacts were multi-step annealed under Ar ambient, similarly to that proposed by Feng *et al.* [2009]. The samples were first annealed at 400°C for three minutes, then at 700°C for 20 s, followed by annealing at 830°C for 30 s and lastly at 900°C for 30 s [van Schalkwyk *et al.*, 2014:94].

## 6.2.4 Schottky contact fabrication

After the fabrication of the ohmic contacts, the second mask defining the Schottky contacts was aligned, using the two large 0.80 mm-diameter contacts and the holes in the mask. Four square ( $0.90 \times 0.90$ ) mm<sup>2</sup> Ir contacts were deposited at  $0.5 \text{ \AA} \cdot \text{s}^{-1}$  in the EBPVD system under a pressure of less than  $10^{-5}$  mbar. The Ir Schottky contacts were 100 Å- and 50 Å-thick on B1 and B2, respectively.

An optimized two-step annealing process for the Schottky contacts was developed after studying the research done by *Kawar et al. [2003]*. They identified the formation of the intermediate semiconducting Ir<sub>2</sub>O<sub>3</sub> phase between 250 °C and 600 °C. Above 600 °C the metallic IrO<sub>2</sub> phase was formed and remained stable up to 700 °C. Upward from 800 °C, the IrO<sub>2</sub> transformed to IrO, because of oxygen loss. Therefore, the Schottky contacts were two-step annealed under O<sub>2</sub> ambient flowing at a rate of  $3 \text{ L} \cdot \text{min}^{-1}$  for 30 minutes at both 600 °C and 730 °C to allow for the formation of the more UV transmissive IrO<sub>2</sub> Schottky contacts [*van Schalkwyk et al., 2014:94*].

## 6.2.5 Probe contact pad fabrication

Once the ohmic and Schottky contacts were fabricated, the final mask that defined the Au probe contact pads were aligned. Four  $0.80 \times 10^{-3} \text{ cm}^2$ , 1500 Å-thick triangular Au contacts were deposited at  $1.0 \text{ \AA} \cdot \text{s}^{-1}$  on top of the outer-most corners of the square IrO<sub>2</sub> Schottky contacts in a resistive evaporation system under a pressure of approx.  $10^{-5}$  mbar. Thereafter, the Au probe contact pads were annealed under O<sub>2</sub> ambient at a flow rate of  $3 \text{ L} \cdot \text{min}^{-1}$  for ten minutes at 500 °C. Figure 6.2 is a photograph taken of the completed four-quadrant detector on B1 taken from wafer 7LS3205-3. The two large 0.80 mm-diameter contacts on either side of the four-quadrant detector were deposited through the alignment



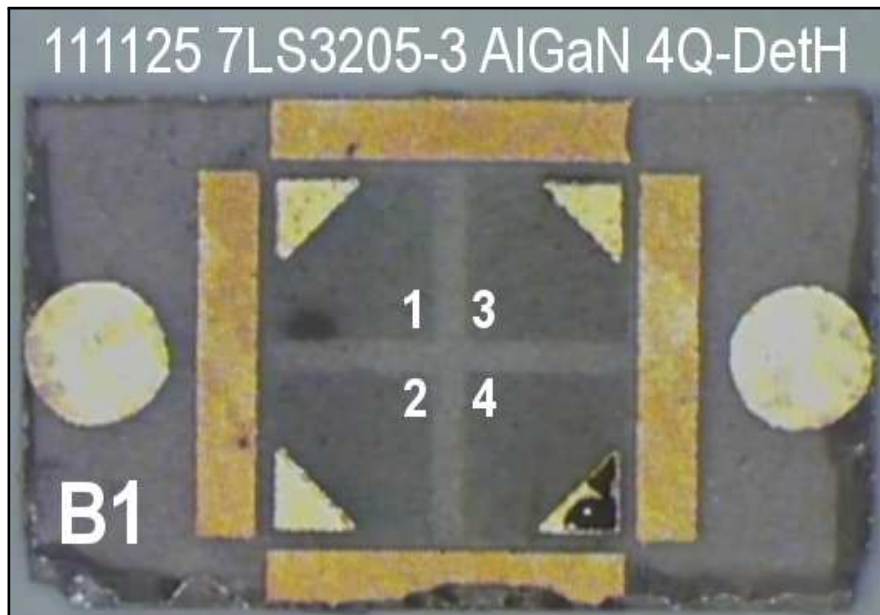


Figure 6.2: Photograph of the first four-quadrant detector fabricated on B1 taken from wafer 7LS3205-3. The two large 0.80 mm-diameter contacts on either side of the four-quadrant detector were used for alignment of the masks. The four outer strips are the multi-step annealed, layered ohmic structures of  $\text{Ti}/\text{Al}/\text{Ni}/\text{Au}$  (300/1800/400/1500 Å), which were annealed under  $\text{Ar}$  ambient for three minutes at 400 °C, 20 s at 700 °C, 30 s at 830 °C and 30 s at 900 °C. Thereafter, four square ( $0.90 \times 0.90$ ) mm<sup>2</sup>, 100 Å-thick  $\text{Ir}$  Schottky contacts were deposited and two-step annealed under  $\text{O}_2$  ambient for 30 minutes at both 600 °C and 730 °C to form the more UV transmissive  $\text{IrO}_2$ . Lastly, four  $0.80 \times 10^{-3}$  cm<sup>2</sup>, 1500 Å-thick triangular  $\text{Au}$  probe contact pads were deposited on top of the outer-most corners of the square  $\text{IrO}_2$  contacts and annealed under  $\text{O}_2$  ambient at 500 °C for ten minutes. The final photosensitive area of each quadrant was  $7.3 \times 10^{-3}$  cm<sup>2</sup>.

holes in each of the deposition masks. The four-quadrant detector fabricated on B2 taken from wafer 7LS3825-2 looked similar. However, the 50 Å-thick UV transmissive  $\text{IrO}_2$  Schottky contacts on B2 were much less visible compared to the 100 Å-thick  $\text{IrO}_2$  contacts on B1.

### 6.2.6 Epoxy wire bonding

The SST competence area of the CSIR MSM unit wanted to mount a four-quadrant detector in a housing integrated with electronics and UV optics to

demonstrate a working solar-blind UV-sensitive electro-optic device. To complete this joint initiative, the four-quadrant detector fabricated on B2 was mounted onto a commercial microchip carrier (Winslow W9513). Then, Al wires were epoxy bonded from the ohmic contacts and Au probe contact pads to the carrier strips using EPO-TEK H20E silver-filled epoxy.

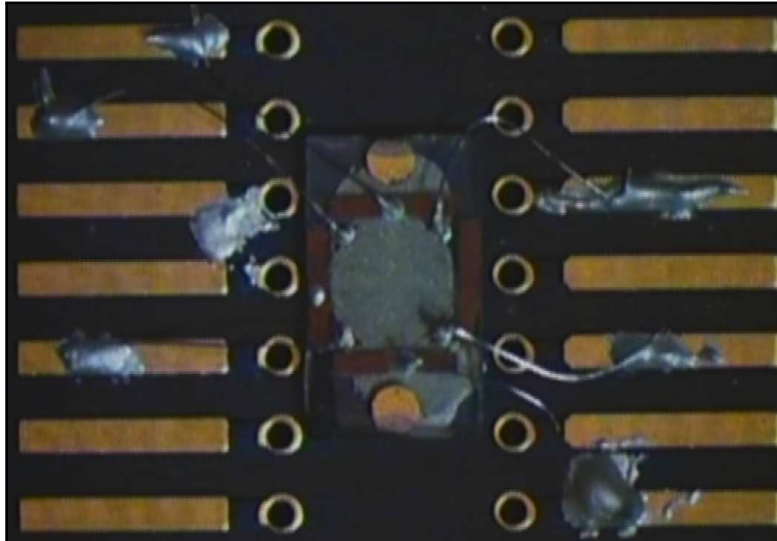
A basic set-up was put together and designed to help control the positioning, placing and holding of a wire on top of either an ohmic or Au contact pad, while the epoxy cured. The set-up was, however, limited in controlling the positioning of the wire to where it had to be fixed on a strip of the microchip carrier. Therefore, after the epoxy cured on a contact, the wire was allowed to bend as it wished and then epoxied to the nearest strip on which the wire came to rest. Figure 6.3(a) is a photograph of the end result of the wire-bonding process on the microchip carrier. Figure 6.3(b) is a photograph done with a different lighting technique and a closer view of the four-quadrant detector, rotated 90° clockwise with respect to Figure 6.3(a).

## 6.2.7 Optoelectronic characterization

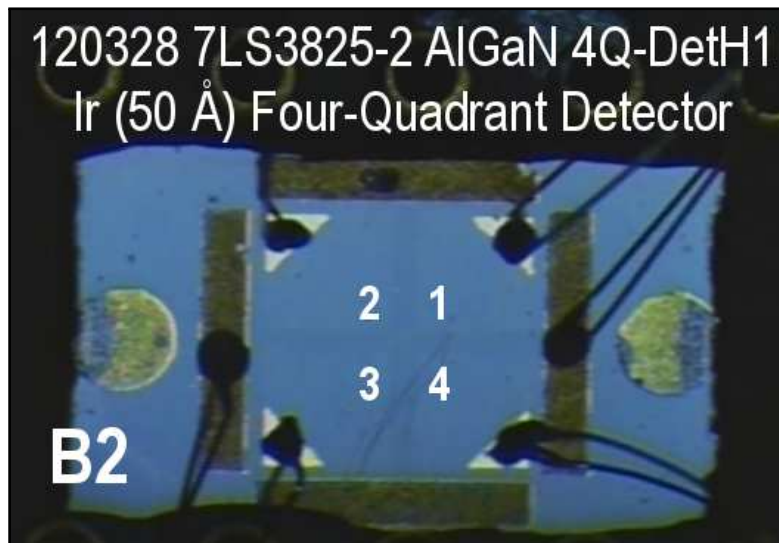
Optoelectronic characterization of the two four-quadrant detectors was performed in the same way as discussed in subsection 5.2.9 of Chapter 5.

### Electrical characterization

The four-quadrant detector fabricated on B1 was directly characterized, while the one on B2 was characterized on the commercial microchip carrier with the completed wire-bonding. Measurements were performed on each quadrant of the four-quadrant detectors with the Schottky contacts having contact areas of  $8.1 \times 10^{-3} \text{ cm}^2$ . The measurements on B2 were made by placing the probes



(a) Wires were bonded by starting from either an ohmic contact or Au probe contact pad and then bonded to a strip on the microchip carrier.



(b) A closer view of the four-quadrant detector using a different lighting technique and rotated 90° clockwise with respect to Figure 6.3(a) above.

Figure 6.3: Photographs of the second four-quadrant detector fabricated on B2 taken from wafer 7LS3825-2, after being mounted onto the commercial microchip carrier and epoxy wire-bonded. The four outer strips are the multi-step annealed, layered ohmic structures of  $\text{Ti}/\text{Al}/\text{Ni}/\text{Au}$  (300/1800/400/1500 Å). The four square (0.90 × 0.90) mm<sup>2</sup>, 50 Å-thick UV transmissive  $\text{IrO}_2$  Schottky contacts are barely visible. On top of the outer-most corners of the square  $\text{IrO}_2$  contacts, the four 0.80 × 10<sup>-3</sup> cm<sup>2</sup>, 1500 Å-thick triangular Au probe contact pads were deposited and annealed. Each quadrant had a final photosensitive area of 7.3 × 10<sup>-3</sup> cm<sup>2</sup>.

on the strips of the microchip carrier. Pairs of strips were selected such that measurements were taken between ohmic and Au probe contact pads that were the nearest to one another.

### **Spectral characterization**

Spectral characterization was again performed after calibrating the monochromatic EMR that exits the fibre end, while using either the deuterium or tungsten-halogen lamp. The tungsten-halogen lamp was also switched on for at least 30 minutes prior to a characterization procedure, allowing the lamp to warm-up and stabilize.

The tungsten-halogen lamp was used as the VIS-to-NIR radiation source to specifically investigate the UV-to-VIS/NIR rejection ratios. The tungsten-halogen lamp power supply was set to operate with a current of 3.50 A. Although the calibration of the lamp was not required to calculate the UV-to-VIS/NIR rejection ratios, the NI LabVIEW routine recorded a calibrated VIS-to-NIR spectral irradiance for the 400 nm to 1100 nm range in 5 nm, similarly to what was done for the UVR source, as a check to see that the photodiode would be irradiated properly. A corresponding dark current density  $J_d$  measurement was taken at each one of the wavelengths ranging from 400 nm to 1100 nm in 5 nm increments for each quadrant of a four-quadrant detector. Thereafter, one of the quadrants of a four-quadrant detector was irradiated and the PCD  $J_p(\lambda_i)$  recorded while the photodiode was being irradiated with an unwanted wavelength  $\lambda_i$ . Using Eq. 3.63 in subsection 3.4.2, the dark current density measurement that corresponded with a measured PCD was subtracted and the rejection ratios calculated with respect to the average PCD  $J_p(\lambda_s)$  that was measured at a desired specified wavelength  $\lambda_s$  over the four quadrants.

Spectral measurements were performed on each quadrant of the four-quadrant detectors with the Schottky contacts having photosensitive areas of  $7.3 \times 10^{-3} \text{ cm}^2$ , after subtracting the opaque  $0.80 \times 10^{-3} \text{ cm}^2$  triangular Au probe contact pad areas.

## 6.3 Results and discussion

This section covers the results obtained through the optoelectronic characterization process of the two four-quadrant detectors by measuring all eight of the Schottky photodiode quadrants.

### 6.3.1 Electrical Characterization

The  $I-V$  characteristics of each quadrant of the two fabricated four-quadrant detectors are presented in Figures 6.4 and 6.5 together with their extracted electrical parameters in Tables 6.2 and 6.3, respectively.

#### The ideality factor

Three of the quadrants of the first four-quadrant detector that was fabricated on B1 had ideality factors below the value of 2 and one with an ideality factor of 2.65, as seen in Table 6.2. The ideality factors of 1.73 and 1.57 for quadrants B1-2 and B1-3, respectively, were slightly higher than the value of 1.47 for the single photodiode A2-4 in Table 5.6 after it had undergone the same fabrication procedure in the previous chapter. The slightly higher ideality factors could be attributed to the larger square ( $0.90 \times 0.90$ ) mm<sup>2</sup>, 100 Å-thick IrO<sub>2</sub> Schottky contacts compared to the circular 0.65 mm-diameter 50 Å-thick IrO<sub>2</sub> Schottky contacts, because larger contacts would have a higher probability of isolated surface effects degrading the contact quality. Furthermore, in Figure 6.2 it was noticed that there was a dark

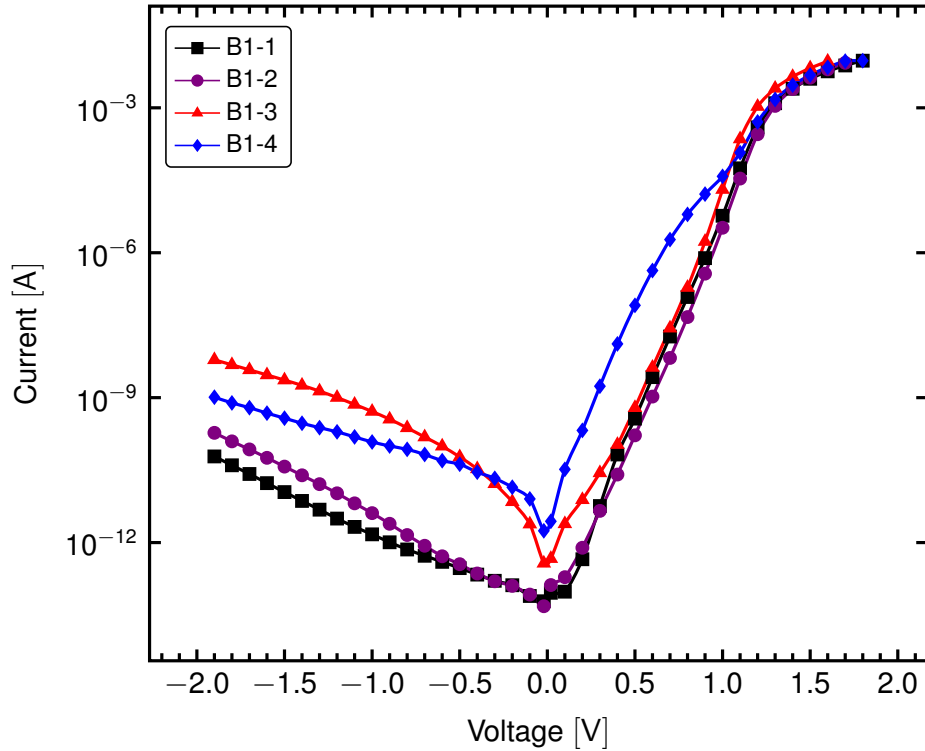


Figure 6.4: The  $I$ - $V$  characteristics for each quadrant of the first developed front-irradiated AlGaIn-based visible-blind UV-sensitive four-quadrant detector that was fabricated on B1 taken from 7LS3205-3.

Table 6.2: The electrical parameters of the first developed front-irradiated AlGaIn-based visible-blind UV-sensitive four-quadrant detector that was fabricated on B1 taken from 7LS3205-3. The parameters included the ideality factor ( $\eta$ ), SBH ( $\phi_{B0}$ ), reverse leakage current density ( $J_R$ ) at 1 V reverse bias, series resistance ( $R_S$ ) and the free carrier concentration ( $N_d$ ) together with the overall averages.

Quadrant	$\eta$	$\phi_B$ [eV]	$J_R$ at $-1$ V [nA $\cdot$ cm $^{-2}$ ]	$R_S$ [ $\Omega$ ]	$N_d$ [ $10^{18}$ cm $^{-3}$ ]
B1-1	1.82	1.11	0.18	50	1.0
B1-2	1.73	1.15	0.50	39	0.91
B1-3	1.57	1.16	64	37	1.0
B1-4	2.65	0.89	15	35	1.0
Avg.:	1.94	1.08	20	40	0.95
Std. dev.:	0.48	0.13	30	6.2	0.03

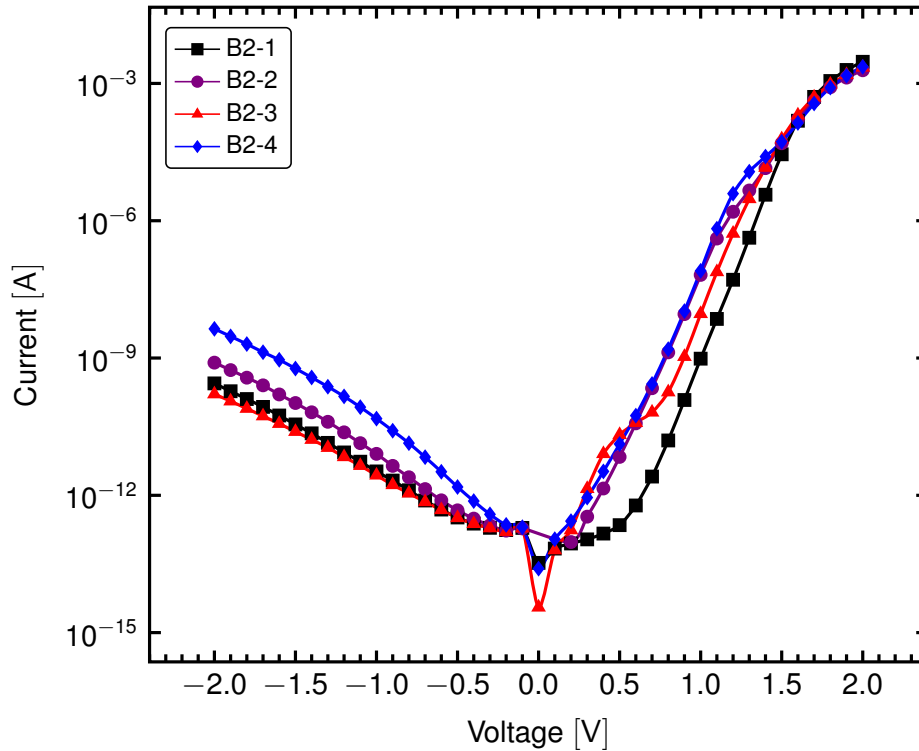


Figure 6.5: The  $I$ - $V$  characteristics for each quadrant of the second developed front-irradiated AlGaIn-based solar-blind UV-sensitive four-quadrant detector that was fabricated on B2 taken from 7LS3825-2. Adapted from van Schalkwyk *et al.* [2014:94], Copyright (2013), with permission from Elsevier.

Table 6.3: The electrical parameters of the second developed front-irradiated AlGaIn-based solar-blind UV-sensitive four-quadrant detector that was fabricated on B2 taken from 7LS3825-2. The parameters included the ideality factor ( $\eta$ ), SBH ( $\phi_{B0}$ ), reverse leakage current density ( $J_R$ ) at 1 V reverse bias, series resistance ( $R_S$ ) and the free carrier concentration ( $N_d$ ) together with the overall averages. Adapted from van Schalkwyk *et al.* [2014:94], Copyright (2013), with permission from Elsevier.

Quadrant	$\eta$	$\phi_{B0}$ [eV]	$J_R$ at $-1$ V [nA $\cdot$ cm $^{-2}$ ]	$R_S$ [ $\Omega$ ]	$N_d$ [ $10^{18}$ cm $^{-3}$ ]
B2-1	1.92	1.30	0.46	90	2.0
B2-2	2.09	1.15	1.1	150	1.7
B2-3	1.91	1.24	0.38	140	1.3
B2-4	1.95	1.18	6.5	110	1.5
Avg.:	1.97	1.22	2.1	120	1.6
Std. dev.:	0.09	0.08	3.3	30	0.3

spot present on B1-1 and that the surface of the triangular Au probe contact pad on B1-4 appeared differently to the rest of the probe contact pads. These unexplained anomalies could have contributed to the higher ideality factors of 1.82 for B1-1 and 2.65 for B1-4 in Table 6.2.

The ideality factors for the four square ( $0.90 \times 0.90$ ) mm<sup>2</sup>, 50 Å-thick IrO<sub>2</sub> Schottky contacts listed in Table 6.3 of the second four-quadrant detector that was fabricated on B2 were all greater than 1.9 with an average ideality factor of 1.97. Although each quadrant displayed good rectifying  $I-V$  characteristics as seen in Figure 6.5, their ideality factors were greater than the majority of the ideality factors obtained thus far. These large ideality factors could be a result of the wire bonding process in that the silver-filled epoxy were not completely isolated to the ohmic contact or Au probe contact pads and under a microscope it was observed that some portions of the epoxy did make direct contact to the AlGaIn surface. However, the standard deviation of the ideality factors was better than expected at less than 5 %.

Apart from the larger IrO<sub>2</sub> Schottky contacts and the wire bonding process that could have contributed to the higher ideality factors, a more likely cause could have been the fact that the Au probe contact pads on the two four-quadrant detectors were annealed for ten minutes at 500 °C and not at 350 °C as was done in the previous chapter.

### **The Schottky barrier height**

The SBHs of 1.11 eV, 1.15 eV and 1.16 eV for quadrants B1-1, B1-2 and B1-3 in Table 6.2, respectively, were at the most 12 % lower than the 1.25 eV SBH obtained for the single photodiode A2-4 in Table 5.6. On the other hand, in Table 6.3 the average SBH for B2 was 1.22 eV with a standard deviation of less than 7 % and in the range of the 1.25 eV SBH obtained for A2-4.



### **The reverse leakage current density at 1 V reverse bias**

The average reverse leakage current density at 1 V reverse bias was calculated to be  $20 \text{ nA} \cdot \text{cm}^{-2}$  with a relatively large relative standard deviation (Table 6.2), similar to what was found in the previous chapter and could again be a result of the significant fluctuations when measuring reverse leakage currents of less than 1 nA. However, the reverse leakage current densities at 1 V reverse bias of  $0.18 \text{ nA} \cdot \text{cm}^{-2}$  for B1-1 and  $0.50 \text{ nA} \cdot \text{cm}^{-2}$  for B1-2 improved and were both lower than the  $0.85 \text{ nA} \cdot \text{cm}^{-2}$  for the single photodiode A2-4 in Table 5.6.

In Table 6.3 the reverse leakage current densities that were measured at 1 V reverse bias on each for the quadrants of B2 were well below  $10 \text{ nA} \cdot \text{cm}^{-2}$  with an average of  $(2.1 \pm 3.3) \text{ nA} \cdot \text{cm}^{-2}$ . The small reverse leakage current densities could be attributed to either the use of an optimized layered ohmic structure together with an improved multi-step annealing method, the proper formation of  $\text{IrO}_2$  through the two-step annealing method at appropriate temperatures or by annealing the Au probe contact pads [van Schalkwyk *et al.*, 2014:94–95].

### **The series resistance**

The average series resistance for B1 in Table 6.2 was  $40 \Omega$  and improved by more than 50 % compared to the  $86 \Omega$  that was measured for the single photodiode A2-4 in Table 5.6. However, two factors may have contributed to this comparably higher series resistance measured for A2-4, one being the distance between the ohmic contact and Schottky contact, which was much greater than that between the ohmic contact and either of the Schottky contacts of the four-quadrant detector, as seen A2-4 in Figure 5.3(b). The second factor was that a significant area of the Au probe contact pad that was deposited on A2-4 made direct contact with the AlGaIn surface. Because the Au made direct contact with the top

layer of the  $\text{AlGaIn}$  semiconductor that had an approx. 38 %  $\text{Al}$  mole fraction content could have formed traces of the highly resistive  $\text{Au-Al}$ -alloys at the interface while being annealed at  $350^\circ\text{C}$ , which was well above the  $250^\circ\text{C}$  as discussed in subsection 6.2.3 previously in this chapter. Therefore, a better comparison is the single photodiode A2-2 in Figure 5.3(b) that had a series resistance of  $46\ \Omega$  in Table 5.3, which was closer to the ohmic contact and with the  $\text{Au}$  probe contact pad properly deposited on top of the 1.0 mm-diameter 50 Å-thick  $\text{IrO}_2$  Schottky contact.

The average resistance for B2 in Table 6.3 was  $120\ \Omega$  with a standard deviation of 25 %. This higher series resistance is likely due to the addition of the silver-filled epoxy and  $\text{Al}$  wires that were used in the wire-bonding process.

### **The free carrier concentration**

An average free carrier concentration of  $(0.95 \pm 0.03) \times 10^{18}\ \text{cm}^{-3}$  was determined from the  $C-V$  measurements for B1 in Table 6.2 and at the most 10 % less than the  $1.0 \times 10^{18}\ \text{cm}^{-3}$  specified for the single  $\text{AlGaIn:Si}$  layer of the 7LS3205-3 wafer.

The average free carrier concentration was  $(1.6 \pm 0.3) \times 10^{18}\ \text{cm}^{-3}$  for B2 in Table 6.3 and was well within the  $(1.0\ \text{to}\ 3.0) \times 10^{18}\ \text{cm}^{-3}$  range that was specified for the 7LS3825-2 wafer.

## **6.3.2 Spectral Characterization**

The spectral responsivities of each quadrant of the two four-quadrant detectors are presented in Figures 6.6 and 6.7 together with their extracted spectral parameters in Tables 6.4 and 6.5, respectively.

### **The cut-off wavelength**

A cut-off wavelength for the first four-quadrant detector that was fabricated on B1 was established at approx. 335 nm and corresponded to 3.70 eV by Eq. 2.1, as seen in Figure 6.6 and Table 6.4. The cut-off wavelength was chosen at the current responsivity that dropped to less than 50 % the maximum current responsivity that was at 320 nm. Using Eq. 3.3 and solving for the Al mole fraction, a mole fraction of 13 % was found for this particular (3.0 × 5.0) mm<sup>2</sup> sample from the 7LS3205-3 wafer that had a (11 to 40) % Al mole fraction specification.

The quadrants of the second four-quadrant detector that were fabricated on B2 had a cut-off wavelength at approx. 275 nm that corresponded to 4.51 eV by Eq. 2.1, as seen in Figure 6.7 and Table 6.5. Here, the cut-off wavelength was chosen as the wavelength at which the current responsivity has dropped to less than 50 % of the current responsivity at 250 nm. Using Eq. 3.3 and solving for the Al mole fraction again, a mole fraction of 46 % was found and corresponded reasonably well with the absorption edge of the 7LS3825-2 wafer that had a (40 to 45) % Al mole fraction specification.

### **The current responsivity and quantum efficiency**

The quadrant B1-1 had a significantly lower spectral current responsivity in comparison with the other three quadrants and was probably due to the dark spot present on B1-1 in Figure 6.2. The dark spot may for one have been 100 Å-thick Ir that for some reason did not properly form IrO<sub>2</sub> and, hence, the photosensitive area was actually smaller than the 7.3 × 10<sup>-3</sup> cm<sup>2</sup> for which the current responsivity was calculated for. However, the average current responsivity at 320 nm for B1 was (25 ± 9.0) mA · W<sup>-1</sup> with an average quantum efficiency of (9.6 ± 5.5) %. When excluding B1-1 from the averages, the average current responsivity was

then  $(29 \pm 2.6) \text{ mA} \cdot \text{W}^{-1}$  with an average quantum efficiency of  $(11 \pm 1.0) \%$ .

The average current responsivity at 250 nm for B2 was  $(28 \pm 1.0) \text{ mA} \cdot \text{W}^{-1}$  with an average quantum efficiency of  $(14 \pm 0.5) \%$ . In comparison, these results for B2 are almost half the average current responsivity of  $(52 \pm 17) \text{ mA} \cdot \text{W}^{-1}$  and quantum efficiency of  $(23 \pm 7.7) \%$  at 275 nm that were obtained for the individual photodiodes A1-3, A1-4 and A2-4 with the as-deposited Au probe contact pads on top of the  $\text{IrO}_2$  in Table 5.7 and can be due to the fact that the samples originated from two different wafers. However, a better comparison can again be made to A2-2 in Table 5.5 that had a current responsivity of  $37 \text{ mA} \cdot \text{W}^{-1}$  and quantum efficiency of 17 % at 275 nm, because of the proper deposition of the Au contact that resulted in similar size photosensitive areas ( $7.2 \times 10^{-3} \text{ cm}^2$  for A2-2).

### **The UV-to-VIS and NIR rejection ratio**

The spectral UV-to-VIS/NIR rejection ratios for each quadrant of the first four-quadrant detector on B1 are presented in Figure 6.8 for the wavelengths ranging from 400 nm to 1100 nm. The rejection ratios were calculated with respect to an average PCD of  $2.2 \text{ nA} \cdot \text{cm}^{-2}$  that was measured at 320 nm over the four quadrants of the detector. The UV-to-VIS/NIR rejection ratio range for each quadrant on B1 is presented in Table 6.4 and on average most of the rejection ratios were between  $10^2$  and  $10^3$ .

Figure 6.9 shows the spectral UV-to-VIS/NIR rejection ratios for each quadrant of the second four-quadrant detector on B2. The rejection ratios were calculated with respect to an average PCD of  $4.6 \text{ nA} \cdot \text{cm}^{-2}$  that was measured at 250 nm over the four quadrants of the detector. The UV-to-VIS/NIR rejection ratio range for each quadrant on B2 is presented in Table 6.5 and on average most of the rejection ratios were between  $10^3$  and  $10^5$ .

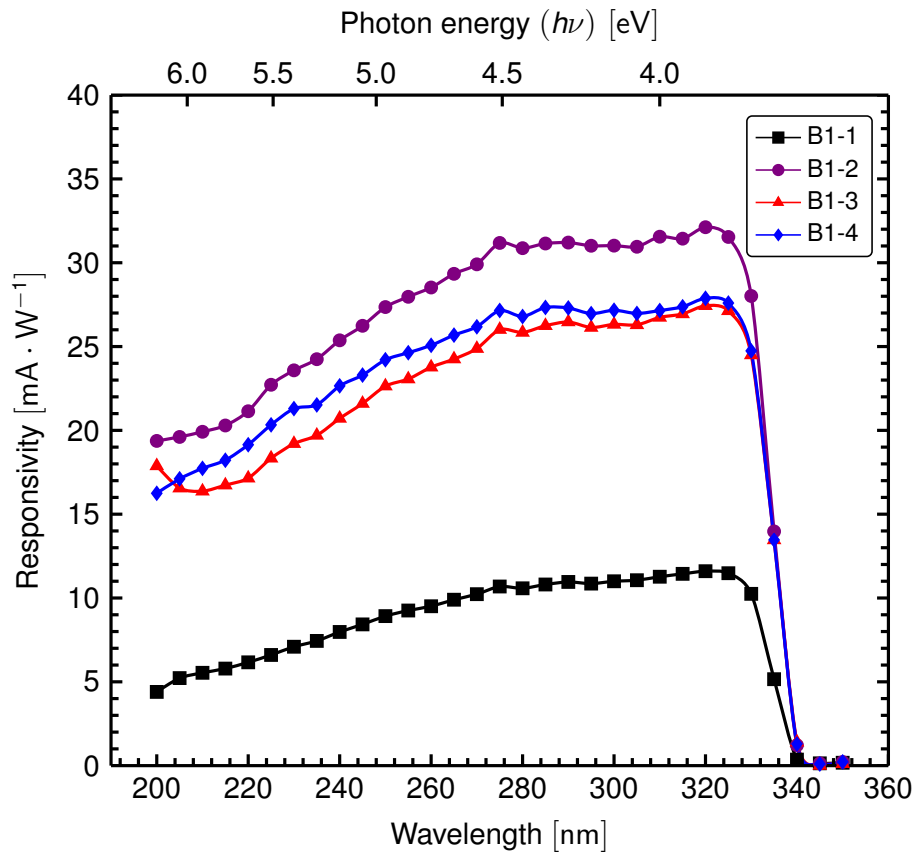


Figure 6.6: Spectral responsivities for each quadrant of the first developed front-irradiated AlGaIn-based visible-blind UV-sensitive four-quadrant detector that was fabricated on B1 taken from 7LS3205-3.

Table 6.4: The spectral parameters of the first developed front-irradiated AlGaIn-based visible-blind UV-sensitive four-quadrant detector that was fabricated on B1 taken from 7LS3205-3. The parameters included the cut-off wavelength ( $\lambda_{\text{cut-off}}$ ), current responsivity ( $\mathcal{R}_{320}$ ), quantum efficiency ( $\eta_{320}$ ) at 320 nm and UV-to-VIS/NIR rejection ratios [ $J_p(\lambda_s)/J_p(\lambda \geq 400)$ ] for each quadrant together with the overall averages.

Quadrant	$\lambda_{\text{cut-off}}$ [nm]	$\mathcal{R}_{320}$ [mA · W <sup>-1</sup> ]	$\eta_{320}$ [%]	UV-to-VIS/NIR [ $J_p(\lambda_s)/J_p(\lambda \geq 400)$ ]
B1-1	335	12	4.5	$10^2$ to $10^3$
B1-2	335	32	12	$10^2$ to $10^3$
B1-3	335	27	11	$10^2$ to $10^4$
B1-4	335	28	11	$10^2$ to $10^2$
Avg.:	335	25	9.6	$10^2$ to $10^3$
Std. dev.:		9.0	5.5	

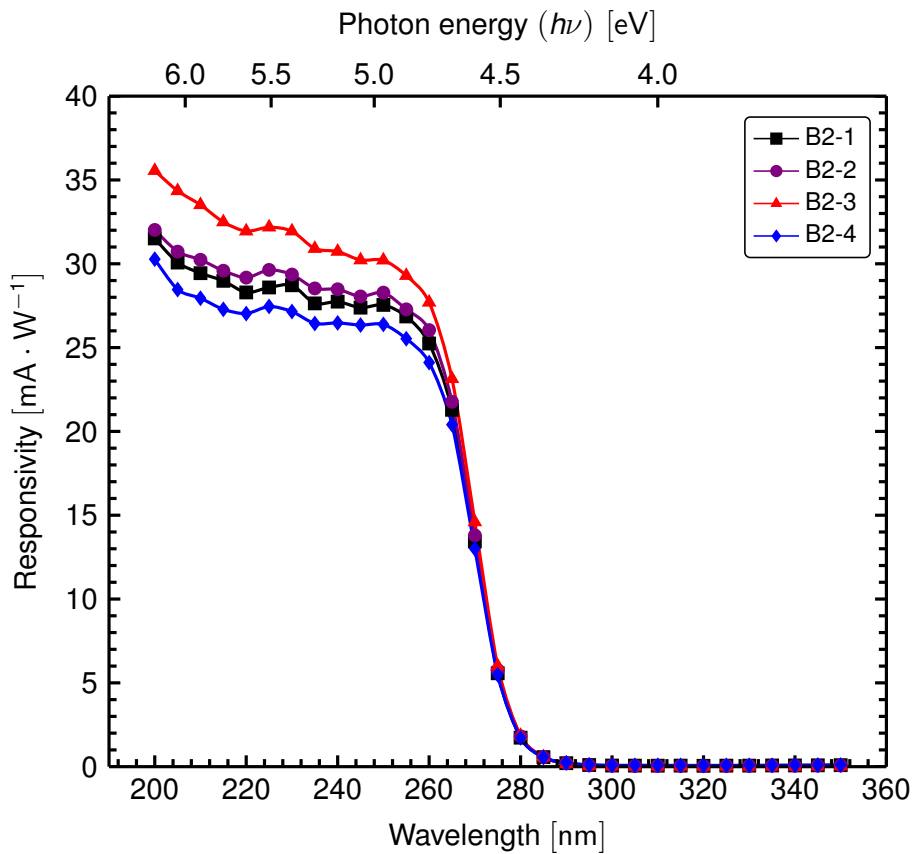


Figure 6.7: Spectral responsivities for each quadrant of the second developed front-irradiated AlGaIn-based solar-blind UV-sensitive four-quadrant detector that was fabricated on B2 taken from 7LS3825-2. Adapted from van Schalkwyk *et al.* [2014:95], Copyright (2013), with permission from Elsevier.

Table 6.5: The spectral parameters of the second developed front-irradiated AlGaIn-based solar-blind UV-sensitive four-quadrant detector that was fabricated on B2 taken from 7LS3825-2. The parameters included the cut-off wavelength, current responsivity ( $\mathcal{R}_{250}$ ), quantum efficiency ( $\eta_{250}$ ) at 250 nm and UV-to-VIS/NIR rejection ratios [ $J_p(\lambda_s) / J_p(\lambda \geq 400)$ ] for each quadrant together with the overall averages. Adapted from van Schalkwyk *et al.* [2014:95], Copyright (2013), with permission from Elsevier.

Quadrant	$\lambda_{\text{cut-off}}$ [nm]	$\mathcal{R}_{250}$ [mA · W <sup>-1</sup> ]	$\eta_{250}$ [%]	UV-to-VIS/NIR [ $J_p(\lambda_s) / J_p(\lambda \geq 400)$ ]
B2-1	275	28	14	$10^2$ to $10^5$
B2-2	275	28	14	$10^2$ to $10^4$
B2-3	275	30	15	$10^2$ to $10^5$
B2-4	275	26	13	$10^2$ to $10^5$
Avg.:	275	28	14	$10^2$ to $10^5$
Std. dev.:		1.0	0.5	

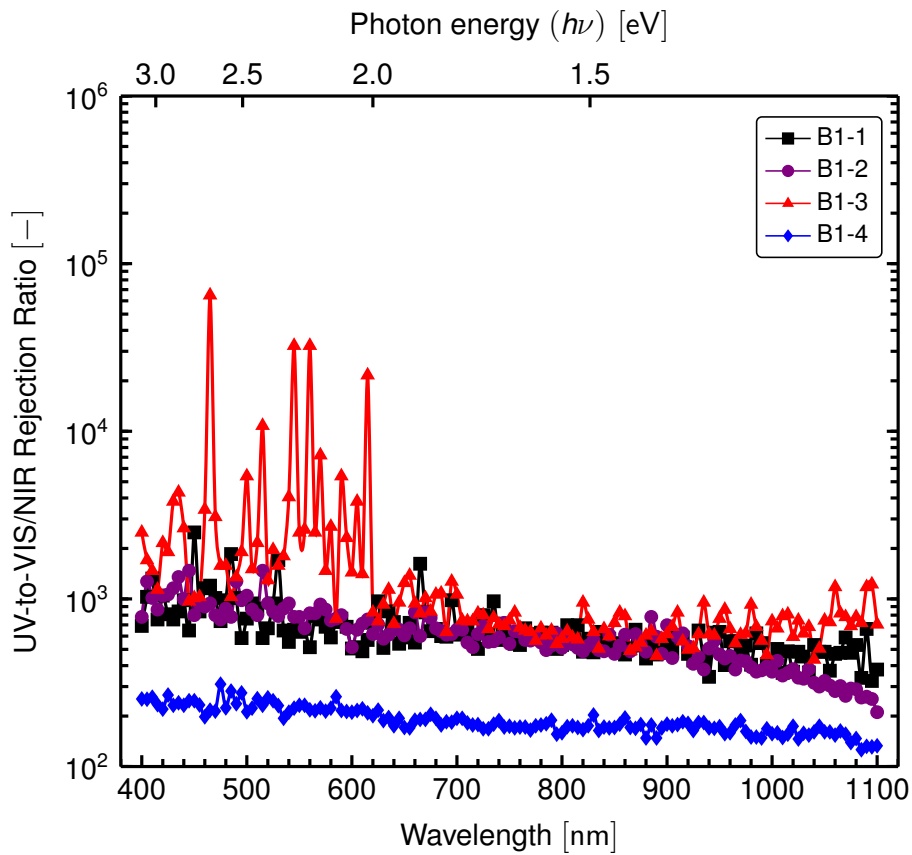


Figure 6.8: The spectral UV-to-VIS/NIR rejection ratios for each quadrant of the first developed front-irradiated AlGaIn-based visible-blind UV-sensitive four-quadrant detector that was fabricated on B1 taken from 7LS3205-3 at zero biasing with respect to the responsivity at 320 nm [ $J_p(\lambda_s) / J_p(\lambda \geq 400)$ ].

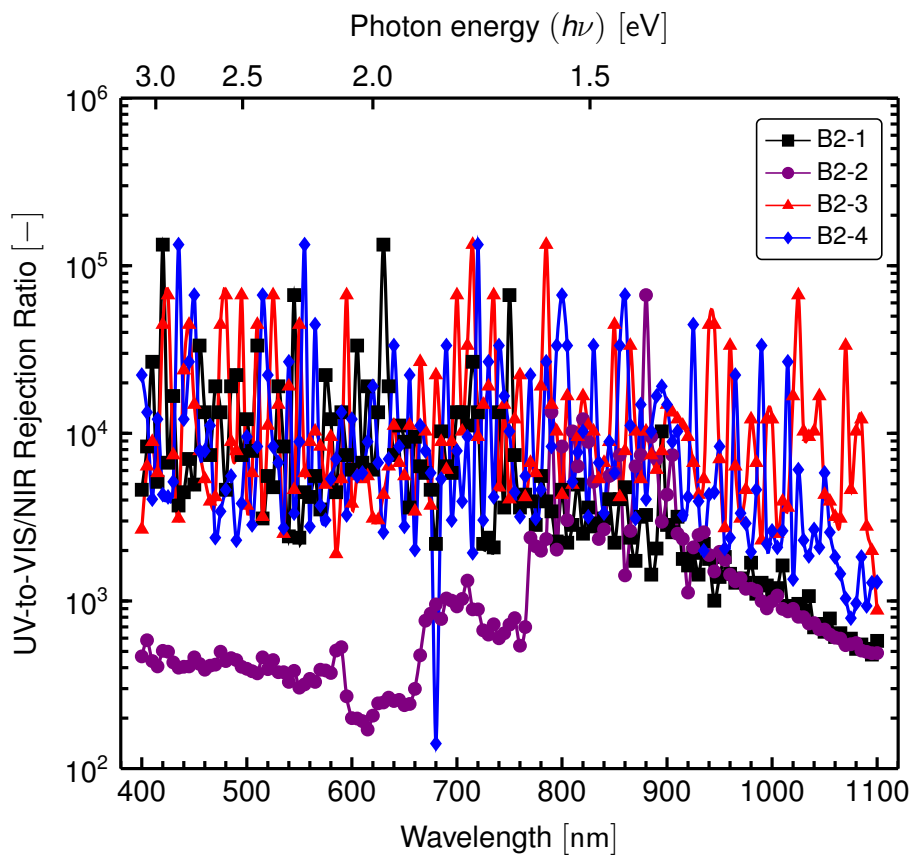


Figure 6.9: Spectral UV-to-VIS/NIR rejection ratios for each quadrant of the second developed front-irradiated AlGaIn-based solar-blind UV-sensitive four-quadrant detector that was fabricated on B2 taken from 7LS3825-2 at zero biasing with respect to the responsivity at 250 nm [ $J_p(\lambda_s) / J_p(\lambda \geq 400)$ ]. Adapted from van Schalkwyk *et al.* [2014:95], Copyright (2013), with permission from Elsevier.



## 6.4 Conclusion

A four-quadrant detector was realised with the use of three different physical contact masks. The one mask defined the layout for the optimized layered ohmic contact structures obtained after depositing a metallization scheme followed by a multi-step annealing method. The second mask defined the layout for the optimized UV transmissive IrO<sub>2</sub> Schottky contacts which were formed after a two-step annealing method under O<sub>2</sub> ambient. The last mask was used for the deposition layout of the Au contacts on top of the IrO<sub>2</sub> Schottky contacts. The metallization technique was performed sequentially through each mask as well as correctly aligning the samples before every deposition phase.

The feasibility of the four-quadrant detector was initially shown with the use of a substandard wafer. The extracted electrical parameters for the four quadrants included an average ideality factor of  $1.94 \pm 0.48$ , a SBH of  $(1.08 \pm 0.13)$  eV, a reverse leakage current density of  $(20 \pm 30)$  nA · cm<sup>-2</sup> at 1 V reverse bias and an average series resistance of  $(40 \pm 6.2)$  Ω. Spectral parameters included a  $(335 \pm 5)$  nm cut-off wavelength that corresponded with the absorption edge of an Al<sub>0.13</sub>Ga<sub>0.87</sub>N semiconductor with a bandgap ranging from 3.76 eV to 3.65 eV, as well as, an average current responsivity at 320 nm of  $(25 \pm 9.0)$  mA · W<sup>-1</sup> with a quantum efficiency of  $(9.6 \pm 5.5)$  % and an UV-to-VIS/NIR rejection ratio between 10<sup>2</sup> and 10<sup>3</sup> for wavelengths ranging from 400 nm to 1100 nm. Because of the cut-off wavelength, it is concluded that the first developed four-quadrant detector was an intrinsically visible-blind UV-sensitive detector.

A second four-quadrant detector was manufactured on an appropriate AlGaIn semiconductor with a high Al mole fraction specification and was mounted onto a commercial microchip carrier, where Al wires were epoxy bonded from the ohmic and Au contacts to the carrier strips, using a silver-filled epoxy. The extracted

electrical parameters for the four quadrants included an average ideality factor of  $1.97 \pm 0.09$ , a **SBH** of  $(1.22 \pm 0.08)$  eV, a reverse leakage current density of  $(2.1 \pm 3.3)$  nA · cm<sup>-2</sup> and an average series resistance of  $(120 \pm 30)$  Ω. Spectral parameters included a  $(275 \pm 5)$  nm cut-off wavelength that corresponded with the absorption edge of an Al<sub>0.45</sub>Ga<sub>0.55</sub>N semiconductor with a bandgap ranging from 4.59 eV to 4.23 eV, as well as, an average current responsivity at 250 nm of  $(28 \pm 1.0)$  mA · W<sup>-1</sup> with a quantum efficiency of  $(14 \pm 0.5)$  % and an **UV-to-VIS/NIR** rejection ratio between 10<sup>3</sup> and 10<sup>5</sup> for wavelengths ranging from 400 nm to 1100 nm. Here, the cut-off wavelength confirmed that the second manufactured four-quadrant detector was an intrinsically solar-blind **UV**-sensitive detector. Furthermore, because of the uniformity in the characteristics across the quadrants, the detector was used in demonstrating a working solar-blind **UV**-sensitive electro-optic device.

It is suggested that the high average ideality factors of both of the four-quadrant detectors were a result of the annealing of the **Au** probe contact pads at the higher 500 °C, as opposed to the 350 °C that was used in the previous Chapter 5. Although the free carrier concentration was high ( $10^{18}$  cm<sup>-3</sup>), the reverse leakage current densities were small (less than 65 nA · cm<sup>-2</sup>) and can be attributed to either the proper formation of the **IrO<sub>2</sub>** Schottky contact through the two-step annealing method at appropriate temperatures or by annealing the properly deposited **Au** probe contact pads [van Schalkwyk *et al.*, 2014:94–95]. The increase in series resistance for the second mounted four-quadrant detector can be due to the addition of the silver-filled epoxy and **Al** wires.

The two four-quadrant detectors were fabricated on samples originating from two different wafers. Both of these wafers differ from the wafer used in the previous Chapter 5 and, therefore, no concrete links or reasons in the variations between the current responsivities and quantum efficiencies were made.

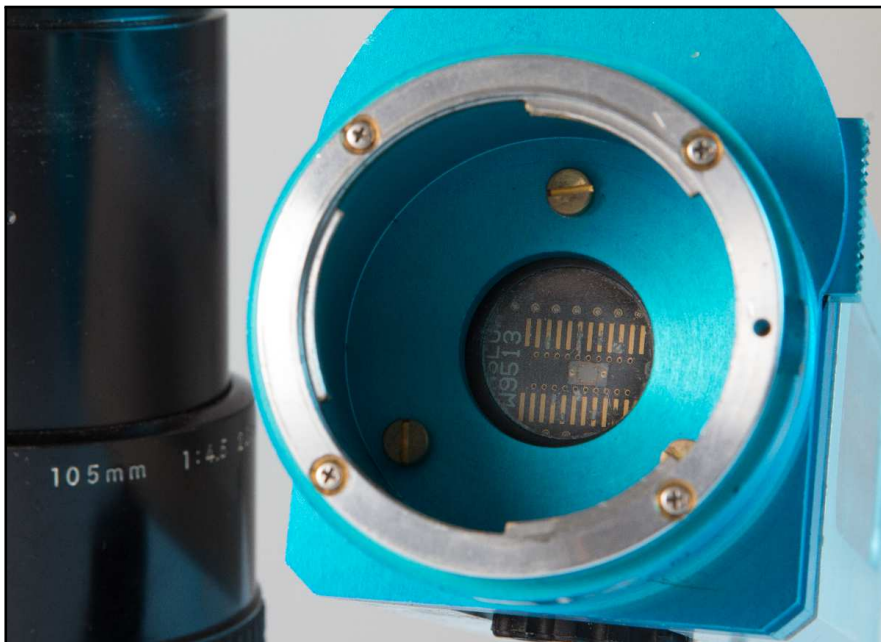
## 6.5 Publication

The results obtained from the optoelectronic characterization of the final four-quadrant detector are covered in the publication which has been included in Appendix E. Furthermore, although the four square ( $0.90 \times 0.90$ ) mm<sup>2</sup>, 50 Å-thick IrO<sub>2</sub> Schottky contacts were not ideal (ideality factors greater than 1.90) and had relatively lower current responsivities, and subsequently lower quantum efficiencies, they were almost identical in their characteristics [van Schalkwyk *et al.*, 2014:95].

This uniformity across the quadrants allowed for the completion of a joint initiative with the SST competence area of the CSIR MSM unit, who successfully mounted the four-quadrant detector in a housing integrated with electronics and used UV optics to demonstrate a working solar-blind UV-sensitive electro-optic device. Photographs of the solar-blind UV-sensitive electro-optic device are presented in Figure 6.10. Furthermore, showing that the implementation of an AlGaIn-based solar-blind UV-sensitive four-quadrant detector is feasible for future UV-sensitive electro-optic devices.



(a) The working solar-blind UV-sensitive electro-optic demonstration device (left) with LED indicators at the back (right).



(b) The epoxy wire-bonded four-quadrant detector mounted on a commercial microchip carrier inside the housing behind a protective quartz glass.

Figure 6.10: Photographs of the develop AlGaIn-based solar-blind UV-sensitive four-quadrant detector mounted by the SST competence area of the CSIR MSM unit in a housing integrated with electronics and UV optics that completed the joint initiative (courtesy of the CSIR MSM unit).

# Chapter 7

## Conclusions

### 7.1 General

An optoelectronic characterization system was constructed for the electrical and spectral characterization of photodiodes. Spectral characterization was made possible with the addition of two radiating sources, a deuterium lamp as a **UV** source and a tungsten-halogen lamp as a **VIS-to-NIR** source, together with a monochromator for wavelength selection and optical filters, onto the existing electrical characterization system. The optoelectronic characterization system was unique in that an optical fibre was used to lead the monochromatic **EMR** from the monochromator to irradiate a photodiode inside the light-tight shielded enclosure, which minimized **EMI** from external noise sources.

The optoelectronic characterization system was calibrated against standards traceable to the **NIST**, by following the photodetector substitution method. Also, an **NI LabVIEW** routine was developed that allowed for some automation of the spectral characterization part that recorded, calculated and saved the measurements in a data file.

The study established that the tuneable front-irradiated **AlGaIn**-based solar-blind **UV**-sensitive Schottky photodiode fabrication procedure comprised of at least six

steps, that included (1) the deposition of a layered ohmic contact structure, (2) the annealing of the ohmic contact, (3) the deposition of an Ir Schottky contact, (4) the annealing of the Ir to form a more UV transmissive IrO<sub>2</sub> Schottky contact, (5) the deposition of a Au probe contact pad and (6) the annealing thereof.

It is concluded that an optimized tuneable front-irradiated AlGaIn-based solar-blind UV-sensitive Schottky photodiode would consist of a Ti/Al/Ni/Au (300/1800/400/1500 Å) ohmic contact that was multi-step annealed under Ar ambient at 400 °C for three minutes, then at 700 °C for 20 s, followed by annealing at 830 °C for 30 s and lastly at 900 °C for 30 s; together with a 50 Å-thick Ir Schottky contact that was two-step annealed in O<sub>2</sub> ambient for 30 minutes at both 600 °C and 730 °C to allow for the formation of the more UV transmissive IrO<sub>2</sub> and finally the deposition of a 1500 Å-thick Au contact on top of the IrO<sub>2</sub> Schottky contact that is then annealed in O<sub>2</sub> ambient for ten minutes at 350 °C, instead of 500 °C.

The study reached its aims in establishing a fabrication procedure for Schottky photodiodes on AlGaIn-based materials and the development of a tuneable front-irradiated AlGaIn-based solar-blind UV-sensitive four-quadrant Schottky detector that was used to prove the feasibility of such a detector in future UV-sensitive electro-optic systems. Moreover, the ternary AlGaIn semiconductor alloy material has (again) proved to be an excellent photonic material for use in tuneable solar-blind UV-sensitive sensors [Razeghi, 2011:264; Razeghi and Rogalski, 1996:7433].

## 7.2 Further research

The metallization technique and multi-step annealing method used for the final optimized layered ohmic structure was derived from research articles about the

topic. The quality of the proposed layered ohmic structure needs to be quantified in terms of contact and specific contact resistances and can be obtained through either the **CTLM** or the transfer length method (**TLM**).

Research can still be done in developing and characterizing tuneable **AlGaIn**-based UV-sensitive Schottky photodiodes, using the recommended fabrication procedures for the ohmic, Schottky and **Au** probe contacts as mentioned in the conclusion earlier. However, the deposition of the ohmic contact directly onto the **GaN:Si** layer is desired and the use of a focused ion beam to remove the first couple of **AlGaIn**-based layers can be investigated.

Certain applications in the 250 nm to 280 nm wavelength range, require devices that can detect signals typically lower than  $20 \text{ fW} \cdot \text{cm}^{-2}$  at 270 nm. Generally, at these low signal levels the photon quantities are considered, that is, devices should be able to detect incident photon-flux densities of lower than  $3.0 \times 10^4 \text{ q} \cdot \text{s}^{-1} \cdot \text{cm}^{-2}$ . The optoelectronic characterization system irradiated the photodiodes with approx.  $100 \text{ nW} \cdot \text{cm}^{-2}$  (greater than  $1.0 \times 10^{13} \text{ q} \cdot \text{s}^{-1} \cdot \text{cm}^{-2}$ ) at 270 nm. The spectral characterization of low signal devices can be done by decreasing the irradiance with neutral density filters. Furthermore, research will probably need to focus on fabricating back-irradiated photodiodes with smaller Schottky contacts while increasing the quantum efficiency and improving the signal-to-noise ratios. Also, operation with or without gain can be considered. Moreover, for the detection of even lower signals, the understanding of defects within the material and their effects will be important and therefore require defect characterization studies.

# Appendices



# Appendix A

## List of symbols

Symbol	Description	Unit
$A$	Area	$[\text{cm}^2]$
$A_c$	Schottky contact area	$[\text{cm}^2]$
$A_p$	Photosensitive area	$[\text{cm}^2]$
$A^*$	Effective Richardson constant	$[A \cdot \text{cm}^{-2} \cdot \text{K}^{-2}]$
$c$	Speed of light in vacuum	$[\text{m} \cdot \text{s}^{-1}]$
$C$	Capacitance	$[\text{F}, \text{C} \cdot \text{V}^{-1}]$
$C_D$	Depletion-region capacitance	$[\text{F}, \text{C} \cdot \text{V}^{-1}]$
$da$	Infinitesimal cross-sectional area of a surface	$[\text{m}^2]$
$dA$	Infinitesimal surface area	$[\text{m}^2]$
$dA_r$	Infinitesimal surface area of receiver	$[\text{m}^2]$
$dA_s$	Infinitesimal surface area of source	$[\text{m}^2]$
$D_{it}$	Interface-trap density	$[\text{cm}^{-2} \cdot \text{eV}^{-1}]$
$e$	Exponential constant	$[-]$
$e_{ms}^-$	Electron flow from metal to semiconductor	$[-]$
$e_{sm}^-$	Electron flow from semiconductor to metal	$[-]$
$E_e$	Irradiance	$[\text{W} \cdot \text{m}^{-2}]$
$E$	Energy	$[\text{J}, \text{eV}]$
$E_0$	Vacuum energy-level	$[\text{eV}]$
$E_C$	Lowest possible conduction band energy-level	$[\text{eV}]$
$E_D$	Donor energy-level	$[\text{eV}]$
$E_F$	Fermi energy-level	$[\text{eV}]$
$E_{Fm}$	Metal Fermi level	$[\text{eV}]$

List of symbols

Symbol	Description	Unit
$E_{Fs}$	Semiconductor Fermi level	[eV]
$E_g$	Bandgap energy	[eV]
$E_i$	Intrinsic Fermi level	[eV]
$E_{ph}$	Optical-phonon energy	[eV]
$E_r$	Receiver irradiance	[W · m <sup>-2</sup> ]
$E_V$	Highest possible valence band energy-level	[eV]
$\tilde{E}_e$	Normalized irradiance	[-]
$\vec{\mathcal{E}}$	Built-in electric field vector	[V · cm <sup>-1</sup> ]
$ \vec{\mathcal{E}} $	Built-in electric field magnitude	[V · cm <sup>-1</sup> ]
$ \vec{\mathcal{E}} _\delta$	Magnitude of the electric field within gap	[V · cm <sup>-1</sup> ]
$h$	Planck constant	[J · s]
$I$	Direct current	[A]
$I_0$	Saturation current	[A]
$I_e$	Radiant intensity	[W · sr <sup>-1</sup> ]
$I_p$	Photocurrent	[A]
$J$	Current density	[A · cm <sup>-2</sup> ]
$J_0$	Saturation current density	[A · cm <sup>-2</sup> ]
$J_d$	Dark current density (or noise)	[A · cm <sup>-2</sup> ]
$J_{ms}$	Reverse current density	[A · cm <sup>-2</sup> ]
$J_p$	photocurrent density (PCD)	[A · cm <sup>-2</sup> ]
$J_R$	Reverse leakage current density	[A · cm <sup>-2</sup> ]
$J_{sm}$	Forward current density	[A · cm <sup>-2</sup> ]
$j$	Imaginary number	[-]
$k$	Boltzmann constant	[J · K <sup>-1</sup> ]
$k_e$	Extinction coefficient	[-]
$K_s$	Dielectric constant of semiconductor	[-]
$L_e$	Radiance	[W · m <sup>-2</sup> · sr <sup>-1</sup> ]
$L_r$	Receiver radiance	[W · m <sup>-2</sup> · sr <sup>-1</sup> ]
$L_s$	Source radiance	[W · m <sup>-2</sup> · sr <sup>-1</sup> ]
$m_0$	Electron rest mass	[kg]
$m^*$	Effective mass	[kg]
$m_{de}^*$	Density-of-state effective mass for electrons	[kg]

List of symbols

Symbol	Description	Unit
$m_{dh}^*$	Density-of-state effective mass for holes	[kg]
$m_{hh}^*$	Effective mass for heavy hole	[kg]
$m_{lh}^*$	Effective mass for light hole	[kg]
$M_C$	Number of equivalent minima in conduction band	[—]
$M_e$	Radiant exitance	[W · m <sup>-2</sup> ]
$n_0$	Refractive index of optical fibre core	[—]
$n_1$	Refractive index of optical fibre cladding	[—]
$n$	Free electron concentration	[cm <sup>-3</sup> ]
$n_i$	Intrinsic carrier concentration	[cm <sup>-3</sup> ]
$n_n$	Electron concentration in $n$ -type semiconductor	[cm <sup>-3</sup> ]
$N_A$	Acceptor impurity concentration	[cm <sup>-3</sup> ]
$N_C$	Effective density of states in conduction band	[cm <sup>-3</sup> ]
$N_d$	Free carrier concentration (= $N_D - N_A$ )	[cm <sup>-3</sup> ]
$N_D$	Donor impurity concentration	[cm <sup>-3</sup> ]
$N_D^+$	Ionized donor impurity concentration	[cm <sup>-3</sup> ]
$N_V$	Effective density of states in valence band	[cm <sup>-3</sup> ]
$\hat{n}$	Normal unit vector to a surface	[—]
$\hat{n}_r$	Normal unit vector to a receiver surface	[—]
$\hat{n}_s$	Normal unit vector to a source surface	[—]
$p$	Free hole concentration	[cm <sup>-3</sup> ]
$\bar{p}$	Crystal momentum	[J · s · cm <sup>-1</sup> ]
$P$	Arbitrary surface	[m <sup>2</sup> ]
$P'$	Projection of an arbitrary surface $P$	[m <sup>2</sup> ]
$q$	Unit electronic elementary charge	[C]
$Q_a$	Absorbed radiant energy	[J]
$Q_e$	Radiant energy	[J]
$Q_i$	Incident radiant energy	[J]
$Q_m$	Surface-charge density on metal	[C · cm <sup>-2</sup> ]
$Q_r$	Reflected radiant energy	[J]
$Q_{sc}$	Space-charge density in semiconductor	[C · cm <sup>-2</sup> ]
$Q_t$	Transmitted radiant energy	[J]
$r$	Radius of curvature of the wave front	[m]
$R$	Resistivity	[Ω · cm]
$\bar{R}^2$	Adjusted coefficient of determination	[—]
$R_S$	Series resistance	[Ω]

List of symbols

Symbol	Description	Unit
$\mathcal{R}_\lambda$	Current responsivity at a specific wavelength	$[A \cdot W^{-1}]$
$T$	Absolute temperature	[K]
$v_{avg}$	Average thermal velocity	$[cm \cdot s^{-1}]$
$V$	Applied voltage	[V]
$V_d$	Voltage across diode	[V]
$V_i$	Intercept on $V$ -axis	[V]
$W_D$	Depletion region width	[cm]
$x$	Mole fraction (of Al)	[—]
$x, y$	Displacement, distance or thickness	[m, cm]
$z$	Distance along optical axis	[m]
$z_{pr}$	Radius of projection hemisphere	[m]
$z_{sa}$	Line-of-sight distance from source to $da$	[m]
$z_{sr}$	Line-of-sight distance from source to receiver	[m]
$\alpha_e$	Attenuation coefficient	[—]
$\delta$	Interfacial layer (vacuum gap) thickness	[cm]
$\Delta$	Electrostatic potential across interfacial layer	[V]
$\epsilon_0$	Permittivity of vacuum	$[F \cdot cm^{-1}]$
$\epsilon_i$	Permittivity of interfacial layer	$[F \cdot cm^{-1}]$
$\epsilon_s$	Permittivity of semiconductor	$[F \cdot cm^{-1}]$
$\eta$	Ideality factor of diode under forward bias	[—]
$\eta_\lambda$	Quantum efficiency at a specific wavelength	[—]
$\theta$	Angle between $\hat{n}$ and line-of-sight of $dA$ and $P'$	[rad, °]
$\theta_r$	Angle between $\hat{n}_r$ and line-of-sight of $dA_r$ and $dA_s$	[rad, °]
$\theta_s$	Angle between $\hat{n}_s$ and line-of-sight of $dA_s$ and $dA_r$	[rad, °]
$\Theta$	Half apex angle of a cone	[rad, °]
$\lambda$	Wavelength of electromagnetic waves	[nm]
$\lambda_{cut-off}$	Cut-off wavelength of responsivity	[nm]
$\lambda_s$	Specific wavelength	[nm]

List of symbols

Symbol	Description	Unit
$\nu$	Frequency of electromagnetic waves	[Hz, s <sup>-1</sup> ]
$\rho$	Charge density in depletion region	[C · cm <sup>-3</sup> ]
$\rho_e$	Radiant reflectance	[—]
$\tau_e$	Transmission coefficient	[—]
$\phi_0$	Neutral energy-level	[V]
$\phi_B$	Schottky barrier height (SBH)	[V]
$\phi_{B0}$	SBH without image force lowering	[V]
$\phi_m$	Work function of metal	[V]
$\phi_n$	Fermi potential from $E_C$ in $n$ -type semiconductor	[V]
$\phi_s$	Work function of semiconductor	[V]
$\Phi_e$	Radiant flux	[W]
$\Phi_p$	Photon flux	[q · s <sup>-1</sup> ]
$\chi_s$	Electron affinity of semiconductor	[V]
$\psi_{bi}$	Built-in or diffusion potential at equilibrium	[V]
$\psi_i$	Semiconductor potential	[V]
$\Psi_e$	Electric field magnitude (optics)	[—]
$\omega$	Geometric solid angle	[sr]
$\omega_a$	Geometric solid angle subtended at origin by $da$	[sr]
$\omega_e$	Angular frequency (optics)	[rad · s <sup>-1</sup> ]
$\Omega$	Projected solid angle	[sr]
$\Omega_a$	Projected solid angle subtended at $dA_s$ by $da$	[sr]
$\Omega_r$	Projected solid angle subtended at $dA_s$ by $dA_r$	[sr]
$\Omega_s$	Projected solid angle subtended at $dA_r$ by $dA_s$	[sr]

# Appendix B

## Physical constants

Quantity	Symbol	Value <sup>a</sup>	Unit
Boltzmann constant	$k$	$1.380\,658 \times 10^{-23}$	[J · K <sup>-1</sup> ]
in electron-volts		$8.617\,385 \times 10^{-5}$	[eV · K <sup>-1</sup> ]
Elementary charge	$q$	$1.602\,177 \times 10^{-19}$	[C]
Electron rest mass	$m_0$	$9.109\,390 \times 10^{-31}$	[kg]
Electron-volt energy	eV	$1.602\,177 \times 10^{-19}$	[J]
Exponential constant	exp, e	2.718 282	[–]
Permittivity of vacuum	$\varepsilon_0$	$8.854\,188 \times 10^{-14}$	[F · cm <sup>-1</sup> ]
Pi	$\pi$	3.141 593	[–]
Planck constant	$h$	$6.626\,076 \times 10^{-34}$	[J · s]
in electron-volts		$4.135\,670 \times 10^{-15}$	[eV]
Speed of EMWs in vacuum	$c_0$	$2.997\,925 \times 10^8$	[m · s <sup>-1</sup> ]

<sup>a</sup>Values were adopted from [Woan \[2000\]](#) and rounded to seven significant figures.

## Appendix C

### List of acronyms and chemical symbols

<b>AC</b>	alternating current
<b>Al</b>	aluminium
<b>AlN</b>	aluminium nitride
<b>AlGaN</b>	aluminium gallium nitride
<b>AlGaN:Si</b>	Si-doped AlGaN
<b>ANSI</b>	American National Standards Institute
<b>Al<sub>2</sub>O<sub>3</sub></b>	sapphire
<b>Ar</b>	argon
<b>ASTM</b>	American Society for Testing and Materials
<b>Au</b>	gold
<b>BNC</b>	Bayonet Neill–Concelman (connector type)
<b>CTLM</b>	circular transfer length method
<b>CSIR</b>	Council for Scientific and Industrial Research
<b>CSR</b>	constant spectral resolution
<b>C–V</b>	capacitance–voltage
<b>D<sub>2</sub></b>	ergocalciferol
<b>D<sub>3</sub></b>	holecalciferol
<b>DC</b>	direct current

*List of acronyms and chemical symbols*

---

<b>DI</b>	de-ionised
<b>I–V</b>	current–voltage
<b>EBPVD</b>	electron-beam <b>PVD</b>
<b>EDS</b>	energy-dispersion spectroscopy
<b>EMI</b>	electromagnetic interference
<b>EMR</b>	electromagnetic radiation
<b>EMW</b>	electromagnetic wave
<b>f/#</b>	f-number (also called the focal ratio or relative aperture)
<b>Ga</b>	gallium
<b>Ga<sub>2</sub>O<sub>3</sub></b>	gallium(III) oxide
<b>GaN</b>	gallium nitride
<b>GaN:Si</b>	<b>Si</b> -doped <b>GaN</b>
<b>H<sub>2</sub>O</b>	water
<b>H<sub>2</sub>O<sub>2</sub></b>	hydrogen peroxide
<b>He</b>	helium
<b>HCl</b>	hydrochloric acid
<b>HNO<sub>3</sub></b>	nitric acid
<b>HP</b>	Hewlett-Packard
<b>HVPE</b>	hybride vapour phase epitaxy
<b>In</b>	indium
<b>InN</b>	Indium nitride
<b>Ir</b>	iridium
<b>IrO</b>	iridium oxide
<b>IrO<sub>2</sub></b>	iridium(IV) oxide
<b>Ir<sub>2</sub>O<sub>3</sub></b>	iridium(III) oxide
<b>IR</b>	infrared
<b>ISO</b>	International Organization for Standardization
<b>J–V</b>	current density–voltage
<b>LED</b>	light emitting diode



*List of acronyms and chemical symbols*

---

<b>LF</b>	low frequency
<b>MOCVD</b>	metal-organic chemical vapour deposition
<b>MSM</b>	Materials Science and Manufacturing
<b>N</b>	nitrogen
<b>N<sub>2</sub></b>	molecular nitrogen
<b>NA</b>	numerical aperture
<b>NH<sub>3</sub></b>	ammonia
<b>Ni</b>	nickel
<b>NI</b>	National Instruments
<b>NIR</b>	near-infrared
<b>NIST</b>	National Institute of Standards and Technology
<b>NCSL</b>	National Conference of State Legislatures
<b>NREL</b>	National Renewable Energy Laboratory
<b>O</b>	atomic oxygen
<b>O<sub>2</sub></b>	molecular oxygen
<b>O<sub>3</sub></b>	ozone
<b>PCD</b>	photocurrent density
<b>PDS</b>	photothermal deflection spectroscopy
<b>PMT</b>	photomultiplier tube
<b>PVD</b>	physical vapour deposition
<b>RTA</b>	rapid thermal annealing
<b>SBH</b>	Schottky barrier height
<b>SCF</b>	Spectral Comparator Facilities
<b>Si</b>	silicon
<b>SID</b>	spatial irradiation distribution
<b>SI</b>	International System of Units
<b>SiC</b>	silicon carbide
<b>SiO<sub>2</sub></b>	silicon dioxide
<b>SMA</b>	Sub-miniature version A connector

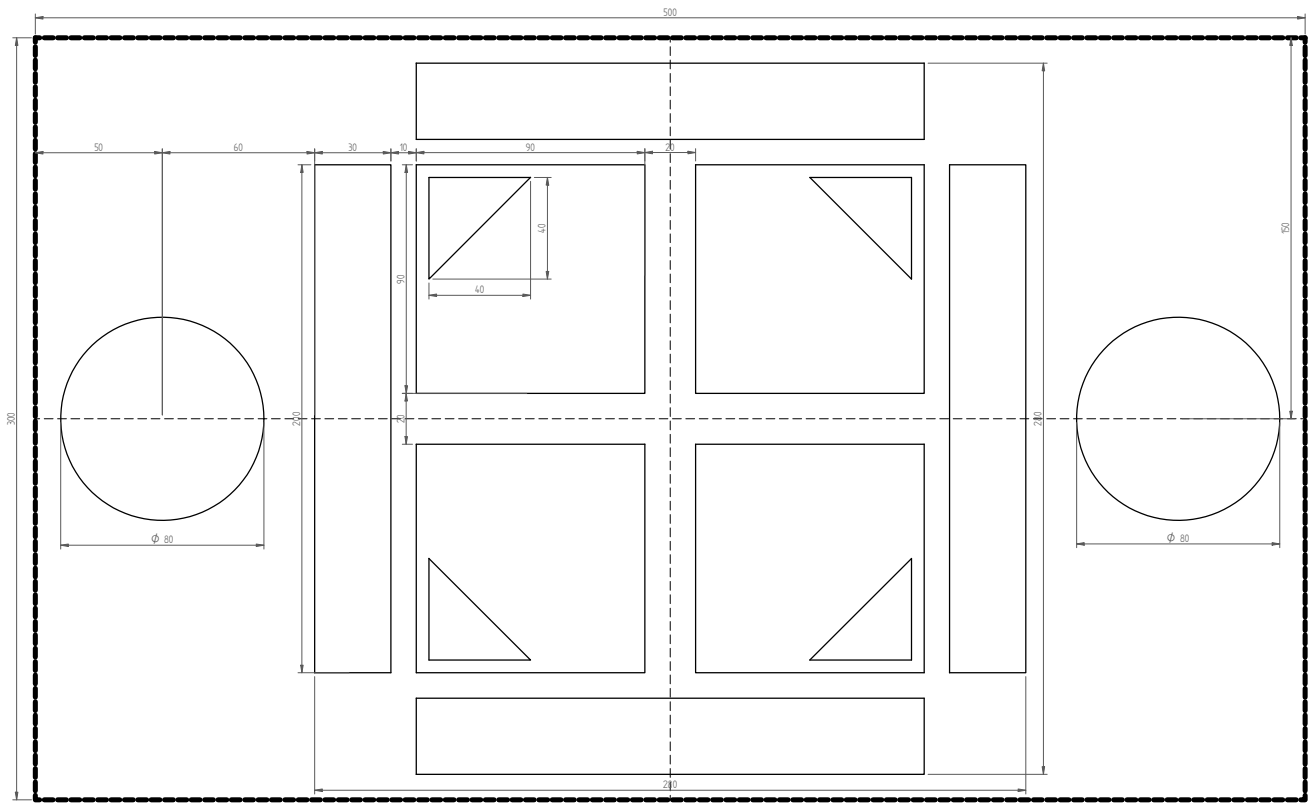
*List of acronyms and chemical symbols*

---

<b>SMARTS</b>	Simple Model of the Atmospheric Radiative Transfer of Sunshine
<b>SP</b>	Spectral Products
<b>SST</b>	Sensor Science & Technology
<b>TCE</b>	trichloroethylene
<b>TDI</b>	Technologies and Devices International, Inc.
<b>Ti</b>	titanium
<b>TiN</b>	titanium nitride
<b>TLM</b>	transfer length method
<b>UV</b>	ultraviolet
<b>UVR</b>	UV radiation
<b>UV-to-VIS/NIR</b>	UV-to-VIS and NIR
<b>VIS</b>	visible
<b>VUV</b>	Vacuum UV
<b>WBG</b>	wide-bandgap
<b>XPS</b>	x-ray photoelectron spectroscopy
<b>XRD</b>	x-ray diffraction
<b>ZnSe</b>	zinc selenide

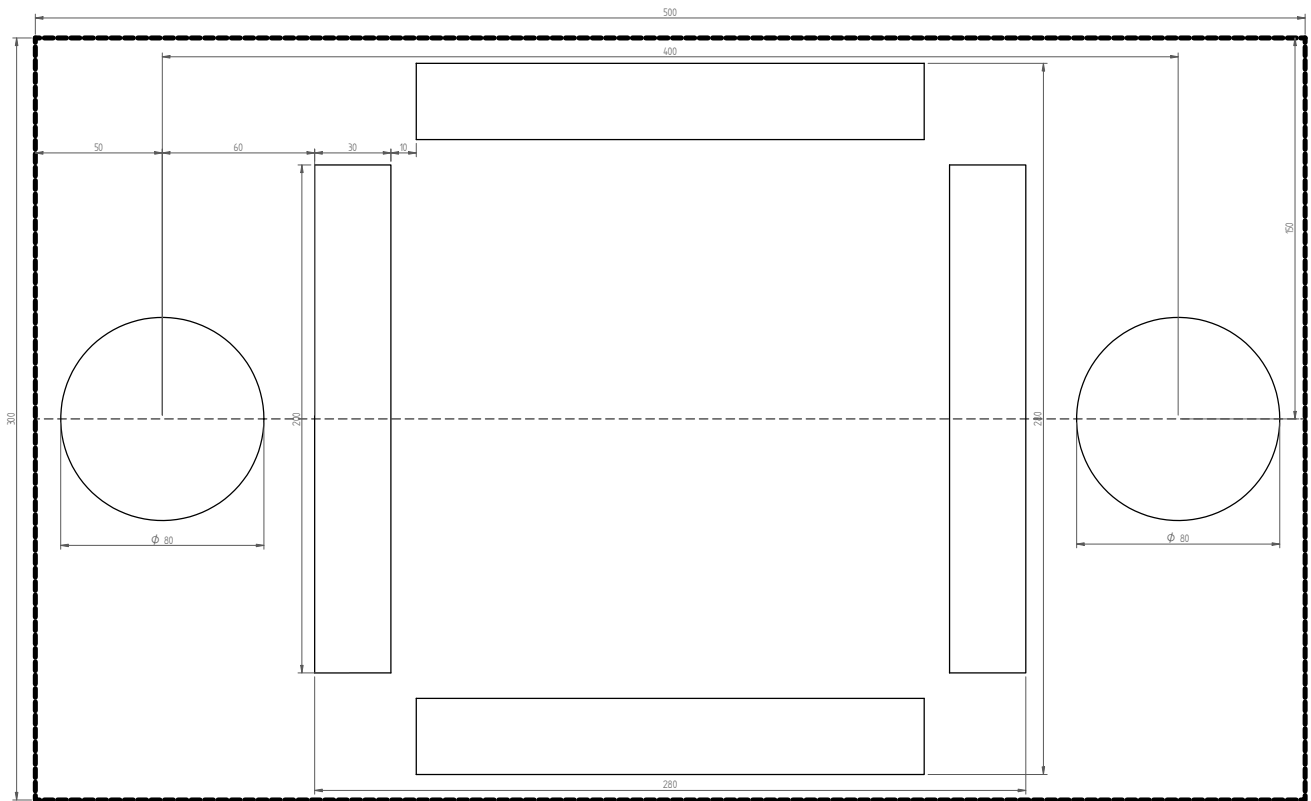
# Appendix D

## Contact mask drawings



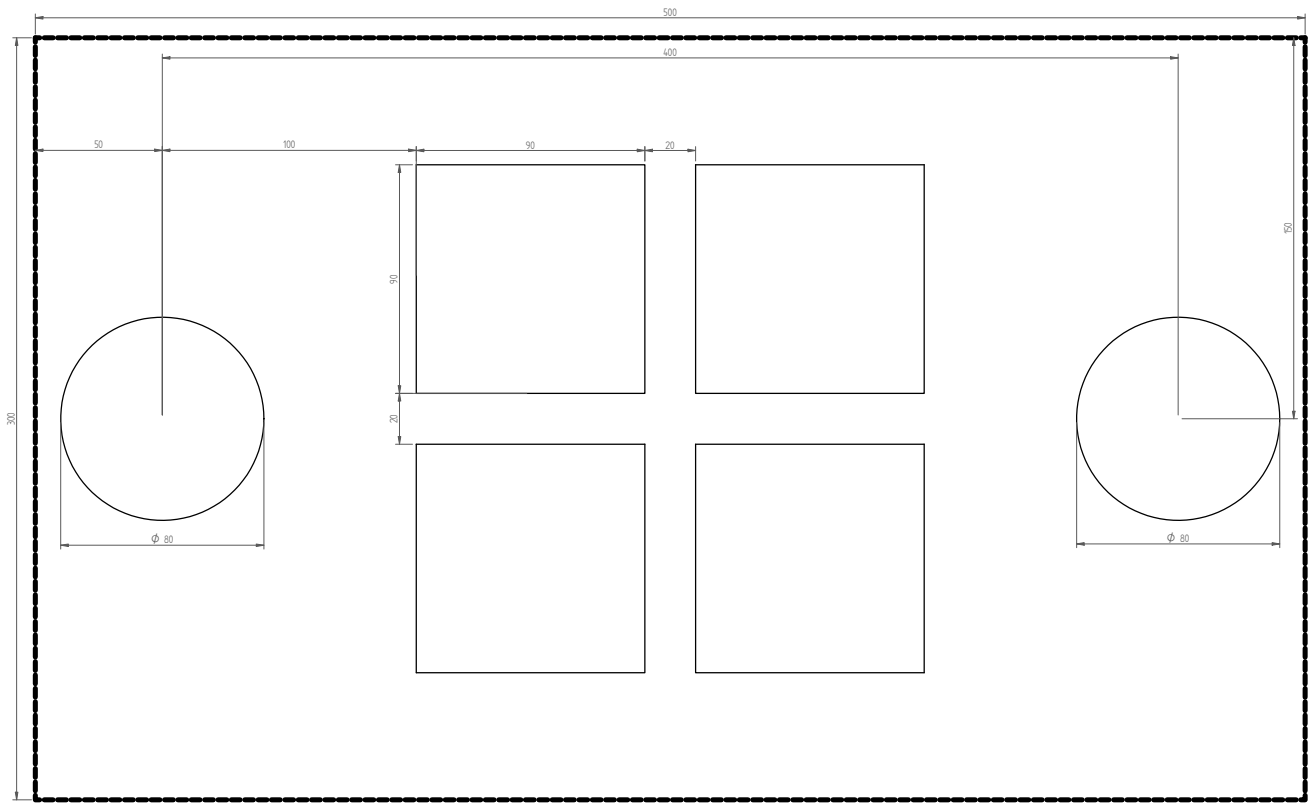
SOLID EDGE ACADEMIC COPY

TITLE	4-Q-Orth All-in-One (MASK 1, 2 & 3)	DATE	14/06/2011	SIZE	A2
SURNAME	van Schalkwyk	INITIALS	L	SCALE	100:1
STUDENT NR.		DISCIPLINE	PHYSICS	FILE NAME	4-Q-OrthLeft
PROJECTION		UNIVERSITY OF PRETORIA			

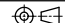


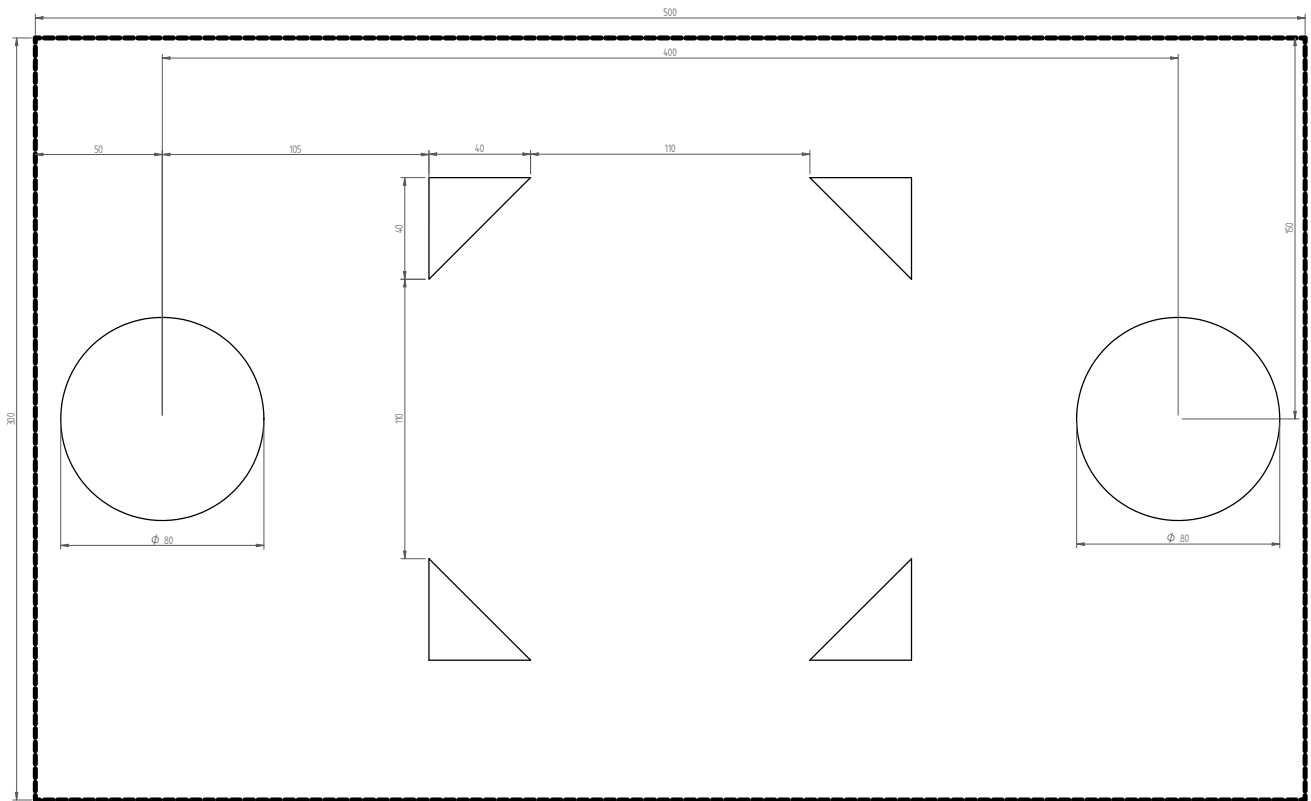
SOLID EDGE ACADEMIC COPY

TITLE	4-Q-Orth MASK 1	DATE	14/06/2011	SIZE	A2
SURNAME	van Schalkwyk	INITIALS	L	SCALE	100:1
STUDENT NR.		DISCIPLINE	PHYSICS	FILE NAME	4-Q-OrthLeft
PROJECTION		UNIVERSITY OF PRETORIA			

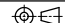


SOLID EDGE ACADEMIC COPY

TITLE	4-Q-DeTh MASK 2	DATE	14/06/2011	SIZE	A2
SURNAME	van Schalkwyk	INITIALS	L	SCALE	100:1
STUDENT NR.		DISCIPLINE	PHYSICS	FILE NAME	4-Q-DeTh1.dwg
PROJECTION		UNIVERSITY OF PRETORIA			



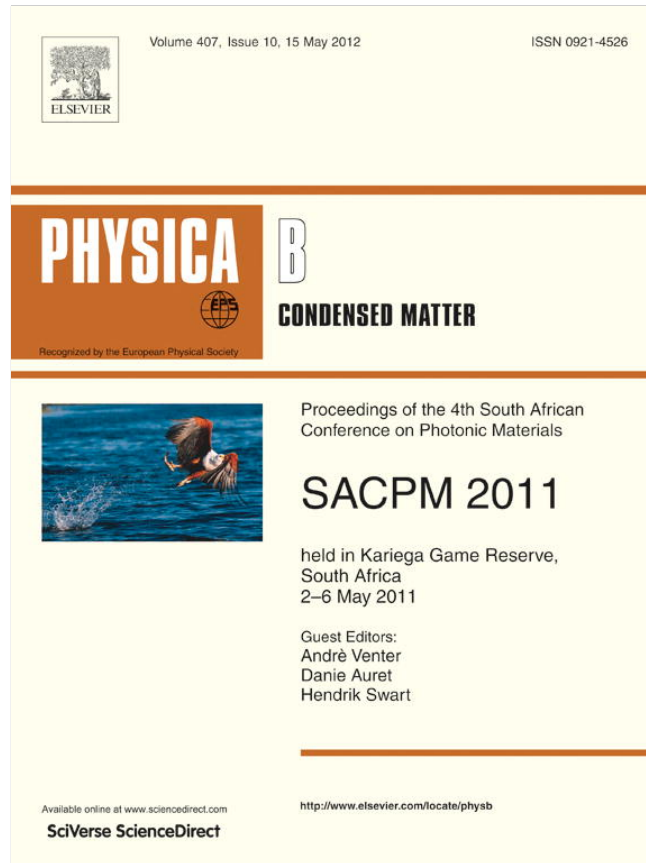
SOLID EDGE ACADEMIC COPY

TITLE	4-Q-DeTh MASK 3	DATE	14/06/2011	SIZE	A2
SURNAME	van Schalkwyk	INITIALS	L	SCALE	100:1
STUDENT NR.		DISCIPLINE	PHYSICS	FILE NAME	4-Q-DeTh1.dwg
PROJECTION		UNIVERSITY OF PRETORIA			

# Appendix E

## Publications

Provided for non-commercial research and education use.  
Not for reproduction, distribution or commercial use.



This article appeared in a journal published by Elsevier. The attached copy is furnished to the author for internal non-commercial research and education use, including for instruction at the authors institution and sharing with colleagues.

Other uses, including reproduction and distribution, or selling or licensing copies, or posting to personal, institutional or third party websites are prohibited.

In most cases authors are permitted to post their version of the article (e.g. in Word or Tex form) to their personal website or institutional repository. Authors requiring further information regarding Elsevier's archiving and manuscript policies are encouraged to visit:

<http://www.elsevier.com/copyright>



Contents lists available at SciVerse ScienceDirect

Physica B

 journal homepage: [www.elsevier.com/locate/physb](http://www.elsevier.com/locate/physb)


## Characterization of AlGa<sub>N</sub>-based metal–semiconductor solar-blind UV photodiodes with IrO<sub>2</sub> Schottky contacts

L. van Schalkwyk\*, W.E. Meyer, F.D. Auret, J.M. Nel, P.N.M. Ngoepe, M. Diale

Department of Physics, University of Pretoria, Private bag X20, Hatfield 0028, South Africa

### ARTICLE INFO

Available online 24 September 2011

#### Keywords:

 AlGa<sub>N</sub>  
 Solar-blind  
 Ultraviolet  
 Iridium oxide  
 Schottky  
 Photodiode  
 Optoelectronic

### ABSTRACT

Intrinsically solar-blind ultraviolet (UV) AlGa<sub>N</sub>-based Schottky photodiodes were fabricated using Iridium oxide (IrO<sub>2</sub>) as the Schottky barrier material. The Ir Schottky contacts were annealed at 700 °C under O<sub>2</sub> ambient and the photodiodes characterized with an optoelectronic system. The main parameters extracted from *I*–*V* measurements were an average ideality factor of 1.38, a Schottky barrier height of 1.52 eV, a reverse leakage current density at –1 V bias of 5.2 nA/cm<sup>2</sup> and series resistance of 250 Ω. After spectral characterization, it was found that annealing, alone, of the Ir contact to form the more UV transmissive IrO<sub>2</sub> does not always improve the responsivity. The deposition of a Au probe contact on the IrO<sub>2</sub> contact increased the responsivity from 40 mA/W to 52 mA/W at 275 nm with respect to the annealed Ir contact. However, the ideality factor degraded to 1.57, Schottky barrier height lowered to 1.19 eV, reverse leakage current density increased to 49 nA/cm<sup>2</sup> and series resistance decreased to 100 Ω with the addition of the Au contact. The radiation hardness of AlGa<sub>N</sub> was also confirmed after studying the effects of 5.4 MeV He-ion irradiation using <sup>241</sup>Am for a total fluence of 3 × 10<sup>13</sup> cm<sup>–2</sup>.

© 2011 Elsevier B.V. All rights reserved.

### 1. Introduction

Al<sub>x</sub>Ga<sub>1–x</sub>N is one of the promising photonic materials for use in tunable intrinsically solar-blind ultraviolet (UV) detectors. These detectors have numerous applications in the scientific, industrial and military fields [1–3].

The UV spectrum is commonly defined as light with a wavelength ranging from 10 nm to 400 nm [1]. Although the Sun radiates over the entire UV spectrum, the Earth's atmosphere absorbs strongly in some regions of the UV spectrum. Specifically, wavelengths between 200 nm and 300 nm are mainly absorbed by ozone [1,2]. Photodiodes sensitive only to wavelengths in the UV-C region (280–200 nm) are referred to as solar-blind UV photodiodes. These photodiodes will therefore only respond to terrestrial sources radiating in the UV-C region.

Al<sub>x</sub>Ga<sub>1–x</sub>N is a ternary semiconductor, of which the bandgap can be varied by changing the Al mole fraction, *x*. This allows for tunability of the range of wavelengths to which Schottky photodiodes manufactured on the AlGa<sub>N</sub> are sensitive [4]. Schottky photodiodes are of particular interest because of their advantages over p–n junction photodiodes, such as higher short-wavelength sensitivity and faster response [1,2]. However, some disadvantages are lower breakdown voltages and large reverse leakage

currents [2]. Through electrical and spectral characterization of AlGa<sub>N</sub>-based Schottky photodiodes the effects of varying parameters, such as metallization, metallization technique, metal thickness and annealing can be investigated in order to optimize the photodiodes for a specific application.

In this paper, front illuminated AlGa<sub>N</sub>-based metal–semiconductor solar-blind UV photodiodes will be considered. For these types of photodiodes it is essential to make use of materials with high optical transmittance in the UV region as Schottky barrier contacts. Iridium oxide (IrO<sub>2</sub>) has been effectively used as a Schottky barrier material for Ga<sub>N</sub> metal–semiconductor–metal UV photodetectors [5]. Being one of the conducting metal oxides, IrO<sub>2</sub> has advantages such as a high work function (> 5 eV), low resistivity (approx. 50 μΩ cm) and high optical transmittance in the UV region [5]. Therefore, in this study we investigate the electrical and spectral characteristics of Ir Schottky contacts on AlGa<sub>N</sub>.

### 2. Experimental procedure

We used Al<sub>0.35</sub>Ga<sub>0.65</sub>N-based (4.2 eV bandgap [4]) samples obtained from Technologies and Devices International, Inc. for this study. These samples were prepared in the same manner as Ga<sub>N</sub>-based samples. Sample preparation consisted of chemical degreasing, followed by wet chemical etching [6,7]. A layered ohmic structure of Ti/Al/Ni/Au (150/2000/450/500 Å) was deposited. The

\* Corresponding author.

 E-mail address: [Louwrens.VanSchalkwyk@up.ac.za](mailto:Louwrens.VanSchalkwyk@up.ac.za) (L. van Schalkwyk).



ohmic contacts were annealed under an argon ambient for 5 min at both 500 °C and then at 700 °C. Circular 0.65 mm-diameter 50 Å-thick Ir contacts were deposited through a metal contact mask as Schottky contacts. The Schottky photodiodes were annealed in O<sub>2</sub> ambient for 20 min at 700 °C to form the more UV transmissive IrO<sub>2</sub> Schottky contacts. Thereafter, 0.3 mm-diameter 1000 Å-thick circular Au probe contacts were deposited on the Schottky contacts. This was done to investigate the effect of future wire bonding on the Schottky photodiodes.

Electrical and spectral characterization were done after each of the fabrication steps. Finally, the effects of 5.4 MeV He-ion irradiation using <sup>241</sup>Am for a total fluence of 3 × 10<sup>13</sup> cm<sup>-2</sup> were studied.

Characterization of the Schottky photodiodes was done with an optoelectronic system. For electrical characterization a programmable HP4140B pA meter/DC source for current–voltage (*I*–*V*) measurements and a HP4192A Low Frequency Impedance Analyzer for capacitance–voltage (*C*–*V*) measurements were used. Parameters were extracted from the *I*–*V* and *C*–*V* characteristics as discussed in Sze and Ng [8, Chapter 3].

Spectral characterization in the UV region was done using a 30 W deuterium lamp, mounted directly onto a Digikröm DK240 1/4-m Czerny–Turner type monochromator. An optical fibre led the light from the monochromator to the photodiode, which was placed inside a light-tight shielded enclosure that eliminates electromagnetic interference from external noise sources. The irradiance (W/cm<sup>2</sup>) of the monochromatic light incident on the photodiode was calibrated using Gamma Scientific's flexOptometer with a Si-based detector.

The photodetector substitution method was followed for the calibration of the UV source [9, Chapter 3]. The optical fibre was placed perpendicular to the calibration detector such that the photosensitive area was overfilled. The constant spectral resolution function of the monochromator was enabled to provide a constant bandwidth of 1.5 nm throughout the calibration and measurement procedure. The UV source irradiance was calibrated for wavelengths ranging from 200 nm to 350 nm. The optical fibre was then placed perpendicular and closer to the photodiode under investigation such that the photosensitive area was still overfilled. Hence, the sample subtended a similar solid angle as the detector used for calibration.

Using radiometry and assuming a point source, it can be shown that the irradiance (W/cm<sup>2</sup>) at the photodiode can be calculated from

$$E_{\lambda}^{\text{PD}} = E_{\lambda}^{\text{CD}} \left( \frac{R_{\text{CD}}}{R_{\text{PD}}} \right)^2 \quad (1)$$

where  $E_{\lambda}^{\text{CD}}$  is the irradiance (W/cm<sup>2</sup>) at a specific wavelength as measured by the calibration detector at a distance  $R_{\text{CD}}$  from the optical fibre end, and  $R_{\text{PD}}$  the distance of the photodiode to the optical fibre end.

The two main parameters studied from the spectral characterization is the current responsivity and quantum efficiency. Current responsivity (A/W) is the ratio between the short-circuit photocurrent density (A/cm<sup>2</sup>) and the irradiance of the light source [1]. The current responsivity (A/W) at a specific wavelength was calculated from

$$\mathcal{R}_{\lambda} = \frac{J_{\lambda}^{\text{ph}}}{E_{\lambda}^{\text{PD}}} \quad (2)$$

where  $J_{\lambda}^{\text{ph}}$  is the photocurrent density (A/cm<sup>2</sup>) during illumination at a specific wavelength of monochromatic light. The photocurrent generated during the illumination of the photodiode was measured with the HP4140B pA meter at zero bias.

The number of electron–hole pairs generated (photocurrent) per incident photon is referred to as the quantum efficiency [1]. The quantum efficiency is related to the current responsivity as follows:

$$\eta_{\lambda} = \mathcal{R}_{\lambda} \frac{hc}{\lambda} \quad (3)$$

where  $\lambda$  is the wavelength,  $c$  the speed of light and  $h$  the Planck constant [1].

### 3. Results and discussion

#### 3.1. Electrical characterization

Dark *I*–*V* and *C*–*V* measurements were made before any UV illumination after each of the fabrication steps and after He-ion irradiation. Typical dark *I*–*V* characteristics of a good Ir Schottky photodiode is shown in Fig. 1. The average values of the parameters extracted from the *I*–*V* characteristics of the samples are listed in Table 1.

For the Ir Schottky photodiodes, the average ideality factor ( $n$ ) improved after annealing from 1.63 to 1.38 with respect to the as-deposited state, this can also be seen in Fig. 1. The Schottky barrier height ( $\phi_{\text{B}}$ ) was 1.34 eV at the as-deposited state, but increased to 1.52 eV after annealing with a 15% standard deviation. Jeon and Lee [10] observed the same effect of Schottky barrier height increase after annealing. They had an increase from 0.68 eV to 1.07 eV for the Ir contact on their sample. The series resistance ( $R_{\text{S}}$ ) also decreased significantly from 1200 Ω to 250 Ω after annealing with a 25% standard deviation. The average reverse leakage current density ( $J_{\text{R}}$ ) has increased by a factor of approx. 30, but in some cases the reverse leakage current actually decreased, as seen in Fig. 1 and also found by Jeon and Lee [10].

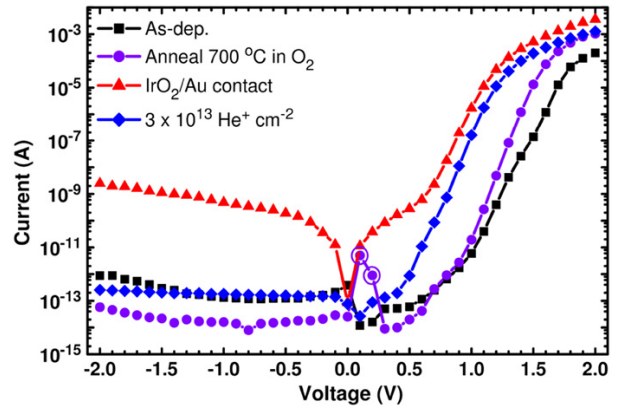


**Fig. 1.** *I*–*V* characteristics of the Ir Schottky photodiodes for each of the fabrication steps and after 5.4 MeV He-ion irradiation. Circled data points were negative current readings obtained during forward bias measurements.

**Table 1**

Average ideality factor, Schottky barrier height, reverse leakage current density and series resistance of the Ir Schottky photodiodes for each of the fabrication steps and after He-ion irradiation.

Fabrication step	$n$	$\phi_{\text{B}} \pm 15\%$ (eV)	$J_{\text{R}}$ at $-1$ V (nA/cm <sup>2</sup> )	$R_{\text{S}} \pm 25\%$ (Ω)
As-dep.	1.63	1.34	0.18 ± 0.23	1200
Annealed	1.38	1.52	5.2 ± 8.4	250
IrO <sub>2</sub> /Au	1.57	1.19	49 ± 84	100
He <sup>+</sup>	1.86	1.17	0.08 ± 0.04	310

The deposition of the Au probe contact on the IrO<sub>2</sub> Schottky photodiode resulted in an even lower series resistance of 100 Ω. The Schottky barrier height lowered to 1.19 eV in comparison with the as-deposited and annealed states. This value for the Schottky barrier height was also more comparable to the 1.07 eV obtained by Jeon and Lee [10]. The ideality factor however degraded to 1.57, but was still better than the as-deposited state. A difference in the reverse leakage current density was also observed. It increased further by a factor of approx. 10 on average, or as seen in Fig. 1 by a factor of 30 000 for one of the samples. Fluctuations in the small reverse leakage currents ( $< 10^{-10}$  A) measured, resulted in the large standard deviations of the averages.

After the He-ion irradiation the average ideality factor degraded for most of the samples even more to 1.86, but the ideality factor for the one sample presented in Fig. 1 improved to that obtained after annealing. The Schottky barrier height did not change significantly compared to that of the deposited Au contact. The series resistance increased to 310 Ω, which was somewhat greater than after annealing. The reverse leakage current density has however improved significantly on average, as seen in Fig. 1. The Au probe contacts started to flake off and this reduction in Au probe contact definitely contributed to the increase in series resistance, lower reverse leakage current measurements and degraded ideality factor.

The free carrier concentration was found to be approx.  $1.4 \times 10^{18} \text{ cm}^{-3}$  from C–V measurements. After He-ion irradiation it has decreased by at least 30% to  $1.0 \times 10^{18} \text{ cm}^{-3}$ .

### 3.2. Spectral characterization

After each dark *I*–*V* and C–*V* measurement, the measurement probes were left in place and the optical fibre was positioned. Fig. 2 shows the spectral responsivities measured at zero bias for a photosensitive area of 0.33 mm<sup>2</sup> of the same photodiode used for Fig. 1.

A clear cut-off at approx. 295 nm (4.2 eV) was observed for all the photodiodes as seen in Fig. 2 which corresponded well with the absorption edge of Al<sub>0.35</sub>Ga<sub>0.65</sub>N. Considering the responsivity at 275 nm ( $\mathcal{R}_{275}$ ) the as-deposited Ir Schottky photodiodes gave an average of  $(48 \pm 16)$  mA/W and a quantum efficiency ( $\eta_{275}$ ) of  $(23 \pm 6)\%$ .

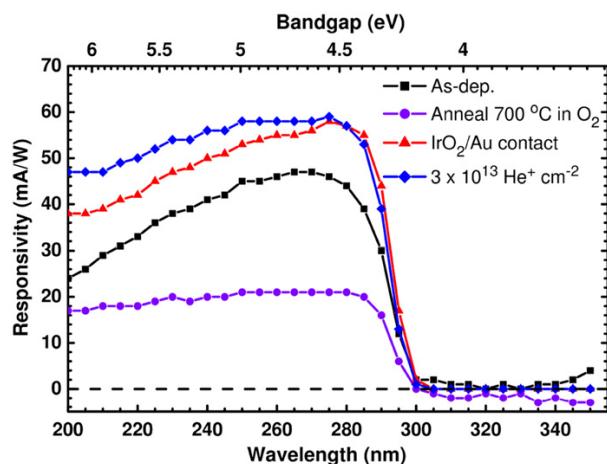


Fig. 2. Spectral responsivities of the Ir Schottky photodiodes for each of the fabrication steps and after 5.4 MeV He-ion irradiation at zero biasing.

To obtain the more UV transmissive IrO<sub>2</sub> the photodiodes were annealed, but the  $\mathcal{R}_{275}$  and  $\eta_{275}$  decreased to  $(40 \pm 26)$  mA/W and  $(18 \pm 12)\%$  respectively, which was not expected. The deposition of the Au probe contact resulted in a smaller photosensitive area of 0.261 mm<sup>2</sup>, but the  $\mathcal{R}_{275}$  and  $\eta_{275}$  increased to  $(52 \pm 17)$  mA/W and  $(23 \pm 7)\%$  respectively.

After the He-ion irradiation there was an unexpected improvement on the  $\mathcal{R}_{275}$  and  $\eta_{275}$  to  $(64 \pm 8)$  mA/W and  $(29 \pm 3)\%$  respectively. This was again attributed to the reduction in Au probe contact as the Au flaked off, which led to parts where the UV light could pass through. Because of this, the photosensitive area of 0.261 mm<sup>2</sup> used in the calculations was not valid and could have been larger.

### 4. Conclusions

Electrical characterization indicated that, after annealing the series resistance decreased significantly for all photodiodes. The addition of a Au probe contact on the IrO<sub>2</sub> brought a further reduction in series resistance. On average, the series resistance of the 0.65 mm Schottky photodiodes decreased from 1200 Ω for the as-deposited Ir, to 250 Ω after annealing and to 100 Ω after the addition of Au probe contacts.

Annealing improved the average ideality factor and the reverse leakage current densities were still of reasonable order. The average reverse leakage current density at  $-1$  V bias was larger after the deposition of the Au probe contacts, increasing from 5.2 nA/cm<sup>2</sup> to 49 nA/cm<sup>2</sup>. An average Schottky barrier height of 1.52 eV and 1.19 eV was calculated from *I*–*V* measurements, after annealing and the addition of Au probe contacts, respectively.

Spectral characterization showed that, in all cases the cut-off wavelength was at approx. 295 nm (4.20 eV) which corresponded well to the bandgap as predicted when using 35% mol fraction Al. Wavelengths shorter than the cut-off wavelength successfully generated electron–hole pairs per incident photon.

However, annealing did not improve the average responsivity and quantum efficiencies as compared to both the as-deposited Ir and addition of Au probe contacts. It is suggested that the thin 50 Å-thick Ir Schottky contact does not make sufficient contact with the probe used to measure the small photocurrent after annealing, compared to when the Au probe contact was deposited. Therefore it is not only important to use materials with high optical transmittance in the UV region, but the photocurrent must also be effectively conducted. Hence, future wire bonding to the Schottky photodiodes can further improve responsivities.

The III–V nitrides are known to be very radiation hard [2]. Apart from the 30% decrease in the free carrier concentration, the effects observed after a total fluence of  $3 \times 10^{13} \text{ He}^+ \text{ cm}^{-2}$  were not significant and are inconclusive, because of the loss in the Au probe contacts. To obtain more reasonable results in the future, the Au probe contacts should be annealed and the sample subjected to higher fluences of He-ion irradiation.

### Acknowledgements

The authors gratefully acknowledge the financial support of the South African National Research Foundation (NRF) and the Technology Innovation Agency (TIA).

*Disclaimer:* Any opinion, findings and conclusions or recommendations in this material are those of the author(s) and therefore the NRF do not accept any liability in regard thereto.

## Author's personal copy

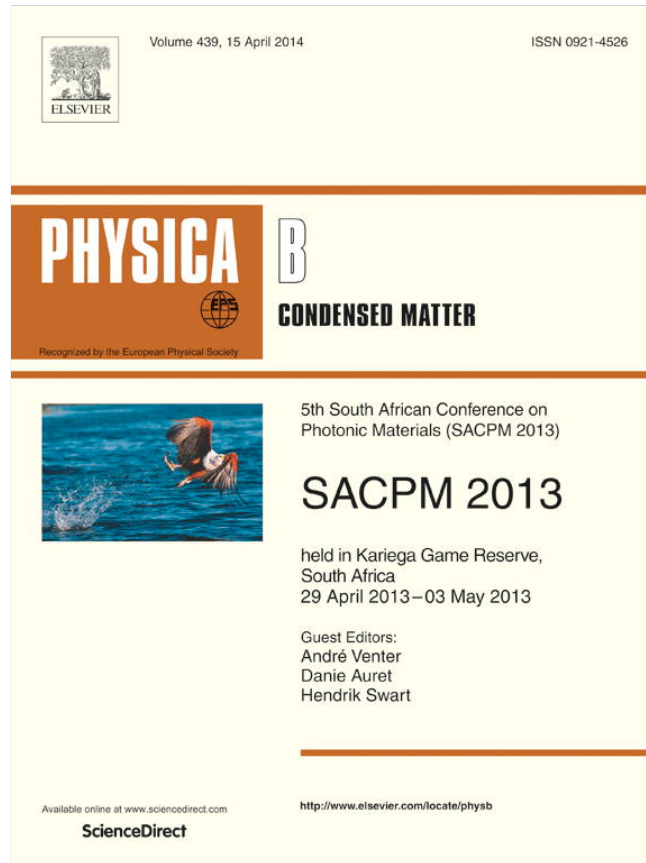
1532

*L. van Schalkwyk et al. / Physica B 407 (2012) 1529–1532*

### References

- [1] Y.A. Goldberg, *Semicond. Sci. Technol.* 14 (7) (1999) 41.
- [2] M. Razeghi, A. Rogalski, *J. Appl. Phys.* 79 (10) (1996) 7433.
- [3] E. Monroy, F. Calle, J. Pau, E. Muñoz, F. Omnès, B. Beaumont, P. Gilbert, *J. Cryst. Growth* 230 (3–4) (2001) 537.
- [4] F. Omnès, N. Marengo, B. Beaumont, P. de Mierry, E. Monroy, F. Calle, E. Muñoz, *J. Appl. Phys.* 86 (9) (1999) 5286.
- [5] J.K. Kim, H.W. Jang, C.M. Jeon, J.L. Lee, *Appl. Phys. Lett.* 81 (24) (2002) 4655.
- [6] M. Diale, F. Auret, N. van der Berg, R. Odendaal, W. Roos, *Appl. Surf. Sci.* 246 (1–3) (2005) 279.
- [7] P. Janse van Rensburg, F. Auret, V. Matias, A. Vantomme, *Physica B: Condens. Matter* 404 (22) (2009) 4411.
- [8] S. Sze, K. Ng, *Physics of Semiconductor Devices*, 3rd ed., John Wiley & Sons, Hoboken, 2007.
- [9] T.C. Larason, J.M. Houston, *Spectroradiometric Detector Measurements: Ultraviolet, Visible, and Near-Infrared Detectors for Spectral Power*, vol. 41, National Institute of Standards and Technology Special Publication 250-41, Gaithersburg, 2008.
- [10] C.M. Jeon, J. Lee, *J. Appl. Phys.* 95 (2) (2004) 698.

Provided for non-commercial research and education use.  
Not for reproduction, distribution or commercial use.



This article appeared in a journal published by Elsevier. The attached copy is furnished to the author for internal non-commercial research and education use, including for instruction at the authors institution and sharing with colleagues.

Other uses, including reproduction and distribution, or selling or licensing copies, or posting to personal, institutional or third party websites are prohibited.

In most cases authors are permitted to post their version of the article (e.g. in Word or Tex form) to their personal website or institutional repository. Authors requiring further information regarding Elsevier's archiving and manuscript policies are encouraged to visit:

<http://www.elsevier.com/authorsrights>



Contents lists available at ScienceDirect

Physica B

 journal homepage: [www.elsevier.com/locate/physb](http://www.elsevier.com/locate/physb)


## Implementation of an AlGa<sub>N</sub>-based solar-blind UV four-quadrant detector



L. van Schalkwyk\*, W.E. Meyer, J.M. Nel, F.D. Auret, P.N.M. Ngoepe

Department of Physics, University of Pretoria, Private Bag X20, Hatfield 0028, South Africa

### ARTICLE INFO

Available online 9 November 2013

#### Keywords:

 AlGa<sub>N</sub>  
 Solar-blind  
 Ultraviolet  
 Iridium oxide  
 Four-quadrant  
 UV-to-visible rejection ratio

### ABSTRACT

An AlGa<sub>N</sub>-based front illuminated intrinsically solar-blind ultraviolet four-quadrant Schottky detector was fabricated and characterized. A layered ohmic structure was deposited followed by a multi-step annealing method. Ultraviolet transmissive iridium oxide was used as the Schottky barrier material and formed by a two-step annealing method. Au contacts were deposited on the Schottky contacts and annealed. The detector was mounted onto a commercial chip carrier and wires were epoxy bonded from the ohmic and Au contacts to the carrier strips. The detector had an average ideality factor of  $1.97 \pm 0.08$ , a Schottky barrier height of  $(1.22 \pm 0.07)$  eV, a reverse leakage current density of  $(2.1 \pm 4)$  nA/cm<sup>2</sup>, a series resistance of  $(120 \pm 30)$  Ω and a free carrier concentration of  $(1.6 \pm 0.3) \times 10^{18}$  cm<sup>-3</sup>. Spectral characterization on the photosensitive area of  $7.3 \times 10^{-3}$  cm<sup>2</sup> yielded a cut-off wavelength at  $(275 \pm 5)$  nm (4.59 eV to 4.23 eV) for each quadrant, corresponding to the absorption edge of a  $(46 \pm 3)\%$  Al content AlGa<sub>N</sub>-based material. The detector had an average responsivity of  $(28 \pm 2)$  mA/W and a quantum efficiency of  $(14 \pm 1)\%$  at 250 nm. The ultraviolet-to-visible and near-infrared rejection ratio was between  $10^3$  and  $10^5$  for most of the quadrants. Characterization showed uniformity across the quadrants, proving the detector feasible for implementation in future ultraviolet-sensitive electro-optic devices.

© 2013 Elsevier B.V. All rights reserved.

### 1. Introduction

The Sun radiates over the entire ultraviolet (UV) spectrum, however, ozone in the Earth's atmosphere strongly absorbs wavelengths between 200 nm and 300 nm [1,2]. Solar-blind UV detectors are sensitive only to wavelengths in the UV-C region (200–280 nm) and therefore only respond to terrestrial sources radiating in this region [3].

UV research began in the latter half of the 19th century and the development of electro-optic systems for studying objects emitting in the UV region (10–400 nm) was stimulated after World War II, because of their military, industrial and scientific applications [1,2,4]. These systems and their components need to be robust, withstand UV radiation, and have good signal-to-noise ratios ( $S/N$ ). They also need to be compact, environmentally friendly and cost effective. However, traditional electro-optics systems make use of sensors that consist of photomultiplier tubes (PMT) and Si-based detectors [5]. The wide range in wavelength response of these detectors requires expensive additional filters that result in added electronics to improve  $S/N$ , and PMT are needed for high photosensitivity which use high-voltage power supplies, resulting in bulky systems [1,5].

Advances in material growth techniques and processing of group-III-nitrides resulted in a unique semiconductor material system, one being the ternary semiconductor Al<sub>x</sub>Ga<sub>1-x</sub>N [6,7]. The AlGa<sub>N</sub> semiconductor system offers a wide direct bandgap that is tuneable over a spectral range by varying the Al mole fraction ( $x$ ) [5]. This allows detectors not to respond to certain (longer) wavelengths, making them intrinsically “blind” to specific wavelengths, eliminating the need for expensive filters in systems. Moreover, the III-nitride optoelectronic devices promise to have higher efficiencies, are environmentally friendly, robust and being compact, will diversify their application [7].

We investigated the implementation of an AlGa<sub>N</sub>-based solar-blind UV four-quadrant detector, after success in studying front illuminated intrinsically solar-blind UV AlGa<sub>N</sub>-based Schottky photodiodes with iridium oxide (IrO<sub>2</sub>) as the Schottky barrier material, and feasibility of wire bonding with the addition of Au contacts [3].

### 2. Experimental procedure

An Al<sub>0.45</sub>Ga<sub>0.55</sub>N-based (4.47 eV bandgap [8]) sample obtained from Technologies and Devices, Inc. was used for the fabrication and characterization of a front illuminated four-quadrant intrinsically solar-blind UV Schottky detector. Sample preparation consisted of chemical degreasing, followed by wet chemical

\* Corresponding author.

 E-mail address: [Louwrens.VanSchalkwyk@up.ac.za](mailto:Louwrens.VanSchalkwyk@up.ac.za) (L. van Schalkwyk).



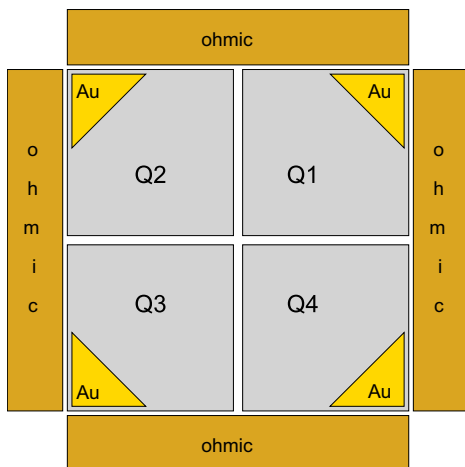


Fig. 1. Schematic illustration of the deposited metal contacts forming a four-quadrant detector.

etching [9,10]. Fabrication was done by performing depositions through three different metal contact masks defining the ohmic, Schottky and Au contacts as illustrated in Fig. 1. A layered ohmic structure of Ti/Al/Ni/Au (300/1800/400/1500 Å) was deposited [11]. The ohmic contacts were multi-step annealed under an argon ambient for 3 min at 400 °C, 20 s at 700 °C, 30 s at 830 °C and 30 s at 900 °C [11,12]. Square (0.9 × 0.9) mm, 50 Å-thick Ir contacts were deposited as Schottky contacts. The Schottky diodes were two-step annealed in O<sub>2</sub> ambient for 30 min at both 600 °C and 730 °C to form the more UV transmissive IrO<sub>2</sub> Schottky photo-diodes [13–15]. Thereafter, 0.8 × 10<sup>-3</sup> cm<sup>2</sup>, 1500 Å-thick triangular Au contacts were deposited on top of the outermost corners of the Schottky contacts and annealed in O<sub>2</sub> ambient for 10 min at 500 °C. The detector was mounted onto a commercial chip carrier and wires were epoxy bonded from the ohmic and Au contacts to the carrier strips using EPO-TEK H20E silver-filled epoxy.

Each quadrant was characterized with an optoelectronic system [3]. Measurements were made by placing the probes on the chip carrier strips that were epoxy wire bonded to the corresponding contacts. Electrical characterization was performed on the 8.1 × 10<sup>-3</sup> cm<sup>2</sup> Schottky contacts and consisted of current–voltage (*I*–*V*) and capacitance–voltage (*C*–*V*) measurements. The main parameters determined from the *I*–*V* measurements were the ideality factors (*n*), the Schottky barrier height ( $\phi_B$ ), the reverse leakage current density ( $J_R$ ) at –1 V bias and series resistance ( $R_S$ ). The free carrier concentration ( $N_D$ ) was determined from *C*–*V* measurements.

Spectral characterization included the cut-off wavelength ( $\lambda_{\text{cut-off}}$ ), responsivity ( $\mathcal{R}_i$ ), quantum efficiency ( $\eta_i$ ) at specific wavelengths and also the UV-to-visible and near-infrared (UV-to-VIS/NIR) rejection ratio of each quadrant with a photosensitive area of 7.3 × 10<sup>-3</sup> cm<sup>2</sup>. We calculated the UV-to-VIS/NIR rejection ratio as follows:

$$J_{\text{ph}}(\lambda_s)/J_{\text{ph}}(\lambda \geq \lambda_s) = \frac{J_{\text{ph}}(\lambda_s)}{J_{\text{ph}}(\lambda_i) - J_{\text{ph}}(\lambda_d)} \quad (1)$$

Here, we first measured the dark photocurrent density (PCD) or noise ( $J_{\text{ph}}(\lambda_d)$ ) of each quadrant for a chosen wavelength range, followed by measuring the illuminated PCD ( $J_{\text{ph}}(\lambda_i)$ ) of each quadrant for the same wavelength range. The PCD at a specified wavelength ( $J_{\text{ph}}(\lambda_s)$ ) was then divided by the illuminated PCD after subtracting the dark PCD at the corresponding wavelengths. The spectral PCD measured in the visible-to-near-infrared region was

done using a 30 W tungsten-halogen lamp mounted directly onto a Czerny-Turner type monochromator [3]. A 400 nm cut-on wavelength order sorting filter was also added to aid in eliminating higher-order diffraction effects.

### 3. Results and discussion

#### 3.1. Electrical characterization

Dark *I*–*V* and *C*–*V* measurements were made on each quadrant before any UV illumination. The *I*–*V* characteristics of each quadrant are presented in Fig. 2. The values of the parameters extracted from the electrical characteristics of the quadrants are listed in Table 1.

Electrical characterization resulted in an average ideality factor of 1.97 ± 0.08, a Schottky barrier height of (1.22 ± 0.07) eV, a reverse leakage current density of (2.1 ± 4) nA/cm<sup>2</sup>, a series resistance of (120 ± 30) Ω and a free carrier concentration of (1.6 ± 0.3) × 10<sup>18</sup> cm<sup>-3</sup>.

Comparing the parameters to that of a previous study done by the same authors [3], we found that the average ideality factor degraded by approximately 20% from 1.57 to 1.97, a 3% higher Schottky barrier height from 1.19 eV to 1.22 eV and a 16% increase in series resistance from 100 Ω to 120 Ω. The degradation in ideality factor and higher Schottky barrier height could be a result of the epoxy bonding process, by which some of the epoxy may have made direct contact to the semiconductor material. The addition of the epoxy and connecting wires would have contributed to an increased series resistance. The average reverse leakage current density greatly improved by almost a factor of 25 from 49 nA/cm<sup>2</sup> to 2.1 nA/cm<sup>2</sup>, even with the free carrier concentration being almost 13% more than 1.4 × 10<sup>18</sup> cm<sup>-3</sup> found in [3]. This can either be attributed to the use of an optimized layered ohmic structure

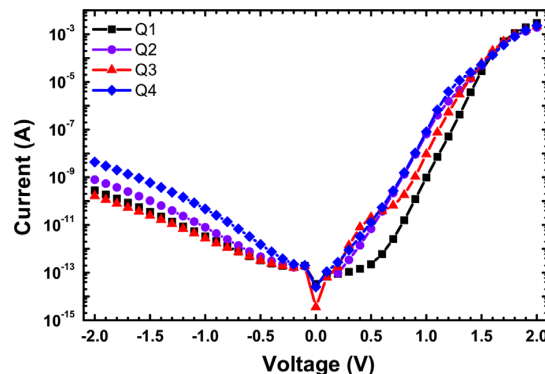


Fig. 2. *I*–*V* characteristics for each quadrant of the front illuminated four-quadrant intrinsically solar-blind UV Schottky detector.

Table 1

Ideality factor, Schottky barrier height, reverse leakage current density, series resistance and free carrier concentration of each quadrant of the front illuminated four-quadrant intrinsically solar-blind UV Schottky detector, together with the overall average.

Quadrant	<i>n</i>	$\phi_B$ (eV)	$J_R$ at –1 V (nA/cm <sup>2</sup> )	$R_S$ (Ω)	$N_D$ (10 <sup>18</sup> cm <sup>-3</sup> )
Q1	1.92	1.30	0.5	90	2.0
Q2	2.09	1.15	1.1	150	1.7
Q3	1.91	1.24	0.4	140	1.3
Q4	1.95	1.18	6.5	110	1.5
Average	1.97	1.22	2.1	120	1.6

together with an improved multi-step annealing method, the proper formation of IrO<sub>2</sub> through the two-step annealing method at appropriate temperatures or by annealing the Au contacts.

### 3.2. Spectral characterization

The dark *I*-*V* and *C*-*V* measurements were followed by spectral characterization for wavelengths ranging from 200 nm to 350 nm. Fig. 3 shows the spectral responsivities measured for each quadrant at zero bias.

Fig. 4 was obtained by first measuring the dark PCD of each quadrant for wavelengths ranging from 400 nm to 1100 nm, followed by measuring the illuminated PCD for the same wavelength range. The PCD measured at 250 nm was then divided by the illuminated PCD after subtracting the dark PCD. The parameters extracted from the spectral characteristics are listed in Table 2.

A cut-off wavelength at  $(275 \pm 5)$  nm for each quadrant was observed, corresponding to the absorption edge of an AlGa<sub>N</sub>-based material having a  $(46 \pm 3)\%$  Al content with a bandgap ranging from 4.59 eV to 4.23 eV [8]. This agreed with the Al<sub>0.45</sub>Ga<sub>0.55</sub>N-

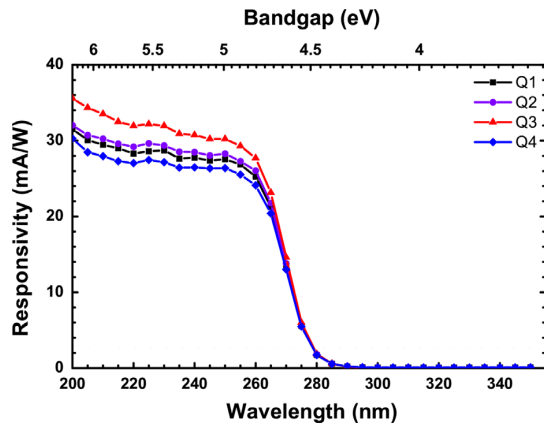


Fig. 3. Spectral responsivities for each quadrant of the front illuminated four-quadrant intrinsically solar-blind UV Schottky detector at zero biasing.

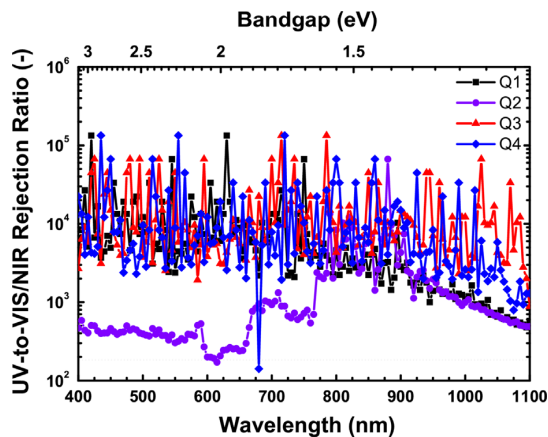


Fig. 4. Spectral UV-to-visible and near-infrared rejection ratios for each quadrant of the front illuminated four-quadrant intrinsically solar-blind UV Schottky detector at zero biasing with respect to the responsivity at 250 nm ( $J_{ph}(\lambda_s)/J_{ph}(\lambda \geq 400)$ ).

**Table 2**

Cut-off wavelength, responsivity, quantum efficiency at 250 nm and the UV-to-visible and near-infrared rejection ratio of each quadrant of the front illuminated four-quadrant intrinsically solar-blind UV Schottky detector, together with the overall average.

Quadrant	$\lambda_{cut-off}$ (nm)	$\mathcal{R}_{250}$ (mA/W)	$\eta_{250}$ (%)	UV-to-VIS/NIR $J_{ph}(\lambda_s)/J_{ph}(\lambda \geq 400)$
Q1	275	28	14	$10^2$ – $10^5$
Q2	275	28	14	$10^2$ – $10^4$
Q3	275	30	15	$10^2$ – $10^5$
Q4	275	26	13	$10^2$ – $10^5$
Average	275	28	14	$10^2$ – $10^5$

based sample supplied. An average responsivity of  $(28 \pm 2)$  mA/W and a quantum efficiency of  $(14 \pm 1)\%$  at 250 nm were found. The UV-to-VIS/NIR rejection ratio was between  $10^3$  and  $10^5$  for most of the quadrants across the considered range.

Comparing some of the parameters again to that found in a previous study done by the same authors [3], we found that both the average responsivity and the quantum efficiency almost halved, from 52 mA/W to 28 mA/W and from 23% to 14%. The samples used may have contributed to the latter, because they originated each from wafers grown differently.

## 4. Summary and conclusions

A front illuminated AlGa<sub>N</sub>-based four-quadrant intrinsically solar-blind UV Schottky detector was fabricated by depositing through three different metal contact masks defining the ohmic, Schottky and Au contacts. The detector was then mounted onto a commercial chip carrier and silver-filled epoxy was used to perform wire bonding from the ohmic and Au contacts to the carrier strips.

The fabrication technique resulted in that the detector had a 20% average degradation in ideality factor, a 3% higher Schottky barrier height, a 16% increase in series resistance. The average reverse leakage current density, however, improved by a factor of 25.

Every quadrant had a cut-off wavelength at  $(275 \pm 5)$  nm, corresponding to a bandgap ranging from 4.59 eV to 4.23 eV. The detector had an average responsivity of  $(28 \pm 2)$  mA/W and a quantum efficiency of  $(14 \pm 1)\%$  at 250 nm. The high UV-to-VIS/NIR rejection ratios between  $10^3$  and  $10^5$  proved the detector to be intrinsically solar-blind for wavelengths ranging from 400 nm to 1100 nm.

Even though the Schottky contacts were not ideal and the quadrants had relatively lower responsivities, and subsequently lower quantum efficiencies, they were almost identical in their characteristics. This allowed for the completion of a joint initiative with the Sensor Science & Technology Competence Area of CSIR's Materials Science and Manufacturing (MSM) Unit, who successfully mounted the four-quadrant detector in a housing integrated with electronics and used UV optics to demonstrate a working UV-sensitive electro-optic device.

The fact that the detector was successfully mounted onto a commercial chip carrier, epoxy wire bonded for easy electronic integration, characterized and yielded uniformity across the quadrants, makes the implementation of an AlGa<sub>N</sub>-based solar-blind UV four-quadrant detector feasible for future UV-sensitive electro-optic devices.

## Author's personal copy

### Acknowledgements

The authors wish to thank the Sensor Science & Technology Competence Area of CSIR's MSM Unit for integrating the four-quadrant detector with UV optics to demonstrate the UV-sensitive electro-optic device. This work is based upon research supported by the Technology Innovation Agency (TIA) and the National Research Foundation (NRF). *Disclaimer:* Any opinion, findings and conclusions or recommendations expressed in this material are those of the author(s) and therefore the NRF does not accept any liability in regard thereto.

### References

- [1] M. Razeghi, A. Rogalski, J. Appl. Phys. 79 (10) (1996) 7433.
- [2] Y.A. Goldberg, Semicond. Sci. Technol. 14 (7) (1999) 41.
- [3] L. van Schalkwyk, W.E. Meyer, F.D. Auret, J.M. Nel, P.N.M. Ngoepe, M. Diale, Phys. B: Condens. Matter 407 (10) (2012) 1529.
- [4] E. Monroy, F. Omnès, F. Calle, Semicond. Sci. Technol. 18 (4) (2003) R33.
- [5] E. Muñoz, Phys. Status Solidi B 244 (8) (2007) 2859.
- [6] M. Razeghi, R. McClintock, J. Cryst. Growth 311 (10) (2009) 3067.
- [7] M. Razeghi, IEEE Photonics J. 3 (2) (2011) 263.
- [8] F. Omnès, N. Marenco, B. Beaumont, P. de Mierry, E. Monroy, F. Calle, E. Muñoz, J. Appl. Phys. 86 (9) (1999) 5286.
- [9] M. Diale, F.D. Auret, N.G. van der Berg, R.Q. Odendaal, W.D. Roos, Appl. Surf. Sci. 246 (1–3) (2005) 279.
- [10] P.J. Janse van Rensburg, F.D. Auret, V.S. Matias, A. Vantomme, Phys. B: Condens. Matter 404 (22) (2009) 4411.
- [11] B. Jacobs, J. Cryst. Growth 241 (1–2) (2002) 15.
- [12] Q. Feng, L.-M. Li, Y. Hao, J.-Y. Ni, J.-C. Zhang, Solid State Electron 53 (9) (2009) 955.
- [13] J.K. Kim, H.W. Jang, C.M. Jeon, J.L. Lee, Appl. Phys. Lett. 81 (24) (2002) 4655.
- [14] B.R. Chalamala, Y. Wei, R.H. Reuss, S. Aggarwal, S.R. Perusse, B.E. Gnade, R. Ramesh, J. Vac. Sci. Technol. B 18 (4) (2000) 1919.
- [15] R.K. Kawar, P.S. Chigare, P.S. Patil, Appl. Surf. Sci. 206 (2003) 90.



## References

- Andrews, D.G. 2010. *An Introduction to Atmospheric Physics*. Cambridge University Press.
- ASTM Standard E490-00a. 2006. *Standard Solar Constant and Zero Air Mass Solar Spectral Irradiance Tables*. [Online] Available at: [rredc.nrel.gov/solar/spectra/am0/ASTM2000.html](http://rredc.nrel.gov/solar/spectra/am0/ASTM2000.html) [Accessed: 2013-09-26].
- ASTM Standard G173-03. 2012. *Standard Tables for Reference Solar Spectral Irradiances: Direct Normal and Hemispherical on 37° Tilted Surface*. [Online] Available at: [rredc.nrel.gov/solar/spectra/am1.5/ASTMG173/ASTMG173.html](http://rredc.nrel.gov/solar/spectra/am1.5/ASTMG173/ASTMG173.html) [Accessed: 2013-09-26].
- Calaprice, A. 2011. *The Ultimate Quotable Einstein*. Princeton University Press.
- Callister, Jr., W.D. 2003. *Materials Science and Engineering: An Introduction*. 6th edn. John Wiley & Sons, Inc.
- Chalamala, B.R., Wei, Yi, Reuss, R.H., Aggarwal, S., Perusse, S.R., Gnade, B.E., & Ramesh, R. 2000. Stability and chemical composition of thermally grown iridium-oxide thin films. *J. Vac. Sci. Technol. B*, **18**(4), 1919–1922.
- Diale, M., Auret, F.D., van der Berg, N.G., Odendaal, R.Q., & Roos, W.D. 2005. Analysis of GaN cleaning procedures. *Appl. Surf. Sci.*, **246**(1-3), 279–289.
- Dungan, D. 2011. *Don't Follow Me, I'm The Leader*.
- Elhamri, S., Newrock, R., Mast, D., Ahoujja, M., Mitchel, W., Redwing, J., Tischler, M., & Flynn, J. 1998.  $\text{Al}_{0.15}\text{Ga}_{0.85}\text{N}/\text{GaN}$  heterostructures: Effective mass and scattering times. *Phys. Rev. B*, **57**(3), 1374–1377.
- Envall, J., Kärhä, P.i, & Ikonen, E. 2006. Calibration of broadband ultraviolet detectors by measurement of spectral irradiance responsivity. *Rev. Sci. Instrum.*, **77**(6), 063110–1–8.

- Feng, Qian, Li, Li-Mei, Hao, Yue, Ni, Jin-Yu, & Zhang, Jin-Cheng. 2009. The improvement of ohmic contact of Ti/Al/Ni/Au to AlGaIn/GaN HEMT by multi-step annealing method. *Solid State Electron.*, **53**(9), 955–958.
- Goldberg, Yu A. 1999. Semiconductor near-ultraviolet photoelectronics. *Semicond. Sci. Tech.*, **14**(7), R41–R60.
- Grundmann, M. 2010. *The Physics of Semiconductors*. 2nd edn. Springer.
- Haigh, J.D. 2007. The Sun and the Earth's Climate. *Living Reviews in Solar Physics*, **4**(2), Chap. 5.
- Hayes, M., Auret, F.D., Wu, L., Meyer, W.E., Nel, J.M., & Legodi, M.J. 2003. Electrical defects introduced during high-temperature irradiation of GaN and AlGaIn. *Phys. B: Condens. Matter*, **340-342**(Dec.), 421–425.
- Hecht, J. 2006. *Understanding Fiber Optics*. 5th edn. Pearson Education, Inc.
- Isaacs, A. (ed). 2003. *A Dictionary of Physics*. 4th edn. Oxford University Press.
- ISO. 2007. *Space environment (natural and artificial). Process for determining solar irradiances*. 1st edn. Space Environment Technologies.
- Jacobs, B, Kramer, M.C.J.C.M., Geluk, E.J., & Karouta, F. 2002. Optimisation of the Ti/Al/Ni/Au ohmic contact on AlGaIn/GaN FET structures. *J. Cryst. Growth*, **241**(1-2), 15–18.
- Janse van Rensburg, P.J., Auret, F.D., Matias, V.S., & Vantomme, A. 2009. Electrical characterization of rare-earth implanted GaN. *Phys. B: Condens. Matter*, **404**(22), 4411–4414.
- Jeon, Chang Min, & Lee, Jong-Lam. 2004. Investigation of IrO<sub>2</sub> and RuO<sub>2</sub> Schottky contacts on AlGaIn/GaN heterostructure. *J. Appl. Phys.*, **95**(2), 698–704.
- Kawar, R.K., Chigare, P.S., & Patil, P.S. 2003. Substrate temperature dependent structural, optical and electrical properties of spray deposited iridium oxide thin films. *Appl. Surf. Sci.*, **206**, 90–101.
- Khare, R.P. 2004. *Fiber Optics and Optoelectronics*. 1st edn. Oxford University Press.
- Kim, Jong Kyu, Jang, Ho Won, Jeon, Chang Min, & Lee, Jong Lam. 2002. GaN metal–semiconductor–metal ultraviolet photodetector with IrO<sub>2</sub> Schottky contact. *Appl. Phys. Lett.*, **81**(24), 4655–4657.

- Kittel, C. 2005. *Introduction to Solid State Physics*. 8th edn. John Wiley & Sons, Inc.
- Larason, T.C., & Houston, J.M. 2008. *Spectroradiometric Detector Measurements: Ultraviolet, Visible, and Near-Infrared Detectors for Spectral Power*. Vol. 41. Gaithersburg: Natl. Inst. Stand. Technol. Spec. Publ. 250-41.
- Liu, Q.Z., & Lau, S.S. 1998. A review of the metal–GaN contact technology. *Solid State Electron.*, **42**(5), 677–691.
- Monroy, E., Calle, F., Pau, J.L., Sánchez, F.J., Muñoz, E., Omnès, F., Beaumont, B., & Gibart, P. 2000. Analysis and modeling of  $\text{Al}_x\text{Ga}_{1-x}\text{N}$ -based Schottky barrier photodiodes. *J. Appl. Phys.*, **88**(4), 2081–2091.
- Monroy, E., Calle, F., Pau, J.L., Muñoz, E., Omnès, F., Beaumont, B., & Gilbert, P. 2001. AlGa<sub>N</sub>-based UV photodetectors. *J. Cryst. Growth*, **230**(3-4), 537–543.
- Monroy, E., Omnès, F., & Calle, F. 2003. Wide-bandgap semiconductor ultraviolet photodetectors. *Semicond. Sci. Tech.*, **18**(4), R33–R51.
- Morkoç, H., Strite, S., Gao, G.B., Lin, M.E., Sverdlov, B., & Burns, M. 1994. Large-band-gap SiC, III-V nitride, and II-VI ZnSe-based semiconductor device technologies. *J. Appl. Phys.*, **76**(3), 1363–1398.
- Muñoz, E. 2007. (Al,In,Ga)N-based photodetectors. Some materials issues. *Phys. Status Solidi B*, **244**(8), 2859–2877.
- Neudeck, G.W. 1989. *The PN junction diode*. 2nd edn. Modular series on solid state devices, vol. 2. Addison-Wesley.
- Nicodemus, F.E., & Kostkowski, H.J. 1978. *Self-study Manual on Optical Radiation Measurements: Part 1–Concepts, Chapters 4 and 5*. Washington, D.C.: NIST.
- Nicodemus, F.E., Kostkowski, H.J., & Hattenburg, A.T. 1976. *Self-Study Manual on Optical Radiation Measurements: Part 1–Concepts, Chapters 1 to 3*. Washington, D.C.: NIST.
- NREL. 2010. *Simple Model of the Atmospheric Radiative Transfer of Sunshine (SMARTS)*. [Online] Available at: [www.nrel.gov/rredc/smarts/](http://www.nrel.gov/rredc/smarts/) [Accessed: 2013-09-26].
- Omnès, F., Marenco, N., Beaumont, B., de Mierry, Ph., Monroy, E., Calle, F., & Muñoz, E. 1999. Metalorganic vapor-phase epitaxy-grown AlGa<sub>N</sub> materials for visible-blind ultraviolet photodetector applications. *J. Appl. Phys.*, **86**(9), 5286–5292.

- Palmer, J.M., & Grant, B.G. 2009. *The Art of Radiometry*. SPIE.
- Pedrotti, F.L., & Pedrotti, L.S. 1993. *Introduction to Optics*. 2nd edn. Prentice-Hall, Inc.
- Philofsky, E. 1970. Intermetallic formation in gold-aluminum systems. *Solid State Electron.*, **13**(10), 1391–1394.
- Pierret, R.F. 1989. *Semiconductor fundamentals*. 2nd edn. Modular series on solid state devices, vol. 1. Addison-Wesley.
- Razeghi, M. 2011. III-Nitride Optoelectronic Devices: From Ultraviolet Toward Terahertz. *IEEE Photonic. J.*, **3**(2), 263–267.
- Razeghi, M., & McClintock, R. 2009. A review of III-nitride research at the Center for Quantum Devices. *J. Cryst. Growth*, **311**(10), 3067–3074.
- Razeghi, M., & Rogalski, A. 1996. Semiconductor ultraviolet detectors. *J. Appl. Phys.*, **79**(10), 7433–7473.
- Rhoderick, E.H. 1982. Metal-Semiconductor Contacts. *IEE Proceedings*, **129**(1), 1–14.
- Rhoderick, E.H. 1970. The physics of Schottky barriers. *J. Phys. D: Appl. Phys.*, **3**, 1153–1167.
- Ruvimov, S., Liliental-Weber, Z., Washburn, J., Duxstad, K.J., Haller, E.E., Fan, Z.-F., Mohammad, S.N., Kim, W., Botchkarev, A.E., & Morkoç, H. 1996. Microstructure of Ti/Al and Ti/Al/Ni/Au Ohmic contacts for *n*-GaN. *Appl. Phys. Lett.*, **69**(11), 1556–1558.
- Scannel, J. 2000. *Spreuke van Langenhoven*. Tafelberg-uitgewers Beperk.
- Schroder, D.K. 2006. *Semiconductor Material and Device Characterization*. 3rd edn. Wiley-Interscience.
- Schühle, Udo, & Hochedez, Jean-François. 2013. *Solar-blind UV detectors based on wide band gap semiconductors*. ISSI Scientific Report Series, vol. 9. Springer.
- Streetman, B.G., & Banerjee, S.K. 2006. *Solid State Electronic Devices*. 6th edn. Prentice-Hall, Inc.
- Strehlow, W.H., & Cook, E.L. 1973. Compilation of Energy Band Gaps in Elemental and Binary Compound Semiconductors and Insulators. *J. Phys. Chem. Ref. Data*, **2**(1), 163.

- Sze, S.M. 1985. *Semiconductor Devices, Physics and Technology*. 1st edn. John Wiley & Sons, Inc.
- Sze, S.M., & Ng, K.K. 2007. *Physics of Semiconductor Devices*. 3rd edn. John Wiley & Sons, Inc.
- Taylor, J.R., Zafiratos, C.D., & Dubson, M.A. 2004. *Modern physics for scientists and engineers*. 2nd edn. Prentice-Hall, Inc.
- Thompson, A., & Taylor, B.N. 2008. *Guide for the Use of the Internasional System of Units (SI)*. NIST Special Publication 811.
- van Schalkwyk, L., Meyer, W.E., Auret, F.D., Nel, J.M., Ngoepe, P.N.M., & Diale, M. 2012. Characterization of AlGaIn-based metal–semiconductor solar-blind UV photodiodes with IrO<sub>2</sub> Schottky contacts. *Phys. B: Condens. Matter*, **407**(10), 1529–1532. (Permission granted under CCC licence no. 3420300755774 for both print and electronic reuse of full article in thesis or dissertation).
- van Schalkwyk, L., Meyer, W.E., Nel, J.M., Auret, F.D., & Ngoepe, P.N.M. 2014. Implementation of an AlGaIn-based solar-blind UV four-quadrant detector. *Phys. B: Condens. Matter*, **439**(Apr.), 93–96. (Permission granted under CCC licence no. 3420660708760 for both print and electronic reuse of full article in thesis or dissertation).
- Woan, G. 2000. *The Cambridge Handbook of Physics Formulas*. Cambridge University Press.
- Young, H.D., & Freedman, R.A. 2004. *University Physics with Modern Physics*. 11th edn. Addison-Wesley.

# Index

- bandgap energy, 37
- blackbody, 20
- cladding, 90
- core, 90
- current responsivity, 72
- cut-off wavelength, 28, 72
- depletion approximation, 56
- direct transition, 40
- direct-bandgap, 40
- effective mass, 40
- electron affinity, 50
- electron-volt, 47
- external photoelectric effect, 31
- external photoemissive detector, 31
- extrinsic semiconductor, 42
- Fermi level, 35
- free carrier concentration, 42
- geometric solid angle, 13
- ideality factor, 62
- indirect transition, 41
- indirect-bandgap, 40
- insulator, 38
- internal photoelectric effect, 31
- internal photoemissive detector, 31
- intrinsic semiconductor, 42
- intrinsically, 44
- irradiance, 17
- light, 8
- measurement equation, 19
- metals, 36
- phonon, 41
- photoconductive detector, 32
- photoelectric detector, 31
- photon, 9
- photovoltaic detector, 32
- projected solid angle, 13
- quanta, 9
- quantum efficiency, 73
- radiance, 15
- radiant exitance, 15
- radiant flux, 15
- radiant intensity, 15
- radiometry, 10
- Schottky barrier height, 53
- semiconductor, 37
- solar-blind, 29
- spectral responsivity, 72
- standard detector, 79
- thermal radiation, 20
- tuneable, 44
- UV-A, B, C, 24
- vacuum UV, 24
- visible-blind, 28
- wide-bandgap semiconductor, 37
- work function, 47